COLLAGEN-BASED SCAFFOLDS FOR HEART VALVE TISSUE ENGINEERING

QI CHEN

WOLFSON COLLEGE



A THESIS SUBMITTED FOR THE DEGREE OF

DOCTOR OF PHILOSOPHY

DEPARTMENT OF MATERIALS

UNIVERSITY OF OXFORD

MICHAELMAS TERM 2013

Abstract

Collagen-Based Scaffolds for Heart Valve Tissue Engineering

D.Phil Thesis Qi Chen

Michaelmas Term 2013 Wolfson College

Tissue engineered heart valve (TEHV) is believed to be a promising candidate for curative heart valve replacements. Collagen, elastin and chondroitin-4-sulfate (C4S) comprise the extra-cellular matrix (ECM) of native heart valves and therefore are suitable materials for TEHV scaffolds.

Freeze-drying technique was able to produce scaffolds with relative densities of 0.3%-2.0% and pore sizes of 33.2μm-201.5μm, without having any major effects on the ultra-structures on the scaffold materials. Subsequent dehydrothermal (DHT) treatment and ultra-violet (UV) irradiation introduced inter- or intra-molecular crosslinks in the scaffolds in forms of ester and amide bonds, as well as the accompanying denaturation of the proteins (i.e. ultra-structure transition from helices to random coils).

The collagen-based scaffolds had tensile, compressive and effective bending moduli ranging from 39.8kPa to 1082kPa, from 2.4kPa to 213.9kPa, and from 11.0kPa to 415.8kPa, respectively. The different behaviours of the wall stretching and the wall buckling in the individual pores of the scaffolds contributed to the different tensile, compressive and bending moduli. The mechanical properties could be tailored through controlling the freezing temperature, the relative density and the composition of the scaffolds. A lower freezing temperature might lead to lower mechanical properties because different pore structures were introduced. When the the relative density of the scaffold increased, the values of the moduli increased exponentially, with an exponential dependence factor larger for the compressive modulus than for the tensile modulus. Adding elastin or C4S into the collagen scaffolds lowered the mechanical properties due to the decrease in the collagen content. Layered structures that combined collagen-rich layers with elastin-rich and/or C4S -rich layers allowed the scaffolds to make use of the different mechanical properties of different layers, and hence to show anisotropic bending behaviour depending on the loading directions. The lower effective bending modulus (9.6 to 25.0kPa) in the *with curvature* (WC) direction than that (18.1kPa to 39.3kPa) in the *against curvature* (AC) direction mimicked the characteristic behaviour of the native heart valves and would be beneficial for a mechanically desirable TEHV. The DHT treatment and UV irradiation were able to increase the mechanical properties of the scaffolds to up to 2.5 times of the original values, by reinforcing the scaffold materials with more crosslinks. In the hydrated status, the hydrophilic C4S improved the water uptake ability of the scaffold and the hydrophobic elastin reduced it. The hydrated layered scaffolds still exhibited bending

anisotropy despite much lower effective bending modulus. Finite element models of the scaffolds produced results that were in agreement with the experiments, and enabled us to perform distributed loading and internal stress analysis on the scaffolds.

The collagen-based scaffolds were seeded with cardiosphere-derived cells (CDCs), and they attached to the scaffolds and showed visible cell division, proliferation and migration. The CDCs exhibited preferred proliferation behaviours on the collagen-C4S scaffolds to that on the collagen-elastin scaffolds because of the cell affinity to the C4S, as well as the elastin-induced contractile cell phenotype and scaffold volume shrinkage. This difference seemed to be less evident in the layered scaffolds due to the cell communication between the layers. The crosslinking process also had effects on the cell proliferation in the ways that it induced ultra-structure changes or volume shrinkage in the scaffolds.

The layered scaffold-cell constructs designed and produced in this study served as a forwarding step towards a mechanically desirable and biologically active TEHV.

Preface

The research described in this thesis was carried out by the author in the Department of Materials at the University of Oxford between October 2009 and December 2013, under the supervision of Dr. Jan. T. Czernuszka. No part of this thesis has been submitted or accepted for any other degree at this university or elsewhere.

Parts of this work have been peer-reviewed and published in Journals, or presented at international conferences as follows:

1. Q Chen, J Czernuszka, Mechanical Properties of Collagen-Elastin Scaffolds for Heart valve Tissue Engineering, Asian Congress on Biotechnology, Shanghai, China, 2011

2. Q Chen, J Czernuszka, Multi-layer Scaffolds for Heart Valve Tissue Engineering, International Conference on Tissue Science and Engineering, Chicago, USA, 2012

3. Q Chen, A Bruyneel, K Clarke, C Carr, J Czernuszka, Collagen-Based Scaffolds for Potential Application in Heart Valve Tissue Engineering, Journal of Tissue Science and Engineering, S11-03, 2012

4. Q Chen, A Bruyneel, C Carr, J Czernuszka, Bio-mechanical Properties of Novel Bi-layer Collagen-Elastin Scaffolds for Heart Valve Tissue Engineering, Procedia Engineering, 59:247, 2013

Acknowledgement

I would like to acknowledge the following supports from all the generous people, without whom this thesis would never have been completed.

First and foremost, I would like to express my great gratitude to my supervisor, Dr. Jan Czernuszka, for giving me the opportunity to conduct this exciting research project, and for his patient guidance and insightful help throughout my D.Phil studies.

I would like to thank my funding bodies, China Scholarship Council, and China Oxford Scholarship Fund, for the financial support for my D.Phil, and for the friendly and helpful scholar networks they have established.

My acknowledgement goes to Dr. Carolyn Carr and Mr. Arne Bruyneel from the Cardiac Metabolism Research Group in the Department of Physiology Anatomy and Genetics for an enjoyable and fruitful collaboration, particularly Arne for training and helping me on the cell experiments.

I would like to thank Prof. Chris Grovenor, Prof. Steve Roberts, and Prof Angus Wilkinson for the laboratory facilities provided. My sincere gratitude goes to Ms. Gabriella Chapman, Dr. Neil Young, and Mr. Shaoyang Yeh for their kind help with SEM, TEM, and MPM, respectively.

Former and current group members and colleagues are thanked here: Dr. Hannah Lee, Dr. Robin Walton, Dr. Yuan-tsan Tseng, Dr. Matthew Thomas, Dr. Hao Zhang, Dr. Asma Yahyouche, Dr. Jenni Tilley, Dr. Zamri Radzi, Ms. Xuan Du, Ms. Maryam Tamaddon, Mr. Park Maneepairoj, Mr. Kerem Bayrakçeken, Ms. Jessica Smith, Ms. Yun Zhu, Mr. Aman Sharma, and Ms. Xue Min, for the inspiring discussions and the valuable knowledge shared.

I am very grateful to have met so many great friends in Oxford, which has filled my life here with joy and love.

Finally my special thanks are going to my beloved ones: my girlfriend Miss. Meng Jiang for sharing with me every happy and difficult moment during my D.Phil, and my parents and grandparents, for their unconditional support and encouragement throughout my stay in the UK.

Table of Contents

Abstract i

Preface iii

Acknowledgement iv

Chapter 1. Introduction 1

Chapter 2. Literature Review 4

2.1 Introduction 4

2.2 Heart Valves 5

2.2.1 Physiological Functions 5

2.2.2 Layered Structures 7

2.2.3 Microscopic Components 9

2.2.4 Heart Valve Mechanics 19

2.3 Heart Valve Tissue Engineering 25

2.3.1 Scaffolds 27

2.3.2 Cells Sources 37

2.3.3 Signals 39

2.4 Summary 42

Chapter 3. Scaffolds Manufacturing and Morphology 44

3.1 Introduction 44

3.2 Materials and Methods 45

3.2.1 Scaffolds Manufacturing 45

3.2.2 Scaffold Morphology 48

3.2.3 Crosslinking 49

3.2.4 Transmission Electron Microscopy 50

3.2.5 Fourier Transform Infra-red Spectroscopy 51

3.2.6 Statistics 51

3.3 Results 52

3.3.1 Scaffold Manufacturing 52

3.3.2 Scaffold Morphology 55

3.3.3 Crosslinking 60

3.3.4 Scaffold Ultra-structures (TEM, FTIR) 62

3.3.5 Layered Scaffolds 72
3.4 Discussion 74
3.4.1 Scaffold Manufacturing and Ultra-structures 74
3.4.2 Scaffold Morphology 78
3.5 Conclusions 83
Chapter 4. Scaffold Mechanical Properties 85
4.1 Introduction 85
4.2 Materials and Methods 87
4.2.1 Mechanical Characterization 87
4.2.2 Finite Element Modelling 88
4.3 Results 91
4.3.1 Uniform-Composition Scaffolds 91
4.3.2 Layered Scaffolds 96
4.3.3 Finite Element Modelling 98
4.3.4 Effects of crosslinking 106
4.4 Discussion 108
4.4.1 Uniform-Composition Scaffolds 108
4.4.2 Layered Scaffolds 115
4.4.3 Effects of Crosslinking 120
4.5 Conclusions 121
Chapter 5. Hydrated Scaffolds 123
5.1 Introduction 123
5.2 Materials and Methods 123
5.2.1 Water Uptake 123
5.2.2 Mechanical Characterization 124
5.2.3 Statistics 124
5.2.4 Finite Element Modelling 125
5.3 Results 125
5.3.1 Water Uptake 125
5.3.2 Mechanical Characterization 126
5.3.3 Finite Element Modelling 132
5.4 Discussion 137

5.5 Conclusions 140
Chapter 6. Cell Behaviour on Scaffolds 141
6.1 Introduction 141
6.2 Materials and Methods 142
6.2.1 CDCs Harvest and Isolation 142
6.2.2 Culture of CDCs on scaffolds 143
6.2.3 Assessment of CDCs Attachment and Proliferation 144
6.2.4 Scanning Electronic Microscopy (SEM) 146
6.2.5 Multi-photon Microscopy (MPM) 146
6.3 Results 148
6.3.1 CDCs Culture on Scaffolds 148
6.3.2 SEM Imaging 153
6.3.3 MPM Imaging 154
6.3.4 Effects of Crosslinking 160
6.4 Discussion 163
6.4.1 CDCs Behaviours on Scaffolds 163
6.4.2 Effects of Crosslinking 167
6.5 Conclusions 169
Chapter 7. Conclusions 172
Chapter 8. Future Work 177
Appendix A 181
Appendix B 184
References 187

Chapter 1. Introduction

The heart, undoubtedly, has one of the most indispensable functions in the human body: to pump the oxygenated blood to the whole body for cellular metabolism. Crucial to maintaining this function are the heart valves, whose delicate opening-closures synchronize with the contraction-relaxations of the heart chambers, regulating the forward flow of the blood [1]. Therefore, heart valve diseases may cause significant morbidity and mortality if no prompt treatment is given. Stenosis (obstruction of the blood flow by the valve) and regurgitation (reversal blood flow across an incompetent valve) are the two major types of diseases that require valve replacement [1].The etiologies of these diseases could vary: for stenosis, congenital abnormal valves are the most common causes for the patients under 70, while valve thickening and calcification are the most common causes for patients over the age of 70; for regurgitation the reasons may include congenital bicuspid valves, infective endocarditis, trauma, calcific degeneration, rheumatic disease, systemic hypertension, etc. [2]

Before the 1950s, surgery on the heart valves seemed to be a nearly insurmountable goal, due to uncontrollable bleeding, and introduction of air emboli during surgery, both of which would have fatal effects on the patients [3]. Amongst the mere 12 attempts of heart valve surgeries between 1913 and 1928, only two patients had survived [1]. The development of the cardiopulmonary bypass procedure at the beginning of the 1950s brought the surgeons a great hope for complex open heart surgeries such as heart valve replacements [1, 4, 5].

In September 1952, Hufnagel successfully introduced the first artificial heart valve to a 30-year-old female patient who had severe aortic valve damage [6, 7]. Known as the

cage-and-ball valve, Hufnagel's valve prosthesis model was improved and received by over 200 patients in the following years [8, 9]. The 60s and 70s saw the hayday of the development of heart valve prostheses. Two more artificial valve designs, the disc valves and the bileaflet valves, came into the market, and together with the cage-and-ball valves, were categorized into 'mechanical valves', as they were mechanically replicating the functions of the native heart valves.

In the meantime, there were those surgeons who were in doubt that the mechanical valves could mimic the elegant movement of the native valves [1]. Especially when the long term complications of the mechanical valves such as thrombosis started to unfold, the research of heart valve prosthesis in another category, biological valves, drew more and more attention. In 1967, Ross completed the first successful human valve replacement using biological valves. The patient's diseased aortic valve was replaced by his own pulmonary valve, and a donor's tissue valve was then used for the pulmonary valve [1]. The biological valves had significant advantages over their mechanical counterparts, such as good hemodynamic properties and low rates of thrombosis [10]. However, even to date, there are still issues associated with calcification and degeneration remaining to be solved [11-13].

With the continuously increasing demand for heart valve replacement (predicted to triple from 290,000 in 2003 to over 850,000 in 2050 [14]), there is a need to find innovative heart valve prostheses that can overcome the limitations in the traditional mechanical and biological valves. The tissue engineering techniques are reported to have produced functional prosthetic heart valves that have the abilities of tissue regeneration and have shown promising results in initial human applications [15-17]. Further success of the tissue engineered heart valves (TEHVs) will depend on the fulfilment of the following requirements: the ability to grow and adapt with the patient,

non-thrombogenicity, non-immunogenicity, minimal or no regurgitation, high durability, and suitable biomechanical properties [1]. These are no easy tasks to accomplish, but the researchers of TEHVs are becoming well prepared to confront these issues.

This thesis is hoping to makes a contribution towards the understanding and the development of TEHVs, mainly from the point of view of materials science. The focus of this study is on the structures and properties of the specific collagen-based materials that act as the scaffolds in the heart valve tissue engineering. The thesis will be divided into the following chapters. Chapter 2 will review the literature for the background knowledge of native heart valves and the extra-cellular matrix materials. It will also discuss the current development of the TEHVs. Chapter 3 will describe the manufacturing route of the collagen-bases scaffolds for TEHVs, and give suggestions of the optimal conditions. It will demonstrate the effects of processing, including freeze-drying and crosslinking, on the scaffolds, by characterizing the ultra-structure and the morphology of the scaffolds. Chapter 4 will study in detail, using both experimental testing and finite element modelling, the mechanical properties of the collagen-based scaffolds, trying to provide a better guidance for designing a mechanically qualified scaffold for TEHVs. Chapter 5 will follow Chapter 4 in characterizing the mechanical properties of the scaffolds in the hydrated state, which is closer to the physiological condition. Chapter 6 will investigate the interactions between cells and scaffolds in vitro, evaluating their biological properties by assessments of cell activities on the scaffolds, coupled with image analysis. Chapter 7 will present the conclusions of this thesis. Chapter 8 will suggest some further improvements that could be made to this work, and will provide recommendations for the future research aspects of the scaffolds.

Chapter 2. Literature Review

2.1 Introduction

Heart valves are very important cardiac organs as they ensure the unidirectional flow of the blood in circulation. Heart valve disease is a major health issue and a significant cause of mortality worldwide. According to the American Heart Association, heart valve diseases were the direct causes of 19,989 deaths, and were contributing to another 42,590 deaths in the US in 2003 [18].

These heart valve diseases can be either congenital or acquired, usually referring to congenital leaflet defects and age-related valve degeneration, respectively. With very limited human valve donors, the most common treatment of these diseases is the implantation of heart valve prostheses. The last 50 years have seen a rapid increase in the clinical application of prosthetic heart valves [19]. After the first successful human valve implantation performed in 1952 [6, 7], more than 80 types of prosthetic heart valves have been designed [20]. There are approximately 200,000 operations involving prosthetic heart valves performed each year worldwide [21], with a growth of 5% per year in the US [22]. Lives of numerous patients have been prolonged by the heart valve replacements.

However, further success of current prosthetic designs is restricted by their intrinsic properties. Limitations such as the risk of thrombosis and calcification, the risk of fatigue, the abnormal hemodynamic flow, and the lack of tissue regeneration ability are still motivating the research for novel heart valve prostheses that exhibit more desirable mechanical properties and biocompatibilities.

So far, the tissue engineered heart valve (TEHV) is believed to be a very promising alternative for a long-lasting and curative heart valve replacement [23]. This chapter, therefore, will attempt to present a comprehensive understanding of heart valves first, covering macro and micro structures of heart valves and their mechanical behaviours, and then review the current TEHV techniques, paying specific attention to collagen-based TEHV scaffolds which is the research topic of this thesis.

2.2 Heart Valves

2.2.1 Physiological Functions

There are two types of heart valves, depending on their anatomical positions in the heart: semilunar valves and atrio-ventricular valves.

The semilunar valves (the aortic valve and the pulmonary valve) are located at the base of the respective artery (see Fig 2.1), and each of them has three symmetrical half-moon shaped leaflets that are attached to the vessel wall at one end and can coapt with one another at their free edges. The leaflets flip towards the arteries during systole to allow the outflow of blood from the ventricles, and the commissure of the free edges during diastole prevents the backflows. The atrio-ventricular valves (the tricuspid valve and the mitral valve) are located between the atria and ventricles, tricuspid valve on the right and mitral valve on the left (see Fig 2.1). Unlike semilunar valves, they are not formed of equally sized leaflets and do not have symmetrical geometries [24].The mitral valve has two leaflets, specified as the anterior and the posterior, the shape of which resembles a mitre of a bishop, from which it received its name. The tricuspid valve usually consists of three leaflets but may also occur with two or four leaflets, and the

number may change during one's life [25]. Both of the atrio-ventricular valves are connected to the papillary muscles on the inner walls of the ventricles via some chord-like collagenous tendons called chordae tendineae. During diastole the leaflets sag into the ventricles in relaxation, allowing the blood to enter the ventricles from the atria. During systole, blood pressure in the ventricles forces the leaflets to close. At the same time the chordae tendineae are in tension, preventing the leaflets from over-flipping into the atria and thus keeping the proper closure of the valves. Regulated by these heart valves, the blood flow can therefore run smoothly in every cardiac cycle and repeat in the whole lifetime for approximately 3×10^9 times [24].

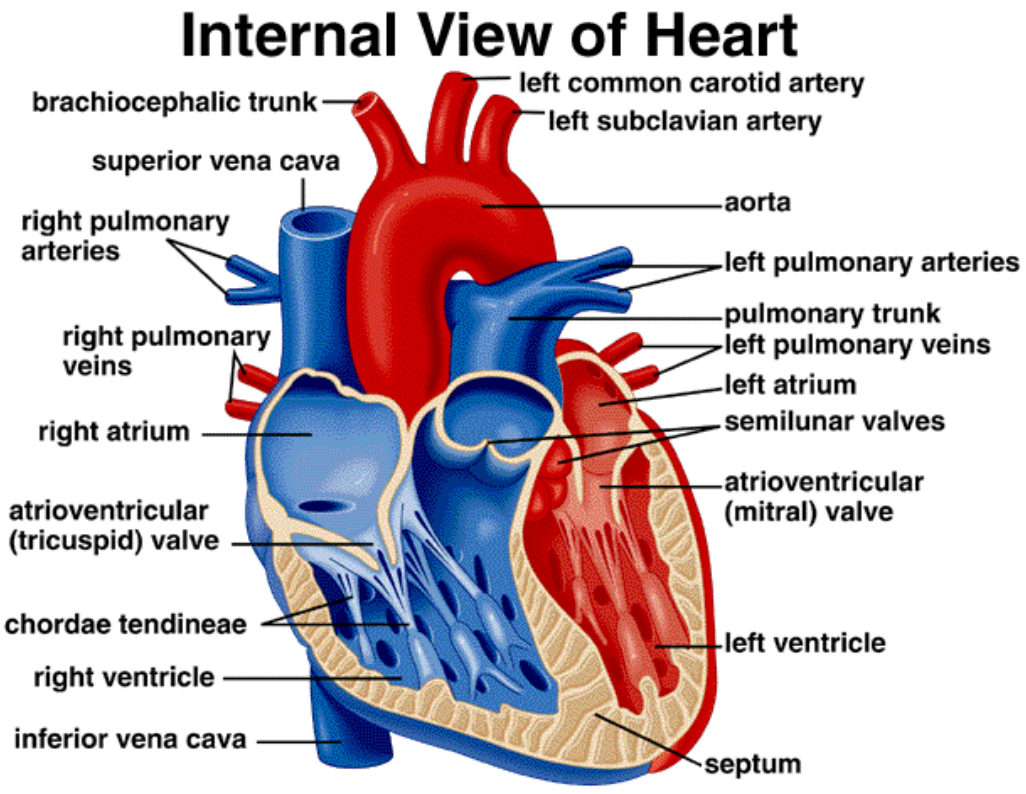


Fig 2.1 Anatomical structure of heart [26]

2.2.2 Layered Structures

All the leaflets of both types of heart valves can be seen to have three distinctive layers: fibrosa, spongiosa, and ventruclaris/atrialis (the former for semilunar valves and the latter for atrio-ventricular valves). It is usually most illustrative to use an aortic valve as an example of the layered structures, as is shown in Fig 2.2.

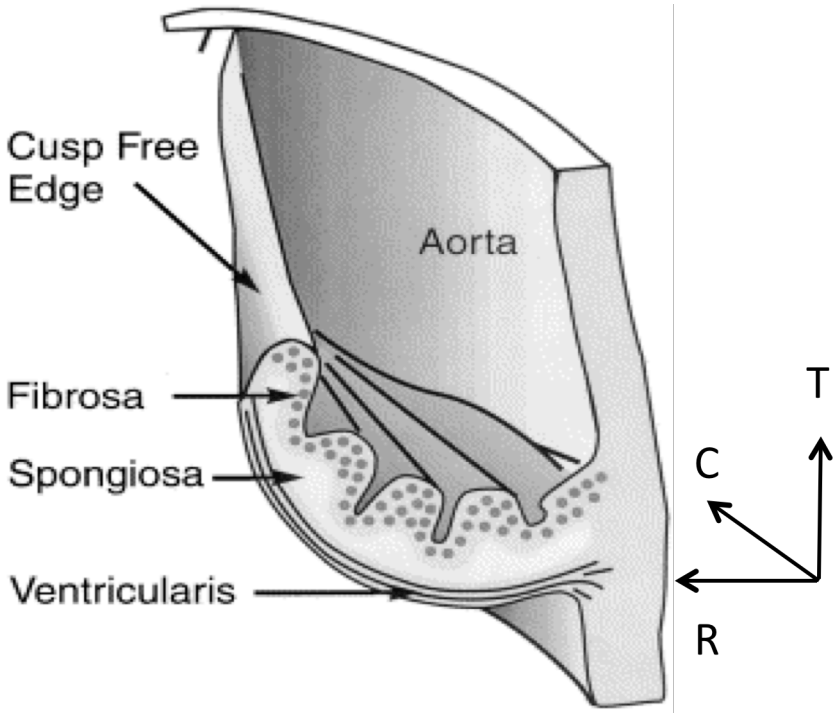


Fig 2.2 Schematic graph of the cross-section of an aortic heart valve [27]. T, C, and R stand for transvalvular direction, circumferential direction and radial direction respectively.

The layer on the aorta side surface of the aortic valve leaflet is called the fibrosa, accounting for approximately 40% of the 0.4~0.8mm thickness of the entire leaflet [28, 29]. It is abundant in densely packed and circumferentially aligned collagen fibres. At the area close to the aorta wall, the collagen fibres form continuous sheets, while at the area close to the free edge, which is much thinner, the collagen fibres form isolated bundles [30]. In relaxation, the fibrosa is radially corrugated, with a crest periodicity of

approximately 1mm [31], which is believed to enable the fibrosa to expand radially during diastole (30% approx. [32]). Meanwhile, the collagen fibres provide the fibrosa a high stiffness in the circumferential direction (13kPa [32]), which accommodates the transvalvular pressure, so that there is no large deformation in the leaflet after it closes. Besides, in the situations of atrio-ventricular valves, the fibrosa is directly connected with the collagen core of the chordae tendineae mentioned above, which holds taut the leaflets against the billow from the ventricle during systole [33, 34].

The ventricularis is the layer on the ventricle side surface of the aortic valve leaflet, and is thinner than the fibrosa (taking up 29%~37% of the leaflet thickness) [28, 29, 35]. It is predominantly comprised of radially aligned elastin fibres and has also some multidirectional collagen fibres [21]. The highly compliant elastin fibres allow the large radial extension of ventricularis during diastole (up to 60% [27]). The collagen fibres, however, will resist further deformation of the valve after the elastin fibres are fully extended, by realigning themselves along the loading direction [31, 32].

Between the fibrosa and the ventricularis is a layer called the spongiosa of loosely arranged connective tissue in a semi-fluid ground substance, with approximately 30% of the leaflet thickness [28, 29, 36]. It consists of mainly glycosaminoglycans (GAGs), with some randomly oriented collagen as well, and is also thicker near the aortic wall and virtually absent at the free edge [31]. The negatively charged GAGs introduce hydration to the matrix [37], which enables the spongiosa to dampen shocks during the opening and closure of the valve [38]. Moreover, the spongiosa also generates inter-layer shearing between the fibrosa and the ventricularis, which contributes to the radial flexibility of the leaflet on top of the folding and flattening of the corrugations in fibrosa [39].

In addition to the above three layers, there is a monolayer of endothelial cells sheathing the whole leaflet, which has no known mechanical functions but is histologically indispensable, as it is forming the non-thrombogenic surface directly contacting the blood. [31, 40]

With this complex and anisotropic layered structure, a native heart valve is therefore able to exhibit different mechanical behaviour in different cardiac phases, and thus ensures a desirable hemodynamic condition in the heart. The biomechanics of the heart valve will be discussed in more detail later in 2.2.4.

2.2.3 Microscopic Components

At a smaller scale, the heart valve can be seen as a composite of cells and the extracellular matrix (ECM), which consists of collagen, elastin, and GAGs (see Fig 2.3).

The cells play very important roles in regulating the normal architecture of the valve and meanwhile they themselves are also crucial build blocks for the architecture. The two major types of cells in the heart valves are the valvular interstitial cells (VICs), and the valvular endothelial cells (VECs).

VICs are present within all three layers of heart valves and are identified to have heterogeneous phenotypes, e.g. smooth muscle cells, fibroblasts and myofibroblasts [24]. Smooth muscle cells have the properties of both contractility and secretion. Their ability to contract serves to maintain a limited intrinsic valvular force and withstands hemodynamic pressures [41]. Their secretory property, along with that of the fibroblasts, is responsible for the generation, maintenance and remodelling of the ECM [42]. Myofibroblasts have the characteristics of both smooth muscle cells and fibroblasts. Although their dualistic nature is not clearly understood, they are believed to be critical

to the valve pathophysiology [24], in the way that whether their phenotypic state is myo-like or fibro-like is an indicator of current remodelling demands of the tissue [43].

VECs sheathe the valve with a single layer, forming the protective, non-thrombogenic surface that is directly in contact with the blood [40]. It is also proposed that VECs have another likely function of regulating the underlying VICs [42], to maintain the integrity of valve tissues and potentially mediate disease [44]. There is a complex interaction between VECs and VICs: for example, VECs can modulate the collagen synthesis and degradation of the fibroblasts [45], and can both stimulate and inhibit the growth of the smooth muscle cells [46].

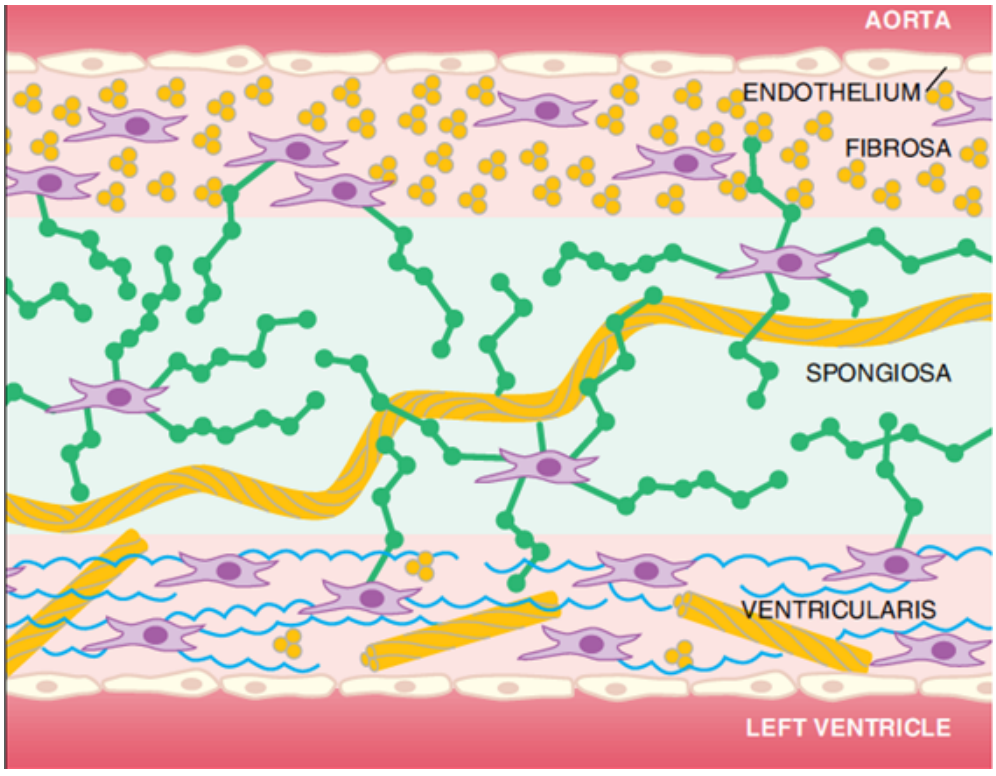


Fig 2.3 Components of a heart valve leaflet: Collagen (yellow, circumferentially aligned in fibrosa, multidirectionally distributed in ventricularis, randomly oriented in spongiosa), GAGs (green, loosely arranged in spongiosa), Elastin (blue, radially aligned in ventricularis), valvular interstitial cells (purple), and valvular endothelial cells (white) [21] .

In the ECM of the heart valve, collagen is the most prevalent protein, accounting for about 50% of the dry weight of the valve [47]. As with all proteins, a collagen molecule is assembled with polypeptide chains. However, there is a triple-helical conformation of the polypeptide chains that distinguishes the collagen family from most of the other proteins.

As is shown in Fig 2.4, the three polypeptide chains, known as α-chains, have formed a rope-like coil, with each α-chain having a characteristic repeating sequence of 3 amino acids G-X-Y [37], where G is representing glycine, and X and Y can be any other amino acids (X being frequently proline and Y hydroxyproline) [48].

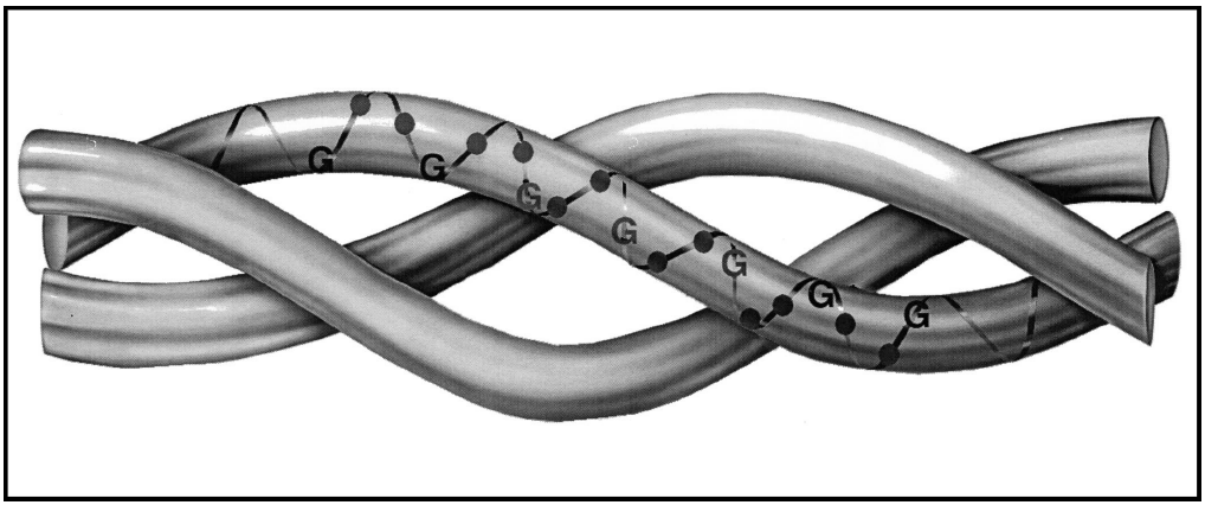


Fig 2.4 Triple-helix Structure of Collagen [37]

Based on the variations of X and Y, and whether the 3 α-chains are identical, collagen can be further subdivided into 29 types [49], and human heart valves normally contain 74% type I, 24% type III and 2% type V collagen [50].

As the smallest amino acid, glycine always occupies the position in the α-chain facing the axis of the triple helix, leaving the other two amino acid residues pointing outwards [37]. The backbone -NH- of the glycine forms hydrogen bond with the backbone -CO-

of the Y residue on the right-hand side α-chain [51]. This connection is essential to collagen as it gives the triple helix an inherent resistance to tension[37].

Once assembled, the triple helix is secreted out of the cell and then tailored into a molecule of approximately 300nm in length and 1.5nm in diameter, which becomes a tropocollagen, as the precursor to collagen (see Fig 2.5 a). Five tropocollagens then aggregate to form a microfibril (about 4nm in diameter [52]), in which they are staggered longitudinally from each other by about 67nm, referred as the D-period. As can be seen in Fig 2.5 b, each D-period contains one segment with all the five tropocollagens in the cross section and the other segment with only four. This results in the overlap-gap structure which can be observed as the characteristic banding pattern with the periodic length of the D-period under electron microscopes [52] (see Fig 2.5 c).

The microfibrils are then assembled into fibrils, with various diameters from 30 to 500nm (30-50nm for human heart valve collagen fibrils) [52]. Finally, the fibrils are further bundled up to collagen fibres with the aid of glycoproteins and proteoglycans, which bridge the fibrils and further strengthen the collagen fibres [48, 53].

Due to this complex hierarchical structure, collagen fibres have a high Young's modulus of 0.1-1 GPa [54], which almost makes them intrinsically inelastic in human bodies. However, the collagen fibres are longitudinally crimped with a periodicity of approximately 20 μm, which can give them an extensibility of approximately 10% under a relatively lower stress [31, 55].

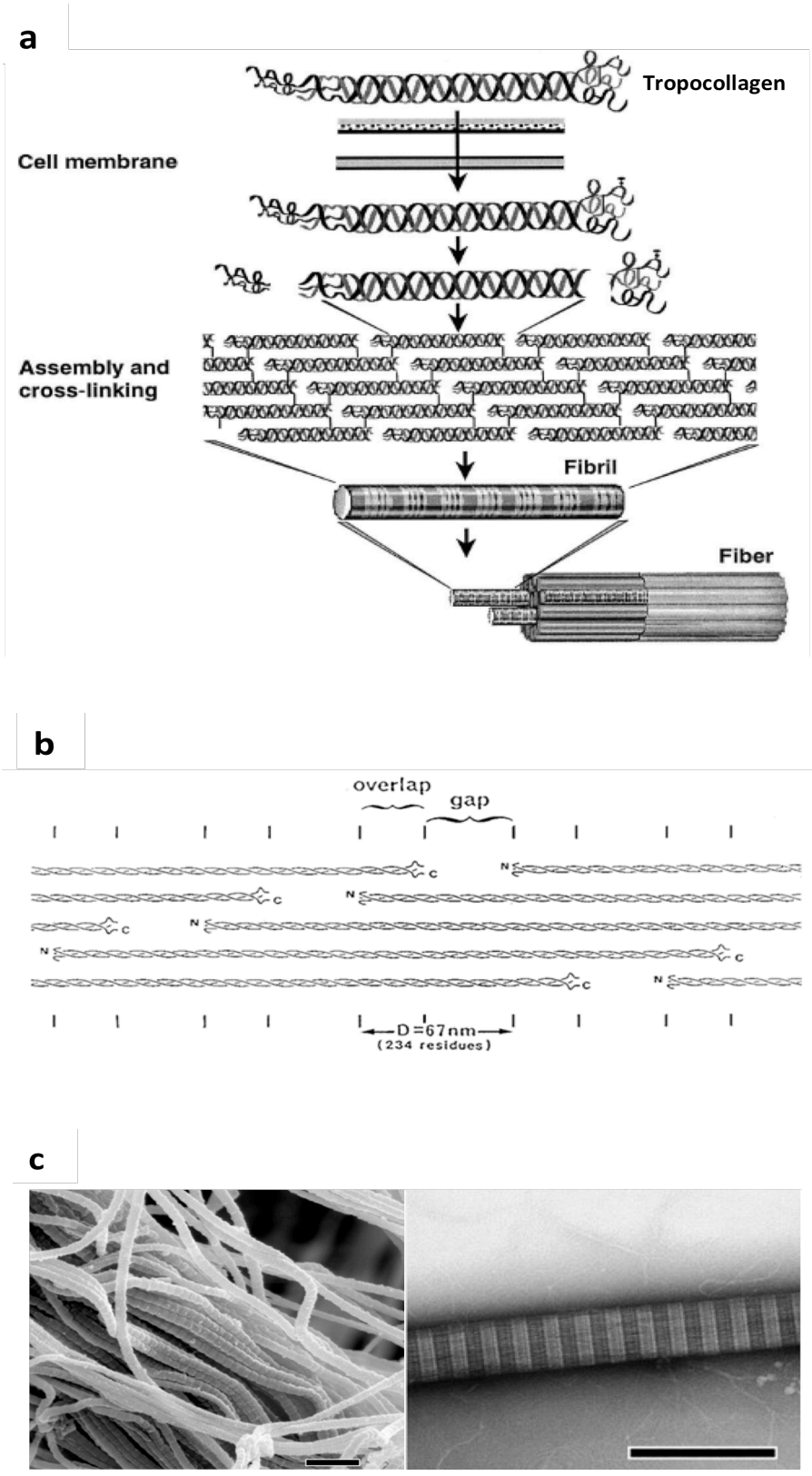


Fig 2.5 (a) Hierarchy of collagen fibres [52]; (b) collagen microfibril and the D-period [56]; (c) SEM image (left) and TEM image (right) of collagen fibrils (scale bar = 300nm) [57, 58].

Elastin is another major structural component of the heart valve, accounting for approximately 13% of its dry weight [47], and is responsible for the elasticity of the valve tissue.

Human elastin is firstly synthesized as its precursor, tropoelastin, by various cells including smooth muscle cells, endothelial cells, fibroblasts and chondrocytes [59]. As with collagen molecules, glycine takes place in every three amino acid residues in the tropoelastin polypeptide chains, and there is also a high amount of proline present (13%wt) [60]. With other amino acid residues such as alanine, valine and lysine, tropoelastin molecule usually contains 850-870 amino acid residues and has a molecular weight of 72k-74k Daltons [61]. The polypeptide chain also frequently shows repetitive sequence of these three peptide units: Pro-Gly-Gly-Val, Pro-Gly-Val-Gly-Val, and Gly-Val-Gly-Val-Ala [61].

Tropoelastin molecules are converted to elastins by forming intermolecular desmosine and isodesmosine crosslinks, which are derived from lysine residues. As is shown in Fig 2.6, four lysine residues from two tropoelastin molecules interact with each other to form desmosine and isodesmosine [59], which makes the tropoelastin molecules an extensively crosslinked array. As a result, soluble tropoelastin becomes highly insoluble elastin, which is reported to have a half-life of 70 years and is known to be one of the most stable proteins [62].

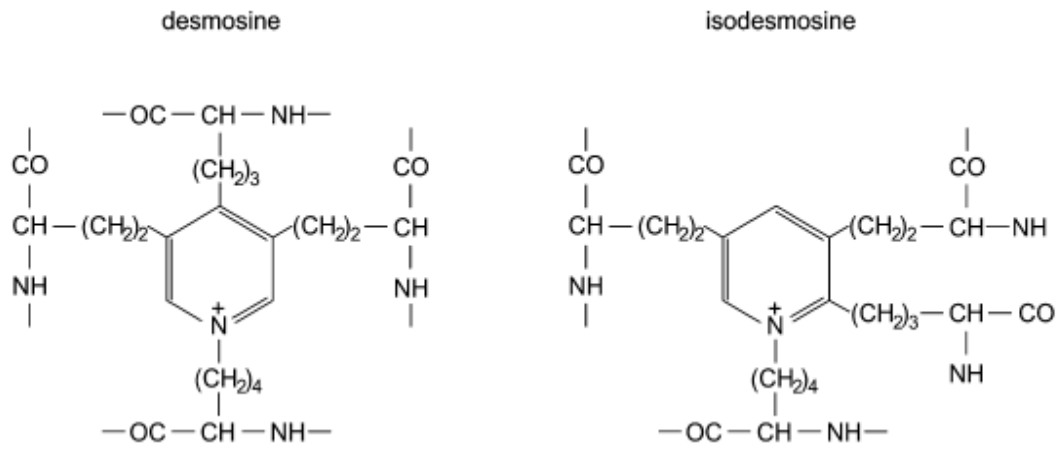


Fig 2.6 Desmosine and isodesmosine crosslinks [59]

The elastin molecule does not have the triple helical structure as collagen does, and in comparison is much more amorphous than collagen in its secondary structure. However, it still has some featured organized domains, as shown in Fig 2.7. In the crosslinked regions, an α-helical confirmation is favoured, with lysine residues protruding to the axis of the helix in forms of desmosine and isodesmosine. Regions between crosslinks rich in glycine, proline and valine favour another type of structure known as β-turn, which is made by four amino acid residues (Pro-Gly-Gly-Val for example), where the polypeptide chain turns back on itself and forms intramolecular hydrogen bonds [63]. It is reported that there are approximately 10% α-helices, 35% β-turns and 55% undefined conformations in the secondary structure of human elastin [64].

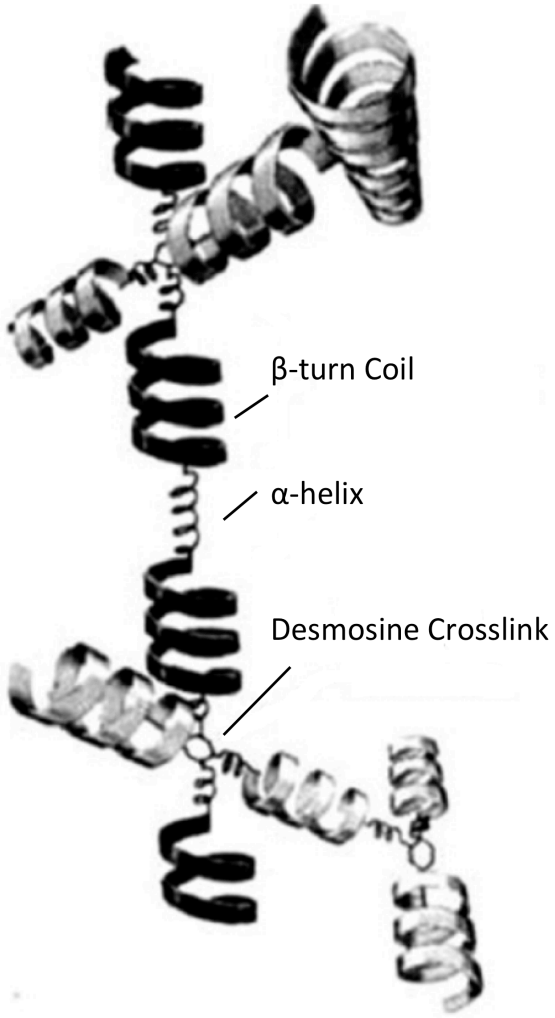


Fig 2.7 Molecular structure of elastin [63]

Further crosslinked elastin forms the network of elastin fibres (see Fig 2.8), with the ability to stretch and recoil like a rubber band [65] (Young's modulus around 0.4 MPa and strain of failure around 140% [66]). This is what gives the heart valve tissue its required elasticity and extensibility.

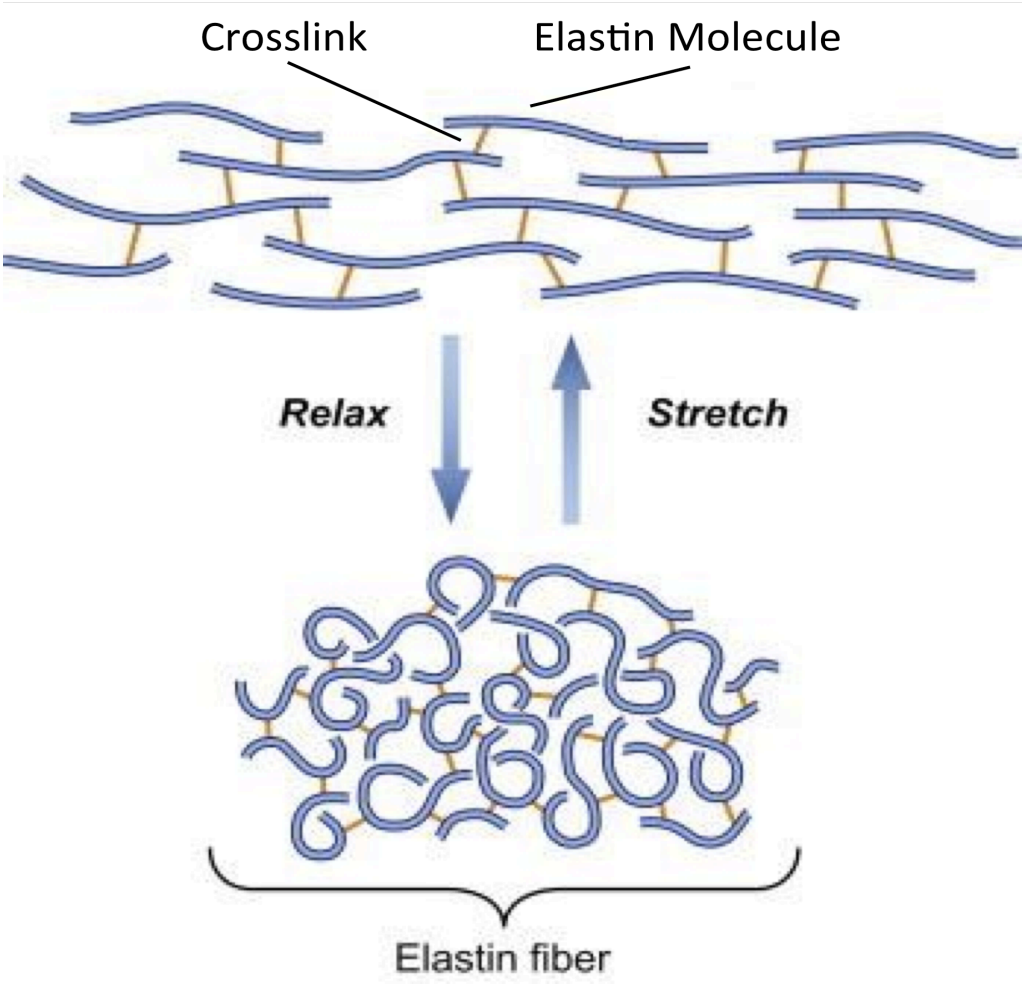


Fig 2.8 Network of elastin fibres [67]

Glycosaminoglycans (GAGs) is a coined name of glycosamine (amino sugar) and glycans (polysaccharides) [68]. As is suggested by the name, GAGs are long linear polysaccharides with a repeating disaccharide unit of one hexose and one hexosamine [69], and are usually sulphated. Fig 2.9 shows the disaccharide unit of chondroitin sulphate (CS), one of the major sulphated GAGs in human heart valves [39].

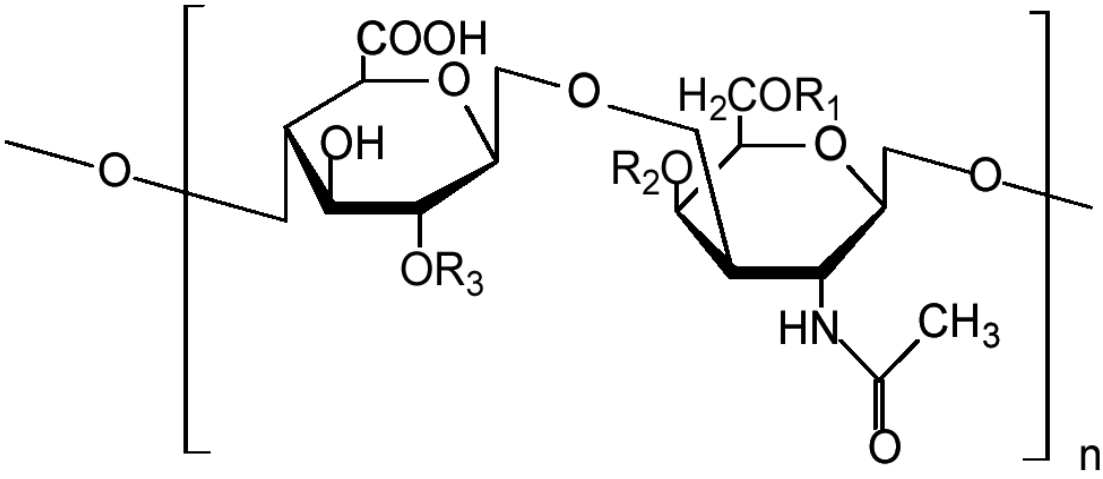


Fig 2.9 Disaccharide unit of chondroitin sulphate. Chondroitin-4-sulphate: R_1 = H; R_2 = SO_3H; R_3 = H. Chondroitin-6-sulphate: R_1 = SO_3H; R_2, R_3 = H. [70]

Because of their carboxyl and sulphate groups, the GAGs are highly negatively charged under physiological conditions [68], attracting cations and therefore creating osmotic pressure [71]. The hydration introduced by the osmotic pressure then plays an important role in opposing the compression forces during the valve opening and closure [72]. GAGs may also form covalent bonds to proteins to become proteoglycans, regulating collagen fibrils diameters and fibrous tissue organization in the heart valves [73], as mentioned above.

Besides its mechanical and structural significance, GAGs also have other physiological functions such as binding and modulation of growth factors, inhibition of proteases, and involvement in adhesion, migration, proliferation and differentiation of cells [74].

GAGs vary in the disaccharide units and can be classified as chondroitin sulphate, dermatan sulphate, keratan sulphate, heparan sulphate, hyaluronic acid, heparin, etc. In the heart valves, the most abundant GAG is hyaluronic acid, followed by dermatan sulphate and chondroitin sulphate [39]. The GAGs content varies with the valves, higher in the mitral valves and aortic valves than in the tricuspid valves and pulmonary

valves, due to the greater compression resistance required in the former valves where the blood pressure is higher [39, 75]. The composition (ratios of different subclasses of GAGs) and fine structures (chain length) of the GAGs are also dependent on the valve type, and more importantly, can change with the age [76]. The total amount of GAGs is reported to be increasing with age in young heart valves (0~6 years) and decrease with age in adults, as do many subclasses of GAGs [75-77]. Moreover, these subclasses of the GAGs also change in proportions during the aging process: increase in dermantan sulphate and chondroitin sulphate, and decrease in dermatan sulphate [78, 79]. The mechanism governing the changes of the amount and composition of the GAGs throughout aging, however, is still not well understood. Mechanical functions of valves (developing during young ages and deteriorating during old ages) necessitating the according content of the GAGs has been a plausible explanation [76, 80]. Yet other age-related factors such as collagen synthesis and tendency of calcification have also been correlated with the changes in specific GAGs subclasses [47, 76, 78, 81, 82].

2.2.4 Heart Valve Mechanics

The mechanical behaviour of the heart valve regulates the surrounding hemodynamic environment, which in return determines the cell shape, proliferation and fibre formation in the heart valve, and consequently its mechanical properties [38]. Therefore, it is essential to understand the mechanics when studying heart valves.

When the heart valve opens during systole, the leaflet is in a relaxed state. The blood flow rapidly reaches its peak velocity of 1.35±0.35 m/s [83], and begins to decelerate afterwards. As the adverse axial pressure gradient is developed, the low momentum blood near the aortic wall is affected more than that at the centre [84], and therefore causes vortices behind the leaflets which are believed to facilitate a quick closure of the

valve [85]. In the deceleration phase of systole, the ventricularis starts to extend while the fibrosa starts to unfold. Upon the closure of the valve, the leaflet has undergone a radial extension of 31% [86], and the load (i.e. the transvalvular pressure) is shifted from the ventricularis to the fibrosa [87].

During diastole, the valve remains closed and the leaflets are withstanding a transvavular pressure of 0-12 kPa [88]. The 'hoop stress' within the leaflet can be estimated by the classical relationship between pressure and stress in a pressure-inflated membrane [89]:

$$\boldsymbol{S = \frac{PR}{2t}} \qquad \text{Eq. 2.1}$$

where *S* is the stress, *P* is the pressure, *R* is the local radius of curvature of the leaflet and t is the thickness of the loaded membrane. Considering the centre of the leaflet, where the relationship is more valid, the radius of curvature is approximately 10mm and the thickness is about 0.5mm [89]. Therefore, the maximum stress within the leaflet will be at the level of 0.1MPa [31, 90].

When studying the mechanics of native heart valves in vitro, uniaxial tension has been the mostly conducted test, utilized by various researchers to investigate specific aspects such as effects of the location of the valve tissue, effects of fixation, and strain rate dependency [91-94]. One thing in common amongst their findings was the prominent anisotropy between the circumferential and radial direction of the valves. In the circumferential direction, the valve tissue was reported to have a stiffness of 3~8 MPa, an extensibility of 10%~30%, and a failure strength of 0.15~1.5MPa, whilst in the radial direction the valve tissue is more compliant, with the respective mechanical parameters being approximately 1MPa, 60%~100%, and 0.12~0.2MPa [30, 91, 95]. This is mainly due to the different architectures of collagen and elastin in the fibrosa

and the ventricularis. To further illustrate the roles played by the individual layers, Vesely performed uniaxial tensile tests on the fibrosa and the ventricularis separately [27, 32]. The results showed that the ventricularis functioned much alike the whole heart valve, with an extensibility of ~20% circumferentially and ~60% radially. The fibrosa, however, showed a similar extensibility of ~20% in both circumferential and radial directions, which was inconsistent with the anisotropic behaviour of the heart valve. This inconsistency was then explained when the preloaded status in the layers was discovered: when the heart valve was in the relaxed state, the fibrosa was radially under compression and the ventricularis under tension, in other words, the ventricularis was maintaining the fibrosa in the corrugated state mentioned in 2.2.2. This corrugation gave the fibrosa more room of radial extensibility on top of that measured at its flattened state after separation from the ventricularis, which was then in line with the radial extensibility of the whole heart valve.

More recently, biaxial tensile tests have been applied to yield more understanding about this anisotropy of the heart valve. Sacks and Merryman have confirmed that the heart valve leaflet is also remarkably stiffer circumferentially than radially under biaxial tension (see Fig 2.10) [96], and have generated more insights to the mechanism of the anisotropy from the coupled strain behaviour in the circumferential and radial directions. They suggested that, while it was very difficult for the circumferentially aligned collagen fibres to extend, it was much easier for them to rotate to form an angular distribution (see Fig 2.11.), giving the valve a larger extensibility in the radial direction even after the collagen fibres were fully extended [24]. Biaxial tensile tests on individual layers were also performed by Stella and Sack [29]. This time, the fibrosa exhibited distinct anisotropic responses to the biaxial loading, unlike under uniaxial tension, corroborating the above theory of collagen fibre rotation.

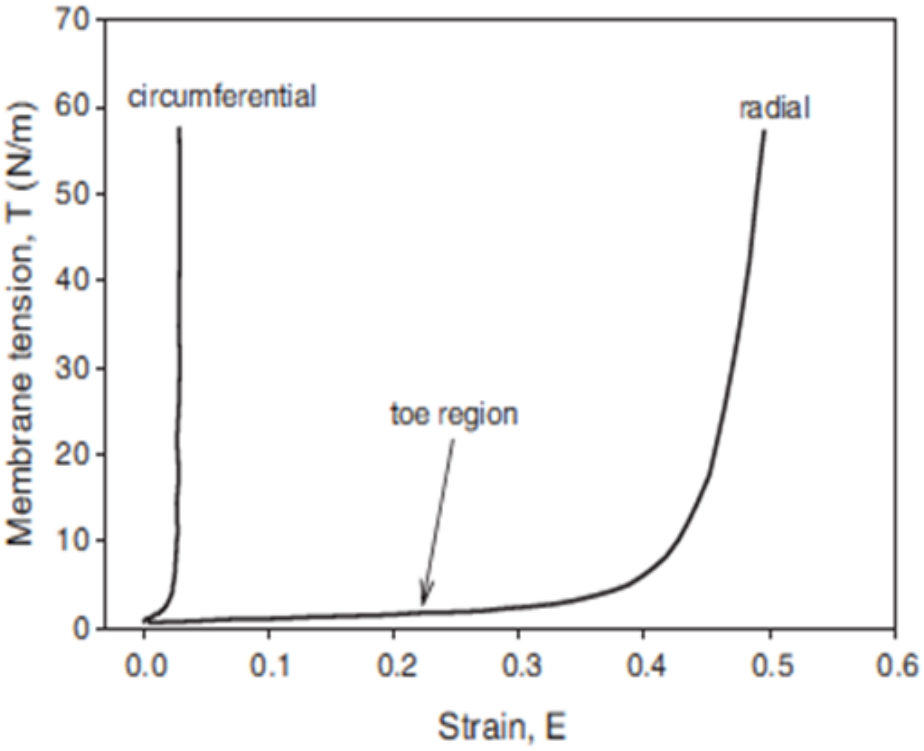


Fig 2.10 Biaxial response of a native porcine aortic leaflet [96]

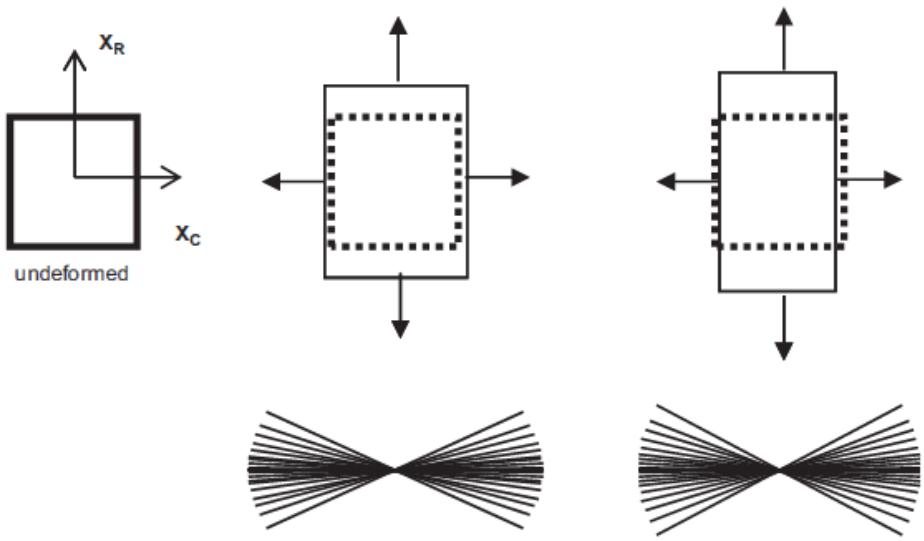


Fig 2.11 Schematic graph of collagen fibres rotating under biaxial loading [24]

With this anisotropic behaviour in the circumferential and radial directions, the heart valve leaflets can therefore stretch radially to the required extent under a relatively low

transvalvular pressure so as to form a tight coaptation with each other, and as the full transvalvular pressure develops upon valve closure, they can exhibit sufficient stiffness to resist the load without prolapsing to the ventricle [24, 97].

Besides stretching, flexure is another important mechanical behaviour of the heart valves, in which anisotropy also exists. In the natural state, i.e. when relaxed, the heart valve leaflet is curved towards the ventricularis side (both circumferetially and radially), which is referred as 'Natural Curvature'. Then by bending the leaflet in both directions, two flexural states can be defined as 'With Curvature' (WC) and 'Against Curvature' (AC), as is shown in Fig 2.12.

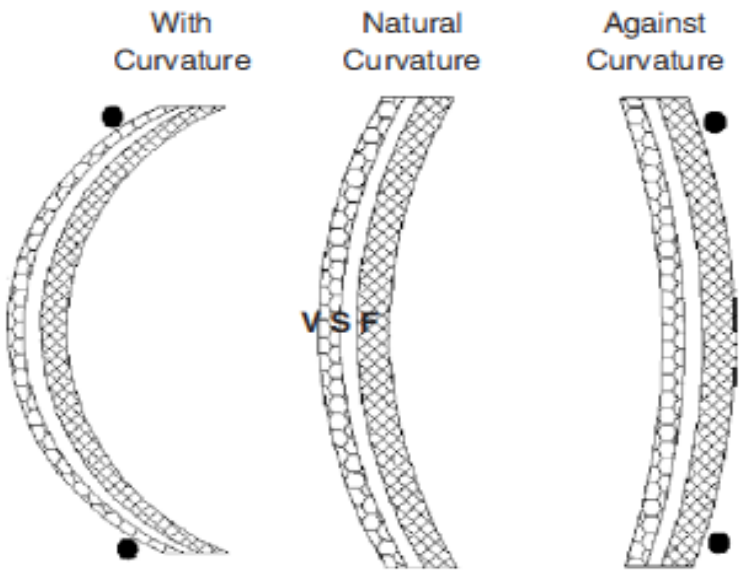


Fig 2.12 Schematic graphs of flexural states in different bending directions [98]. V, S and F stand for ventricularis, spongiosa and fibrosa respectively.

When the leaflet is in flexure, it has different stress status (tensile and compressive) in different layers. When bent in the WC direction, the leaflet will have the fibrosa in compression and the ventricularis in tension. Since the architecture of collagen fibres in the fibrosa are not designed to withstand compression, the effective stiffness in the WC

direction is mainly contributed by the elastin fibres in the ventricularis. In contrast, when bent in the AC direction, the fibrosa is in tension and the ventricularis is compression. This time the thicker fibrosa with stiffer collagen fibres is contributing more to the effective stiffness of the leaflet. Not surprisingly, the measured effective stiffness is higher in AC direction (~700kPa) than in WC direction (~500kPa) (data were from experiments on porcine aortic valves) [99]. This feature also has its biomechanical significance, that is, to prevent a sharp reverse curvature during valve opening which may cause leaflet flexure fatigue [100].

The above studies mainly used quasi-static tests to characterise the elastic behaviour of the heart valves, and the properties seemed to be predominantly governed by the fibrosa and ventricularis, with little contribution from the spongiosa. However, in the real physiological conditions the heart valves are subjected to dynamic loading and are exhibiting viscoelastic behaviour, in which the spongiosa in playing a critical role. It has been generally agreed that the spongiosa allows for the internal shear between fibrosa and spongiosa during the motion of the valve leaflet, and dampens the sudden changes of stress in the leaflet [24, 38, 101-105]. Vesely, Boughner and Song demonstrated the inter-layer shearing by imaging a bent valve strip with polarized light microscope [104, 106]. Anssari-Benam and Screen characterised and simulated the damping effects of spongiosa in uniaxial tension with a range of strain rates [105]. They suggested that the damping effect was much lower in the radial direction than the circumferential direction, which could imply a quick radial stretch of the leaflet to form coaptation, and a less abrupt loading in the circumferential direction upon the ultimate tranvalvular pressure, both desirable for the heart valve function. They also proposed a shear-thinning mechanism in the spongiosa which would facilitate the inter-layer shearing in the leaflet, so as to reduce the shearing stress on the leaflet surface [105].

Most recently, however, Sacks et al raised a different view from the results of cyclic biaxial tension and flexure tests coupled with finite element modelling [107, 108]. They argued that the heart valve leaflet was a well-bonded unit and there was no inter-layer shearing during the valve deformation. Moreover, it was also suggested that the damping effect from spongiosa should not be considered contributing to the viscoelasticity in the extensional deformation of the valve, but rather as a resistance to the compressive stress to reduce flutter during full systolic flow [101, 107]. Compared with the static mechanical properties, the time-dependent properties of heart valves are more complex and less well studied, and therefore should be the subjects of future investigations.

2.3 Heart Valve Tissue Engineering

Tissue engineering, as a discipline on its own, emerged more than 20 years ago when the term 'tissue engineering' was coined by Fung in October 1987 at a National Science Foundation workshop in Washington, DC [22]. It soon found its place in the field of heart valve replacement.

Before the exploration of tissue engineered heart valves, there have been other types of heart valve prostheses (i.e. mechanical valves and biological valves) that were well developed and commercially available. However, they constantly suffered from problems such as risks of thrombosis and infection, lack of cellular functions, and non-native valve geometry and hemodynamic conditions [109]. Tissue engineered heart valves (TEHVs), in contrast, can address all these issues, and therefore hold the promises for the future.

The basic concept of TEHVs is, as can be seen from Fig 2.13, to seed autologous cells to a 3-D scaffold (usually shaped to resemble the dimensions of a native heart valve), and to let them organize and develop in vitro into a desired tissue (or even organ) before implantation, so that the implant will be living and be able to integrate with the native tissues and form a durable valve.

There are three main elements involved in the approach of heart valve tissue engineering: the scaffolds which provide dimensional support and living environment, the cells which proliferate and generate the new tissues, and the signals which guide and stimulate the tissue regeneration.

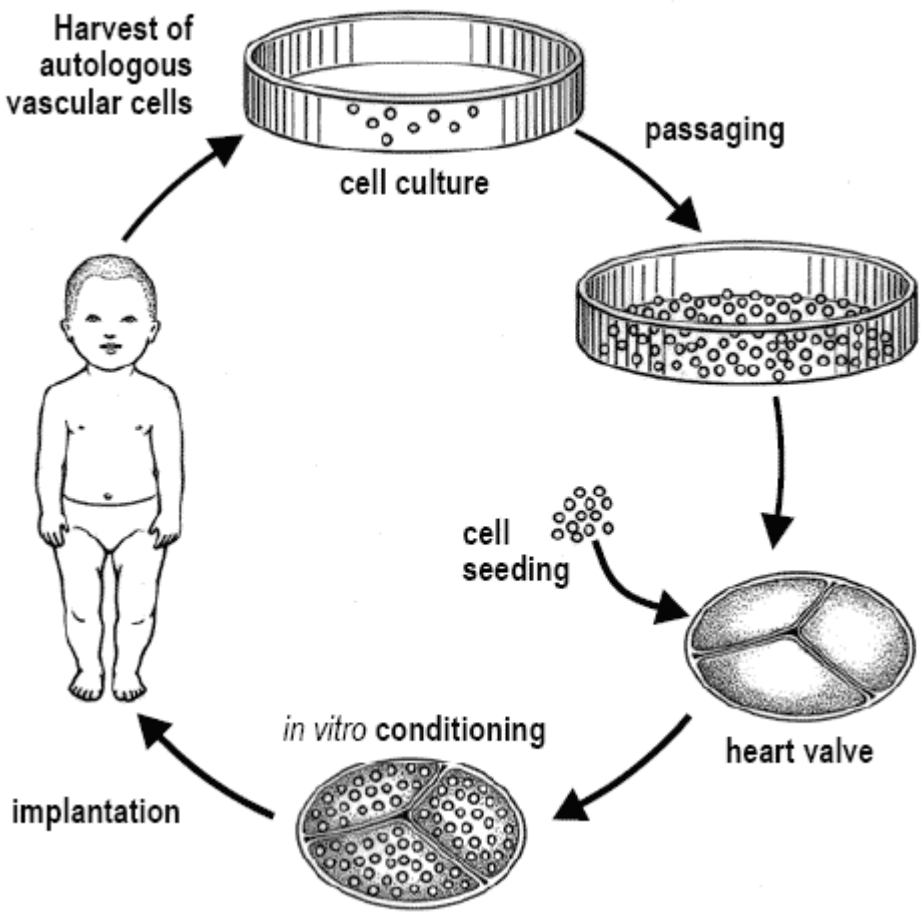


Fig 2.13 Concept of tissue engineered heart valves [110]

2.3.1 Scaffolds

The materials used for tissue engineering scaffolds should have: (1) controlled biodegradability or bioresorbability so that the tissue will eventually replace the scaffold, (2) appropriate surface chemistry for cell attachment, differentiation and proliferation, and (3) adequate mechanical properties to resist the load during handling in vitro or at the implantation site in vivo [111]. Many candidate materials have been investigated according to these requirements for heart valve engineering, including natural polymers (collagen, GAGs, elastin, chitosan, fibrin, etc.), synthetic polymers (polyglycolic acid, polylactic acid, poly-lactic-co-glycolic acid, polyhydroxyalkanoates, etc.), and decellularized tissues [87, 112-115]. Every material has different biological and mechanical properties, and has its own pros and cons.

Decellularized heart valve scaffolds, both xenografts and allografts, are achieved by the removal of cellular components from native valves with various detergents such as EDTA, trypsin, SDS, RNase, DNase, and Triton® X-100 [116, 117]. They have maximally respected the complexicity and integrity of the extracellular matrix in the heart valve given by nature [118]. Implantation of these decellularized scaffolds repopulated with autologous cells has shown good results in sheep and dogs, which includes high survival rates, regeneration of valvular tissues, and confluent endothelial surface coverage [119, 120]. However, the application in human has seen mixed results. Simon et al used the Synergraft® decellularized porcine valve for valve replacements in four pediatric patients. These decellularized valves were not seeded with cells before implantation, and suffered from strong inflammatory responses and rapid degeneration. Three of the four patients died within one year after the surgery and the fourth had prophylactic removal of the valve. Incomplete decellularization and lack of recellularization were thought to be the causes of the failure [121]. In contrast, Dohmen

et al have successfully created a TEHV with a decellularized allograft pulmonary valve seeded with the patient's vascular endothelial cells. This TEHV exhibited excellent hemodynamic behaviour after implantation, and remained normally functioning with no evidence of calcification at one-year follow-up [122]. This therefore implies the issues of using decellularized valve tissue as TEHV scaffolds: for the xenografts, immunological rejection might still occur despite even near-complete decellularization [123], and for the allografts, the availability of donor valves is still very limited [23].

Synthetic polymer scaffolds have the advantages of greater reproducibility, fewer immunogenic reactions, and unlimited supply over the decellularized scaffolds [116]. Attempts of using synthetic polymers for TEHV scaffolds began in the 1990s with polyglycolic acid (PGA) and polylactic acid (PLA), which were already FDA-approved to be biocompatible [123]. Shinoka et al were the pioneer in that era. They have investigated PGA-based scaffolds seeded with autologous cells in the ovine pulmonary models, and favourable collagen and elastin expression was shown on the implanted valves, although the thickness and stiffness were larger than the native valve [124-126]. To better match the stiffness of the scaffold materials to the native heart valve, the more flexible polyhydroxyalkanoates (PHAs) family have been investigated as an alternative or additive material to PGA [17, 43, 115, 127-129]. Sodian and Hoerstrup et al have conducted in vivo studies on PHA scaffolds, and demonstrated that they have improved functions compared with the PGA scaffolds, including comparable mechanical properties to native heart valves, rich collagen and GAGs content and existence of elastin, and complete degradation by 8weeks. However, limitations still existed such as lack of endothelialisation, valve construct dilation and regurgitation, and the general concern of the toxicity of the degradation products [17, 116, 130].

Collagen has well conserved structures across all species and is minimally immunogenic compared to other structural proteins [131, 132]. Therefore, there is abundant collagen from various animal sources (such as bovine achilles tendon, bovine dermis, and rat tail tendon) that qualifies for the wide usage in human TEHV research. Moreover, it has outstanding cell-binding abilities and superior mechanical properties amongst the natural polymers. This thesis therefore has chosen collagen as the basic scaffold material for TEHVs and will review the collagen-based scaffolds in more details here.

The collagen-based scaffolds are generally designed to be highly porous in order to favour tissue integration and vascularisation [111]. To achieve this high porosity, various fabrication methods are used, including electrospinning, freeze-drying, critical point drying, etc [133].

Electrospinning is a electric-field-assisted process for polymer fibre formation and deposition, and has been popular as it is remarkably efficient and inexpensive [134]. A schematic illustration of the electrospinning apparatus is shown in Fig 2.14 a. The collagen solution is injected with a high electric potential which is usually generated by connecting a high voltage power source to the feeding tip. When the electrostatic force overcomes the surface tension of the collagen solution, a charged jet will form and be accelerated to the grounded substrate, during which the solvent (i.e. hexafluoroisopropanol for collagen) evaporates and collagen fibres are collected on the substrate as nonwoven meshes, as shown in Fig 2.14 b [134, 135]. With the parameters (such as solution concentration, accelerating voltage, feed rate, needle-to-substrate distance, and orifice size) adjustable [136], electrospinning can have control over the porosity, pore size, and collagen fibre diameter of the scaffold [137].

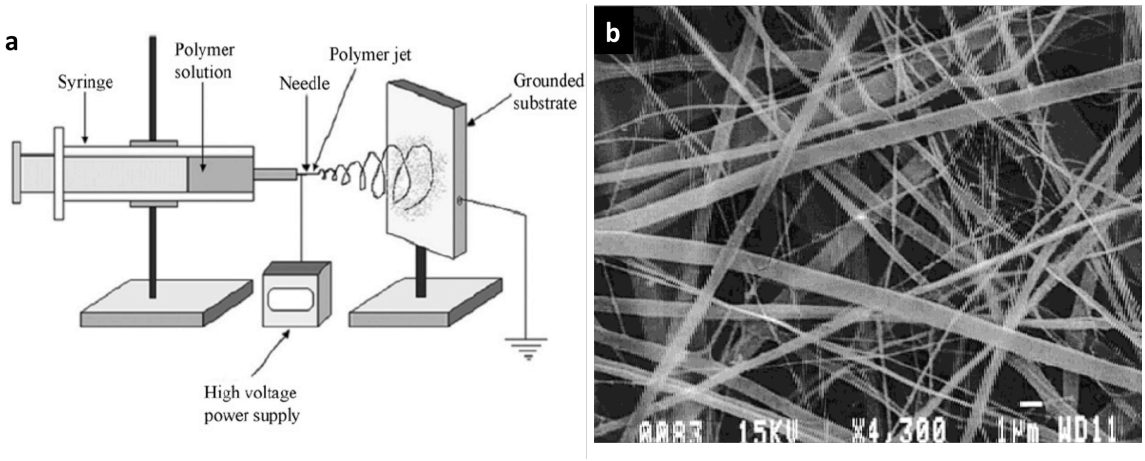


Fig 2.14 (a) Schematic graphs of the electrospinning apparatus and (b) structure of the electrospun scaffold [134, 138]

Freeze-drying adopts another way of creating porous structure in the collagen scaffolds, i.e. introduction and removal of ice crystals. The solution of collagen is prepared in an aqueous solvent (usually 0.05 m ethanoic acid [139]). It is then homogenized and frozen at various temperatures. During freezing, ice crystals form and force the scaffold materials to aggregate into the intercrystalline spaces, creating an interconnected matrix. Subsequently, ice crystals are removed by sublimation at high vacuum, leaving the porous solid scaffolds. The route of the phase changes of the water during this process is shown in Fig 2.15. This technique successfully eliminates the disruptions from the water to the pore structures caused by the inter-phase surface tension at the liquid-gas phase boundary.

The freeze-dried collagen scaffold has a morphology shown in Fig 2.16. The pore size can be controlled by the freezing rate, in the way that a faster freezing process (or a lower freezing temperature) results in finer pores [140].

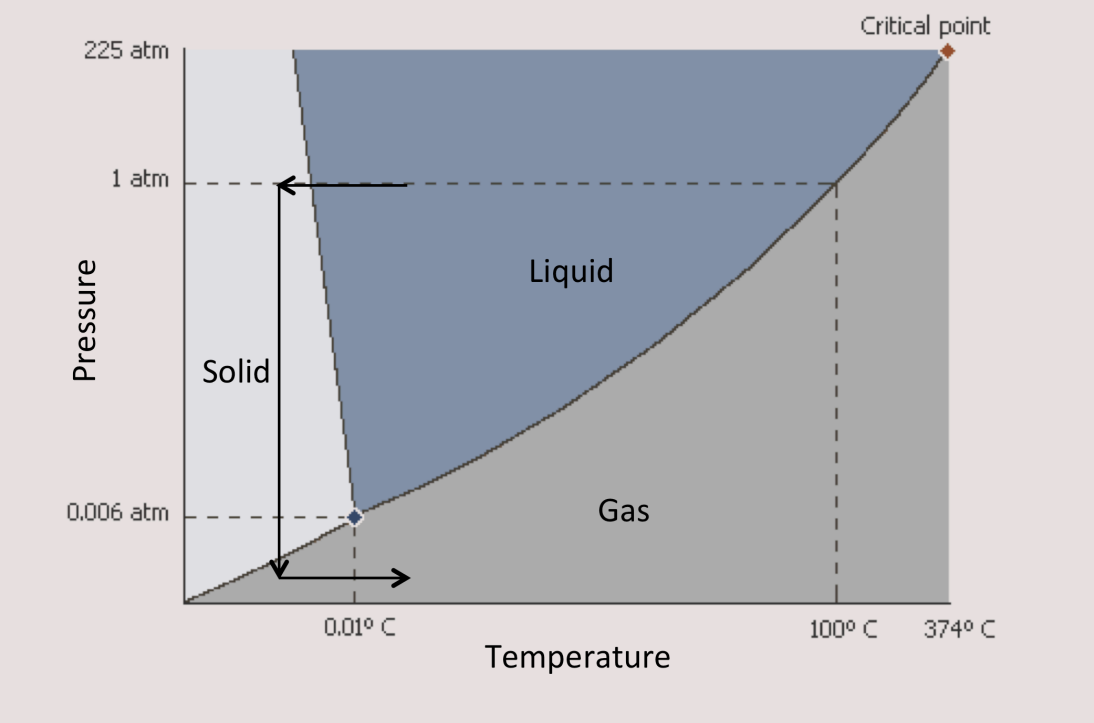


Fig 2.15 Phase diagram of water and the route of freeze-drying [141]

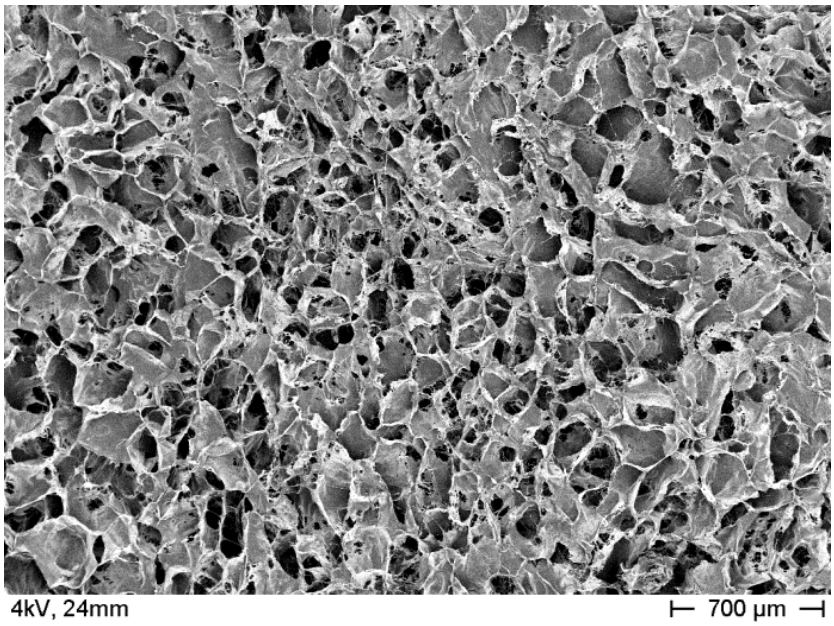


Fig 2.16 Morphology of freeze-dried collagen scaffold [142]

The critical point drying method has the similarity to freeze-drying that a freezing process is also needed to create the porous structures. However, it adopts another route

to avoid passing the liquid-gas phase boundary, and has a more complicated procedure of removing the ice crystals.

The frozen solution is firstly washed in ethanol so that the ice crystals are replaced by liquid ethanol. Further exchange of ethanol with CO_2 is then conducted at a moderate temperature (15˚C approx.) but at a high pressure (50atm approx.), as point A in Fig 2.17, where CO_2 is in its liquid status. After the CO_2 has completely replaced the ethanol, the temperature and pressure are both increased to the point (point B) beyond the critical point of CO_2. Instead of passing the liquid-gas boundary, the liquid CO_2 becomes gas by passing through the supercritical fluid region as the pressure is lowered to point C. Finally, CO_2 gas is cooled (point D) and released, leaving a dry scaffold with a porous structure shown in Fig 2.18.

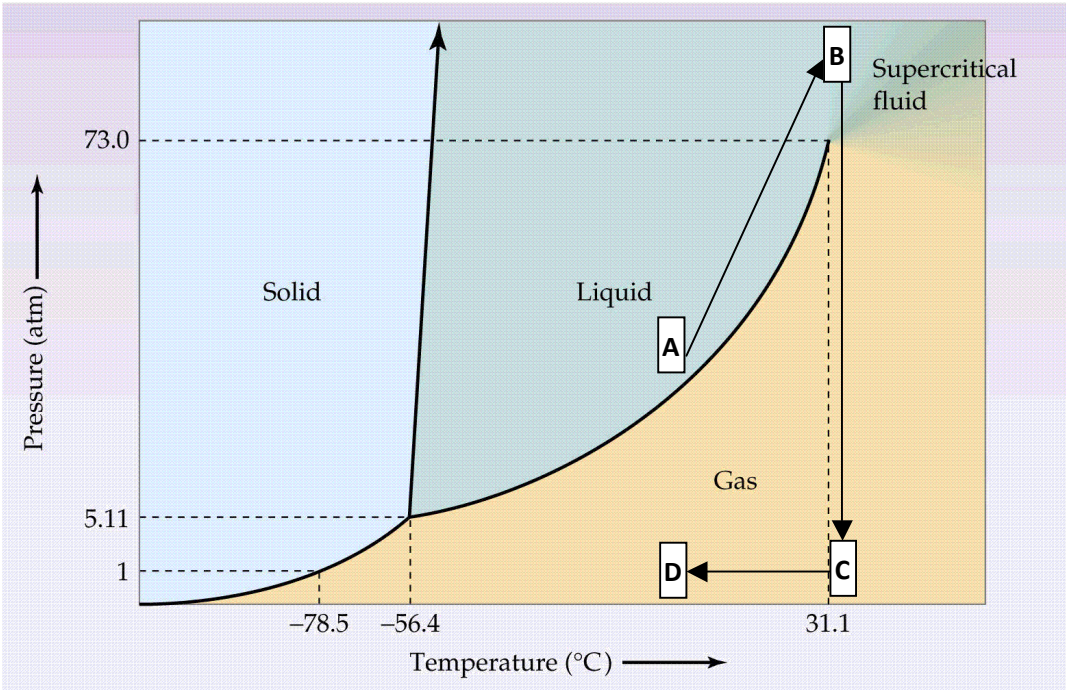


Fig 2.17 Phase Diagram of CO_2 and the Route of Critical Point Drying [143]

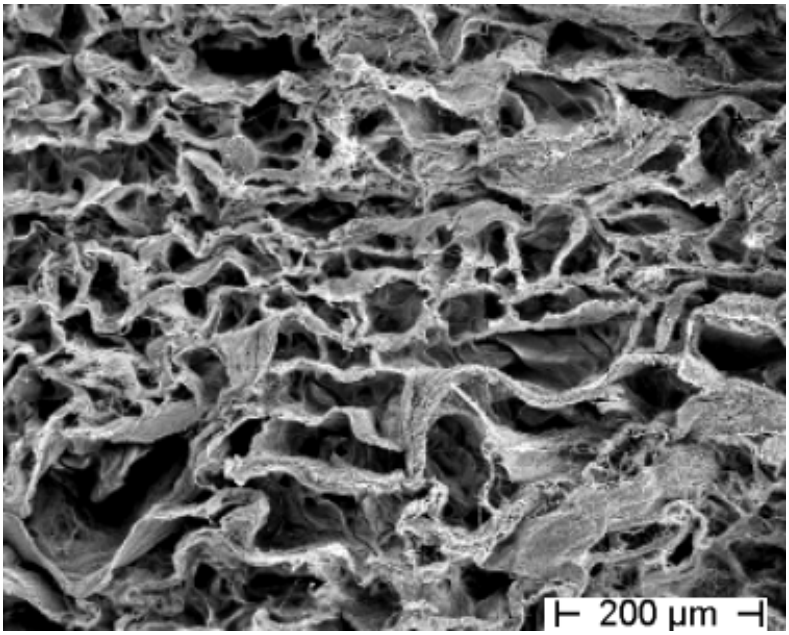


Fig 2.18 Morphology of critical point-dried collagen scaffold [144]

When fabricated, the scaffolds usually undergo further treatments of crosslinking, in order to stabilize the collagen and control the rate of degradation [145]. Moreover, crosslinking is effective in suppressing the the antigenicity of collagen and can improve the mechanical properties [145]. Two major categories of crosslinking techniques are commonly used: the chemical process and the physical process.

Popular chemical agents used for crosslinking collagen include glutaraldehyde, formaldehyde, polyether oxides, carbodiimides, and acyl azides. These chemicals can react with the amino groups or carboxyl groups on the collagen and form crosslinks between collagen chains [145]. The chemical crosslinking methods can significantly increase the mechanical properties of the collagen scaffolds, yet are sometimes questioned due to the potential cytotoxicity that may be caused by the chemical residues [146].

In comparison, the primary advantage of the physical process is that it does not introduce additional chemicals to the scaffolds, dehydrothermal (DHT) treatment and ultraviolet (UV) irradiation being two of the most commonly applied methods.

DHT treatment introduces covalent crosslinks between the polypeptide chains of the collagen fibres, by subjecting the scaffolds to a temperature of 105~180 ˚C and a vacuum below 1kPa [147, 148]. This process strengthens the scaffold without affecting the pore structures, and the degree on crosslinks can be controlled by the length of the treatment (varying from hours to days) [147]. Short wave length (254nm) UV irradiation generates free radicals on the aromatic amino acid residues of collagen, which then form crosslinks [149]. Since chain scission of collagen can be caused as a side effect by the UV irradiation, the dosage of the UV exposure has to be carefully controlled (usually < 5 hours) [146].

As the scaffold is providing the structural environment for the cells, its mechanical properties have always been of great interest, not only because the scaffold should have a good resistance to the handling during the surgery and a satisfactory initial stiffness after implantation, but also because the mechanical properties are known to affect cell response [150, 151].

The porous collagen scaffold usually behaves as elastomeric foam. In compression (see Fig 2.19a), the stress-strain curve of the scaffold is characterized by three regimes: a linear elastic regime (dominated by struts bending), a stress plateau (dominated by struts buckling and pore collapse), and densification (dominated by pore collapse throughout the scaffold) [152]. In tension (see Fig 2.19b), the stage of linear elastic deformation is the almost the same as is observed in compression. However, as the strain in the scaffold increases, the pore walls begin to be realigned in the direction of

the strain, giving a more favourable load-bearing orientation. Therefore, the Young's modulus keeps increasing thereafter, until tensile failure occurs [153].

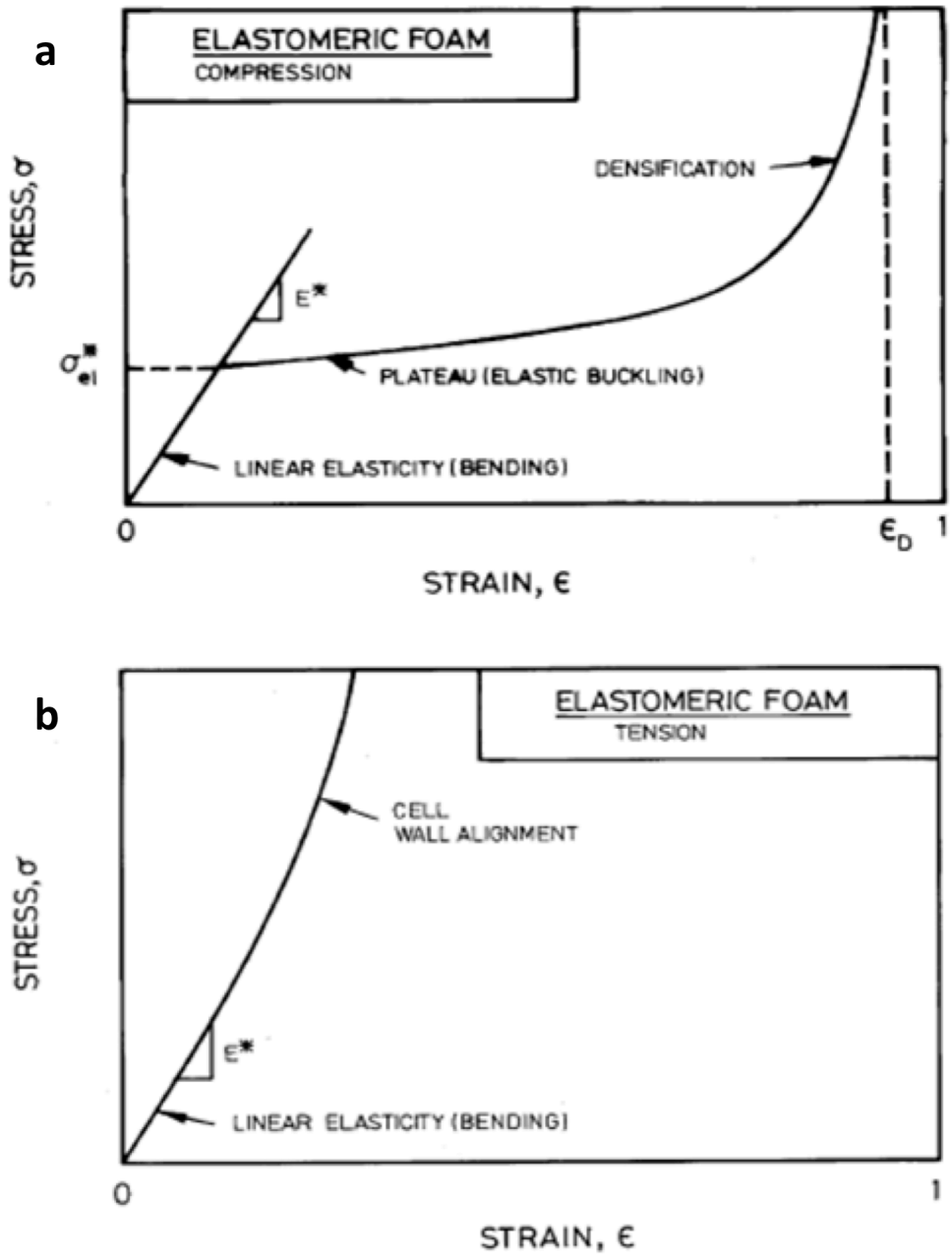


Fig 2.19 Schematic uniaxial stress–strain curves (a) Compression, (b) Tension [153]

Cellular solids models have also been developed to study the mechanical properties of the scaffolds. The Young's Modulus (E) and the elastic strength (σ^*_{el}) have been linked

to the relative densities ($\frac{\rho}{\rho_s}$) of the scaffolds (ρ and ρ_s being the density of the scaffolds and the solid materials, respectively), as shown in Eq 2.2 and Eq 2.3 [152]:

$$\frac{\mathbf{E}}{\mathbf{E_s}} = \mathbf{C_1}(\frac{\boldsymbol{\rho}}{\boldsymbol{\rho_s}})^{\mathbf{2}} \quad \text{Eq 2.2}$$

$$\frac{\boldsymbol{\sigma}^{*}_{\mathbf{el}}}{\mathbf{E_s}} = \mathbf{C_2}(\frac{\boldsymbol{\rho}}{\boldsymbol{\rho_s}})^{\mathbf{2}} \quad \text{Eq 2.3}$$

where E_s is the Young's Modulus of the solid materials, which is generally quoted as being between 0.1-1.0 GPa for collagen [66], and C_1 and C_2 are both geometry-dependent constants of the cellular model. For a typical collagen-based scaffold with $\frac{\rho}{\rho_s}$ around 1%, the Young's Modulus is predicted to be within the range of 10^4 Pa to 10^5 Pa, and is validated by various researchers [151, 154]. When the scaffold is hydrated, which is its actual working condition in vivo, the E* and σ^*_{el} can be reduced by over 100 times [151]. Since the native heart valve has an E of 500~700kPa (2 orders of magnitude higher than that of a hydrated scaffold) [99], it is a critical task to improve the mechanical properties of the scaffolds. Efforts have been made by increasing the relative density [154], crosslinking the scaffolds [147, 148], and introducing structural hierarchy or orientation [155]. Moreover, research has shown that the cells, when incorporated into the scaffolds, can also introduce significantly higher mechanical properties [156, 157], promising a feasible way of achieving mechanically qualified tissues from the highly porous scaffolds.

Investigations on collagen TEHV scaffolds are less extensive compared with the decellularized scaffolds and the synthetic polymer scaffolds, yet promising results have implied their suitability for heart valve tisse engineering. Yacoub et al have studied collagen scaffolds seeded with valve interstitial cells and adipose-derived stem cells [158-161]. In the studies the cells have shown active remodelling of the ECM

(including expression of remodelling enzymes and ECM genes, and synthesis of collagen and elastin), which is critical for the success of TEHV, as the original collagen scaffolds are still different from the native valve ECM in composition and architecture, and can cause poor valve function if not remodelled [160]. Therefore, more closely mimicking the layered composition of native valve ECM and optimizing the architecture, so as to better facilitate the ECM remodelling, seems to be the direction of further development of the collagen-based scaffolds for TEHVs [159, 161].

2.3.2 Cells Sources

There are varieties of cell sources for heart valve tissue engineering. One straight forward cell source is the organ-specific cells harvested by biopsy. Researchers have successfully expanded a single 1-mm diameter biopsy from a tricuspid valve to over one million cells in a month [21], indicating a good potential of proliferation of this source. However, due to its critical position, a biopsy from a heart valve is usually infeasible, and the vascular-derived cells from peripheral vein segments are then considered to be an alternative source [162]. Experiments have demonstrated that human aortic myofibroblasts and endothelial cells are easy to isolate and culture [17, 163], and are able to form layered cell distribution on scaffolds [164], which is desirable for TEHVs as the cells can then produce and assemble ECM components and at the same time provide a non-thrombogenic surface to the valve [1].

With the recent emerging interests in stem cell research, investigations are also carried out in using stem cells as the cell source for the TEHVs. For instance, human bone marrow stromal cells (a type of mesenchymal stem cells) have been reported to have created functional TEHVs when seeded on polyglycolic acid scaffolds [129]. Compared with the cardiovascular tissue-specific cells, the bone marrow stromal cells have the

advantages of easy cell harvest (avoiding laceration of intact cardiovascular tissues), potential of differentiating into multiple cell lineages (avoiding the need of multiple times of seeding to achieve layered cell distribution), and immunological characteristics that gives persistence in allogenic settings [165, 166]. Colazzo et al further compared adipose-derived stem cells with bone marrow mesenchymal stem cells on collagen scaffolds for TEHVs, showing that the adipose-derived stem cells have even more favourable abilities to synthesize ECM and to populate the scaffolds [161]. As its acquisition can be done by a less invasive method, and in a considerably larger quantity, the adipose-derived stem cell is regarded as a suitable candidate for TEHVs. For a special group of patients, i.e. the paediatric patients, efforts have been made to create living TEHVs aiming to repair congenital heart valve malformations even before or shortly after birth [166]. Prenatally harvested stem cells, such as umbilical cord-derived stem cells, amniotic fluid-derived stem cells and chorionic villi-derived stem cells, have been identified as the most promising candidates for this approach [167-170]. Embryonic stem cells, as the star candidate for tissue engineering due to their highest pluripotency, have been successfully used to engineer cardiac tissues that demonstrated desirable cell phenotype and organization, vascularisation, and eletromechanical function [171-173], and therefore could as well be an option for heart valve tissue engineering, although the embryo-destructive harvesting may cause ethical concerns and limit their clinical use [174]. A ground-breaking technology of induced pluripotent stem cells (iPSCs) was introduced by Takahashi et al a few years ago, in which terminally differentiated cells can be reprogrammed into embryonic-like stem cells by a set of transcription factors [175, 176]. The iPSCs do not raise ethical concerns and can also be differentiated into various types of cardiovascular cells [177, 178]. Therefore, they can be another cell source for TEHVs. The major obstacle for the iPSCs to be

widely applied, however, is the potential carcinogenicity caused by the viral transduction [166].

2.3.3 Signals

A simple cell-scaffold construct may not always be able to successfully 'engineer' a piece of living tissue, as the cells on the scaffolds not only need to exhibit their rudimentary behaviour (e.g. attachment and proliferation), but also are requested to perform functions for higher-level tissue regeneration (e.g. ECM synthesis and differentiation). Under normal culture condition, the cell-scaffold construct may suffer from difficulties of cell migration and endothelialisation [179, 180], and insufficient secretory function and low rate of remodelling [180, 181]. Therefore, in addition to the combination of the cells and the scaffolds, appropriate signalling is also needed for heart valve tissue engineering, both chemically and mechanically. Chemical signals may include growth factors, cytokines, and hormones, which can help cell adhesion, proliferation, and gene expression [19]. Mechanical signals (or stimuli) such as fluid flow, shearing, tension and flexure have all been proven to enhance cell and tissue growth [182-184].

Collagen itself contains peptide sequences, such as arginine-glycine-aspartic acid (RGD) or tyrosine-isoleucine-glycine-serine-arginine (YIGSR) [185] , which serve as biochemical signals mediating the cell adhesion on the scaffolds. In many researches on TEHVs, growth factors such as vascular endothelial cell growth factor (VEGF), transforming growth factor-beta (TGF-β), fibroblast growth factor (FGF) and hepatocyte growth factor (HGF) also have been incorporated into the scaffolds, and in response the cells have shown enhanced proliferation, differentiation and endothelialization, with a more organized ECM synthesis [186-189].

Compared with the chemical signals, even more significant progress has been made in examining the improvement that mechanical stimulation can introduce to the cell and tissue growth [19]. Various types of 'bioreactors' have been designed and have played critical roles in the investigations. They apply mechanical stimuli to the cells and scaffolds, and meanwhile maintain the desired mass transfer (gas, nutrients, waste, etc.) to and from the growing tissue, hence better simulating the overall physiological environments [182, 190].

A bioreactor could be as simple as a rotating flask or vessel, in which the shear stress caused by the medium flow is cast onto the tissue constructs as the mechanical stimuli modulating the activities of endothelialization [183, 190-192]. To be specialized for heart valve tissue engineering, more complex bioreactors with pulsatile perfusion have been developed [193] (see Fig 2.20). The heart valve tissue construct is placed in a perfusion chamber and encounters pulsatile flows and periodical displacements, which mimics the open-close cycles of the heart valve in the physiological milieu. It has been found by Hoerstrup et al, that the TEHVs grown in the pulsatile flow environment exhibited denser tissue and smoother surface than the statically cultured ones. Moreover, the bioreactor-cultured TEHVs are more pliable and more competent during valve closure [17]. Engelmayr Jr. et al further designed a bioreactor to investigate the independent effects of cyclic flexure on in vitro TEHV development (see Fig 2.21) [194]. Cyclic three-point bending was introduced to the sample at a frequency of 1 Hz, by two actuated pins in the centre and four stationary pins at the ends. The results revealed an increase in collagen content, stiffness, vimentin expression, as well as a more homogenous transmural cell distribution in the scaffold [194].

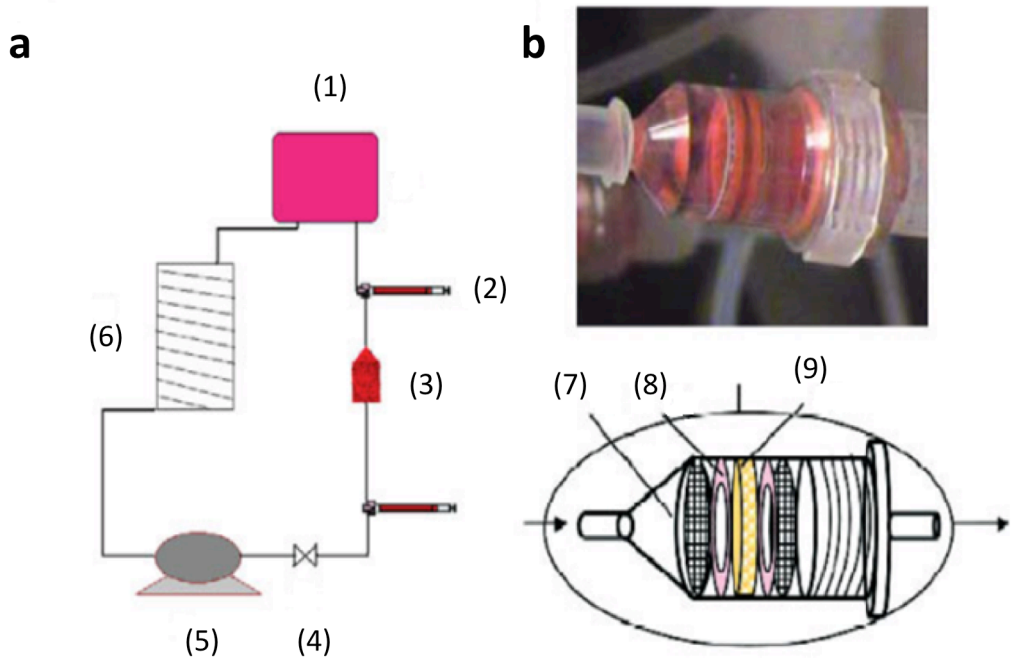


Fig 2.20 Pulsatile flow bioreactor. (a) schematics of the perfusion loop: (1) medium reservoir, (2) debubbling syringes, (3) perfusion chamber, (4) solenoid pinch valve, (5) peristaltic pump, and (6) gas exchanger. (b) Perfusion chamber includes (7) polypropylene meshes, (8) silicone gaskets, and (9) cardiac tissue construct. [193]

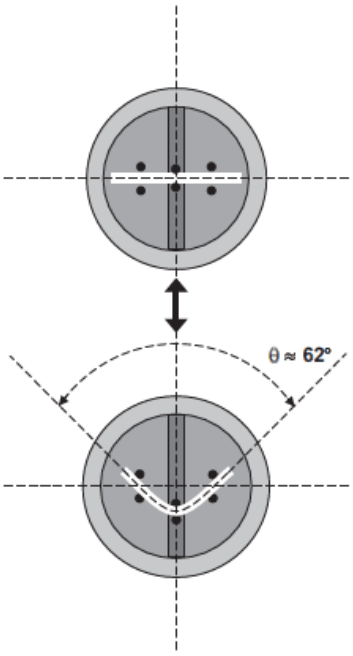


Fig 2.21 Schematic graph of cyclic flexure bioreactor [194]

2.4 Summary

In this Chapter, the structure and function of the heart valves have been studied through reviewing the literature, and the physiological significance stated. The reported worldwide situations of heart valve diseases are ensuring a great interest in TEHVs.

The techniques for TEHVs were then presented, with an emphasis on the collagen-based scaffolds. The novel TEHV, as a frontier research area, is drawing the attentions of researchers from many disciplines, to have every one of its facets improved. Mechanical properties of the scaffold are being enhanced by refining the micro-architectures; optimal cell sources are being sought to achieve a better differentiated and grown tissue in vitro; and various signals are applied to better mimic the cardiovascular environment by the concept of bioreactors.

To the author's knowledge, as well as from the perspective of materials science, the scaffold is the most important one amongst the three factors of TEHVs, and should be prioritized. It is believed that, with every aspect of the scaffold carefully examined (material selection, scaffold design, fabrication technique, micro-structure, bioactivities, and biodegradability), it could lead to the TEHVs that are of great potential to realize the goal of a living reparative heart valve. Therefore, several specific objectives are identified amongst these aspects to constitute the study in this thesis, which the author wishes could advance the TEHV field. Firstly, this study will aim to maximally mimic the layered structures and compositions of the native heart valve ECM in the scaffolds, to provide a solution to the current non-layered designs and the less controllable and repeatable decellularization process. Secondly, this study will try to recreate the above-mentioned anisotropic mechanical behaviour of heart valves in the scaffolds using the layered structures, so that the TEHV will have the potential to exhibit better

hemodynamic properties than the current mechanical valves and biological valves. Finally, this study will endeavour to achieve desirable cell behaviour on every layer of the novel scaffolds, to ensure they can successfully form viable heart valve tissues in the future.

Chapter 3. Scaffolds Manufacturing and Morphology

3.1 Introduction

The scaffolds will be acting as analogs of the extra-cellular matrix (ECM) in the tissue engineering process, and therefore need to be able to provide the cells with desirable chemical and structural micro-environments.

In this thesis, collagen, elastin, and glycosaminoglycans (GAGs) have been chosen as the scaffold materials because of their known biocompatibilities [59, 195, 196], and their prevalence in native heart valves [98]. The scaffolds need to have a porous microarchitecture (with suitable morphologies and pore sizes), as well as desired three-dimensional (3-D) shapes. Moreover, to even more closely mimic native heart valves, this project aims to create layered structures in the scaffolds. The freeze-drying technique, widely used for manufacturing scaffolds of various types [113, 197], meets the general requirements and will be adopted as the drying method for the scaffolds in the work of this thesis.

Crosslinking of the scaffolds is an essential process to give the scaffolds higher mechanical properties. Physical crosslinking methods have the advantage over chemical crosslinking methods in better preserving the homogeneity of the pore structures in the scaffolds [147], and therefore have been the preferred methods in this thesis. The dehydrothermal (DHT) treatment and the ultra-violet (UV) irradiation have been applied and compared.

This chapter will demonstrate the capability of the freeze-drying technique to produce porous collagen-based scaffolds with controlled 3-D shapes and adjustable pore sizes. Each of the contributory factors affecting the pore sizes (freezing temperature, relative

density, composition, and crosslinking) will be investigated. The impacts of the scaffold manufacturing route (i.e. the freeze-drying and the crosslinking processes) on the ultra-structures of the scaffold materials will also be studied by the means of transmission electron microscopy (TEM) and Fourier transform infra-red (FTIR) spectroscopy. The combination of the variables that generate the most suitable pore sizes, together with the justified manufacturing route, will then be applied to achieve the aimed layered scaffolds. A breakdown of the study in this chapter is shown in the flowchart in Figure 3.1.

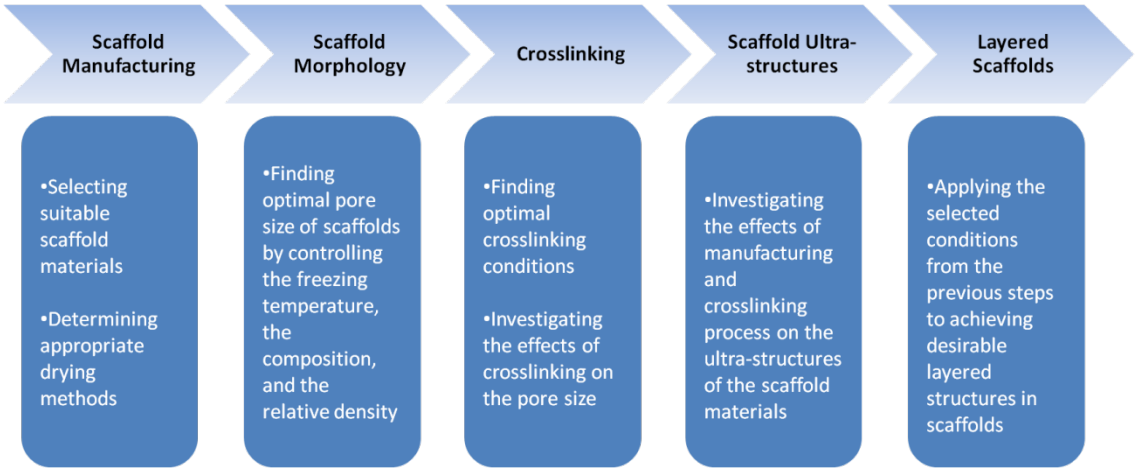


Fig 3.1 Flowchart: steps of the investigation of Chapter 3.

3.2 Materials and Methods

3.2.1 Scaffold Manufacturing

Type I collagen (from bovine Achilles tendon), chondroitin-4-sulfate (C4S) (sodium salt, from bovine trachea) and elastin (from bovine neck ligament), were selected as representative scaffold materials, and were all obtained from Sigma-Aldrich Ltd, UK.

Two major types of scaffolds were fabricated, one with uniform composition throughout the scaffolds, the other with different compositions in different layers (see Table 3.1). The scaffold materials were all firstly made into a suspension with various compositions and concentrations as shown in Table 3.1.

Table 3.1 Composition and suspension concentration of different types of scaffolds.

Scaffold	Composition	Concentration (wt/v)
Uniform-composition	100%collagen	0.5%, 1%, 2.5%
	50%collagen-50%elastin	0.5%, 1%, 2.5%
	20%collagen-80%elastin	0.5%, 1%, 2.5%
	90%collagen-10%C4S	0.5%, 1%, 2%
	50%collagen-50%C4S	0.5%, 1%, 2%
Bi-layer	100%collagen/50%collagen-50%elastin	1%
	100%collagen/20%collagen-80%elastin	1%
	100%collagen/90%collagen-10%C4S	1%
	100%collagen/50%collagen-50%C4S	1%
Tri-layer	100%collagen/90%collagen-10%C4S/50%collagen-50%elastin	1%
	100%collagen/50%collagen-50%C4S/20%collagen-80%elastin	1%

For collagen and collagen-elastin scaffolds, 0.05M ethanoic acid (pH 3.2) was prepared as the solvent, in which collagen fibrils would have maximum swelling due to lyotropic effects [198, 199] and therefore would be most easily suspended. Collagen and elastin were weighed (AB204, Mettler Toledo, UK, precision 0.1mg) according to the requested composition (100%collagen, 50%collagen-50%elastin, 20%collagen-80%elastin) and suspension concentration (0.5% wt/v, 1% wt/v, 2.5% wt/v), eventually giving the scaffolds different compositions and relative densities. The weighed proteins was blended in the acidic solvent with a blender (HR1611/01, 650W, Philips, UK) until

it became a homogeneous suspension. This process was carried out in an ice bath to prevent denaturation of the proteins that might be caused by the heat generated during blending.

For the collagen-C4S scaffolds, different compositions (90%collagen-10%CS, 50%collagen-50%C4S) and suspension concentrations (0.5% wt/v, 1% wt/v, 2% wt/v) were also applied. The collagen was firstly suspended in the ethanoic acid as described above. Then the C4S was added into the suspension, instantly co-precipitating with collagen and forming agglomerates. The agglomeration was reduced by drop-wise addition of 2M sodium hydroxide solution to the suspension until the pH value reached 7 [196]. The collagen-C4S suspension was blended again (also conducted in ice bath), resulting in a homogeneous suspension of fine collagen-C4S co-precipitates.

After the suspension was made, it was subjected to a vacuum of 10Pa for 1 hour at room temperature to remove the entrapped air bubbles. The de-gassed suspension was then cast into various polytetrafluoroethylene (PTFE) moulds according to the required dimensions of the samples, and was frozen at the required temperatures (-20˚C or -80˚C) (EU7120C, Electrolux, UK and MDF-U76VA, SANYO, USA).

For scaffolds with layered structures, multiple casting-freezing procedures were performed. The 100%collagen layer was firstly cast and frozen, followed by other subsequent layers (see Table 3.1). When a subsequent layer was cast onto a frozen layer, it was left under room temperature for 2 minutes before being frozen again, in order to allow good inter-layer connection. The volume of the suspension for each layer was controlled so as to give an equal thickness to each layer (native valve has different thickness for each layer, but they were kept equal in this thesis so that later

investigations of various properties of the layers would not be affected by the thickness and hence would be less complicated).

Two methods, freeze-drying and critical point drying, were evaluated for drying the frozen suspension. For freeze-drying, the samples were placed in a Christ I-5 freeze-dryer (Martin Christ Gefriertrocknungsanlagen GmbH, Germany) for 24 hours in a vacuum of 5Pa, removing the ice crystals by sublimation and leaving the porous solid scaffolds (see 2.3.1). For critical point drying, the frozen samples were immersed in 99.9% ethanol, which dissolved the ice crystals. The remaining scaffolds containing ethanol were placed in a critical point dryer (E3100, Quorum technologies, UK) for the the exchange of ethanol with liquid CO_2 at room temperature and a pressure of 5.0 MPa. The exchange was repeated at 10, 20, 30, 60, 120, and 180 minutes to ensure the ethanol was completely replaced by liquid CO_2, after which, the temperature of the critical point dryer was raised to 37°C (above the critical temperature of liquid CO2), with a concomitant increase in pressure to 9.0 MPa. The gas-release valve was then slowly opened to lower the pressure in the critical point dryer, transforming the CO_2 from supercritical fluid state to gaseous state and therefore releasing it. After the CO_2 was completely released, the temperature of the critical point dryer was reduced to room temperature and porous scaffolds were obtained (see 2.3.1) [200, 201].

3.2.2 Scaffold Morphology

Scaffold morphology was characterized by scanning electron microscopy (SEM) JSM840F (JEOL Ltd, Japan) at an accelerating voltage of 4kV. Samples were sectioned with a sharp razor blade, and the cross-sections were examined. Before imaging, the samples were mounted on to aluminium stubs with adhesive carbon tabs. As all the scaffold materials were non-conductive, samples were coated with 3nm thick platinum

by a 208HR sputter coater (Cressington Scientific Instruments Ltd, UK). From the images taken, the mean pore sizes of the scaffolds were calculated by measuring the diameters of the pores using ImageJ (National Institutes of Health, USA). 2-3 samples were imaged for each group, with 30-40 measurements on each sample. Measurements from the samples in the same group had no statistically significant difference, and the mean pore size was calculated using all the measurements from the group.

3.2.3 Crosslinking

DHT treatment was conducted following the protocol established by Yahyouche [147]. The freeze-dried scaffolds were subjected to a temperature of 110˚C and a vacuum of 1Pa in a Heraeus Vacutherm vacuum oven (Kendro Laboratory Products GmbH, Germany) for 72 hours. When the treatment was finished, the temperature was allowed to return to 20 ˚C before the vacuum oven was ventilated.

UV irradiation was carried out using a Stratalinker UV Crosslinker (Stratagene, USA). The freeze-dried scaffolds were placed 15cm under five 15W 254-nm UV light bulbs for 4 hours. all scaffolds were turned over half way through the irradiation [202]. Researchers have reported various optimal UV dosages for collagen samples [146, 149, 202, 203], and they were all dependent on factors such as the wavelength of the UV light, the type of collagen, the efficiency of the apparatus, and the condition of the atmosphere [204]. For the specific collagen source and the apparatus used in this thesis, the 4 hours irradiation time was determined so as to give an optimal mechanical property to the scaffolds. The process of selecting the optimal irradiation time is as follows.

UV irradiation on 1%wt/v 100% collagen scaffolds was carried out with the methods detailed above, with a series of UV irradiation times (1h, 2h, 4h, 8h, and 48h).

Mechanical characterizations were then conducted on the UV irradiated scaffolds (compression for 1h, 2h, 4h, 8h, and 48h samples; tension for 2h, 4h, and 8h samples), using the protocols detailed in 4.2.1. The irradiation time rendering the highest mechanical properties was selected to be the standard UV irradiation time for all the scaffolds in this thesis. It had been acknowledged that scaffolds with different compositions might have different optimal irradiation times. However, the collagen layer, as the major load-bearing layer in the layered scaffolds, should enjoy the priority in the mechanical property improvement. Therefore, the optimal irradiation time was determined by examining the 100%collagen scaffolds only.

3.2.4 Transmission Electron Microscopy

The longitudinally staggered molecules give the collagen fibrils a distinct banded structure, which can be observed under TEM and used as an indicator of ultra-structure changes of the collagen [205].

A 2000FX TEM (JEOL Ltd, Japan) was used in this project to examine the banding patterns of the collagen at different stages of the manufacturing route (i.e. raw, freeze-dried, DHT treated, and UV irradiated).

Before observation, the collagen samples were firstly re-suspended in distilled water, subsequently collected by copper TEM grids (Agar Scientific, UK), and then air-dried overnight. No staining was applied in order not to introduce any additional effects on the collagen molecules [200]. Observation was conducted in bright field imaging mode at an accelerating voltage of 200kV. The images were analyzed by ImageJ (National Institutes of Health, USA) for the periodic distance of collagen fibrils.

3.2.5 Fourier Transform Infra-red Spectroscopy

FTIR spectroscopy is extensively used for chemical characterization in the biomedical fields, because of its non-destructive approach and minimal requirements for sample preparation [206]. It is based on the absorption of the infrared radiation by the molecules, which changes the molecular vibration and rotation status. By analyzing the absorption peaks on the spectrum, the existent chemical bonds can be identified and hence the molecular structures determined.

This project used a Varian FTIR spectrometer (UMA600, Palo Alto, CA) to investigate the changes in the primary and secondary structures of the collagen, C4S and elastin during the freeze-drying and crosslinking processes, in order to see whether the manufacturing route had any effects on the nature of the materials. Spectra of infra-red absorbance were measured in the mid-infrared region (wavenumber 4000-600cm^{-1}) with a resolution of 2cm^{-1} and were recorded as averages of 64 scans for each sample, with 3 replicas for each group. Numerical analysis was conducted on the spectra with EssentialFTIR (Operant, LLC. FL) and PeakFit (SeaSolve Software, Inc. MA).

3.2.6 Statistics

All data were reported as means, with the standard deviations as the errors. One-way analysis of variance (ANOVA) followed by Tukey's test was used to compare groups of data, with a probability value of 95% ($p < 0.05$) to determine statistical significance.

3.3 Results

3.3.1 Scaffold Manufacturing

Fig 3.2 shows the suspensions of different materials in the homogenization process. It can be seen that collagen and collagen-elastin mixture were able to form a homogeneous suspension in the acidic environment, while collagen-C4S mixture formed flocculent co-precipitates at pH 3.2. The collagen-C4S co-precipitates were reduced when the pH value was increased to 7.

Fig 3.3 shows the scaffolds produced by freeze-drying and critical point drying with the same mould. It was found that the critical point-dried scaffold had drastic volume shrinkage, which brings uncontrollability over the relative density of the scaffold. Therefore, the critical point drying method was discontinued and all the scaffolds were freeze-dried in the rest of this thesis.

Fig 3.4 shows the freeze-dried scaffolds of various sizes, and the respective moulds. Adopting the density values of the scaffold materials from literature (1.3 g/cm^3 for collagen, 1.3 g/cm^3 for elastin [54], and 1.94 g/cm^3 for C4S [207]), the scaffolds had porosities ranging from 99.68% to 98.08%, and accordingly the relative densities ranging from 0.32% to 1.92%. For scaffolds of the same composition ratios, the concentration of the suspension was proportional to the relative density, and therefore was used to express the relative density for convenience in this thesis.

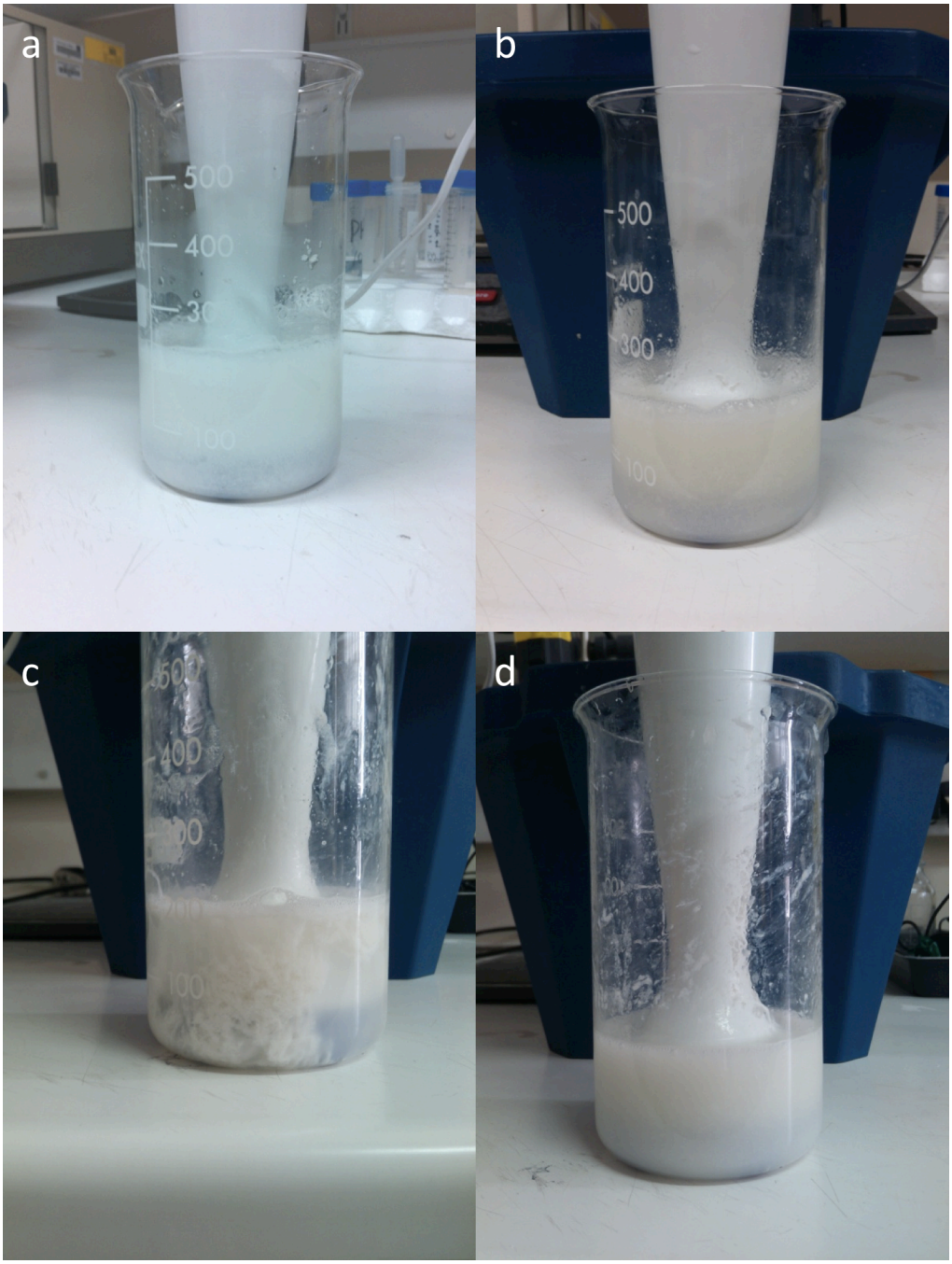


Fig 3.2 Suspensions of (a) collagen at pH3.2, (b) collagen-elastin mixture at pH3.2, (c) collagen-C4S mixture at pH3.2, and (d) collagen-C4S mixture at pH7.



Fig 3.3 Left: mould; centre: freeze-dried scaffold; right: critical point-dried scaffold.

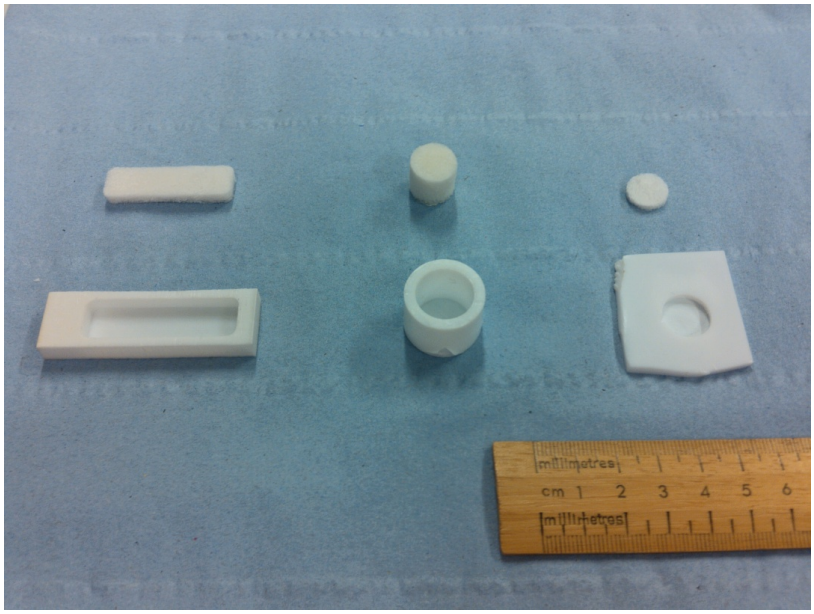


Fig 3.4 Left: scaffold for tensile and bending tests (40mm in length, 12mm in width, and 5mm in thickness) and its mould. Centre: scaffold for compression tests (15mm in diameter and 15mm in height) and its mould. Right: scaffold for cell culture (12.5mm in diameter and 1.5 mm in thickness).

3.3.2 Scaffold Morphology

Fig 3.5 shows representative SEM micrographs of the 100%collagen scaffolds with various relative densities and freezing temperatures, and the mean pore sizes of the scaffolds are listed in Table 3.2. The pore size of the scaffolds is observed to be larger for a higher freezing temperature and smaller for a higher relative density ($\frac{\rho}{\rho_s}$).

Fig 3.6 shows representative SEM micrographs of the collagen-elastin scaffolds with various relative densities and collagen-elastin ratios, and the mean pore sizes of the scaffolds are listed in Table 3.3. We find that the pore size of the collagen-elastin scaffolds also decreases with an increase of the relative density (with an exception of the 0.5% wt/v 20%collagen-80%elastin group). Compared with the 100%collagen scaffolds with correspondent relative densities, the collagen-elastin scaffolds generally have larger pores, and less solid pore walls.

Fig 3.7 shows representative SEM micrographs of the collagen-C4S scaffolds with different relative densities and collagen-C4S ratios, and the mean pore sizes of the scaffolds are listed in Table 3.4. We can see that the higher relative density does not cause visible reduction on pore size in the collagen-C4S scaffolds, which is different from what is observed in the collagen and collagen-elastin scaffolds. However, low relative density does cause the loss of pore wall integrity in the collagen-C4S scaffolds (especially in the 0.5%wt/v 50%collagen-50%C4S scaffolds where the pore structures are totally lost and a mesh-like structure is exhibited instead), see Fig 3.7 a, b. Moreover, the different collagen-C4S ratios do not have an obvious effect on the pore size either, although a difference in the pore morphology can be observed in Fig 3.7: the pore walls of the 50%collagen-50%C4S scaffolds are ‘wavier’ than those of the 90%collagen-10%C4S scaffolds.

Table 3.2 Pore sizes of 100% collagen scaffolds with different relative densities and freezing temperatures. [a] denotes statistically significant difference ($p<0.05$) to the scaffolds with the same freezing temperature. [b] denotes statistically significant difference ($p<0.05$) to the scaffolds with the same relative density.

100%Collagen	-20˚C	-80˚C
0.5%wt/v	173.7±37.1[a,b] µm	55.3±13.8[a,b] µm
1%wt/v	147.6±38.4[a,b] µm	41.4±8.6[a,b] µm
2.5%wt/v	65.4±12.2[a,b] µm	33.2±10.3[a,b] µm

Table 3.3 Pore sizes of collagen-elastin scaffolds with different relative densities and collagen-elastin ratios (freezing temperature is -20˚C). [a] denotes statistically significant difference ($p<0.05$) to the scaffolds with the same collagen-elastin ratio. [b] denotes statistically significant difference ($p<0.05$) to the scaffolds with the same relative density.

Collagen-Elastin	50%-50%	20%-80%
0.5%wt/v	201.5±50.6[a,b] µm	148.8±21.7[b] µm
1%wt/v	179.9±35.8[a] µm	187.6±36.5[a] µm
2.5%wt/v	120.5±30.5[a,b] µm	155.2±20.1[b] µm

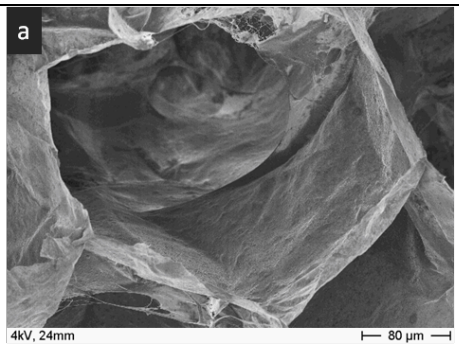
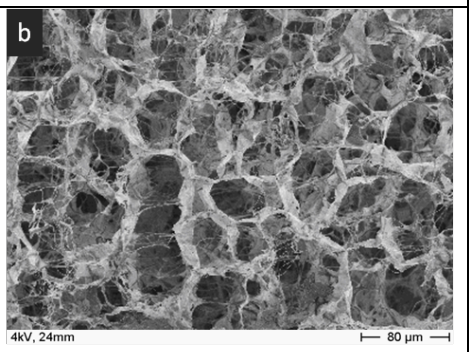
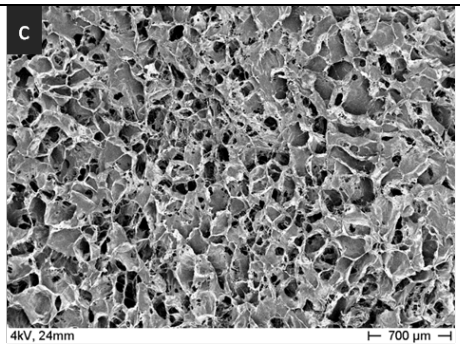
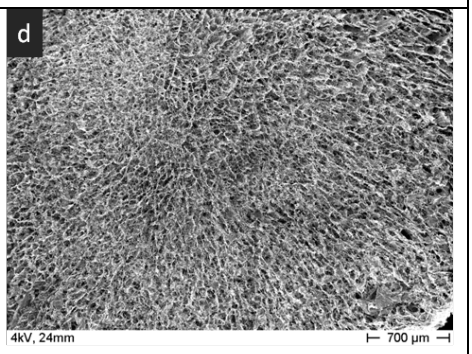
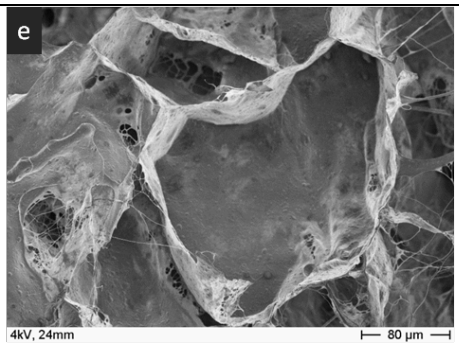
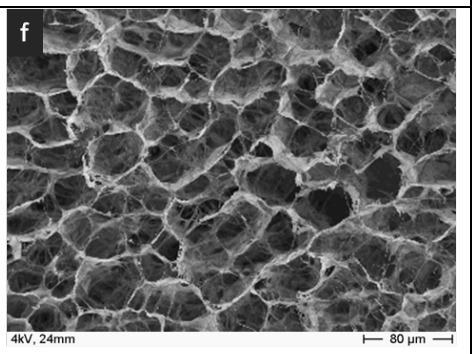
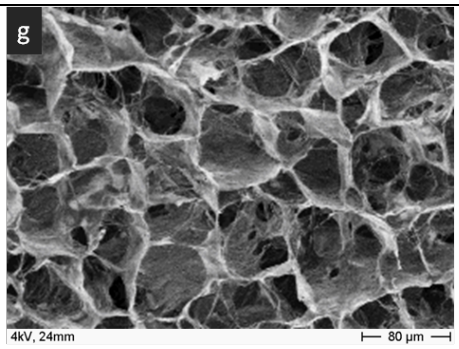
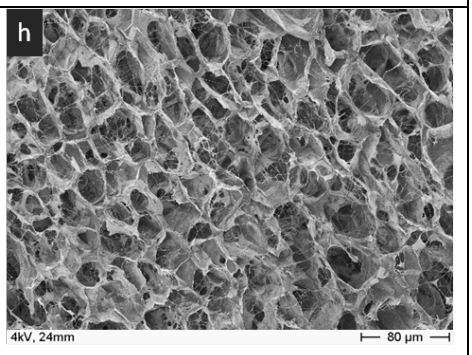
	-20˚C	-80˚C
0.5%wt/v		
1%wt/v Low Magni-fication		
1%wt/v		
2.5%wt/v		

Fig 3.5 Representative SEM micrographs of various 100%collagen scaffolds.

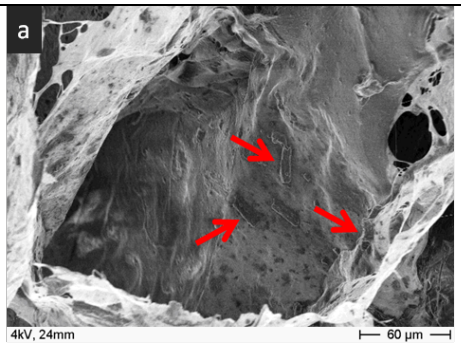
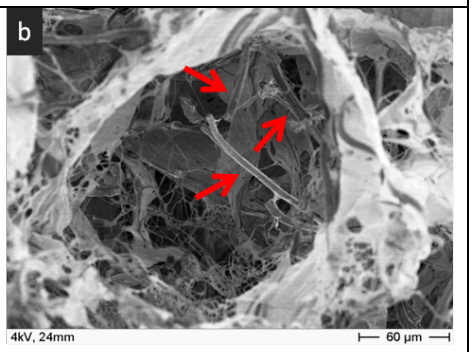
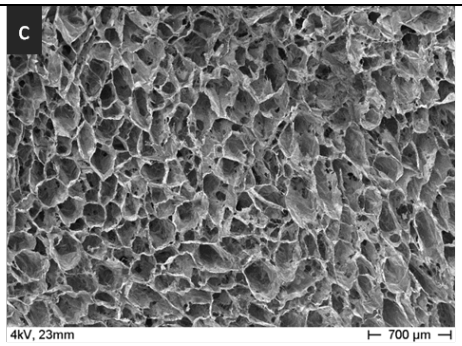
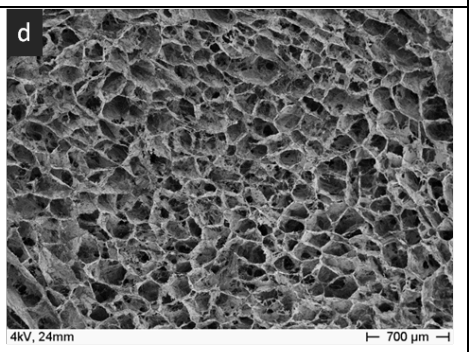
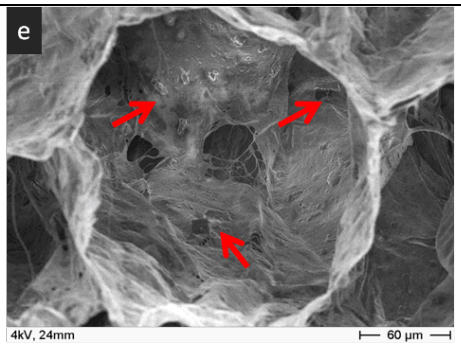
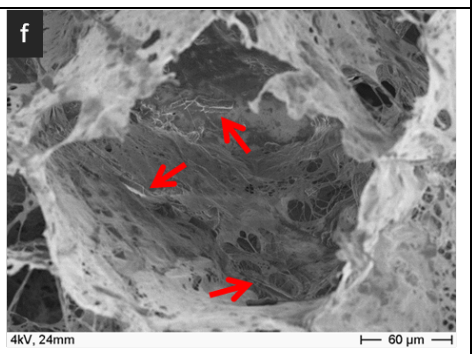
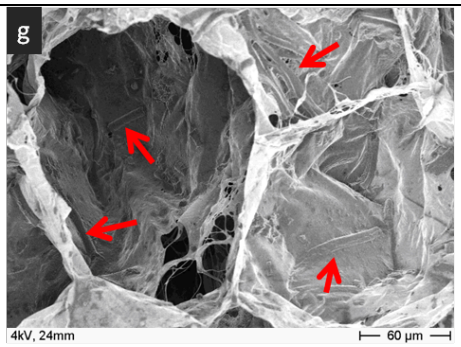
	50%Collagen-50%Elastin	20%Collagen-80%Elastin
0.5%wt/v		
1%wt/v Low Magni-fication		
1%wt/v		
2.5%wt/v		

Fig 3.6 Representative SEM micrographs of various collagen-elastin scaffolds. Freezing temperature is all -20˚C. Red arrows denote elastin.

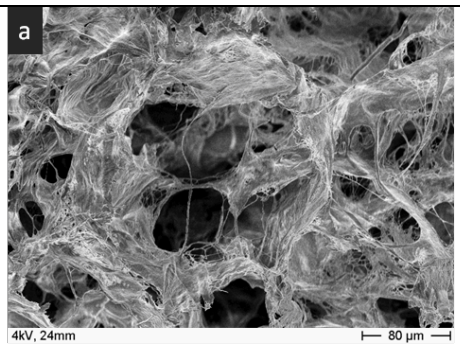
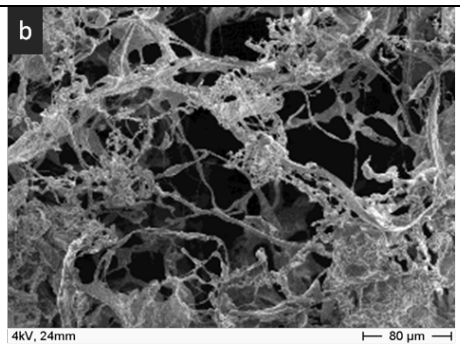
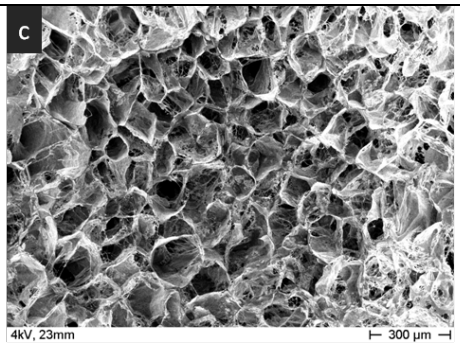
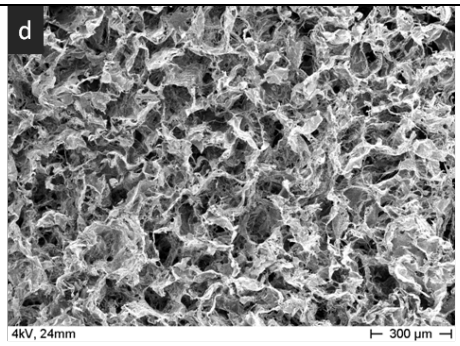
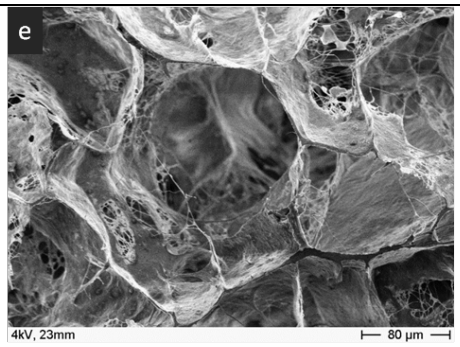
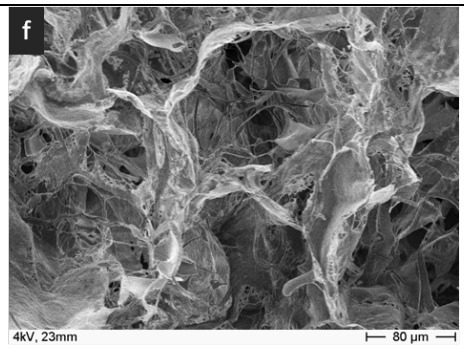
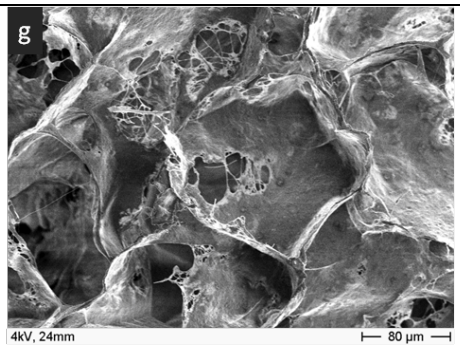
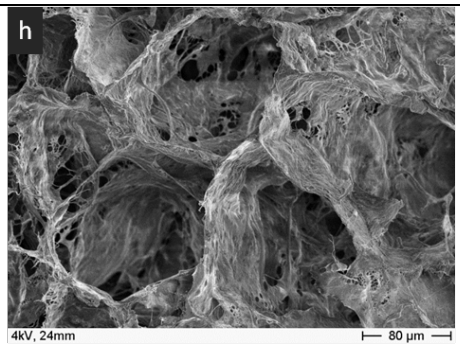
	90%Collagen-10%C4S	50%Collagen-50%C4S
0.5%wt/v		
1%wt/v Low Magni-fication		
1%wt/v		
2%wt/v		

Fig 3.7 Representative SEM micrographs of various collagen-C4S scaffolds. Freezing temperature is all -20˚C.

Table 3.4 Pore sizes of collagen-C4S scaffolds with different relative densities and collagen-C4S ratios (freezing temperature is -20˚C). There was no statistically significant difference amongst all the groups. * The 0.5%wt/v 50%collagen-50%C4S scaffolds showed a mesh-like structure and therefore is not applicable for a pore size measurement.

Collagen-C4S	90%-10%	50%-50%
0.5%wt/v	123.4±25.2 μm	N/A*
1%wt/v	115.6±27.6 μm	116.8±17.8 μm
2%wt/v	125.9±27.0 μm	116.6±18.6 μm

3.3.3 Crosslinking

In the process of optimization of the UV irradiation time, the compressive and tensile moduli (E_{comp} and E_{ten}) of the non-crosslinked and the UV irradiated collagen scaffolds were derived from the mechanical tests (see 4.3.1 for details), and are listed in Table 3.5. From the results of the compression tests, we can see that the UV irradiation caused no significant improvement in the E_{comp} during the first two hours. The E_{comp} then saw a significant increase during 2h to 4h irradiation time, but started to decrease afterwards. In the extreme case of 48h irradiation time, the value of E_{comp} was even lower than that of the non-crosslinked scaffolds. The values of E_{ten} confirmed this trend, exhibiting an increase from 2h to 4h and then a decrease from 4h to 8h. Therefore, 4h was determined as the optimal irradiation time and was used for this thesis.

Table 3.5 Compressive and tensile moduli of collagen scaffolds with different UV irradiation times. Statistical differences between groups are reported after the table. > denotes significantly greater value ($p<0.05$), and = denotes no statistically significant difference ($p>0.05$).

	Non-Crosslinked	1h	2h	4h	8h	48h
E_{comp} (kPa)	28.3±4.6	30.1±0.8	29.3±4.8	50.0±3.3	44.1±6.2	23.8±3.5
E_{ten} (kPa)	344.6±42.6	-	680.2±18.5	874.0±78.7	611.6±52.8	-

E_{comp}: 4h > 8h > Non-Crosslinked = 1h = 2h > 48h

E_{ten}: 4h > 2h > 8h > Non-Crosslinked

The optimized UV irradiation time, and the adopted DHT parameters were applied on selected scaffolds to investigate the effects of crosslinking on the pore sizes. After the crosslinking processes, the scaffolds all retained their porous structures. Table 3.6 compares the means pore sizes of non-crosslinked and crosslinked scaffolds. It appears that the crosslinking process have slightly (or, in most cases, hardly) reduced the pore sizes of the scaffolds.

Table 3.6 Pore sizes of non-crosslinked, DHT treated, and UV irradiated scaffolds. * denotes statistically significant difference ($p<0.05$) to the pore size of the non-crosslinked scaffolds.

	Non-crosslinked	DHT	UV
100%Collagen	147.6±38.4 μm	124.6±23.5 * μm	142.6±32.8 μm
50%Collagen-50%elastin	179.9±35.8 μm	166.7±31.5 μm	152.2±25.3 * μm
90%Collagen-10%C4S	115.6±27.6 μm	107.5±20.7 μm	103.9±24.9 μm

3.3.4 Scaffold Ultra-structures (TEM, FTIR)

TEM images (Fig 3.8) show that the D-banding pattern remained visible and the periodic distance remained similar after the freeze drying process, meaning that the quaternary structure (i.e. the longitudinally staggered array) of the collagen molecules was preserved during the process [51]. This indicates that the covalent intermolecular crosslinks remained intact in the process [51, 199].

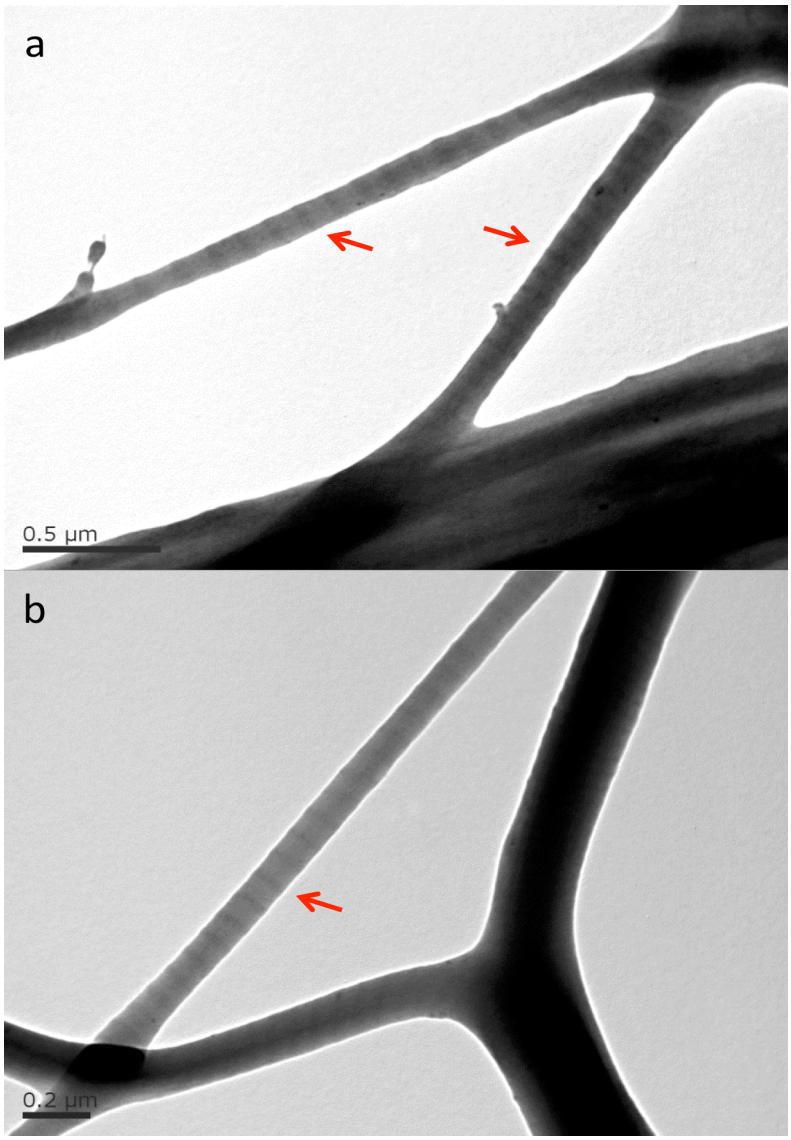


Fig 3.8 TEM images of collagen fibrils (a) before freeze-drying with periodic distance of 75.9±5.5nm, and (b) after freeze-drying with periodic distance of 79.9±6.1 nm. Arrows denote the D-banding patterns.

Spectra of collagen, elastin and C4S are shown in Fig 3.9, both non-freeze-dried and freeze-dried. In Fig 3.9a, both of the spectra contained all the characteristic peaks of collagen and there were no major peak shifts, indicating that the primary structures of collagen had not been changed during freeze-drying. However, a few differences in the spectrum of the freeze-dried sample could still be observed. First, the relative intensity of the peaks at 1164cm^{-1} and 1070cm^{-1} decreased substantially, indicating the correspondent ester groups and sugar groups had reduced in amount [208-211]. Second, the peaks at 948cm^{-1} and 860cm^{-1} (which are not native to collagen but to GAGs [212, 213]) become almost invisible. Fig 3.9b shows that elastin had almost identical spectra before and after freeze-drying, which means freeze-drying had not visibly affected the structure of elastin. In Fig 3.9c, firstly we noticed that the Amide I and Amide II peaks of C4S (located at 1640cm^{-1} and 1553cm^{-1} [214]) were overlapped by the peak of carboxylate at 1610cm^{-1} [215], and therefore were not readily separated on the spectra, resulting in two virtual peaks at 1614cm^{-}1 and 1557cm^{-1}. With peak deconvolution (see Fig 3.10), it can be seen that the carboxylate peak shifted to a lower wavenumber as well as decreased in relative intensity after freeze-drying, and hence changed the relative ratio of the two virtual peaks. In addition, it can also be found in Fig 3.9c that the relative intensities of the peaks at 1414cm^{-1} and 1380cm^{-1} increased after freeze-drying, indicating there were more free carboxyl groups [213].

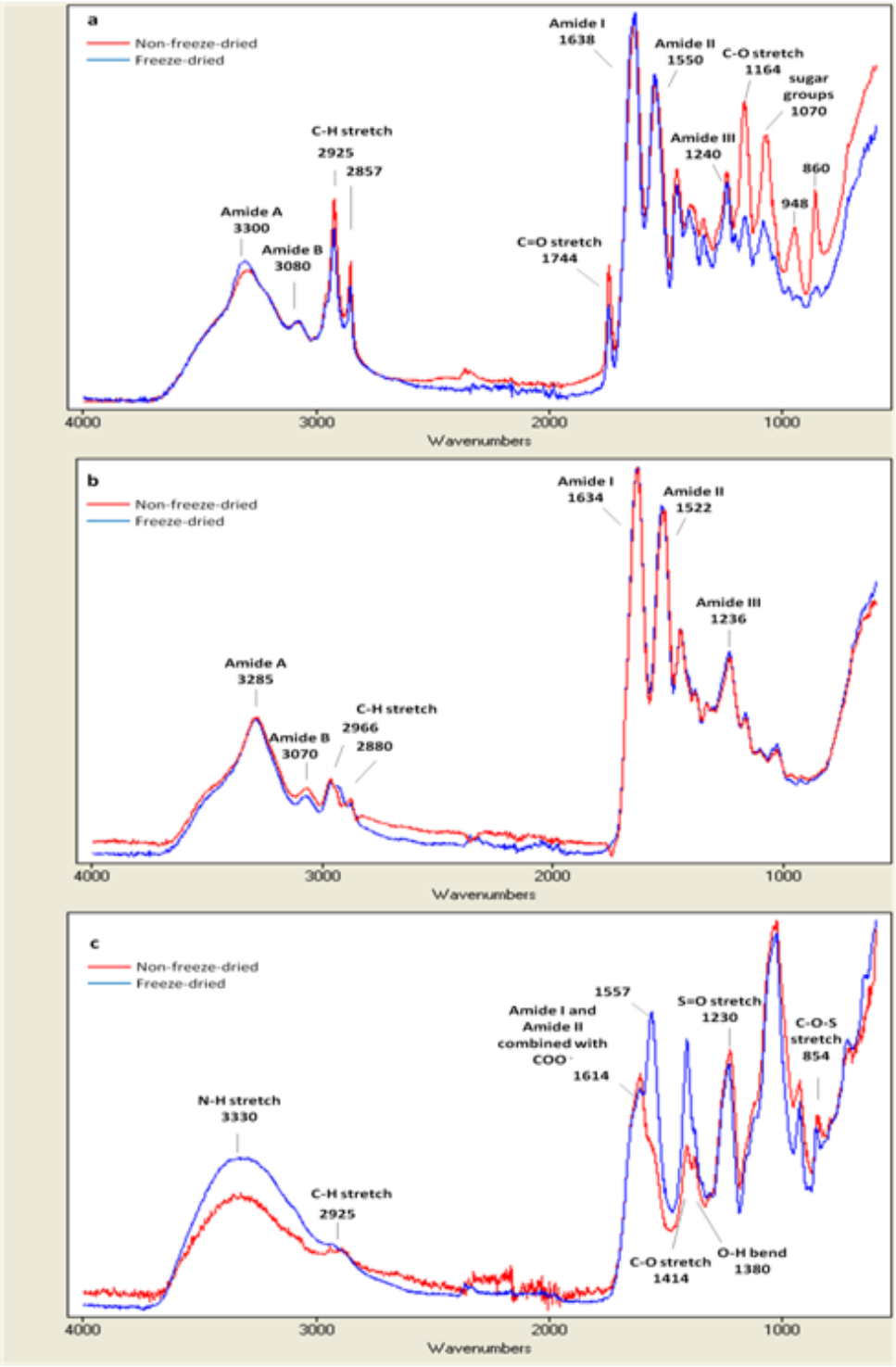


Fig 3.9 FTIR spectra of (a) non-freeze-dried and freeze-dried collagen, (b) non-freeze-dried and freeze-dried elastin, and (c) non-freeze-dried and freeze-dried C4S. Characteristic peaks are identified and labeled according to literature [206, 209, 211-214, 216-218]. Elastin and C4S were freeze-dried alone according to the methods for collagen-elastin scaffolds and collagen-C4S scaffolds in 3.2.1 respectively, in order to measure the FTIR spectra of individual materials.

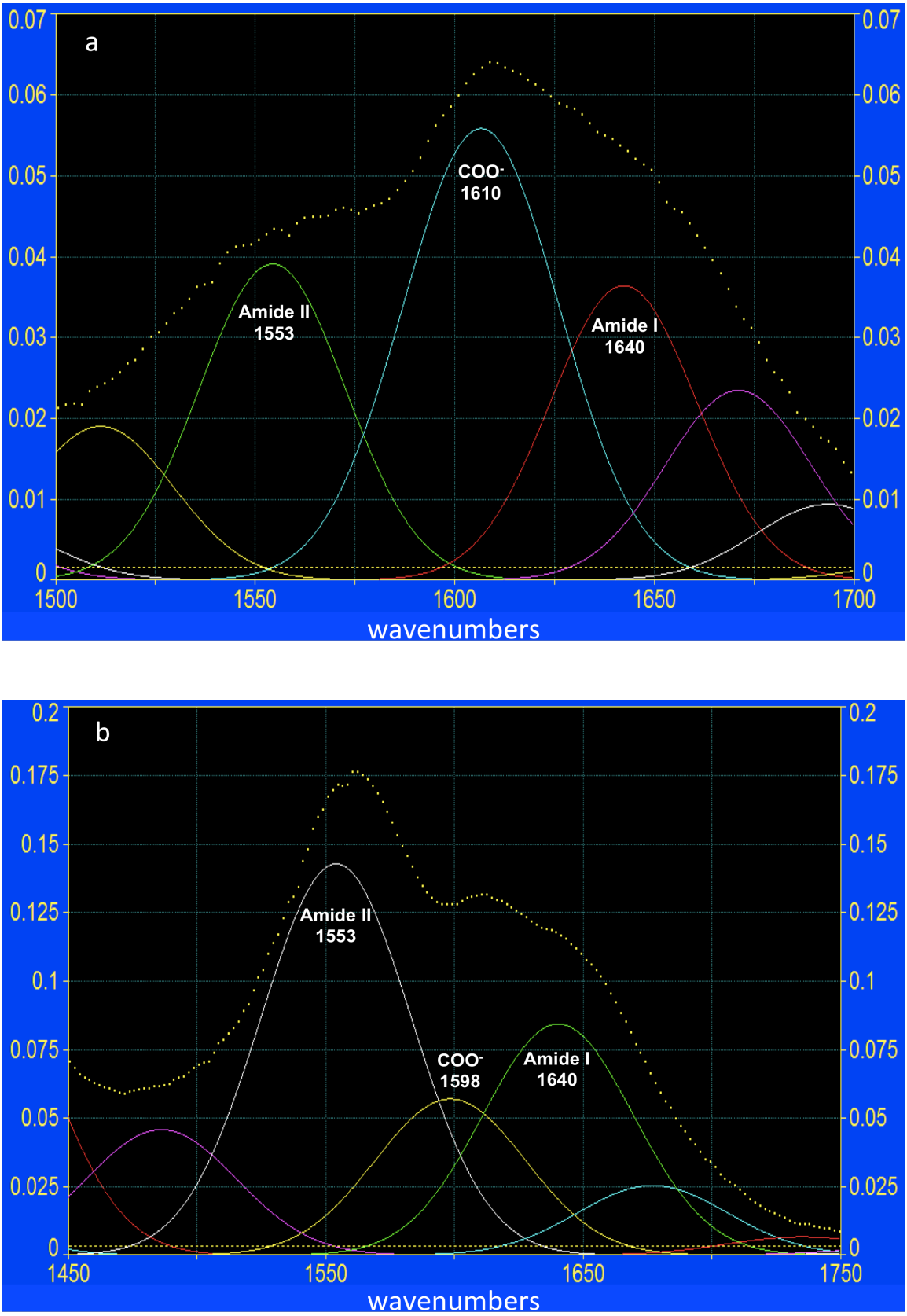


Fig 3.10 Deconvolution of Amide I, Amide II, and carboxylate peaks of (a) non-freeze-dried C4S, and (b) freeze-dried C4S

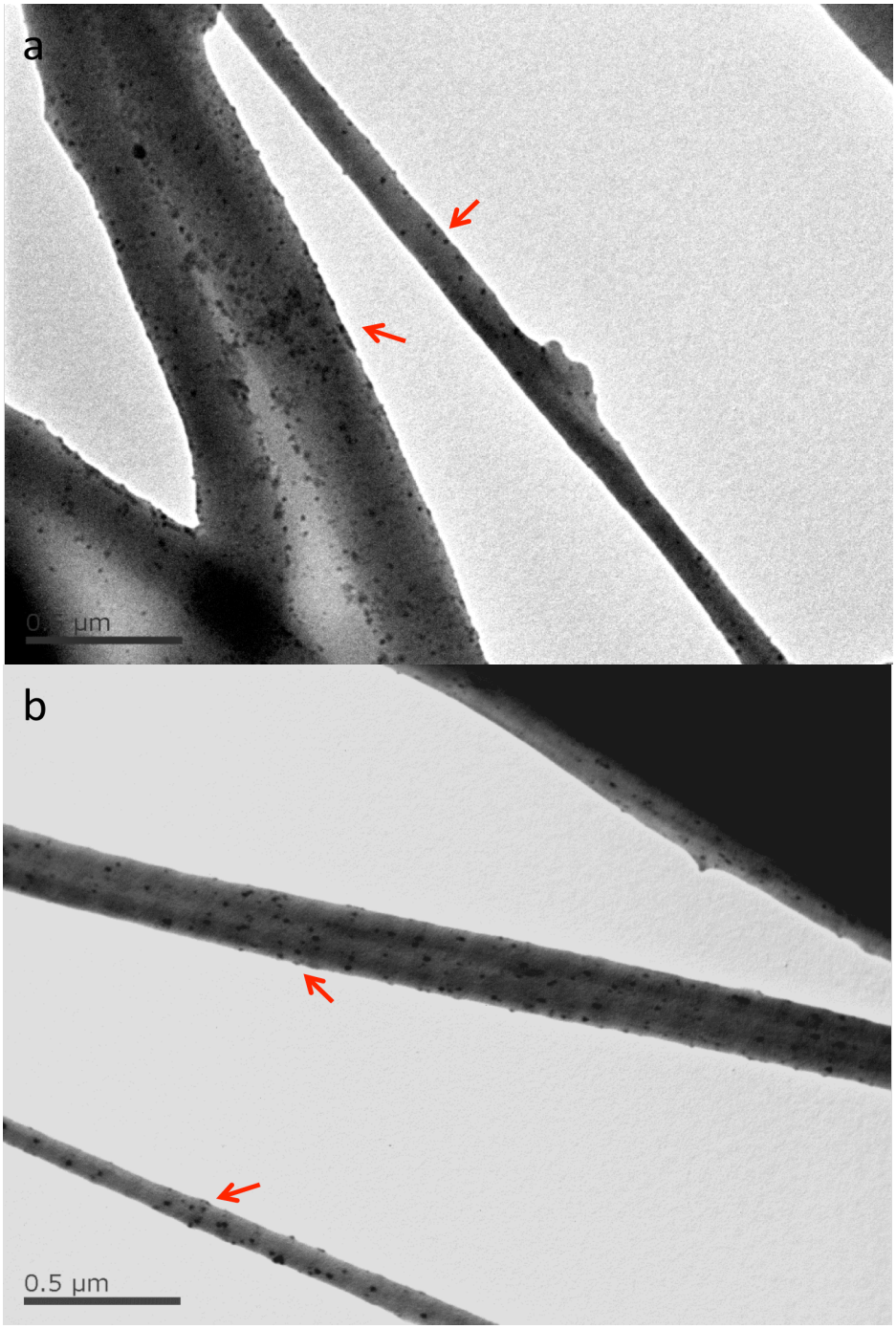


Fig 3.11 TEM images of collagen fibrils (a) after DHT treatment and (b) after UV irradiation. Scale bars are 0.5 µm. Arrows denote the dark dotted areas and the loss of D-banding patterns.

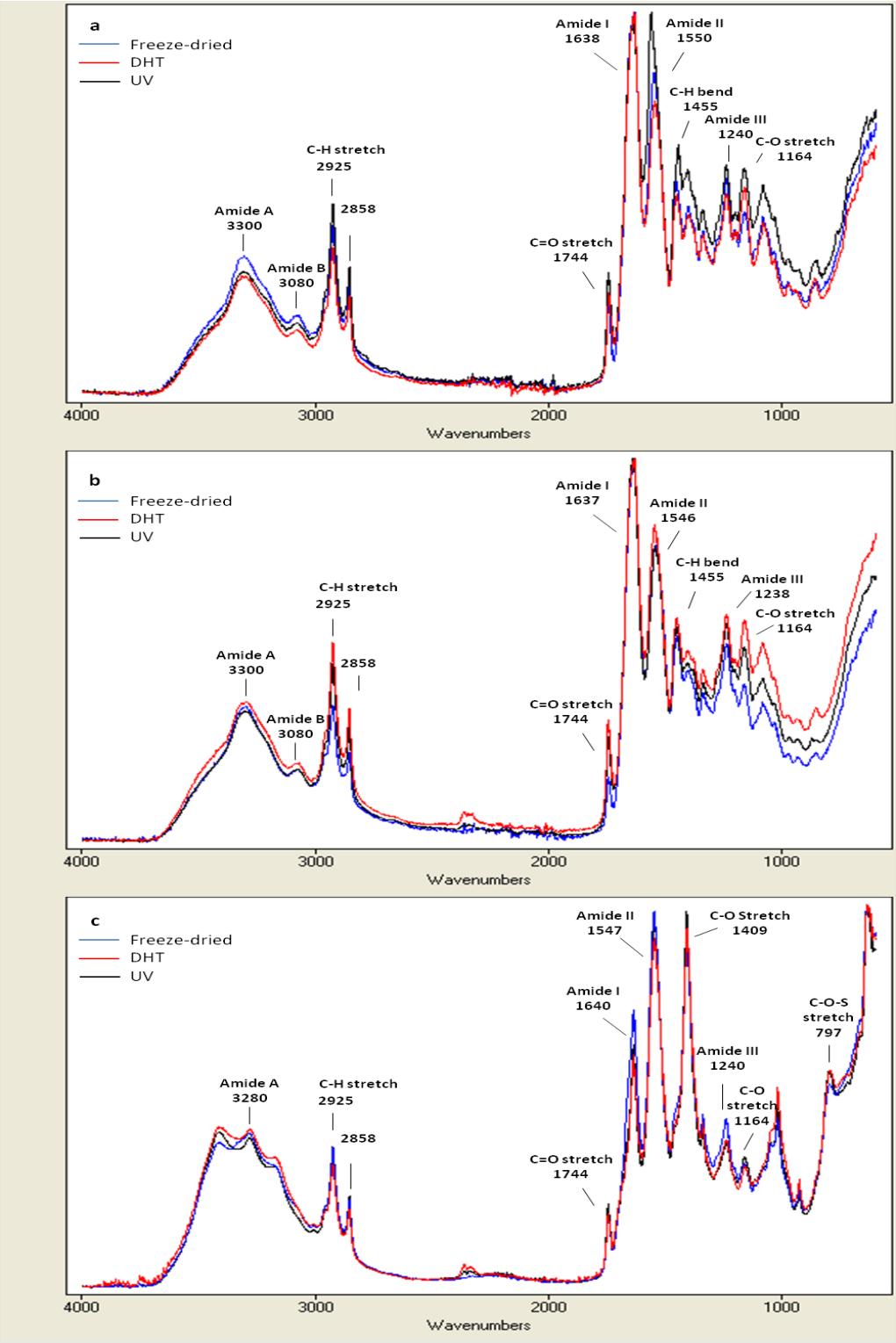


Fig 3.12 FTIR spectra of the (a) 100%collagen, (b) 50%collagen-50%elastin, and (c) 90%collagen-10%C4S scaffolds before crosslinking (Freeze-dried), after DHT treatment (DHT), and after UV irradiation (UV). Characteristic peaks are identified and labeled according to literature [206, 209, 211-214, 216-218].

TEM images of crosslinked collagen samples (Fig 3.11) show that the D-banding patterns of the collagen fibrils were almost lost after DHT treatment and were also less visible after UV irradiation. In addition there appeared dark dotted areas on the fibrils that were not existent in Fig 3.8 before crosslinking. This indicates certain extent of ultra-structure changes were introduced by the crosslinking processes.

Fig 3.12 shows the spectra of the 100%collagen, 50%collagen-50%elastin and 90%collagen-10%C4S scaffolds before and after the crosslinking processes. There were no major shifts of all the characteristic peaks, proving that no additional chemicals were introduced to the scaffolds, which was expected as the advantage of using the physical crosslinking methods.

Further quantitative information can be obtained from the spectra to evaluate the degree of crosslinking and denaturation that took place in the crosslinking process. The peaks at 1744cm^{-1} and 1164cm^{-1} were assigned to C=O stretch and C-O stretch in the ester carbonyl respectively [208-210], and therefore their relative intensities illustrated the amount of ester crosslinks in the scaffolds. Another type of crosslinks introduced by the crosslinking processes, i.e. amide formation [146], could be assessed by analyzing the relative intensity of the Amide II peak near 1550cm^{-1}, which is assigned to the -NH- in the amide bond [219]. Since the C-H bend peak near 1455cm^{-1} was not affected by the crosslinking processes [220, 221], it could be used as a reference for the relative intensities of the above peaks [148]. The C-H bend peak in the spectra of collagen-C4S scaffolds, however, was overlapped with the C-O stretch peak, and therefore needed to be separated by peak deconcolution (see Fig 3.13a). The ratio of the two sub-bands of the Amide I peak at 1630cm^{-1} (associated with random coil form) and 1660cm^{-1} (associated with helical form) [204], can indicate the degree of denaturation of the proteins. Peaks deconvolution was also performed, as shown in Fig 3.13b. The

normalized intensities of the peaks at 1744cm^{-1}, 1164cm^{-1} and 1550cm^{-1}, and the ratio of the sub-bands 1630cm^{-1}/1660cm^{-1} are listed in Table 3.7.

For 100%collagen scaffolds, the relative intensities of the peaks at 1744cm^{-1} and 1164cm^{-1} increased after both crosslinking processes, suggesting more ester crosslinks were introduced. The relative intensity of the peak at 1550cm^{-1} reduced after DHT treatment and remained the same after UV irradiation, indicating that the crosslinking processes did not increase, or even reduced, the amount of amide crosslinks in the collagen scaffolds. The ratio of 1630cm^{-1}/1660cm^{-1} increased after DHT treatment, which meant a certain degree of denaturation was introduced to the collagen. This effect, however, did not seem to be prominent after UV irradiation.

For 50%collagen-50%elastin scaffolds, esterification also increased after both of the crosslinking processes (higher in DHT treated samples than in UV irradiated samples), and no increase in amide formation was observed. Both crosslinking methods also introduced denaturation to the scaffolds.

For 90%collagen-10%C4S scaffolds, the peaks associated with esterification showed unchanged or even lower relative intensities, while the peak associated with amide formation increased in the relative intensities (especially in the DHT treated samples). Denaturation was also observed in the crosslinked scaffolds, more pronounced in DHT treated samples than in UV irradiated samples.

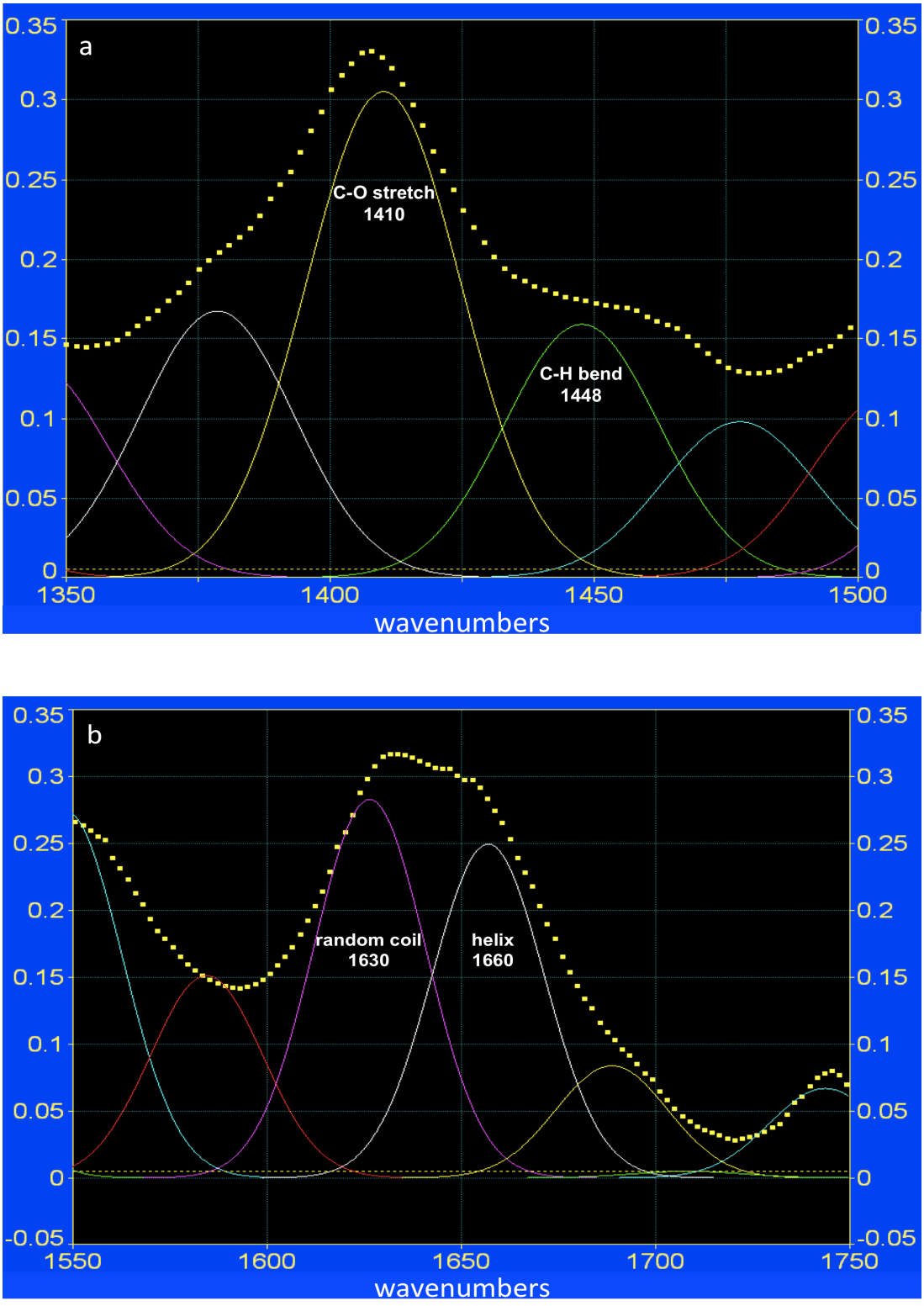


Fig 3.13 Deconvolution of (a) C-H bend peak and C-O stretch peak of freeze-dried 90%collagen-10%C4S scaffold, and (b) sub-bands of Amide I peak of freeze-dried 100%collagen scaffold.

Table 3.7 Degree of crosslinking and denaturation of non-crosslinked, DHT-treated, and UV-irradiated scaffolds. Each data is an average of the measurements from 3 different spectra. * denotes significant difference amongst different crosslink status ($p<0.05$). Data are colour-coded red for increase and green for decrease, relative to the values of the non-crosslinked groups.

100%collagen	ester	ester	amide	denaturation
	$1744cm^{-1}/1455cm^{-1}$	$1164cm^{-1}/1455cm^{-1}$	$1550cm^{-1}/1455cm^{-1}$	$1630cm^{-1}/1660cm^{-1}$
Freeze-dried	0.41±0.04*	0.82±0.03*	1.55±0.05	1.11±0.01
DHT	0.50±0.02	0.99±0.05	1.45±0.01*	1.15±0.01*
UV	0.55±0.07	0.95±0.06	1.55±0.04	1.10±0.02

50%collagen-50%elastin	ester	ester	amide	denaturation
	$1744cm^{-1}/1455cm^{-1}$	$1164cm^{-1}/1455cm^{-1}$	$1546cm^{-1}/1455cm^{-1}$	$1630cm^{-1}/1660cm^{-1}$
Freeze-dried	0.32±0.02*	0.74±0.06*	1.41±0.02	1.08±0.01*
DHT	0.56±0.01*	0.94±0.04*	1.38±0.02	1.20±0.03
UV	0.37±0.02*	0.84±0.01*	1.41±0.02	1.17±0.03

90%collagen-10%C4S	ester	ester	amide	denaturation
	$1744cm^{-1}/1448cm^{-1}$	$1164cm^{-1}/1448cm^{-1}$	$1547cm^{-1}/1448cm^{-1}$	$1630cm^{-1}/1660cm^{-1}$
Freeze-dried	0.45±0.01	0.82±0.02*	2.05±0.09	1.35±0.03*
DHT	0.45±0.04	0.72±0.01	2.35±0.11*	1.83±0.09*
UV	0.38±0.03*	0.73±0.04	2.23±0.13	1.60±0.05*

3.3.5 Layered Scaffolds

The layered scaffolds were successfully fabricated with 1%wt/v suspensions at a freezing temperature of -20˚C. Fig 3.14 shows the cross section micrographs of the bi-layer and tri-layer scaffolds. All of them exhibit distinct layered structures with well connected interfaces.

The pore structures of the layered scaffolds appear to be less organized than the uniform-composition scaffolds. This is more obvious in the collagen-C4S layers. The collagen-C4S layers in the bi-layer scaffolds exhibit elliptical pore shapes elongated in the direction parallel to the plane of the layers (Fig 3.14c,d). The collagen-C4S layers in the tri-layer scaffolds show more random pore structures (Fig 3.14e,f) than those in the uniform-composition collagen-C4S scaffolds (Fig 3.7 c,d).

Same as the uniform-composition scaffolds, the layered scaffolds have no visible morphological changes after the crosslinking processes. The effects of crosslinking on the mechanical properties of the layered scaffolds will be presented in Chapter 4.

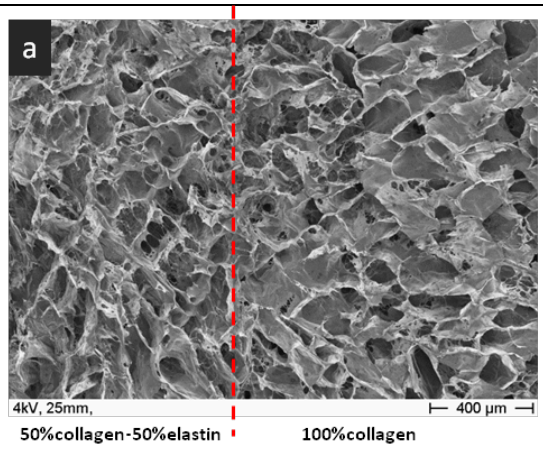
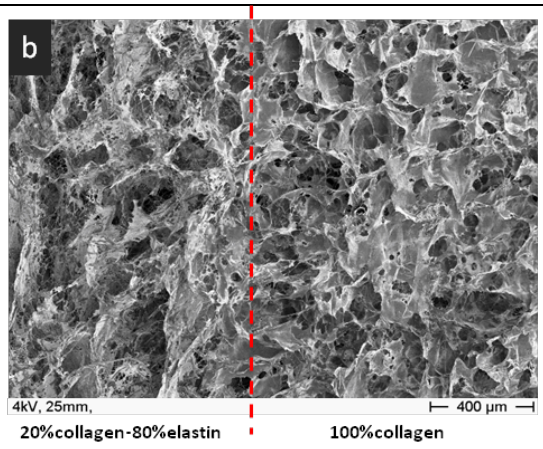
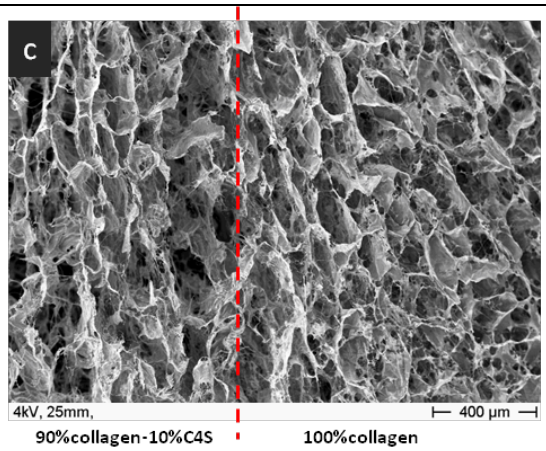
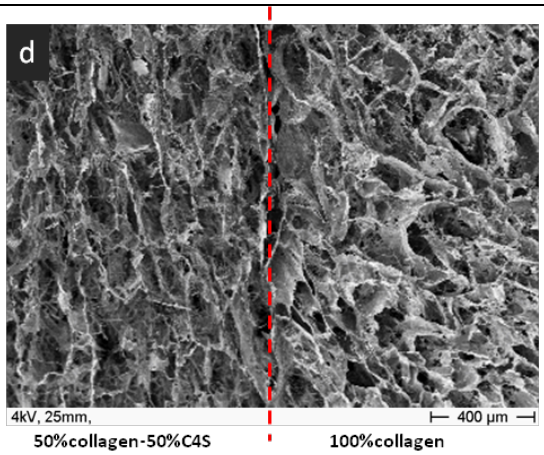
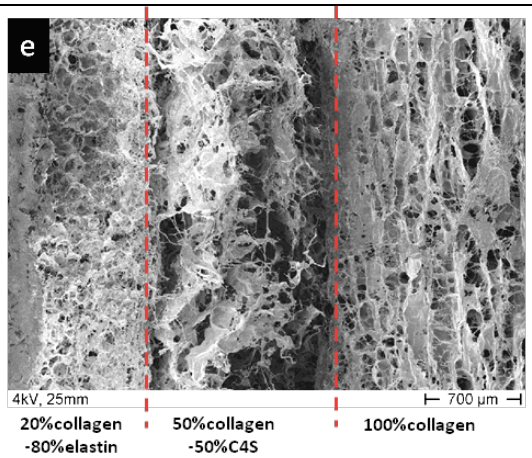
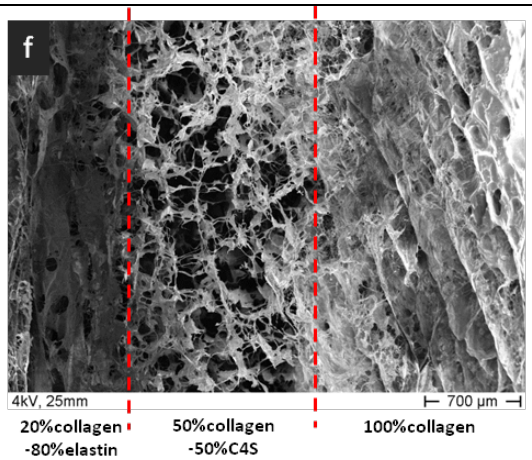
100%Collagen/50%Collagen-50%Elastin	100%Collagen/20%Collagen-80%Elastin
	
100%Collagen/90%Collagen-10%C4S	100%Collagen/50%Collagen-50%C4S
	
100%Collagen/90%Collagen- 10%C4S/50%Collagen-50%Elastin	100%Collagen/50%Collagen- 50%C4S/20%Collagen-80%Elastin
	

Fig 3.14 SEM micrographs of layered scaffolds.

3.4 Discussion

3.4.1 Scaffold Manufacturing and Ultra-structures

The freeze-drying technique is generally considered not to be altering the ultra-structures of biological materials [222-224]. However, the process in this experiment (mainly the homogenization stage) does involve contacts with acid and alkali, and therefore its effect on the scaffold materials is worth investigating.

In the ethanoic acid solution, the pH value is below the isoelectric point of the collagen (7.8 [225]), therefore the collagen undergoes swelling due to the electrostatic repulsion between the positively charged groups on lysine, hydroxylysine, and arginine residues [199]. At the same time, the non-ionized ethanoic acid molecules are competing against the hydroxyl groups on hydroxyproline residues to form hydrogen bonds with the carbonyl oxygen on the adjacent chains, resulting in the peptide chains being wedged apart and hydrated [199]. Moreover, the ester bonds in the collagen are believed to have had certain degrees of hydrolysis in the acidic environment [199], suggested by the reduction in the peak intensity at 1164cm^{-1} in the FTIR spectrum of the freeze-dried collagen (Fig 3.9a). In the FTIR spectrum of the non-freeze-dried collagen (Fig 3.9a), the peaks at 1070cm^{-1}, 948cm^{-1} and 860cm^{-1} (assigned to C-O-C in sugar groups, pyranose ring, and C-O-S stretch respectively [211, 218]) prove that the collagen is naturally grafted with glycoproteins and proteoglycans (which contain the above groups) [48, 53], as mentioned in 2.2.3. For the similar reasons stated above (hydrogen bonds competing and ester bonds hydrolysis), the carbohydrates are freed from the collagen and are very much diluted in the solution. Therefore the characteristic peaks become much less visible in the spectrum after freeze-drying.

The TEM images show that the D-banding patterns are well-preserved and the periodic distance approximately unchanged after freeze-drying (Fig 3.8). It is therefore speculated that the swelling effects on the collagen from the ethanoic acid have mainly happened at an inter-fibrillar level, leaving the intra-fibrillar staggering of the collagen molecules intact. The periodic distances found here agree with other researchers' findings [226-228]. However, they are greater than the usual 67nm periodicity. It is likely that the collagen microfibrils have helical organization in the fibrils [229, 230] (i.e. exhibiting a coiling angle to the fibril axis). Hence the projected periodic distance along the fibril in the TEM images increases [227].

As mentioned in 2.2.3, the elastin with intermolecular desmosine and isodesmosine crosslinks is extremely stable [59, 231], and therefore does not show visible ultra-structure changes after freeze-drying (Fig 3.9b).

C4S co-precipitates with collagen in ethanoic acid (see Fig 3.2c) because of the ionic bonding between the cationic groups of collagen ($-NH_3^+$) and the anionic groups of C4S ($-COO^-$, $-SO_3^-$) [192]. Increasing the pH to above the isoelectric point of collagen reduces the co-precipitation (Fig 3.2d) by having the collagen molecules negatively charged. C4S itself is likely to have exchanged its sodium ions with the protons in the solution and therefore has had more free carboxyl groups, as indicated by the decreased intensity of the carboxylate peak (Fig 3.10), as well as the increased peak intensities at $1414cm^{-1}$ and $1380cm^{-1}$ (Fig 3.9c). The carboxyl hydrogen then contributes to the formation of hydrogen bonds between the C4S molecules, which further results in a lower wavenumber of the carboxylate peak (Fig 3.10). These free carboxyl groups are also potential sites to form ester or amide bonds with collagen in the collagen-C4S scaffolds.

Overall, the freeze drying technique used in this research is likely to have only affected the collagen at the inter-fibril level and have not further changed the ultra-structures of the other scaffold materials. Therefore, it is believed that the freeze-dried scaffolds will maintain their intrinsic bioactivities, although stronger evidence will be drawn from further biological assessments in later chapter.

The DHT treatment and UV irradiation, although shown not to introduce additional chemical moieties while crosslinking the scaffolds, caused certain extent of denaturation on all types of scaffolds.

In the collagen scaffolds, direct evidence can be observed from the TEM images, in which the collagen fibrils more or less lost their D-banding patterns. This is because that the intermolecular crosslinks were ruptured by the energy obtained from the heat or the UV rays, and the thermal movements of the collagen molecules were increased, changing the staggered molecules into a less organized alignment [199]. Moreover, the intramolecular links on the collagen backbone (hydrogen bonds) are also affected by the crosslinking processes, making the triple-helical collagen chains unbraided and folded [199, 232], resulting in the denser spots (i.e. the dark dots on the TEM images in Fig 3.11) on the fibrils. It seems that the collagen is more susceptible to the denaturation caused by DHT treatment than UV irradiation. This might be because that the UV irradiation tends to fragment the bonds (-CO-NH-, $-CH_2-N=$, $=CH_2$) along the α chains, rather than break the hydrogen bonds between them, whereas DHT treatment has both effects on collagen [149, 204]. The fragmented α chains are still secured in the triple-helix structures, and therefore no significant change in the random coil to helix ratio was observed in the FTIR spectrum after UV irradiation (Table 3.7).

In elastin, however, the helical structure only contains one polypeptide chain, in which the disruption of the hydrogen bonds in the helix and the fragmentation of the bonds along the α chain will both convert the helical structure into random coils. Therefore, the collagen-elastin scaffolds showed similar denaturation effects after DHT treatment and UV irradiation (Table 3.7).

In the collagen-C4S scaffolds, C4S molecules were located at the periphery of individual collagen fibrils [233], which may have spatially facilitated the denaturation during the crosslinking processes. Again, DHT treatment caused more amount of denaturation than UV irradiation (Table 3.7) due to its more effective cleavage of the hydrogen bonds in the collagen molecules.

In terms of the crosslinks formed during the processes, esterification seems to have dominated in the collagen and collagen-elastin scaffolds. It is likely that the ester bonds that underwent hydrolysis in the ethanoic acid in the freeze-drying process have reformed with the help of the DHT treatment or the UV irradiation. Meanwhile, the amide formation seems to be counteracted by the accompanying bond fragmentation effects (especially in DHT treatment). In contrast, the collagen-C4S scaffolds saw a decrease in the amount of ester bonds and an increase in the amide bonds after crosslinking (Table 3.7). This might be because that the free carboxyl groups generated on C4S (mentioned above) had saturated the sites for esterification on collagen even before the crosslinking. Hence only the bond fragmentation effect was shown for the ester bonds. Moreover, the excessive carboxyl groups were also reacting with the free amino groups on the collagen side chains to form amide crosslinks [196].

Generally speaking, the DHT treatment will cause more denaturation than UV irradiation, and both methods effectively introduce crosslinks to the scaffolds, although there are always concomitant bond fragmentations.

3.4.2 Scaffold Morphology

Morphological characterization has shown that the pore sizes of the scaffolds are influenced by the freezing temperature, the relative density, and the composition of the scaffolds.

The effects of freezing temperature on the pore sizes of the scaffolds have been well studied [197, 234]. In a unit volume of water at a given temperature T, the number of critical nuclei can be given by

$$n^* = n_{liquid} \exp\left(-\frac{\Delta G_c}{kT}\right) \quad \text{Eq 3.1}$$

where n_{liquid} is the number of molecules per unit volume, and ΔG_c is the free energy of condensation (for T below the freezing point of water T_m, $\Delta G_c/T$ decreases when T decreases) [235]. Therefore, lower freezing temperatures will produce more nuclei and hence eventually more ice crystals with smaller sizes. The results in Table 3.2 confirm this general trend and provide the range of the pore size which can be achieved in our laboratory conditions (33.2μm~173.7μm). As an optimal pore size of 100μm~200μm is suggested by the literature for the attachment and proliferation of the cell residing in heart valves (vascular smooth muscle cells and fibroblasts) [236, 237], -20˚C is considered to be the more suitable freezing temperature for fabricating the scaffolds.

In collagen and collagen-elastin scaffolds, higher relative densities lead to smaller pore size by introducing a greater constraint from the collagen network to the growing ice crystals during the freezing process (see Fig 3.15a), and hence smaller crystals [238].

The 0.5% wt/v 20%collagen-80%elastin group scaffolds appear to have a mean pore size that is lower than the trend predicts. This is due to the volume shrinkage of the scaffolds during freeze-drying. The extremely low collagen density in these scaffolds (0.1% wt/v) is not sufficient to form continuous pore walls, without which, the scaffolds are therefore not rigid enough to preserve their original volumes during the drying process. By contrast, the pore sizes of the collagen-C4S scaffolds are not affected by the relative density. This is because of the co-precipitation of collagen and C4S mentioned above, which has displaced the water out of the collagen network [196]. Although a subsequent increase of pH can reduce the co-precipitation, the de-swollen collagen molecules are not able to re-envelop the water again. Therefore the ice crystals can grow, almost freely without constraint from the solid phase, to the same ultimate size disregarding the relative density (see Fig 3.15b). To meet the above-mentioned requirement for pore size in scaffolds with all the compositions, 1%wt is considered the optimal relative density to take forward, based on the results in Table 3.2 – 3.4.

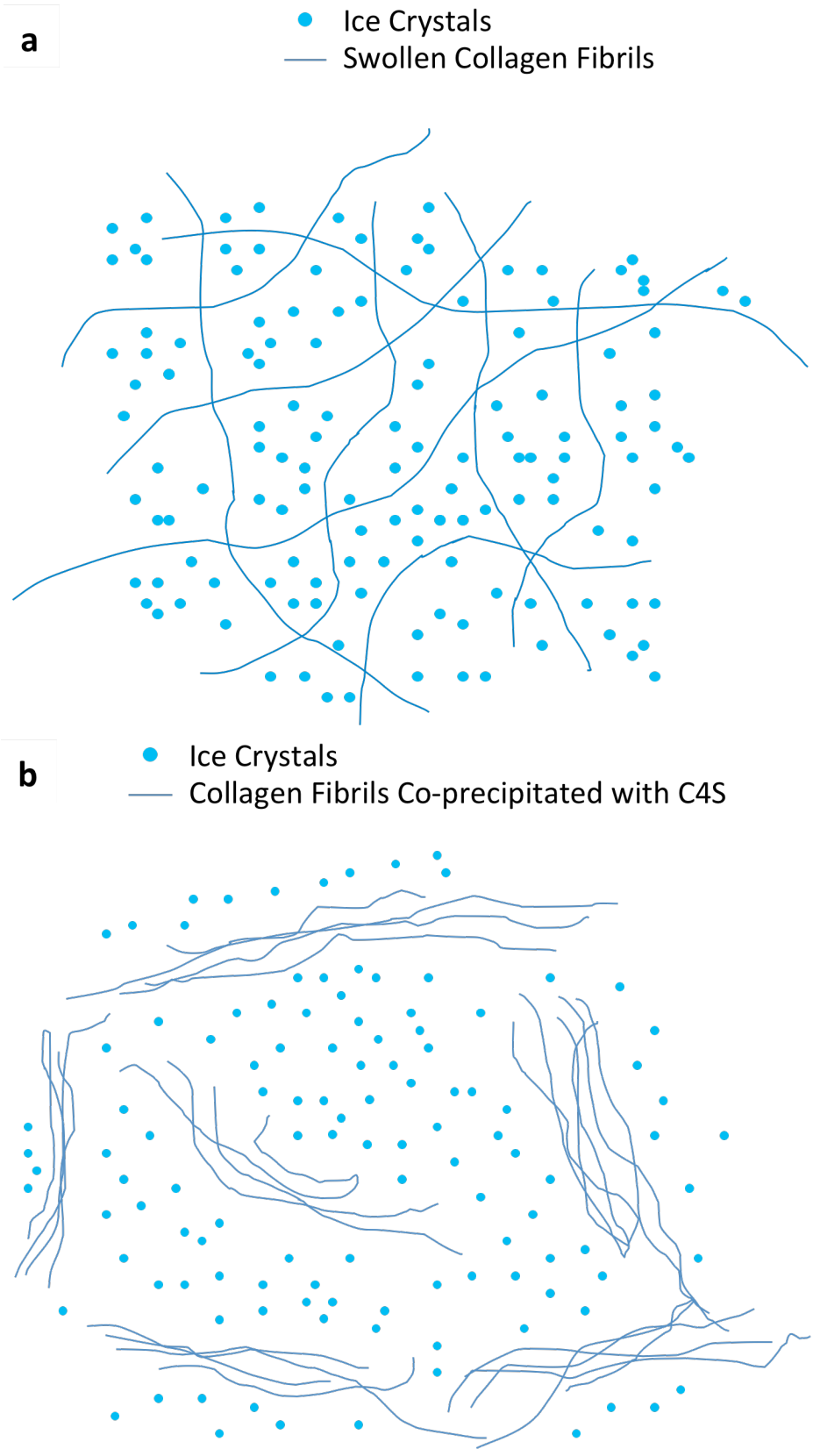


Fig 3.15 Illustration of the ice crystal nucleation in (a) collagen or collagen-elastin suspension, and (b) collagen-C4S suspension

As we can see from Fig 3.6, the elastin does not form continuous sheets in the same way as collagen, but is only embedded in the collagen sheets in the form of short rods. These rods do not contribute to the formation of the pore walls. Therefore, for the scaffolds with the same relative density, the collagen-elastin scaffolds have less amount of pore-wall-forming collagen than the collagen scaffolds, resulting in larger pores due to the same mechanism of relative density affecting the pore size, namely less constraint. Also, the more elastin is in the scaffolds, the less solid the pore walls are.

The 'wavier' pore walls in the 50%collagen-50%C4S scaffolds compared with the 90%collagen-10%C4S scaffolds are likely to be ensuing from the free C4S in the liquid phase of the suspension. Since there is only a certain amount of sites on the collagen that the C4S can bind to [196], when the C4S absorbates saturate the surface of the collagen, the excessive C4S will be freely solubilised in the liquid phase, which is believed to be the case in the 50%collagen-50%C4S suspensions. The presence of C4S lowers the freezing point of the solution [197, 239], and is likely to have forced the liquid phase to undergo hypoeutectic crystallization (see Fig 3.16), producing the ice phase and the ice-C4S eutectic phase in the frozen suspension, which would together form less uniform crystal structures than the ice-only crystals, and hence wrinkle the pore walls .

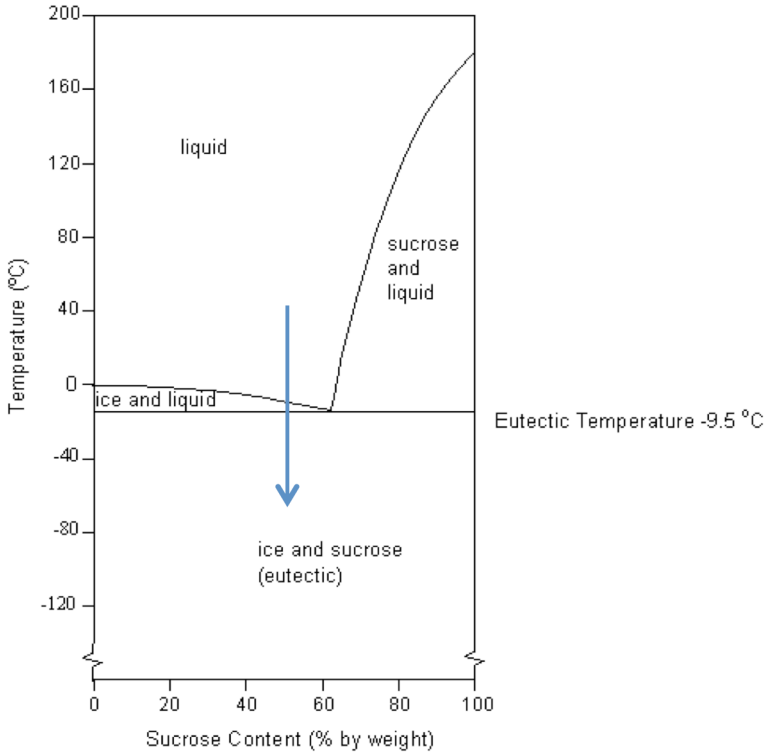


Fig 3.16 Water-sucrose phase diagram [240]. A water-C4S phase diagram could not be found from literature. However it is speculated that the C4S may have similar behaviour to the sucrose.

The layered scaffolds were manufactured with the more suitable -20˚C freezing temperature and 1% relative density, which were obtained from the results of the uniform-composition scaffolds. When preparing the layered scaffolds, a subsequent layer of suspension is cast onto a previous layer that has been frozen. As the heat transfer at the liquid suspension-frozen suspension interface is much quicker than that between the liquid suspension and the ambient, the suspension of the subsequent layer will then freeze more rapidly than it does in the scaffolds with individual compositions, hence introducing a lower degree of uniformity in the pores. The plane close to the frozen layer has a higher degree of undercooling and is preferential for the ice crystal growth, leading to elliptical pores elongated parallel to the plane of the layer. This is more prominent in the collagen/collagen-C4S bi-layer scaffolds because the suspension

has a lower viscosity [241], and hence higher diffusion coefficient as suggested by the Stokes-Einstein equation [242] $D = kT/6\pi r\eta$, where D is the diffusion coefficient, k is the Boltzmann Constant, T is the temperature, η is the viscosity, and r is the hydrodynamic radius. In the tri-layer scaffolds, the collagen-C4S layers do not well maintain the pore structures as in the uniform-composition scaffolds or the bi-layer scaffolds. This is likely to have been caused by the process of casting the collagen-elastin layer onto the frozen collagen-C4S layer. Since the frozen suspensions were briefly left under room temperature for a better connection to the collagen-elastin layer, the ice-C4S crystals might have partially melted due to the lower freezing point mentioned above. When the suspensions were re-frozen, new crystals formed which undoubtedly had different shape to the original crystals, and therefore disrupted the original pore structures of the collagen-C4S precipitates.

After the crosslinking process, the scaffolds exhibit minor volume shrinkage because of the removal of the bound water due to the condensation reactions that have happened [146, 204]. This has lead to the slightly smaller pore sizes in the crosslinked scaffolds in Table 3.6.

3.5 Conclusions

The freeze-drying technique adopted in this thesis was capable of producing highly porous scaffolds (porosity>98%). The method involved suspension-preparation in an acidic environment but had only slightly changed the ultra-structures of the scaffold materials. The inter-fibrilar bonds in collagen were believed to be cleaved when the collagen swelled into a viscous suspension. The elastin remained stable and was uniformly distributed in the suspension, and hence in the collagen-elastin scaffolds. The C4S, however, would first ionically co-precipitate with collagen at the acidic

environment, and later had interactions with collagen in forms of ester bonds or hydrogen bonds in neutral pH, due to the free carboxyl groups generated.

The pore size of the freeze-dried scaffolds was dependent on the freezing temperature, the relative density and the composition of the suspension. A lower freezing temperature produced smaller pores. A lower proportion of collagen and a lower relative density produced larger pores in collagen, and collagen-elastin scaffolds, but did not affect the pore size of the collagen-C4S scaffolds. A freezing temperature of -20˚C and a relative density of 1% were considered the suitable conditions to be applied in the layered scaffolds.

The crosslinking methods, DHT treatment and UV irradiation, were found to increase either ester or amide crosslinks in the scaffolds depending on the compositions, accompanying which there existed a certain degree of denaturation of the scaffolds (generally higher in DHT treatment). The crosslinking processes also reduced the pore size slightly because of the removal of water.

The layer-by-layer casting technique was proven feasible to make scaffolds that possessed distinct layers with good connection at the interfaces, boding well for a compositionally desirable heart valve scaffold.

Chapter 4. Scaffold Mechanical Properties

4.1 Introduction

The mechanical properties of tissues, especially load-bearing tissues, are critical in ensuring their characteristic functions. The replacement tissue produced by tissue engineering, therefore, needs to meet the mechanical requirements for the native tissues (e.g. sufficient stiffness and strength, appropriate viscoelastic properties, and characteristic anisotropies). In the tissue engineering process, the scaffolds and the cells have a synergetic contribution toward these aimed mechanical properties, but compared with the cells, the scaffolds can provide us with more freedom to tailor the mechanical properties for the targeted applications: not only can we select the materials for the scaffolds [243, 244], control the microstructures [151, 154], and introduce hierarchy and anisotropy [155, 245], all of which will have direct effects on the mechanical properties, but we can also utilize various properties of the scaffolds to mediate the behaviours of the cells (attachment, proliferation, contraction, alignment, etc), which would also influence the mechanical properties of the cell-scaffold constructs [139, 234, 246].

Therefore, this chapter studies the mechanical properties of all the scaffolds manufactured in Chapter 3. Firstly, uniform-composition scaffolds will be carefully investigated to find out how the variables in the scaffold manufacturing, i.e. the pore size (the freezing temperature), the composition and the relative density, are affecting the scaffold mechanical properties. The results would serve as a framework to give a better guidance for choosing suitable scaffolds with the required mechanical properties.

Secondly, after understanding the mechanical properties of each type of the uniform-composition scaffolds and the mechanism behind them, the knowledge will be fed into the layered scaffolds to specifically mimic the characteristic bending anisotropy of native heart valves, as mentioned in 2.2.4: the heart valve leaflet is naturally curved towards the ventricularis side, and is easier to bend towards the ventricularis side, referred as 'With Curvature' (WC), than towards the fibrosa side, referred as 'Against Curvature' (AC), as shown in Fig 4.1.

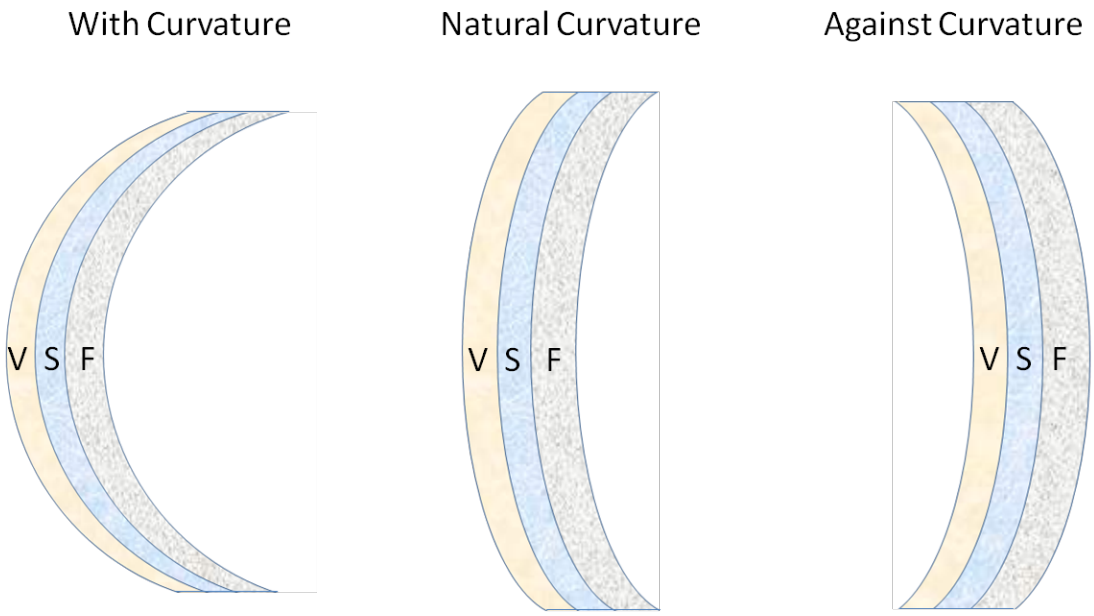


Fig 4.1 Schematic graph of the bending anisotropy of native heart valve. V, S and F stand for ventricularis, spongiosa and fibrosa, respectively. [98]

After the experimental studies, finite element models will be developed for the different types of scaffolds, both the uniform-composition ones and the layered ones. The simulated mechanical tests on these models are able to verify the experimental data, and more importantly, they will provide much easier approaches to examine more complicated geometries and loading conditions, and hence simplify the process of scaffold design optimization.

Lastly, the crosslinking conditions selected in Chapter 3 will be tested to see their effectiveness in increasing the mechanical properties of the scaffolds.

4.2 Materials and Methods

4.2.1 Mechanical Characterization

Unidirectional tension tests were conducted using a Rubicon tensile machine (Denison Mayes Group, UK) with a 30N load cell, and unidirectional compression and three-point bend tests were conducted using a DMA7 (PerkinElmer, MA). All the scaffolds manufactured in Chapter 3, with various freezing temperatures (freezing temperature is -20˚C by default if not otherwise stated), compositions, relative densities, layer structures, and crosslinking conditions, were characterized, in their dry status at room temperature.

For the tensile tests, rectangular samples (length: 40mm, width: 12mm, thickness: 5mm) were tested with a gauge length of 20mm and a strain rate of 3%/min until rupture. For the compression tests, cylindrical samples of 15mm in both diameter and height were loaded at an approximately constant strain rate of 3%/min on all samples. The three-point bend tests also used the 40mm × 12mm × 5mm rectangular samples and the samples were loaded at a cross-head speed of approximately 0.5mm/min with a span of 20mm (see Fig 4.2). The bend tests of the layered scaffolds were conducted in both WC direction (bent towards the collagen-elastin layer or the collagen-C4S layer) and AC direction (bent towards the collagen layer).

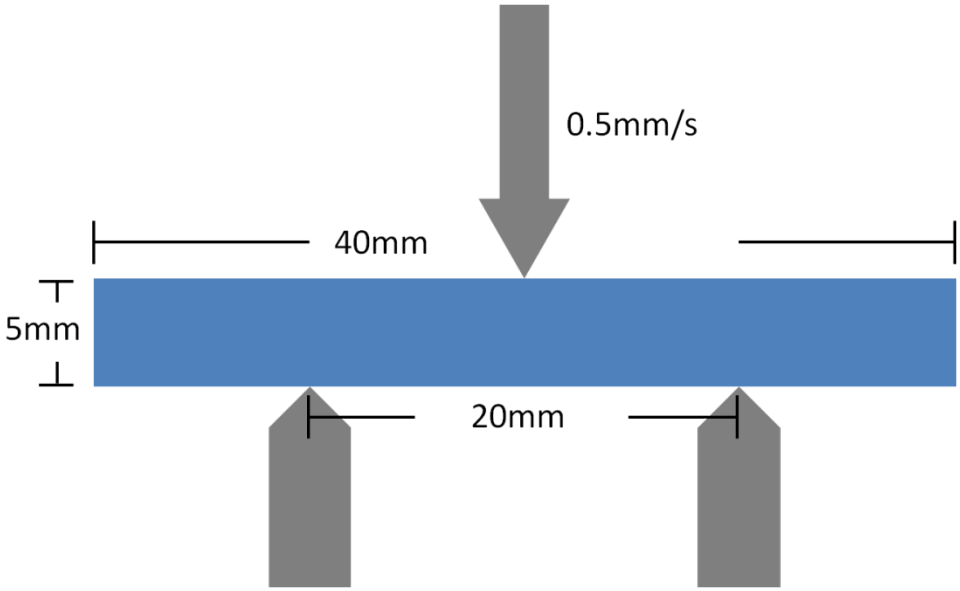


Fig 4.2 Schematic graph of three-point bend test on scaffold.

All data were reported as means, with the standard deviations as the errors. One-way analysis of variance (ANOVA) followed by Tukey's test was used to compare groups of data, with a probability value of 95% ($p < 0.05$) to determine statistical significance. At least 4 samples of each group were tested.

4.2.2 Finite Element Modelling

ANSYS 10.0 was used as the finite element modeling (FEM) platform. A finite element volume of a 20mm×12mm×5mm scaffold (the part between the span) was developed, using the SOLID185 and the 1st order OGDEN HYPERFOAM as the element type and the material type, respectively.

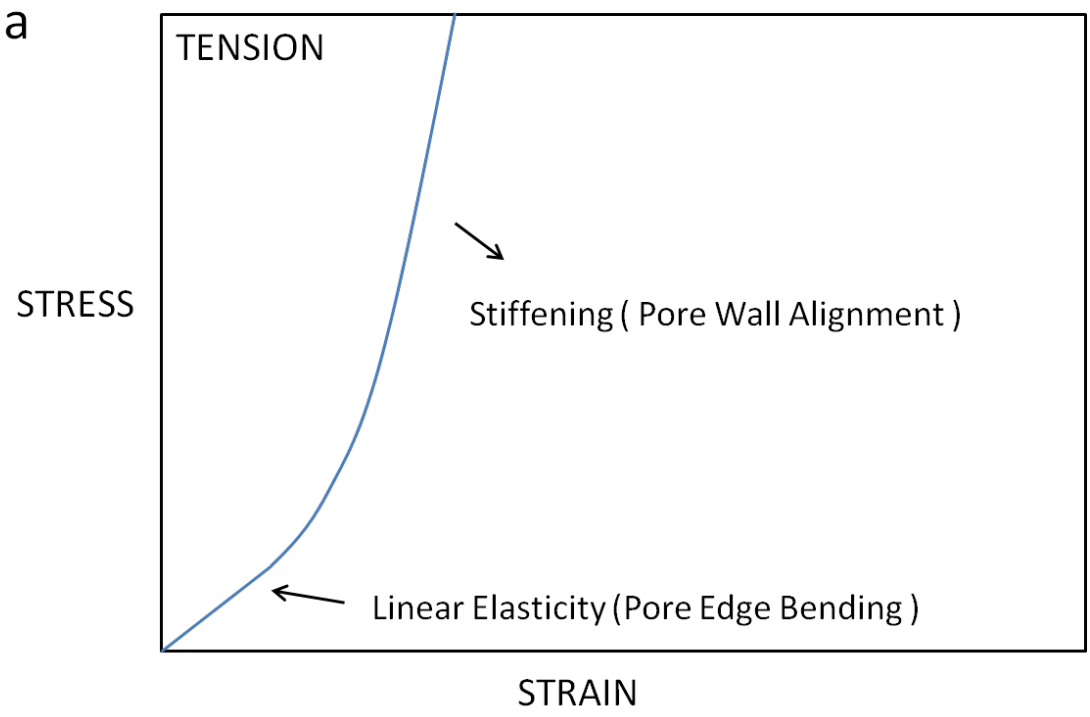
The scaffold behaves as an elastomeric foam, which exhibits the characteristic stress-strain curves shown in Fig 4.3. In tension, the stress-strain curve is characterized by two stages: a linear elastic stage dominated by pore edge bending, and a stiffened stage due to pore wall alignment. In compression, there are three characteristic deformation stages, the first of which is also a linear elastic stage (dominated by pore edge bending),

followed by a stress plateau (dominated by pore wall buckling) and densification (dominated by pore collapse throughout the scaffold) [152].

This stress-strain behaviour can be simulated by the constitutive strain energy potential equation of the 1st order OGDEN HYPERFOAM material [247]:

$$W = \frac{\mu}{\alpha}\left(J^{\frac{\alpha}{3}}\left(\overline{\lambda_1}^{\alpha} + \overline{\lambda_2}^{\alpha} + \overline{\lambda_3}^{\alpha}\right) - 3\right) + \frac{\mu}{\alpha\beta}\left(J^{-\alpha\beta} - 1\right) \qquad \text{Eq 4.1}$$

where W is the strain energy potential, $\overline{\lambda_P}^{\alpha}$ (P=1, 2, 3) is the deviatoric principal stretch ratio, J is the determinant of the elastic deformation gradient, and μ, α, β are materials constants, which are related to the initial shear modulus in terms of $G = \frac{\mu\alpha}{2}$, and to the initial Poisson's ratio in terms of $\nu = \frac{\beta}{1+2\beta}$ [247]. The constants were defined by curve-fitting with the actual tensile and compressive stress-strain curves obtained from the mechanical tests. Simulated three-point bend tests were performed on the models of uniform-composition scaffolds and layered scaffolds to compare with the experimental data. A simulated bending test with distributed load was performed on the model of the tri-layer scaffold, and stress distribution within the scaffold was characterized, in order to give further insights into how the scaffolds would behave under the situations closer to the physiological ones.



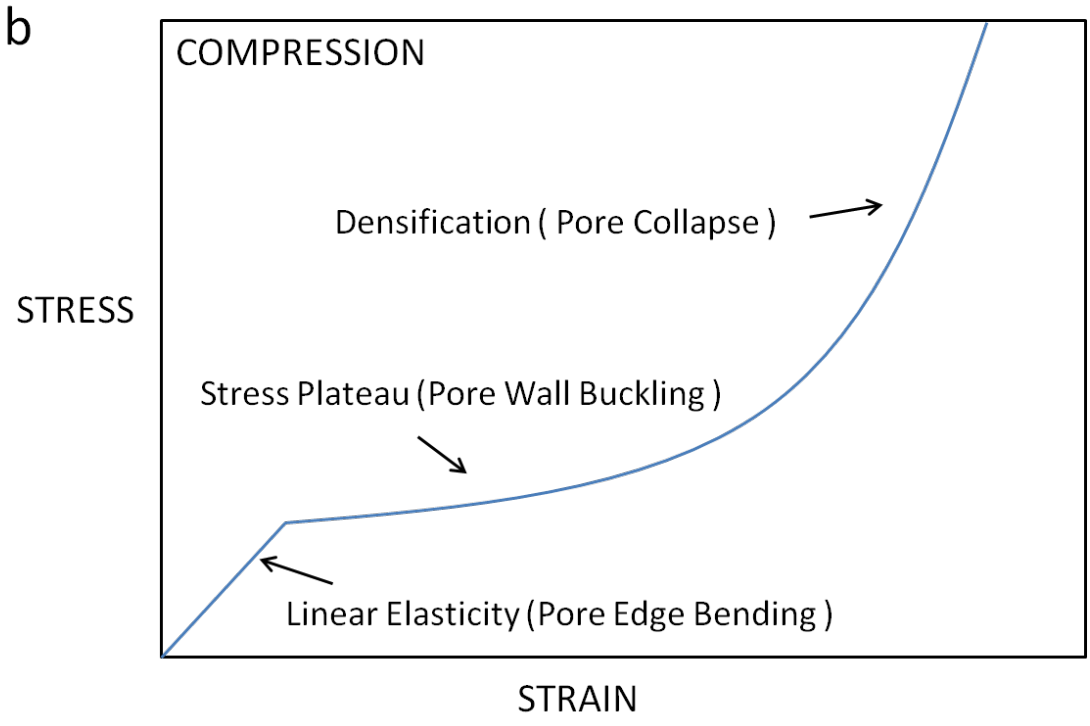


Fig 4.3 Schematic uniaxial stress–strain curves of elastomeric foam in (a) tension, and (b) compression. [152]

4.3 Results

4.3.1 Uniform-Composition Scaffolds

Fig 4.4 shows representative stress-strain curves of the tension and compression tests, and load-deflection curve of the three-point bend test on the uniform-composition scaffolds.

We can see from the tension and compression curves that the scaffolds behave as elastomeric foams, exhibiting the characteristic deformation stages mentioned above [152] (linear elasticity and stiffening in tension; linear elasticity, stress plateau and densification in compression). The tensile and compressive moduli (E_{ten}, E_{comp}) of the scaffolds have been defined as the slopes of the stress-strain curves over the initial linear regions. The failure strain (ε_f) in tension and the linear elastic strain (ε^*) in compression are also derived from the stress-strain curves obtained (Fig 4.4). The results are summarized in Table 4.1-4.3.

The three-point bend tests, in which the scaffolds undergo a combined deformation of tension and compression, produce load-deflection curves with a two-stage shape, as shown in Fig 4.4 c. The effective bending modulus (E_{bend}) of the scaffold is calculated from the slope ($\delta P/\delta D$) of the load-deflection curve, with the equation

$$E_{bend} = \left(\frac{\delta P}{\delta D}\right) \frac{l^3}{48I} \qquad \text{Eq 4.2}$$

where P is the load, D is the deflection, l is the span distance, and I is the second moment of area (l and I remain constant during the test). The effective bending moduli of the first and the second bending stages are hereby addressed as E_{bend1} and E_{bend2} respectively, and are also listed in Table 4.1-4.3.

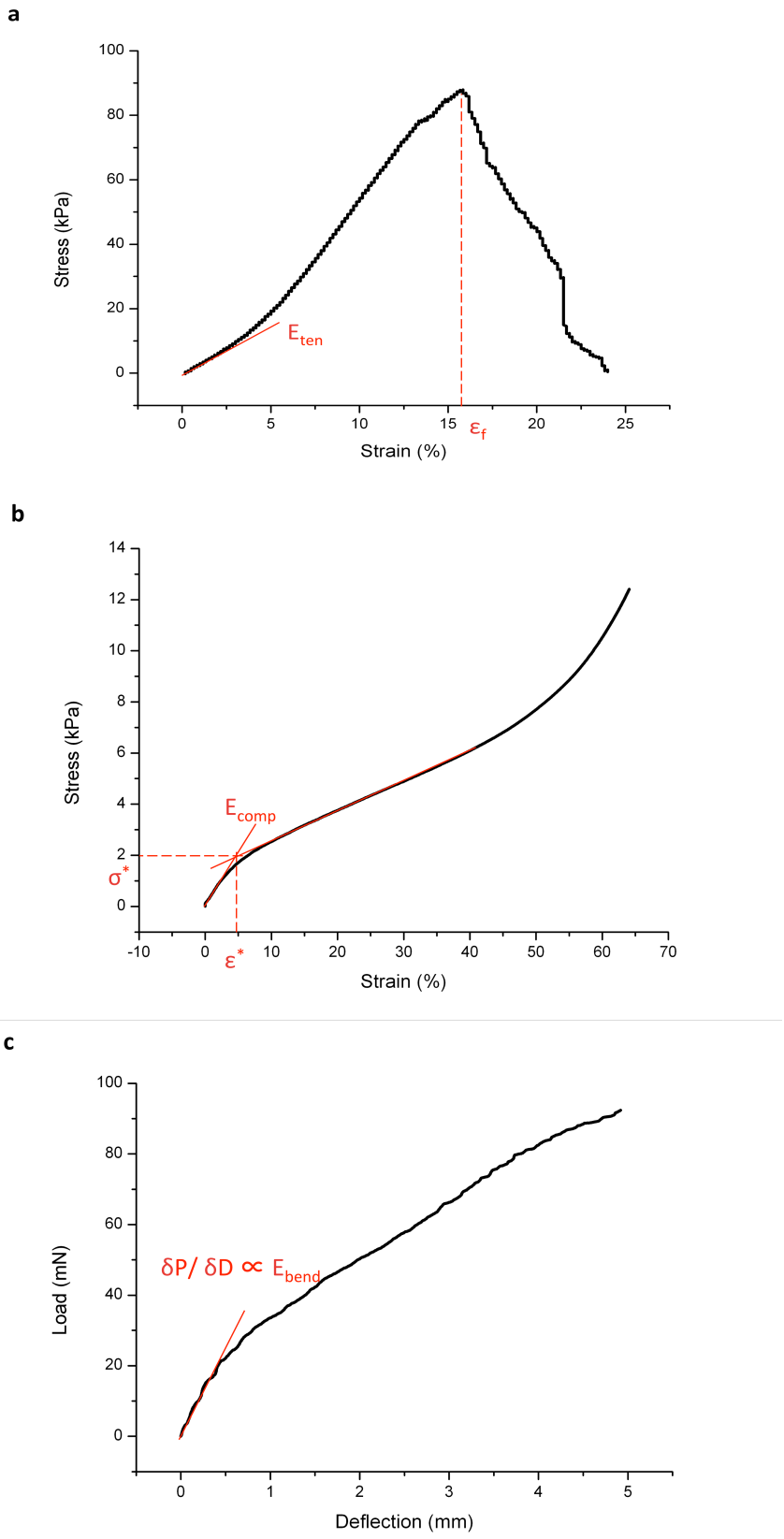


Fig 4.4 Unidirectional (a) tension and (b) compression stress-strain curves, and (c) three-point bend load-deflection curve of 1% wt/v 100%collagen scaffold, obtained from respective test conditions in 4.2.1.

Table 4.1 Summary of mechanical properties of 100%collagen scaffolds. [a] denotes statistically significant difference ($p<0.05$) in mechanical properties between groups of different relative densities. [b] denotes statistically significant difference ($p<0.05$) in mechanical properties between groups of different freezing temperatures.

Freezing Temperature (˚C)	Relative density (% wt/v)	E_{ten} (kPa)	ε_f (%)	E_{comp} (kPa)	ε^* (%)	E_{bend1} (kPa)	E_{bend2} (kPa)
-20	0.5	213.1± 18.9[a b]	10.6± 0.9[a b]	7.9± 2.0[a b]	7.7± 1.0[a b]	31.8± 4.5[a b]	15.0± 3.5[a b]
	1	344.6± 42.6[a]	15.4± 1.6	28.3± 4.6[a]	6.0± 0.3	85.7± 6.0[a]	38.2± 4.4[a]
	2.5	1082± 132[a b]	15.1± 3.7[b]	213.9± 11.2[a b]	6.5± 0.5	415.8± 29.2[a b]	173.1± 11.4[a]
-80	0.5	146.6± 11.4[a b]	20.3± 1.1[b]	4.0± 0.8[a b]	5.4± 1.2[b]	14.3± 1.5[a b]	7.8± 0.7[a b]
	1	309.4± 44.1[a]	18.9± 2.8	26.1± 1.5[a]	6.1± 0.5	80.9± 12.3[a]	44.3± 2.9[a]
	2.5	778.1± 58.4[a b]	10.2± 0.4[a b]	109.2± 9.7[a b]	5.3± 0.7	317.5± 37.4[a b]	157.7± 28.7[a]

Table 4.2 Summary of mechanical properties of collagen-elastin scaffolds. [a] denotes statistically significant difference ($p<0.05$) in mechanical properties between groups of different relative densities. [b] denotes statistically significant difference ($p<0.05$) in mechanical properties between groups of different collagen-elastin ratios. The tensile and three-point bend data of the 20%collagen-80%elastin scaffolds are unavailable due to the values being lower than what the equipment are able to accurately measure.

Collagen-Elastin Ratio	Relative density (% wt/v)	E_{ten} (kPa)	ε_f (%)	E_{comp} (kPa)	ε^* (%)	E_{bend1} (kPa)	E_{bend2} (kPa)
50%-50%	0.5	96.1± 12.9[a]	15.8± 1.4	2.4± 0.3[a b]	8.2± 2.3	11.3± 0.5[a]	5.1± 1.3[a]
	1	230.3± 22.3[a b]	14.3± 1.8	13.2± 2.4[a]	6.7± 2.0	65.1± 9.9[a b]	15.8± 3.1[a b]
	2.5	494.4± 63.4[a b]	14.6± 1.9[b]	106.3± 6.0[a b]	9.8± 1.9[b]	220.0± 32.9[a b]	115.8± 24.7[a]
20%-80%	0.5	-	-	0.53± 0.06[a b]	7.8± 1.8	-	-
	1	39.8± 8.8[a b]	14.7± 2.2[a]	10.2± 1.6[a]	5.8± 1.0	25.4± 5.1[a b]	6.3± 1.2[a b]
	2.5	367.4± 23.1[a b]	9.5± 1.3[a b]	51.0± 2.4[a b]	6.6± 0.2[b]	130.1± 12.2[a b]	104.0± 14.0[a]

Table 4.3 Summary of mechanical properties of collagen-C4S scaffolds. [a] denotes statistically significant difference ($p<0.05$) in mechanical properties between groups of different relative densities. [b] denotes statistically significant difference ($p<0.05$) in mechanical properties between groups of different collagen-C4S ratios. The tensile and three-point bend data of the 50%collagen-50%C4S scaffolds are unavailable due to the values being lower than what the equipment are able to accurately measure.

Collagen-C4S Ratio	Relative density (% wt/v)	E_{ten} (kPa)	ε_f (%)	E_{comp} (kPa)	ε^* (%)	E_{bend1} (kPa)	E_{bend2} (kPa)
90%-10%	0.5	51.6 ± 3.8[a]	18.1± 3.9 [a]	4.2± 0.5[a b]	16.8± 2.4 [a b]	11.0± 1.4[a]	6.2± 1.0[a]
	1	270.3± 46.9[a b]	12.1± 1.5	17.8± 1.7[a b]	10.6± 3.0[b]	52.4± 6.0[a b]	18.6± 1.5[a]
	2	914.3± 112.3 [a b]	10.2± 1.4 [b]	95.4± 15.7 [a b]	11.7± 1.4 [b]	195.3± 27.5 [a b]	55.4± 9.7 [a]
50%-50%	0.5	-	-	0.48± 0.09[a b]	10.2± 1.3 [a b]	-	-
	1	204.4± 36.6 [a b]	10.9± 1.3 [a]	12.8± 1.1.4 [a b]	7.8± 0.7 [a b]	40.3± 5.6 [a b]	16.8± 1.6 [a]
	2	488.9± 68.3 [a b]	16.6± 0.2 [a b]	67.9± 4.1 [a b]	15.5± 0.9 [a b]	135.8± 7.8 [a b]	60.6± 9.1 [a]

From Table 4.1-4.3, we can see that for each type of scaffold (with the same composition and relative density), E_{ten} is between 4~40 times greater than E_{comp}, and the E_{bend1} has values in between those of the tensile and compressive moduli.

When comparing the scaffolds with the same composition but different relative densities in Table 4.1-4.3, we can find that the relative density is positively affecting all the tensile, compressive and bending moduli of the scaffolds. Gibson et al suggested that the moduli of the scaffolds (E) were dependent on the relative density (ρ/ρ_s) by an exponential factor as Eq 4.3 indicated, according to the foam materials theory [152]:

$$\frac{E}{E_s} = C\left(\frac{\rho}{\rho_s}\right)^e \qquad \text{Eq 4.3}$$

where E_s was the Young's Modulus of the solid material of the scaffold, e was the exponential factor, and C was a constant. The values of e can therefore be determined by making ln/ln plots with the data in Table 4.1-4.3 (the moduli against the relative densities). Fig 4.5 shows examples of the ln/ln plots and the complete results of the factor e are listed in Table 4.4.

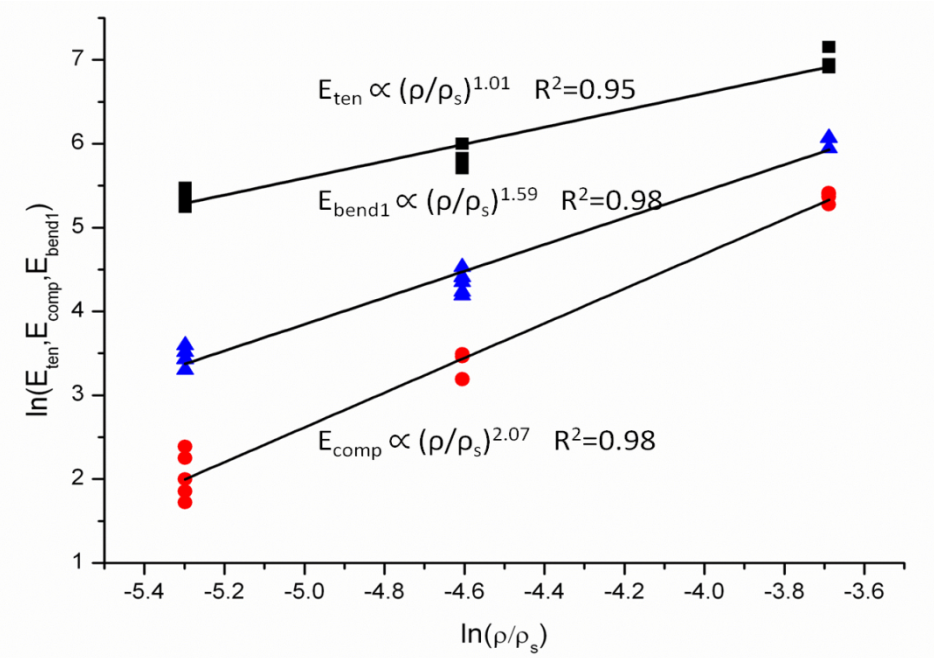


Fig 4.5 ln-ln plots of E_{ten}(squares), E_{comp}(circles), and E_{bend1} (triangles) against the relative density for 100%collagen scaffolds.

Table 4.4. Dependence factor e of E_{ten}, E_{comp}, and E_{bend1} on relative densities of scaffolds with different compositions. * Due to the unavailability of the E_{ten} and E_{bend1} from 0.5% 20%collagen-80%elastin group and 0.5% 50%collagen-50%C4S group, the dependence factors of these two series are statistically less reliable.

	e of E_{ten}	e of E_{comp}	e of E_{bend1}
100%collagen	1.01±0.06	2.07±0.07	1.59±0.07
50%collagen-50%elastin	1.01±0.06	2.37±0.05	1.80±0.09
20%collagen-80%elastin	2.45±0.15*	2.85±0.25	1.79±0.12*
90%collagen-10%C4S	2.06±0.07	2.25±0.06	2.07±0.07
50%collagen-50%C4S	1.27±0.19*	3.51±0.25	1.76±0.11*

It can be seen that by increasing the relative density, the tensile, compressive, and bending moduli of the scaffolds increase to different extents. For 100% collagen scaffolds, the relative density tend to affect the E_{ten} linearly, and to affect the E_{comp} in an approximately squared manner. The dependence factor of E_{bend1} on the relative density falls in between those of E_{ten} and E_{comp}. When the second phases (elastin or C4S) are added to collagen, the dependence factors show various deviations from those of the 100%collagen scaffolds. However, one general trend is maintained, that the factors are higher for E_{comp} than for E_{ten}, and the factors for E_{bend1} rest in between (except for the 20%collagen-80%elastin series).

Apart from the dependence on the relative density, the mechanical properties of the scaffolds have also shown to be influenced by the freezing temperature and the composition. Table 4.1 suggests that the freezing temperature is affecting the mechanical properties of the scaffolds, as we can see that the scaffolds with larger pore size (the -20˚C groups) generally have higher values of the tensile, compressive, and bending moduli. However, at the relative density of 1%wt/v, the differences between the -20˚C groups and the -80˚C groups are not statistically significant. Comparing the mechanical properties of the 100%collagen scaffolds in Table 4.1 with those of the collagen-elastin and collagen-C4S scaffolds in Table 4.2 and Table 4.3, we can see that the values of the tensile, compressive, and bending moduli decrease as the proportion of collagen decreases.

4.3.2 Layered Scaffolds

Three-point bend tests conducted on the layered scaffolds show that they possess bending anisotropy, i.e. when bent in different directions, the scaffolds exhibit different

deflections under the same load, which can be expressed by the difference in E_{bend1} and E_{bend2}.

Fig 4.6 presents the representative load-deflection curves showing the bending anisotropy of the layered scaffolds. The E_{bend1} and E_{bend2} calculated from the slopes on the curves are listed in Table 4.5. We can see that the collagen/collagen-elastin bi-layer scaffolds and the tri-layer scaffolds have similar E_{bend1} values for the WC and AC directions, and have higher E_{bend2} values for the AC direction, whereas for the collagen/collagen-C4S bi-layer scaffolds, the E_{bend1} and E_{bend2} are both higher for the AC direction.

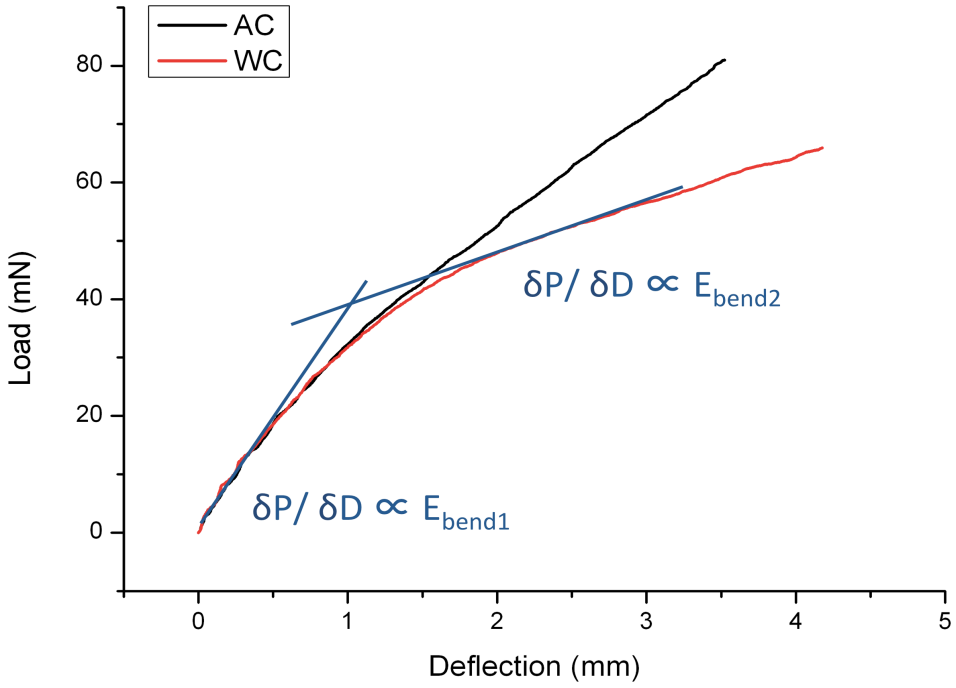


Fig 4.6 Representative load-deflection curves of 100%collagen / 50%collagen-50%elastin bi-layer scaffolds bent in WC and AC directions. Values of E_{bend1} and E_{bend2} are obtained from correspondent slopes according to Eq 4.2.

Table 4.5 Effective bending moduli for the first and second bending stages of the bi-layer and the tri-layer scaffolds. [a] denotes significant difference ($p<0.05$) in the effective bending modulus between WC and AC directions.

Bi-layer Scaffolds	100%collagen/ 20%collagen-80%elastin		100%collagen/ 50%collagen-50%elastin	
	WC	AC	WC	AC
E_{bend1}(kPa)	20.7±5.0	20.7±3.8	70.7±8.5	73.5±4.8
E_{bend2}(kPa)	9.6±2.0 [a]	18.1±1.4 [a]	21.9±4.1 [a]	39.3±3.6 [a]

Bi-layer Scaffolds	100%collagen/ 90%collagen-10%C4S		100%collagen/ 50%collagen-50%C4S	
	WC	AC	WC	AC
E_{bend1}(kPa)	55.6±5.9 [a]	80.4±7.4 [a]	56.4±3.1 [a]	82.3±2.3 [a]
E_{bend2}(kPa)	20.9±0.8 [a]	33.4±6.7 [a]	16.0±1.6 [a]	29.7±2.7 [a]

Tri-layer Scaffolds	100%collagen/90%collagen-10%C4S/50%collagen-50%elastin		100%collagen/50%collagen-50%C4S/20%collagen-80%elastin	
	WC	AC	WC	AC
E_{bend1}(kPa)	53.1±4.0	59.2±7.1	54.9±5.2	50.8±4.9
E_{bend2}(kPa)	25.0±3.3 [a]	35.2±3.4 [a]	13.4±2.1 [a]	30.0±0.9 [a]

4.3.3 Finite Element Modelling

The ODGEN HYPERFOAM models have been assigned to the scaffolds by fitting the stress-strain curves of the models to the experimental tensile and compressive stress-strain data, as shown in Fig 4.7. We can see that curves with good fit can be achieved for all types of scaffolds (see Fig 4.7 a-e), despite certain deviation at the tension-compression transition points. All the characteristic deformation stages are well represented in the models (see Fig 4.7 a). The constants of the model for each type of scaffold are listed in Table 4.6.

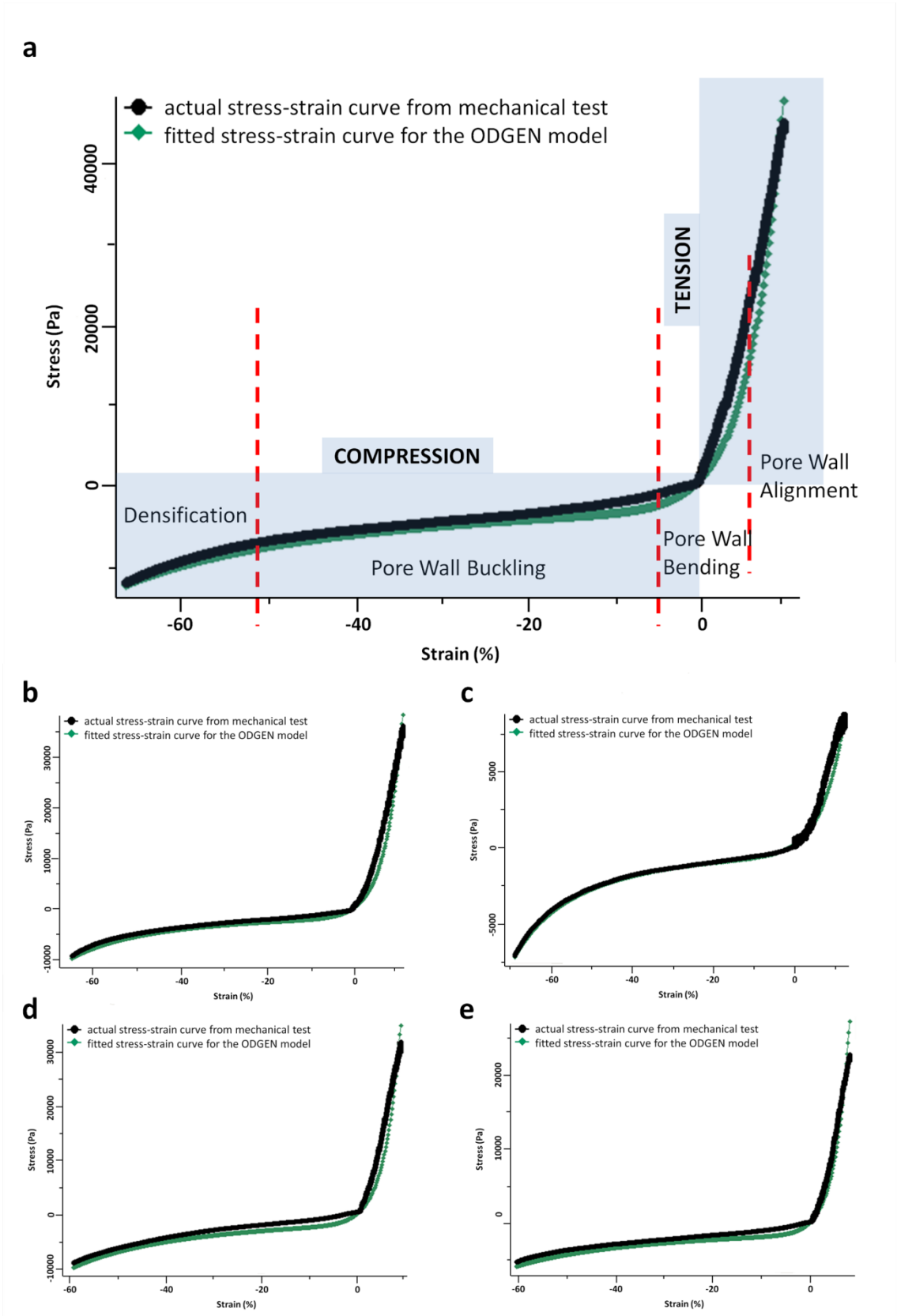


Fig 4.7 Fitted stress-strain curves of the ODGEN HYPERFOAM models for (a) 1%wt/v 100%collagen scaffold, (b) 1%wt/v 50%collagen-50%elastin scaffold, (c) 1%wt/v 20%collagen-80%elastin scaffold, (d) 1%wt/v 90%collagen-10%C4S scaffold, and (e) 1%wt/v 50%collagen-50%C4S scaffold. Regions of tension and compression, and the characteristic deformation stages are labeled in (a).

Table 4.6 Summary of material constants of the ODGEN HYPERFOAM models for the scaffolds.

	100%collagen	50%collagen-50%elastin	20%collagen-80%elastin	90%collagen-10%C4S	50%collagen-50%C4S
μ	3476.8	1836.2	803.5	2589.4	1851.6
α	28.65	27.34	21.37	33.06	36.75
β	0.006086	0.016999	0.039835	0.014896	0.007217

Simulated three-point bending tests conducted on the scaffold models defined by the constants in Table 4.6 produce deformed shapes shown in Fig 4.8, and load-deflection curves shown in Fig 4.9. It can be found that the finite element models are able to exhibit similar bending behaviour to that of the actual scaffolds.

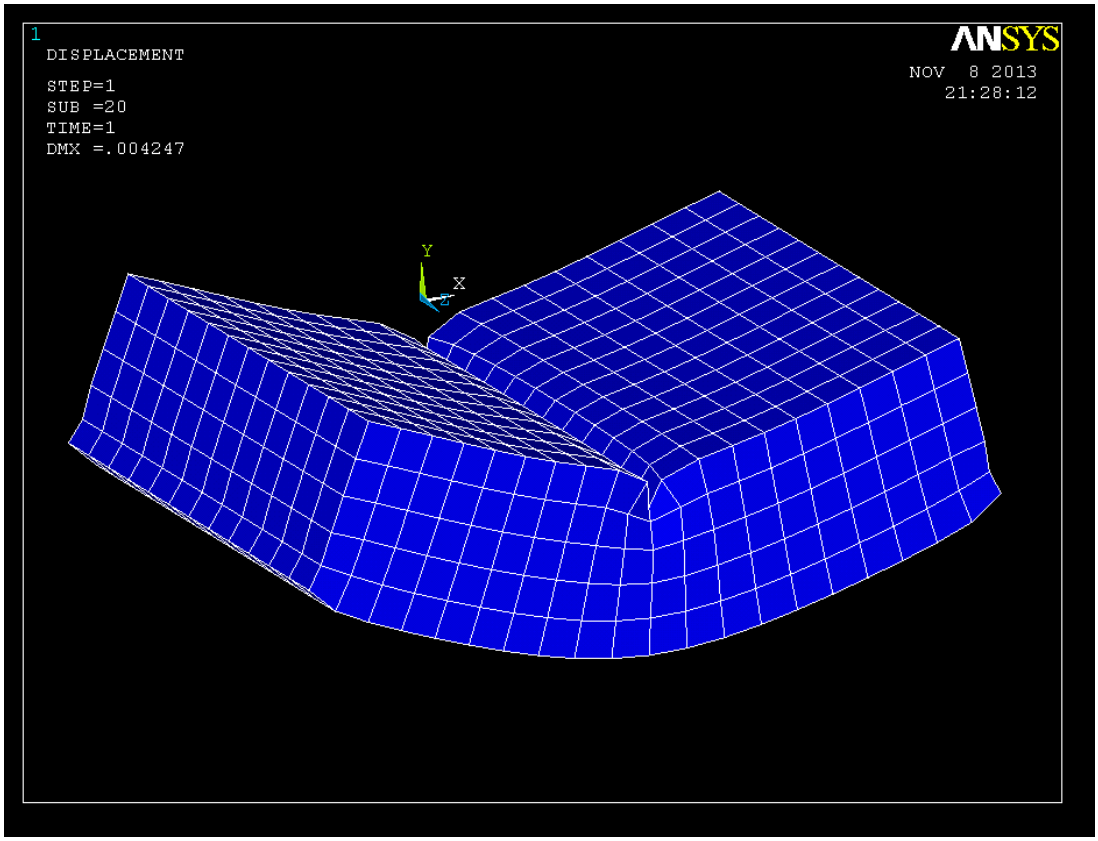


Fig 4.8 Deformed shape of the model of 1%wt/v 100%collagen scaffold in three-point bend test.

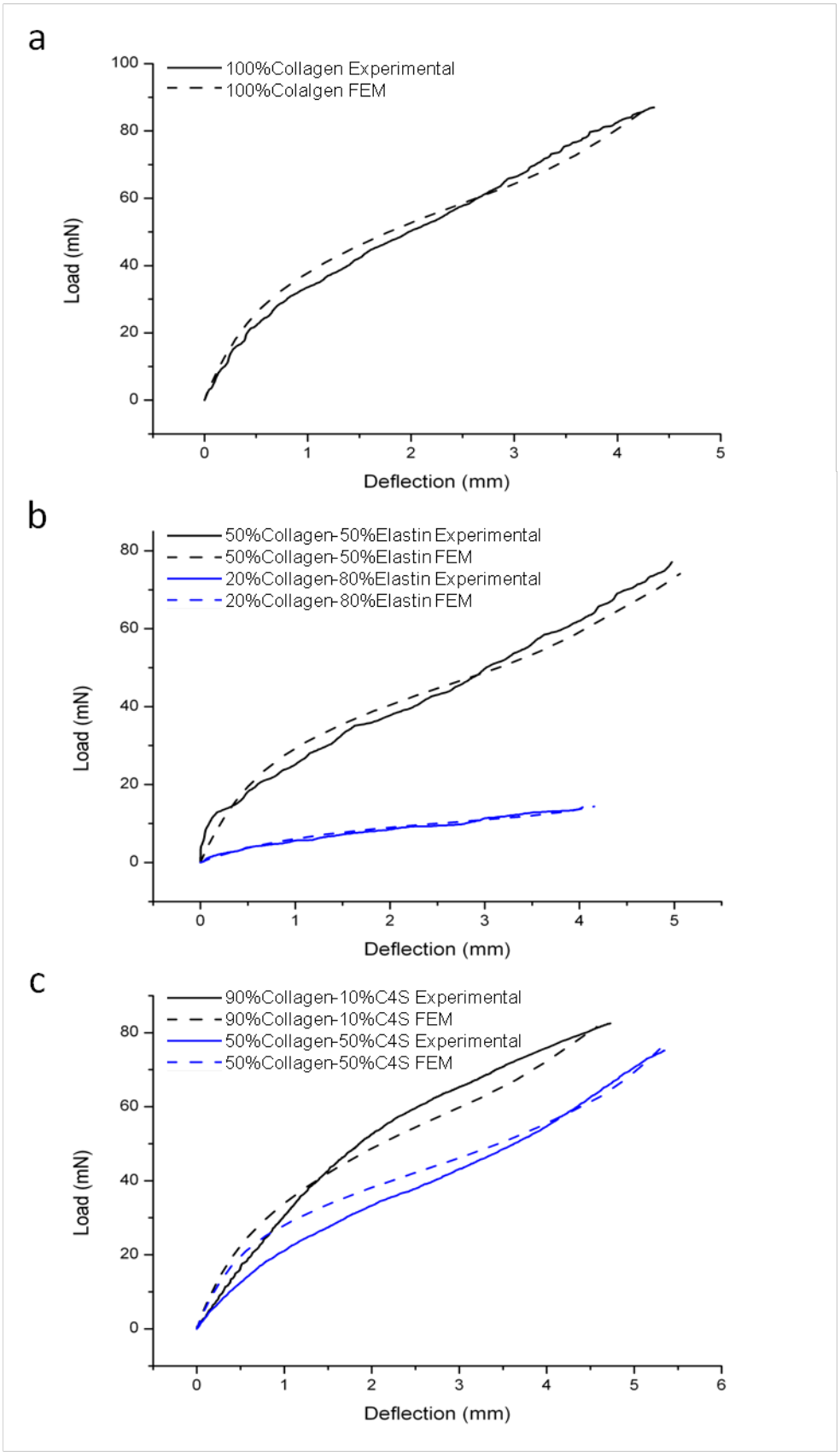


Fig 4.9 Load-deflection curves of experimental and simulated three-point bend tests for (a) 1%wt/v 100%collagen scaffold, (b) 1%wt/v collagen-elastin scaffolds, and (c) 1%wt/v collagen-C4S scaffolds.

In the finite element models of the layered scaffolds, the bending anisotropy between WC and AC directions still exists (Fig 4.10). We can see that the FEM curves well agree with the experimental ones in the WC direction. However, in the AC direction, there is deviation in the FEM curves, especially in the collagen/collagen-elastin bi-layer scaffold and the tri-layer scaffold. Unlike the experimental curves, the FEM AC curves exhibit a much softer second stage, followed by a drastically stiffened third deformation stage. It is at this third stage where distinct differences in the deflection can be observed between the WC and AC directions, whereas in experimental curves, the anisotropy starts to show in the second stage.

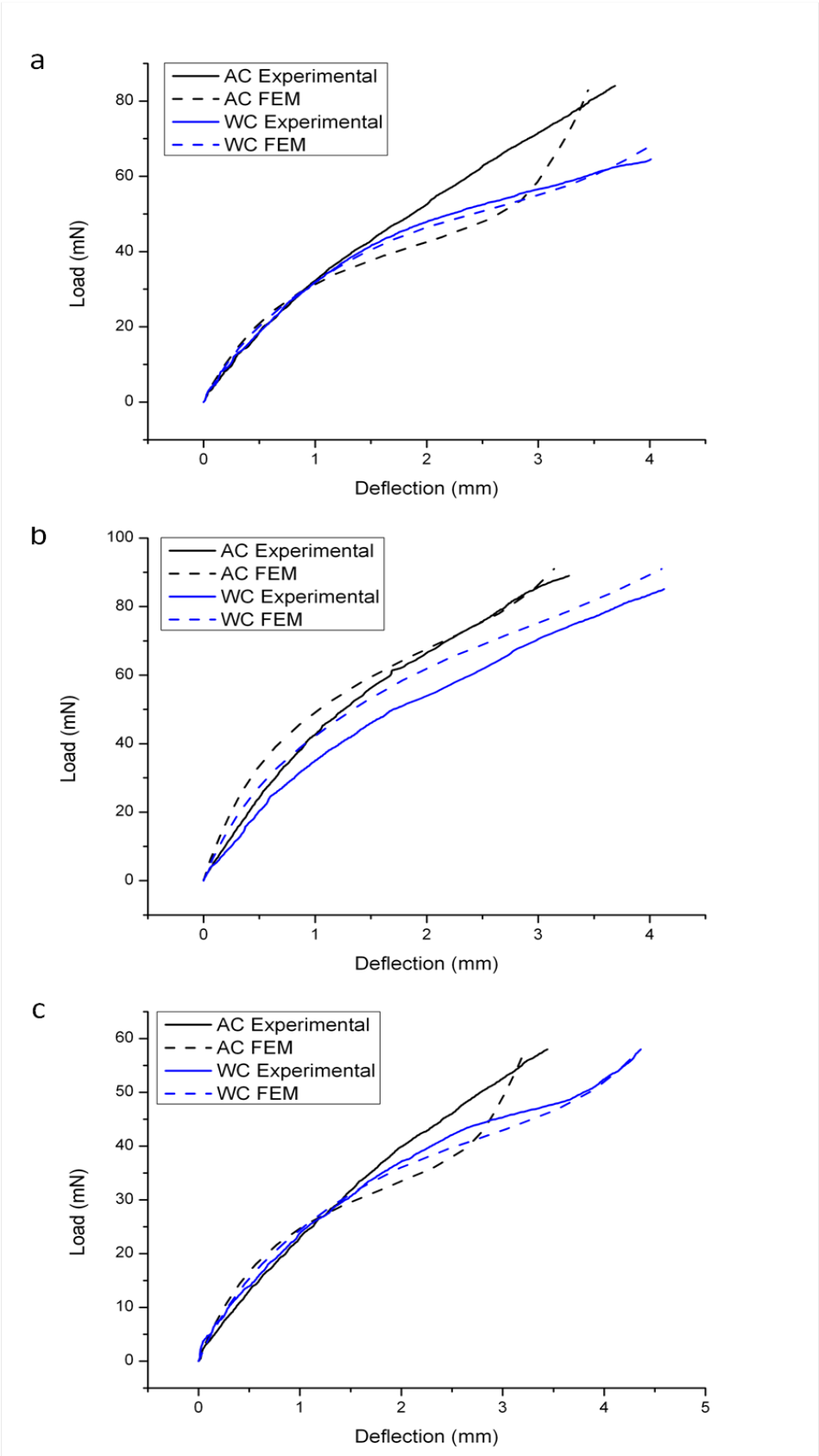


Fig 4.10 Load-deflection curves of experimental and simulated three-point bend tests for (a) 100%collagen/50%collagen-50%elastin scaffold, (b) 100%collagen/90%collagen-10%C4S scaffold, and (c) 100%collagen/90%collagen-10%C4S scaffold/50%collagen-50%elastin scaffold.

When under a distributed load of 2000Pa, the model of the 100%collagen/90%collagen-10%C4S scaffold/50%collagen-50%elastin scaffold undergoes a smaller deflection in the AC direction (4.28mm) than in the WC direction (4.66mm), as shown in Fig 4.11. This anisotropy also occurs in the third deformation stage of the model, and is smaller compared with that observed in the three-point bend tests. In addition, stress analysis was also conducted in the model. From the stress contour plots (Fig 4.12) we can see that, when bent in the WC direction, a larger volume of the scaffold is in tension, and the stress within the tensile region is slightly lower than that in the scaffold bent in the AC direction.

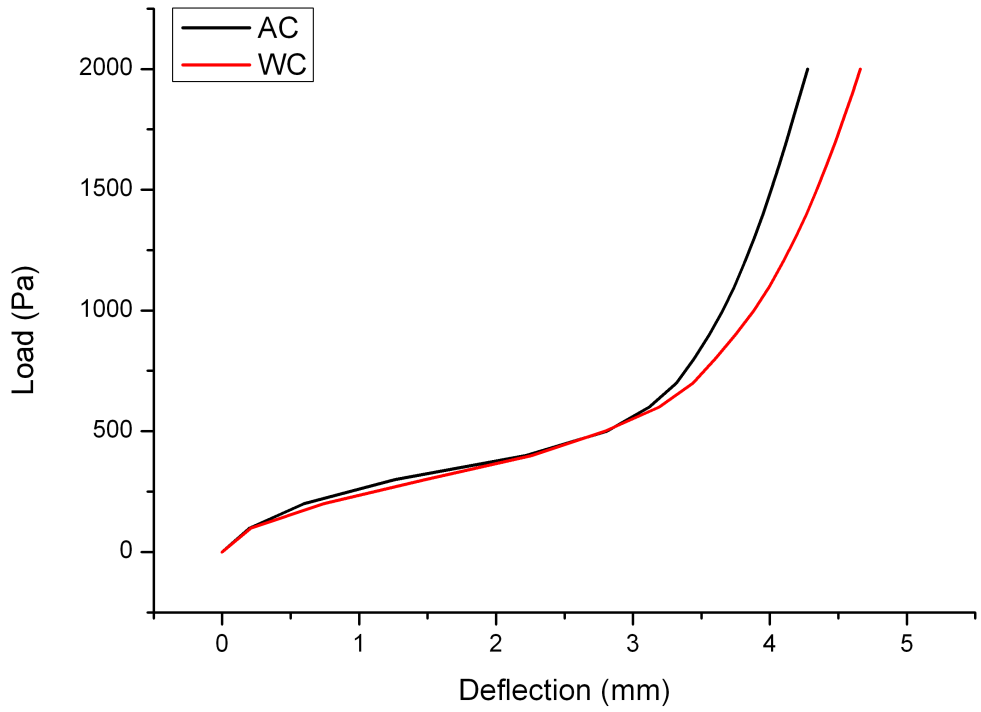


Fig 4.11 Load-deflection curves of simulated bend test with distributed loading on 100%collagen/90%collagen-10%C4S scaffold/50%collagen-50%elastin scaffold.

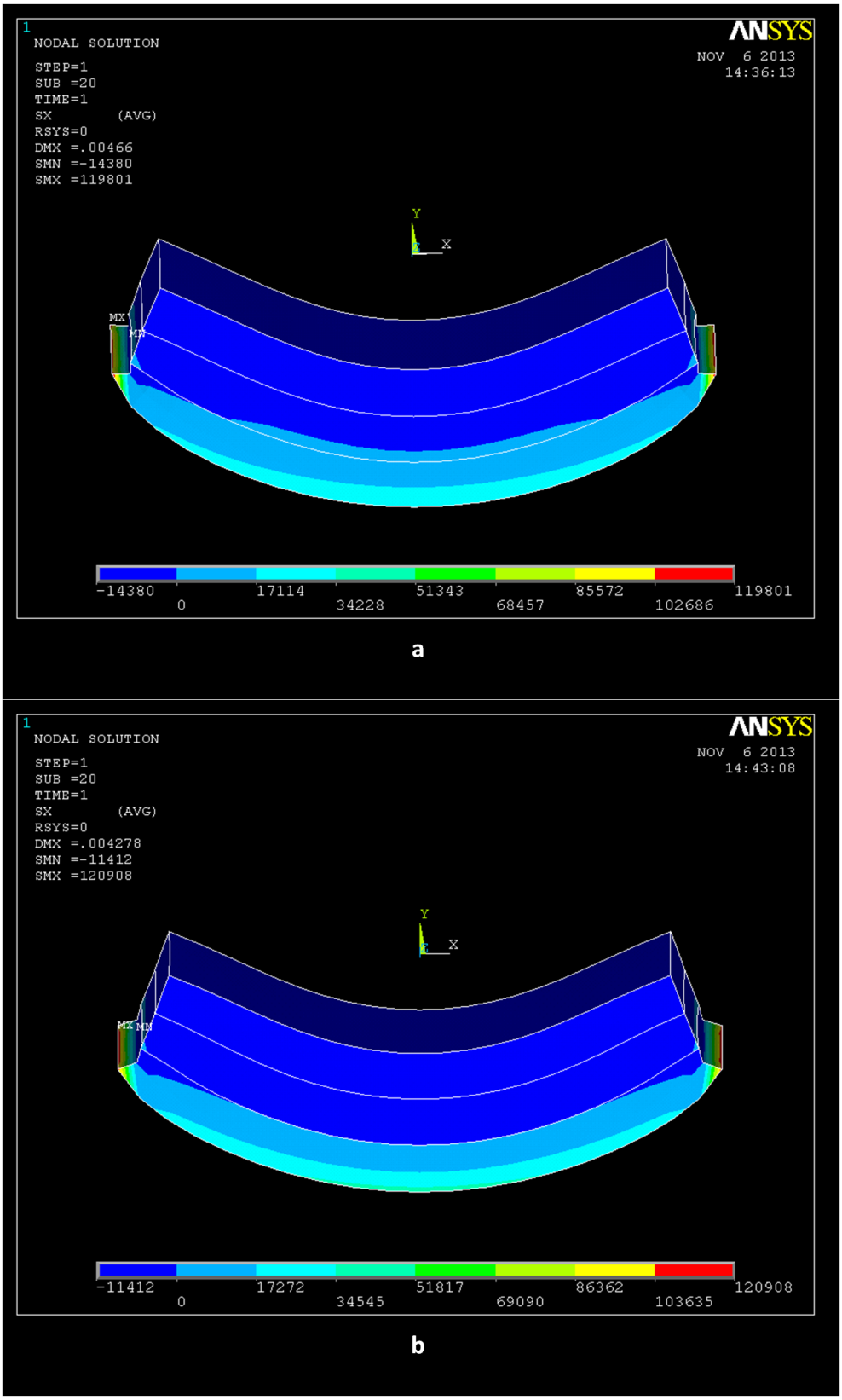


Fig 4.12 Contour plots of the longitudinal (X-direction) component of stress in the model of 100%collagen/90%collagen-10%C4S scaffold/50%collagen-50%elastin scaffold under distributed load in (a) WC direction, and (b) AC direction.

4.3.4 Effects of Crosslinking

Table 4.7 compares the E_{comp} and E_{ten} of the non-crosslinked and crosslinked uniform-composition scaffolds. Generally, the crosslinked scaffolds exhibit higher moduli than the non-crosslinked ones. The UV irradiation introduces better improvement in the mechanical properties to the collagen and collagen-elastin scaffolds, while for the collagen-C4S scaffolds, the DHT treatment seems to be more effective.

All the layered scaffolds also maintained their bending anisotropy after the crosslinking processes, see Table 4.8. The crosslinked 100%collagen/50%collagen-50%elastin and 100%collagen/90%collagen-10%C4S bi-layer scaffolds kept the same trends in E_{bend1} and E_{bend2} as the non-crosslinked ones: for the 100%collagen/50%collagen-50%elastin scaffold, E_{bend1} is similar in WC and AC directions and E_{bend2} is higher in AC direction than in WC direction; for the 100%collagen/90%collagen-50%elastin scaffold, E_{bend1} and E_{bend2} are both higher in AC direction.

The tri-layer scaffolds also see higher values in both E_{bend1} and E_{bend2} in the AC direction. This is different from the non-crosslinked scaffolds where the effective bending moduli for WC and AC directions start to differ only from the second stage.

Table 4.7 Compressive and tensile moduli of the non-crosslinked and crosslinked uniform-composition scaffolds. [a] denotes significant difference ($p<0.05$) in the modulus amongst groups of different crosslinking conditions.

	100%collagen		50%collagen-50%elastin		90%collagen-10%C4S	
	E_{comp} (kPa)	E_{ten} (kPa)	E_{comp} (kPa)	E_{ten} (kPa)	E_{comp} (kPa)	E_{ten} (kPa)
non-crosslinked	28.3±4.6 [a]	344.6±42.6 [a]	13.2±2.4	230.3±22.3 [a]	17.8±1.7	270.3±46.9
UV	50.0±3.3 [a]	874±78.7 [a]	21.1±4.7 [a]	294.9±31.1	18.6±2.8	303.9±18.9
DHT	43.9±4.7 [a]	556.8±91.9 [a]	15.6±3.6	273.5±14.3	28.6±3.2 [a]	352.5±34.1 [a]

Table 4.8 Effective bending moduli for the first and second bending stages of the crosslinked bi-layer and tri-layer scaffolds. [a] denotes significant difference ($p<0.05$) in the effective bending modulus between WC and AC directions.

	Bi-layer Scaffolds	100%collagen/ 50%collagen-50%elastin	
		WC	AC
DHT	E_{bend1}(kPa)	103.7±9.1	92.7±4.0
	E_{bend2}(kPa)	33.6±7.1 [a]	47.1±7.9 [a]
UV	E_{bend1}(kPa)	105.9±8.1	110.2±13.2
	E_{bend2}(kPa)	22.8±2.1 [a]	42.3±4.3 [a]

	Bi-layer Scaffolds	100%collagen/ 90%collagen-10%C4S	
		WC	AC
DHT	E_{bend1}(kPa)	90.3±8.0 [a]	137.4±15.6 [a]
	E_{bend2}(kPa)	35.7±6.6	44.2±2.7
UV	E_{bend1}(kPa)	89.4±2.7 [a]	98.8±7.4 [a]
	E_{bend2}(kPa)	20.4±2.8 [a]	33.9±6.6 [a]

	Tri-layer Scaffolds	100%collagen/ 90%collagen-10%C4S/ 50%collagen-50%elastin	
		WC	AC
DHT	E_{bend1}(kPa)	72.1±10.1 [a]	97.7±2.6 [a]
	E_{bend2}(kPa)	24.8±4.4 [a]	41.5±8.2 [a]
UV	E_{bend1}(kPa)	65.6±11.3 [a]	85.2±0.9 [a]
	E_{bend2}(kPa)	28.4±3.3 [a]	37.6±5.0 [a]

	Tri-layer Scaffolds	100%collagen/ 50%collagen-50%C4S/ 20%collagen-80%elastin	
		WC	AC
DHT	E_{bend1}(kPa)	66.1±2.0 [a]	77.7±11.9 [a]
	E_{bend2}(kPa)	16.3±1.1 [a]	40.1±4.2 [a]
UV	E_{bend1}(kPa)	53.3±4.7 [a]	78.8±12.2 [a]
	E_{bend2}(kPa)	21.7±0.5 [a]	36.3±7.9 [a]

4.4 Discussion

4.4.1 Uniform-Composition Scaffolds

Due to the different deformation regimes in the different stages as mentioned in 4.2.2, the collagen-based scaffolds exhibit the non-linear mechanical properties presented in Fig 4.4.

The tensile modulus of the scaffolds is found to be approximately one order of magnitude higher than that in compression. This phenomenon has been reported by Harley et al, and was explained by the existence of a dense 'air side' layer which stiffened the scaffold in tension [151]. Here, a closer investigation at a microscopic level is paid to the deformation mechanism of the individual pores in the scaffold, and a different point of view on this phenomenon is presented.

The deformation regimes of an elastomeric foam ought to predict equal E_{ten} and E_{comp} of the scaffold, because they are governed by the same deformation mechanism: pore edge bending [152]. The experimental results in Table 4.1-4.3, however, do not follow this behaviour, and so need to be explained by reanalyzing the model of a deforming pore.

Taking a cubic pore as an example (Fig 4.13), we can see that the deforming load is exerted not only vertically onto the pore edges, but also axially onto the side walls, causing their stretching in tension and buckling in compression (similarly mentioned by Gibson as 'beam-column interaction' [5]). Taking these buckling and stretching effects into account, the model in Fig 4.13 produces a relationship between the moduli and the relative density as Eq 4.4 and Eq 4.5 (see Appendix A),

$$\frac{E_{ten}}{E_s} = 2\left(\frac{1-\emptyset}{3}\frac{\rho}{\rho_s}\right)^3 + 4\left(\frac{\emptyset}{3}\frac{\rho}{\rho_s}\right)^2 + \frac{(1-\emptyset)}{3}\frac{\rho}{\rho_s} \quad \text{Eq 4.4}$$

$$\frac{E_{comp}}{E_s} = 2\left(\frac{1-\emptyset}{3}\frac{\rho}{\rho_s}\right)^3 + 4\left(\frac{\emptyset}{3}\frac{\rho}{\rho_s}\right)^2 \quad \text{Eq 4.5}$$

where E_s is the Young's modulus of the solid material, and $\emptyset$ is the fraction of the solid material contained in the pore edges. The first term of the equations is for the contribution of the bending of the pore walls, the second term is for the bending of the pore edges, and the third term is for the stretching of the pore walls. The absence of the third term in Eq 4.5 is because that the pore walls will buckle at a negligibly small strain and lose contribution to the modulus afterwards (see Appendix A). Therefore, from Eq 4.4 and Eq 4.5 we can see E_{comp} will be much smaller than E_{ten} due to the low values of $\frac{\rho}{\rho_s}$ (<0.02).

Also, because of the low $\frac{\rho}{\rho_s}$, the third term in Eq 4.4 predominates over the other two terms (see Appendix A), and gives an approximately linear dependence of E_{ten} on $\frac{\rho}{\rho_s}$ in the 100%collagen scaffolds (see Fig 4.5). Similarly the second term predominates in Eq 4.5 and produces a squared dependence of E_{comp} on $\frac{\rho}{\rho_s}$ (see Fig 4.5).

The cubic pore model in Fig 4.13 is very much simplified compared to the real geometries of the pores in the scaffold. Therefore the Eq 4.4 and Eq 4.5 derived from this model will not be sufficient in predicting the actual values of E_{ten} and E_{comp} due to the inaccurate geometric constants used in the analysis. To accurately predict the values of E_{ten} and E_{comp} with $\frac{\rho}{\rho_s}$, models with more complex geometries, such as dodecahedron and tetrakaidecahedron, need to be adopted [152]. However, the cubic pore model in this study has been sufficient in scaling the effects from different contributing factors in

the deformation, and has served well for illustrating the relationship between E_{ten}, E_{comp} and $\frac{\rho}{\rho_s}$.

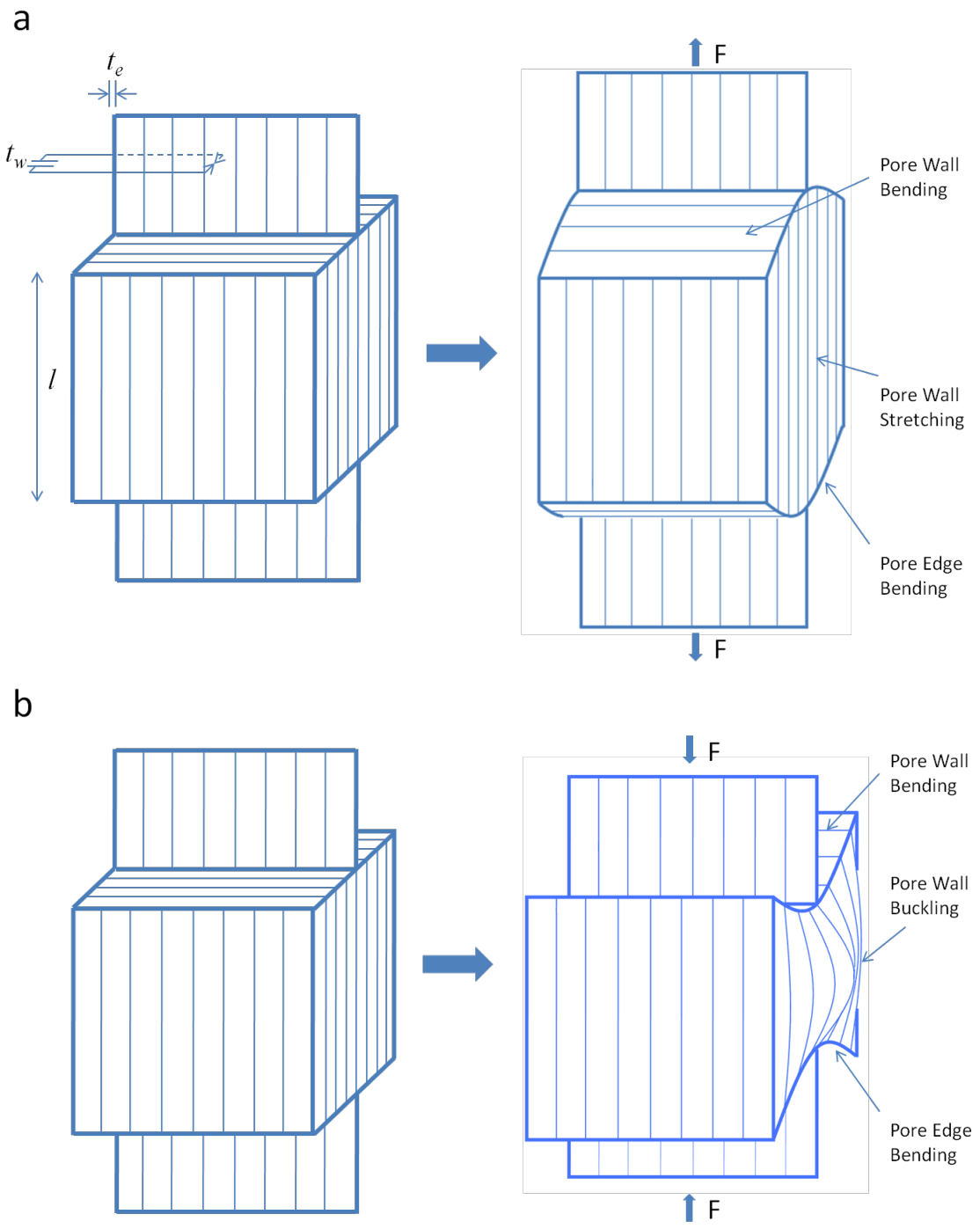


Fig 4.13. Schematic graphs of the deformation of an individual pore (a) in tension, and (b) in compression. The edge length *l*, the thickness of the pore edge t_e, and the thickness of the pore wall t_w are labeled respectively.

The second phases (elastin and C4S) disrupt the pore wall integrity in the scaffolds, which means that the pores have an increased number of hollows on them, see Fig 3.6 and 3.7. When a hollow is introduced to the pore wall, the pore wall would still maintain a large portion of its resistance to bending when the pore is under compression. However, when a hollow is present on the pore edge, the edge would essentially be disconnected and hence would lose its contribution to the compressive modulus. Therefore, as the volume fraction of the second phases increases, more hollows may have occurred on the pore edges and hence have reduced the dominance of the pore edge bending (i.e. the second term in Eq 4.5) over $E_{comp.}$ As a result, the value of the dependence factor *e* of E_{comp} has shifted more towards 3 (see Table 4.4), which is from the first term of Eq 4.5, attributed to pore wall bending.

For the scaffolds with the same relative density, the decrease of the collagen volume fraction lowers the moduli (see Table 4.1-4.3) because elastin and C4S a have much lower stiffness than collagen: Gosline reported an elastic modulus of ~1 MPa for elastin versus ~1 GPa for collagen [54], and Redaelli determined by molecular modelling the stiffness of GAGs and collagen fibrils to be 3.1×10^{-2} N/nm and 0.75×10^{3} N/nm respectively [248]. Also, the above-mentioned disruption of the pore wall integrity caused by elastin and C4S is another reason for the lower moduli.

In the native heart valves, the role of elastin is to give a large extensibility to the ventricularis (up to 60%) [27], while the GAGs act to absorb compressive loads and to resist tissue buckling [72, 249]. The elastin incorporated in the collagen-elastin scaffolds seems not to have achieved its natural function, as from Table 4.1 and 4.2 we can see that the ε_f remained generally unchanged. This is most likely because that the elastin is merely physically attached to the collagen sheets and is not continuous throughout the scaffold (see Fig 3.6, schematically illustrated as Fig 4.14a), hence the ε_f

is still limited by the extensibility of the collagen in the collagen-elastin scaffolds. This suggests that the elastin might need to be incorporated to the collagen network at a lower scale level (such as shown in Fig 4.14 b) for the scaffolds to take more advantage of the properties of elastin. In comparison, the C4S seems to have helped endure the compression, as the ε^* is found to be higher in the collagen-C4S scaffolds than in the collagen scaffolds (see Table 4.1 and 4.3). This may be because the C4S molecules grafted at the periphery of the collagen fibrils have stabilized the pore walls against buckling [233, 249]. It is speculated that the collagen-C4S co-precipitation effect mentioned in 3.4.2 has produced more tightly bundled collagen fibrils, with C4S molecules filling in the inter-fibrillar space. This may have increased the effective thickness of the pore walls to resist the buckling load, and therefore prolongs the linear elastic strain.

Harley et al reported that the pore size does not affect the mechanical properties of the scaffolds provided that they are of the same relative density [151]. In Table 4.1, the results of the 1%wt/v scaffolds agree with this finding. However, the 0.5%wt/v and 2.5%wt/v scaffolds show higher tensile, compressive, and bending moduli when the pore size is larger. This is likely to be due to the difference in the pore structures caused by the different freezing temperatures. For the 0.5%wt/v group, we can see from Fig 3.5 b that the scaffolds frozen at -80˚C have much more porous pore walls than those frozen at -20˚C, which may be responsible for the lower mechanical properties. The much smaller pore size achieved at -80˚C has created much larger surface area in the scaffold. However, there is not sufficient amount of collagen to form continuous pore walls for such a large surface area, and therefore hollows are left on the pore walls. For the 2.5%wt/v group, although there is sufficient material to accommodate the large surface area created at -80˚C, the high freezing rate and the high viscosity of the

suspension has prevented some collagen from moving to the inter-crystal space during the freezing process to form pore walls. As a result, many dangling collagen fibres can be seen on the pores (see Fig 3.5 h). Since these fibres do not fully contribute to the mechanical properties, the -80˚C group is essentially having a lower mechanically effective relative density than the -20˚C group, and hence lower mechanical properties.

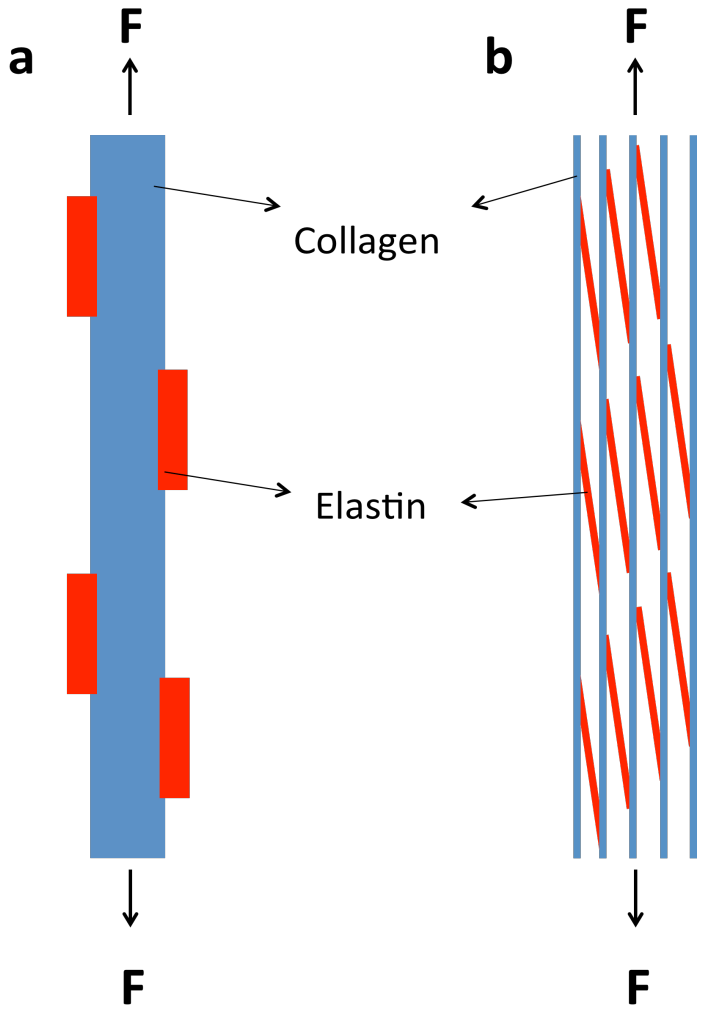


Fig 4.14 Schematic graph of incorporation of elastin in collagen: (a) elastin discontinuously attached to collagen sheet, which is observed in the scaffolds in this thesis, and (b) elastin incorporated between collagen fibrils, which could be potentially beneficial to the scaffolds for making more use of the properties of elastin.

In bending, one side of the scaffold will be in tension and the other side in compression. The effective bending modulus E_{bend} should therefore lie in between of the E_{ten} and E_{comp} (see Table 4.1-4.3) and should follow Eq 4.6 (see Appendix B).

$$E_{bend} = \frac{4}{\left(\frac{1}{\sqrt{E_{ten}}} + \frac{1}{\sqrt{E_{comp}}}\right)^2} \quad \text{Eq 4.6}$$

As E_{ten} is considerably larger than E_{comp}, the neutral axis in bending will lie towards the tensile surface, and the value of E_{bend} will be more affected by E_{comp}. After the initial slope, the compressive region in the scaffold will gradually reach the linear elastic strain ε^* and start to enter the second deformation stage, which will result in a decrease in the modulus of the compressive region (see Fig 4.4 b), and hence a reduced effective bending modulus (i.e. a decreased load-deflection slope in Fig 4.4 c).

It is worth noticing that for the scaffold in this bending experiment the two edges on the span are limited in horizontal displacement. Therefore, as the deflection increases, elongation of the tensile region may become visible and produce a membrane force that will act against the load. The actual loads applied in the bending experiments therefore not only create the bending moments, but also accommodate the membrane effects. As a result, the values of E_{bend1} derived with these loads in Table 4.1-4.3 are likely to have been overestimated. This can be confirmed by comparing the E_{bend1} values from Table 4.1-4.3 with those predicted by Eq 4.6, shown in Table 4.9. We can see that the E_{bend1} measured from the bend tests generally have higher values than the predictions of Eq 4.6.

A better algebraic description of the bending behaviours coupled with the membrane effects for the scaffolds is difficult, especially when the deformation enters the second stage where the membrane effect is going to be more prominent. However, finite

element modelling has been able to provide a numerical simulation that is in agreement with the experimental data (see Fig 4.9).

The small deviation of the FEM bending data from the experimental data is likely to be derived from the errors generated in the curve-fitting process (see Fig 4.7). The difference between the tensile and compressive moduli results in a discontinuous change in the gradient at the tension-compression transition point on the stress-strain curve, which however, cannot be accommodated by the ODGEN HYPERFOAM model. Therefore, the model will have a lower initial E_{ten} and a higher initial E_{comp} than the actual scaffold (see Fig 4.7), and produces a slightly different bending curve in Fig 4.9.

Table 4.9 Measured and predicted initial bending modulus for scaffolds with various compositions and relative densities.

Scaffold Composition	Relative density (% wt/v)	E_{bend1} Measured (kPa)	E_{bend1} Predicted by Eq 4.6 (kPa)
100%collagen	0.5	31.8±4.5	22.2
	1	85.7±6.0	68.4
	2.5	415.8±29.2	409.9
50%collagen-50%elastin	0.5	11.3±0.5	7.2
	1	65.1±9.9	34.4
	2.5	220.0±32.9	198.5
20%collagen-80%elastin	1	25.4±5.1	18.0
	2.5	130.1±12.2	108.3
90%collagen-10%C4S	0.5	11.0±1.4	10.2
	1	52.4±6.0	45.1
	2	195.3±27.5	218.0
50%collagen-50%C4S	1	40.3±5.6	32.8
	2	135.8±7.8	144.1

4.4.2 Layered Scaffolds

Layered structures exist in many other tissues besides heart valves, such as articular cartilage, blood vessels, and bladder. Scaffolds with layered structures for these tissues have been developed and investigated, demonstrating desirable bio-mechanical properties [250-254]. However, there have not been any studies so far on how a layered

structure in the scaffold could be mechanically beneficial to the TEHVs. This study, therefore, after analyzing the uniform-composition scaffolds for each layer of the heart valve, brings the layered scaffolds for TEHVs into being and provides a first insight into their mechanical behaviour.

Bending is the major mode of deformation of the heart valve leaflets in vivo [255], thus the bending behaviour of the heart valve is critical to its function and health. For example, the valves need to exhibit suitable bending stiffness, as a too high or too low bending stiffness will result in incomplete valve opening or regurgitation [98]. Moreover, the complex bending patterns impart a much more uneven stress and strain distribution in the heart valves than that can be introduced by planar tensile or compressive deformation [256]. The maximal stress and strain will occur on the surfaces of the leaflets, and when inappropriate, can cause collagen fibre separation and tissue disruption [104, 257]. Therefore, aiming for a functional TEHV, the bending behaviour has been the primary mechanical property to be investigated on the layered scaffolds.

When the layered scaffolds are bent, the layers in the different regions of the scaffolds will be in either compression or tension. Therefore, the effective bending modulus will take into account of the E_{comp} of the layer(s) in the compressive region and the E_{ten} of the layer(s) in the tensile region. Different combinations of E_{comp} and E_{ten} will be in effect when the scaffold is in different loading directions. Consequently, the effective bending moduli for the WC and AC directions will be different. It is interesting though, to find that the collagen/collagen-elastin bi-layer scaffold and the tri-layer scaffolds have similar values of E_{bend1} for the WC and AC directions, which is also confirmed by the FEM results in Fig 4.10. When the loading direction on these two scaffolds changes from WC to AC, the collagen layer takes over the tensile stress and is expected to

produce a higher membrane force that would increase the effective bending modulus. At the same time, the collagen-elastin layer with a much lower E_{comp} is now in the compressive region instead of the collagen layer, which would reduce the effective bending modulus. These two counteracting effects may have resulted in the numerically unchanged E_{bend1} in the WC and AC directions.

From the first bending stage to the second, the effective bending modulus of the layered scaffold decreases because of the compressive layer(s) passing the linear elastic strain and dropping in E_{comp} as mentioned above. However, the simultaneously increasing elongation of the tensile layer(s) is generating more membrane force that helps to resist the reduction of the bending modulus. Again the collagen layer is able to provide more of this resistance than the other layers. Therefore the layered scaffolds all show a higher E_{bend2} in the AC direction. In the finite element models, however, no big difference in E_{bend2} seems to be present. The bending anisotropy rather exhibits as a drastically stiffened third stage in the AC curves (see Fig 4.10). This is because, in the models, the load applied is concentrated on a single line. This concentrated load tends to cause local deformation at the loading tip (see Fig 4.8), which also contributes to the measured deflection together with the overall deflection of the scaffold. This phenomenon is likely to be more distinct in the AC direction where the E_{comp} of the compressive layer(s) is lower. The load therefore mainly deforms the compressive layer(s) locally at the beginning of the second bending stage. When it reaches the point where a greater load is needed to cause local deformation than to overcome the membrane force, the stiff collagen layer then comes in effect and increases the effective bending modulus rapidly. It is as if the softening effect due to the decrease of E_{comp} in the compressive layer(s) and the stiffening effect due to the increasing membrane force in the tensile layer(s) have taken place in orders in the finite element models, whereas in the actual

experiments they have been in practice at the same time, probably because the loading probe used in the experiments has a curvature of approximately 0.5 mm^{-1} at the tip and therefore does not cause so much local deformation.

To eliminate the local deformation and to further mimic the loading condition in native heart valves, a distributed load has been applied onto the model of the 100%collagen/90%collagen-10%C4S/50%collagen-50%elastin tri-layer scaffold. The load-deflection curves again start to exhibit distinct differences in the third bending stage (see Fig 4.11). The stress analysis reveals that the collagen layer is accommodating a higher tensile stress with a smaller thickness. This confirms that it is the tensile layers producing the membrane forces that are having dominant effects on the bending anisotropy.

In the native heart valves, the fibrosa and the ventricularis were reported to have the elastic modulus of 13.02kPa and 7.41kPa respectively [32], which resulted from the different stiffness of the collagen and elastin fibres, as well as the cell-ECM interaction in each layer [99]. This difference in elastic modulus has lead to the difference in the membrane effects produced by the fibrosa and ventricularis in the respective bending status, which is utilized by the heart valve to achieve the characteristic bending anisotropy [24, 89]. This bending anisotropy is important in ensuring the valves' prompt opening in systole, and in preventing sharp reverse curvature that may cause flexure fatigue in the valve leaflets [100].

The tri-layer scaffolds that have been tested and modelled in this study have mimicked the native heart valves in many aspects. Fig 4.15 illustrates a circumferential portion of the native heart valve which is copied by the tri-layer scaffold. It is of similar dimensions and compositions of layers to the scaffold [258], and the two ends of it are

also restricted by the annulus under the hemodynamic load [24]. Such native heart valve samples were reported to have a bending anisotropy of 491kPa WC versus 703kPa AC [255]. A proportionally similar bending anisotropy (25.0kPa WC versus 35.2kPa AC) was achieved by the 100%collagen/90%collagen-10%C4S/50%collagen-50%elastin tri-layer scaffolds. Therefore, with the close resemblance to the native heart valve, the tri-layer scaffolds are believed to bode well for mechanically desirable TEHVs.

There are still, of course, some features of native heart valves that have not been mimicked by the scaffold, an important one of which was the preferential alignment of the collagen and elastin fibres. As mentioned in 2.2.2, the collagen fibres are circumferentially aligned in the fibrosa, and the elastin fibres are radially aligned in the ventricularis [101]. This introduces another structural anisotropy that helps the leaflets withstand the transvalvular pressure without prolapsing to the ventricle, and at the same time stretch radially to form a tight coaptation with each other [97]. However, due to the nature of the freeze drying technique used in this study, the collagen and elastin in the scaffolds are oriented randomly, and so are the pores, hindering the scaffolds from achieving this property. Research has shown that well defined microstructures of pores (such as a rectangular shape) can guide the orientation of the cells seeded on the scaffolds, as well as the collagen synthesized [259, 260]. Therefore, the above limitation could potentially be addressed by introducing axially oriented pores into the scaffolds, which can be achieved by controlled unidirectional freezing of the suspensions [261-263].

Also, in the layered scaffolds tested in this chapter, the proposed mechanical role of the C4S layer, i.e. resisting the compression as the spongiosa does in the native heart valve [72], seems not to have been very well shown. Since the spongiosa is physiologically

featured by the GAGs-induced hydration, the mechanical function of the C4S layer ought to be further examined in the hydrated scaffolds in Chapter 5.

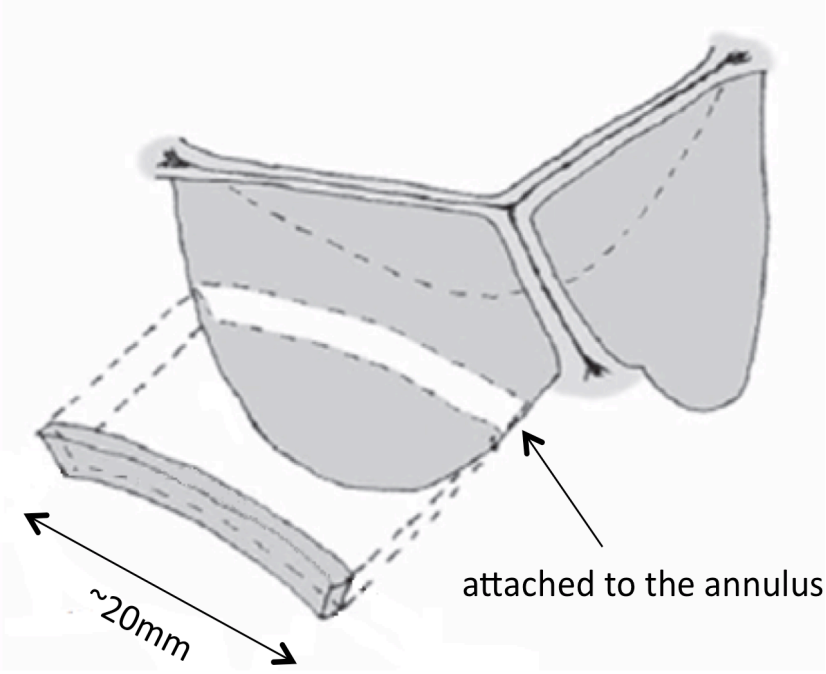


Fig 4.15 Illustration of the portion of native heart valve mimicked by the tri-layer scaffold [24].

4.4.3 Effects of Crosslinking

Crosslinking processes alter the ultra-structures of the scaffold materials (see 3.4.1), and consequently affect the mechanical properties of the scaffolds. In the collagen and collagen-elastin scaffolds, inter-molecular crosslinks (mostly ester bonds, see Table 3.7) prevent collagen fibres from reorienting and sliding over each other [146], and therefore increase the stiffness of the pore walls. On the contrary, the denaturation effects unbraid the triple-helix structure of the collagen molecules [232] (which is what provides the collagen molecules the resistance to tension [37]), and therefore compromise the stiffening effects from the crosslinking [264]. As DHT treatment introduces more denaturation to the scaffolds (see Table 3.7), it is less effective than the UV irradiation

in increasing the E_{comp} and E_{ten} of the scaffolds (see Table 4.7). In the collagen-C4S scaffolds, on the other hand, ester crosslinks are not successfully formed by either of the crosslinking methods (see Table 3.7). While the DHT treatment is still able to enhance the E_{comp} and E_{ten} with the amide crosslinks, the UV irradiation, not forming many amide crosslinks either, has barely had any effect on the mechanical properties (see Table 4.7).

Table 4.8 suggests that the crosslinking processes are able to increase the effective bending moduli of the layered scaffolds without compromising the characteristic bending anisotropy. The crosslinked tri-layer scaffolds start to show bending anisotropy from the first stage instead of the second stage as in the non-crosslinked scaffolds. This may be because the collagen layer has enjoyed larger increases (1.6~2.5 times) in the E_{ten} than the collagen-elastin layer (1.2~1.3 times) during the crosslinking processes (see Table 4.7), improving the E_{bend1} more in the AC direction than the WC direction.

4.5 Conclusions

This chapter has investigated the mechanical properties of the collagen-based scaffolds, which are important not only to the physical functions of the scaffolds, but also to the cell behaviors on the scaffolds [151, 154, 234].

The collagen-based uniform-composition scaffolds studied here had tensile, compressive and effective bending moduli ranging from 39.8kPa to 1082kPa, from 2.4kPa to 213.9kPa, and from 11.0kPa to 415.8kPa, respectively. The moduli increased with the relative density of the scaffold, and decreased as the collagen content decreased. The tensile moduli were approximately one order of magnitude higher than

the compressive moduli, and had smaller exponential dependence factor on the relative density. From the data of all the series of the uniform-composition scaffolds, an applicable model was derived for the deformation mechanism of the scaffolds in tension, compression and bending, which in turn explained the above findings. In the following chapters, study on the uniform-composition scaffolds will focus on the ones with freezing temperature of -20˚C and relative density of 1%wt/v, which were suggested to have more suitable pore sizes in Chapter 3.

The DHT treatment and UV irradiation enhanced the mechanical properties of the scaffolds by introducing crosslinks in the scaffold materials, with UV being more effective on the collagen and collagen-elastin scaffolds and DHT more effective on the collagen-C4S scaffolds.

The layered scaffolds exhibited a bending anisotropy mainly due to the different abilities of the layers to introduce a tensile membrane force that withstands the bending load. The tri-layer scaffolds, as the major novelty of this thesis, thus possessed a native-valve-mimicking mechanical property in addition to the similar structure to the native heart valves, and would also be taken forward for further characterizations.

The FEM tests supported the experimental data and enabled us to predict the mechanical properties of the scaffolds. The FEM models that are easy to adjust in variables (composition, layer thickness, geometry, loading condition, etc.) would facilitate the design and analysis of the scaffolds in the future.

Chapter 5. Hydrated Scaffolds

5.1 Introduction

In the process of heart valve tissue engineering, the scaffold-cell constructs will always be in an aqueous environment: culture medium in vitro, and blood and body fluid in vivo. The ability of the scaffolds to preserve water is an important aspect to investigate [265], as the level of hydration in the scaffolds can affect the absorption of cell nutrients, as well as the mechanical properties [266, 267]. Therefore, this chapter examines the hydrated scaffolds for their water uptake ratios and their mechanical properties, to add to the findings in Chapter 4.

5.2 Materials and Methods

5.2.1 Water Uptake

Scaffolds tested all had a relative density of 1%wt/v and freezing temperature of -20˚C. The scaffolds were firstly weighed (AB204, Mettler Toledo, UK) in the dry status and then were immersed in 0.1M phosphate buffered saline (PBS) at room temperature. After 1 hour of hydration, the scaffolds were removed from the PBS and placed on a wire mesh rack for 1 minute to drain any excessive PBS, after which these hydrated scaffolds were weighed. The water uptake was expressed as the ratio of the mass of the PBS absorbed in the scaffolds to the dry mass of the scaffolds, as shown in Eq 5.1

$$G = \frac{M_{wet} - M_{dry}}{M_{dry}} \times 100\% \qquad \text{Eq 5.1}$$

where G is the water uptake ratio, M_{wet} is the mass of hydrated scaffold, and M_{dry} is the mass of dry scaffold [268].

5.2.2 Mechanical Characterization

Scaffolds all had a relative density of 1%wt/v and freezing temperature of -20˚C, and were hydrated as described in 5.2.1. Tension and compression tests were conducted with the same methods described in 4.2.1. The extremely low load needed in the mechanical characterization of hydrated scaffolds made the tensile and compressive tests very challenging, and the three-point bend test practically infeasible. Therefore, a self-deflection test was designed to give an easier measurement of the mechanical (especially bending) properties of the hydrated scaffolds.

The Self-deflection tests were carried out as shown in Fig 5.1, in which the hydrated scaffolds were clamped on a span of 20mm, and were allowed to self-deflect, with the weight of the PBS absorbed by the scaffolds as the load. The tests on the layered scaffolds were also performed, in both with curvature (WC) and against curvature (AC) directions. The deflections were recorded by a camera (450D, 50mm, F1.8, Canon, Japan) and measured by ImageJ (National Institutes of Health, USA).

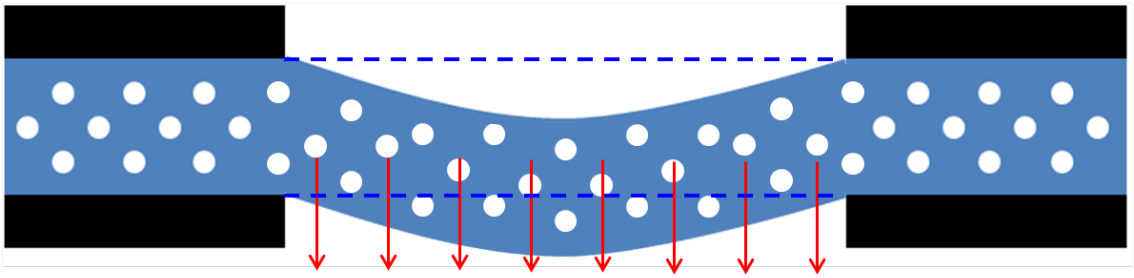


Fig 5.1 Schematic graph of self-deflection test on hydrated scaffold.

5.2.3 Statistics

All data were reported as means, with the standard deviations as the errors. One-way analysis of variance (ANOVA) followed by Tukey's test was used to compare groups of

data, with a probability value of 95% ($p < 0.05$) to determine statistical significance. 3 samples of each group were measured.

5.2.4 Finite Element Modelling

FEM was carried out as described in 4.2.2. A distributed load was applied on the scaffold models to simulate the load in the self-deflection tests introduced by the weight of the retained PBS in the scaffolds.

5.3 Results

5.3.1 Water Uptake

Table 5.1 lists the water uptake ratios of the scaffolds with various compositions. It seems that the water uptake ratio decreases as the volume fraction of elastin in the scaffold increases. Small amount of C4S is found to have improved the hydration ability, while further increasing the volume fraction in the scaffold results in a reduction in G.

Table 5.1 Water uptake ratios of scaffolds G, with various compositions. Statistically significant difference is found between all groups ($p<0.05$).

	G(%)
100%collagen	3045±44
50%collagen-50%elastin	2270±100
20%collagen-80%elastin	1401±9
90%collagen-10%C4S	3269±52
50%collagen-50%C4S	1613±23

5.3.2 Mechanical Characterization

Due to the sensitivity limitation of the equipment, the tension and compression tests have been extremely difficult on the hydrated scaffolds. Only the tests conducted on the 100%collagen scaffolds were able to produce meaningful results. Fig 5.2 presents the tensile and compressive stress strain curves of the hydrated 1%wt/v 100%collagen scaffolds, and the derived tensile and compressive moduli ($E_{ten.wet}$, $E_{comp.wet}$) are listed in Table 5.2. We can see that the hydrated scaffolds still exhibit the characteristic deformation stages [152], and the tensile modulus is also one order of magnitude higher than the compressive modulus, as observed in the dry status (see 4.3.1). Comparing with the E_{ten} and E_{comp}, the $E_{ten.wet}$ and $E_{comp.wet}$ have dropped to 1/24 and 1/42 of the dry values respectively.

Table 5.2 Tensile and compressive moduli of hydrated 1%wt/v 100%collagen scaffolds, in comparison with the correspondent dry values.

	$E_{ten.wet}$ (kPa)	E_{ten} (kPa)	$E_{comp.wet}$ (kPa)	E_{comp} (kPa)
100%collagen	14.3±0.9	344.6±42.6	0.67±0.04	28.3±4.6

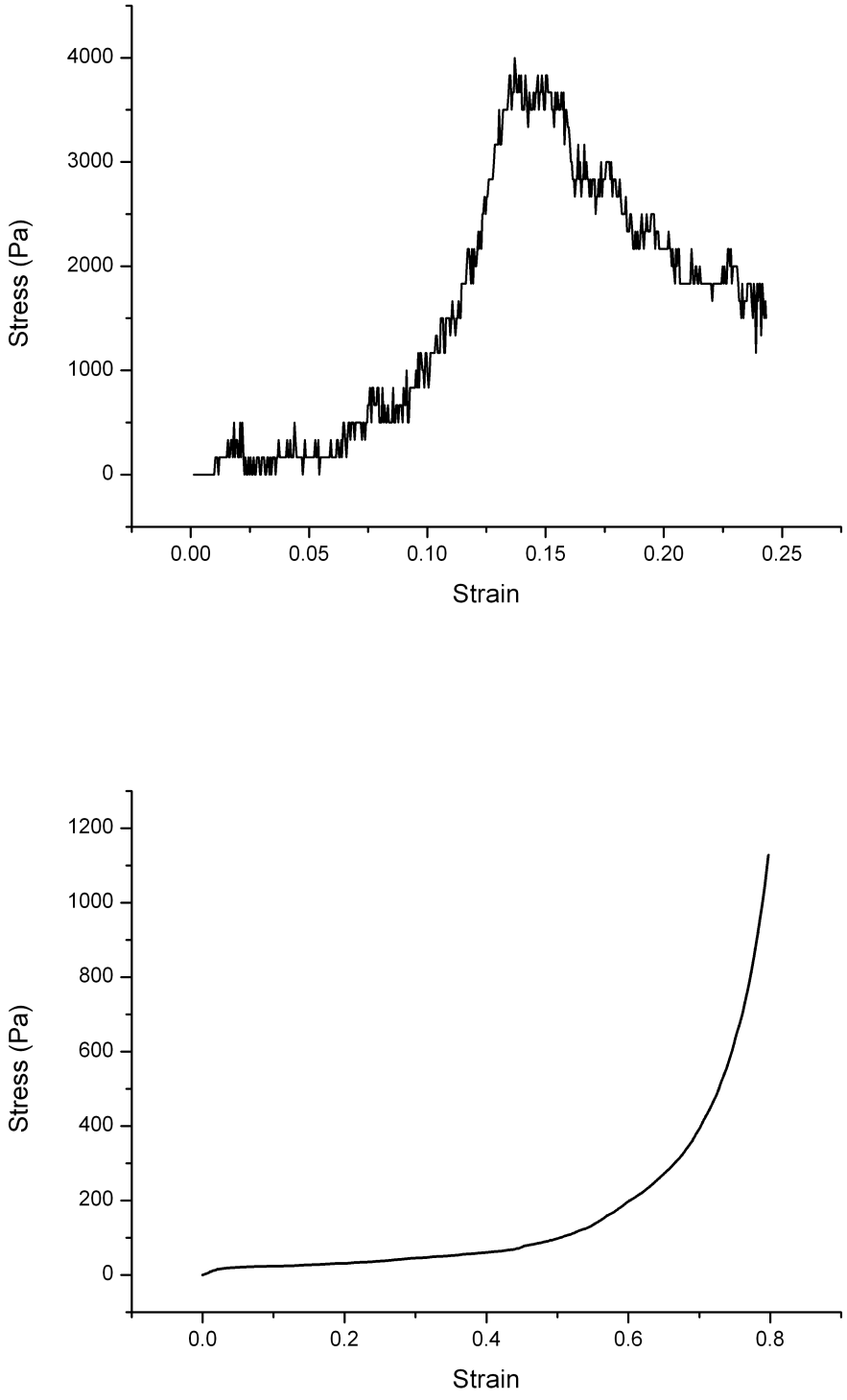


Fig 5.2 Unidirectional (a) tension and (b) compression stress-strain curves of 1% wt/v 100%collagen scaffolds, obtained from respective test conditions in 4.2.1.

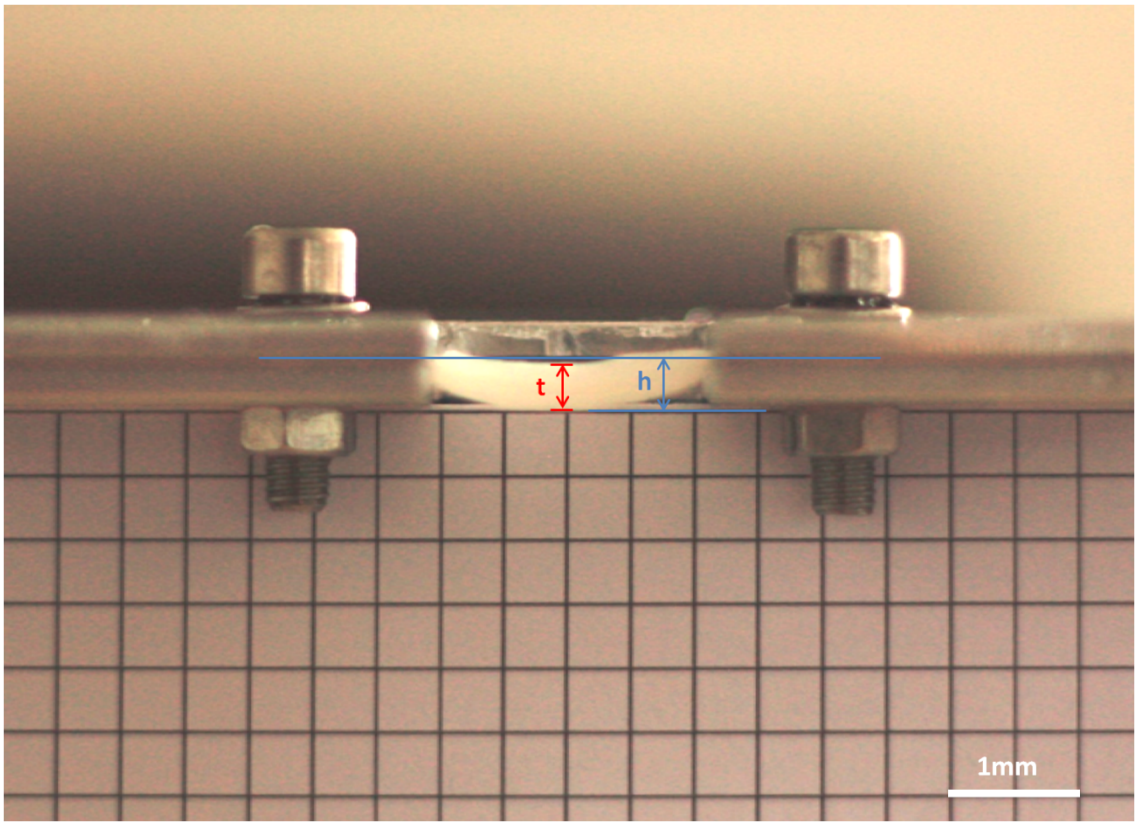


Fig 5.3 Representative image of self-deflection test on hydrated 1% wt/v 100%collagen scaffold.

In order to measure the mechanical properties of the other hydrated scaffolds, self-deflection tests were conducted. Fig 5.3 shows a self-deflected scaffold, whose deflection (D) is determined by Eq 5.2

$$D = h - \frac{t}{2} \qquad \text{Eq 5.2}$$

where t is the thickness of the scaffold, and h is the distance between the central position of the clamps (i.e. the initial central position of the scaffold) and the lower surface of the deflected scaffold. With the water uptake ratios listed in Table 5.1, the bending modulus of the hydrated scaffolds could then be calculated by Eq 5.3

$$E_{bend.wet} = \frac{5ql^4}{384DI} = \frac{5GM_{dry}gl^3}{384DI} \qquad \text{Eq 5.3}$$

where G is the water uptake ratio, M_{dry} is the dry mass of the scaffold, g is the gravitational acceleration, *l* is the span distance, and *I* is the second moment of area.

It needs to be noted that by using Eq 5.3, we have assumed the deflection is in a linear relationship with the load. However, it is likely that the bending behaviour of the hydrated scaffolds is also non-linear as the dry scaffolds (see 4.3.1). Therefore, the $E_{bend.wet}$ calculated by Eq 5.3 is a nominal value, averaged from the effective bending moduli of the first and second bending stages (possibly also a third bending stage as indicated by Fig 4.11). The $E_{bend.wet}$ for various scaffolds, along with the thickness (t) and the deflection (D), is listed in Table 5.3.

It is found that the 100%collagen scaffold has the highest effective bending modulus, while the 50%collagen-50%elastin scaffold has the lowest. The value of $E_{bend.wet}$ of the 100%collagen scaffold is also between those of the $E_{ten.wet}$ and $E_{comp.wet}$, consistent with the results in the dry scaffolds. It is also found that the scaffolds show certain shrinkage from the original thickness (~5mm), and the 50%collagen-50%elastin scaffolds have shrunk less than the other two.

Table 5.3 Thickness, deflection and effective bending modulus for hydrated scaffolds with various compositions. [a] denotes significant difference ($p<0.05$) amongst groups of different compositions.

	t (mm)	D (mm)	$E_{bend.wet}$ (kPa)
100%collagen	3.75±0.17	2.24±0.09 [a]	3.14±0.31 [a]
50%collagen-50%elastin	4.37±0.12 [a]	2.44±0.11 [a]	1.36±0.13 [a]
90%collagen-10%C4S	3.78±0.14	2.80±0.05 [a]	2.64±0.35 [a]

The self-deflection test was also conducted on the 100%collagen/90%collagen-10%C4S/50%collagen-50%elastin tri-layer scaffolds, see Fig 5.4. The effective bending modulus ($E_{bend.wet}$), the thickness (t) and the deflection (D) are listed in Table 5.4.

It can be seen that the bending anisotropy of the tri-layer scaffold is well maintained in the hydrated status, i.e. a larger deflection and a lower $E_{bend.wet}$ in the WC direction than in the AC direction. Meanwhile, the tri-layer scaffold exhibits a slightly larger thickness when deflected in the WC direction.

Table 5.4 Thickness, deflection and effective bending modulus for hydrated tri-layer scaffolds. [a] denotes significant difference ($p<0.05$) between different deflection directions.

	t (mm)	D (mm)	$E_{bend.wet}$ (kPa)
WC	4.23±0.09 [a]	2.87±0.26 [a]	1.62±0.23 [a]
AC	3.98±0.08 [a]	2.25±0.04 [a]	2.46±0.18 [a]

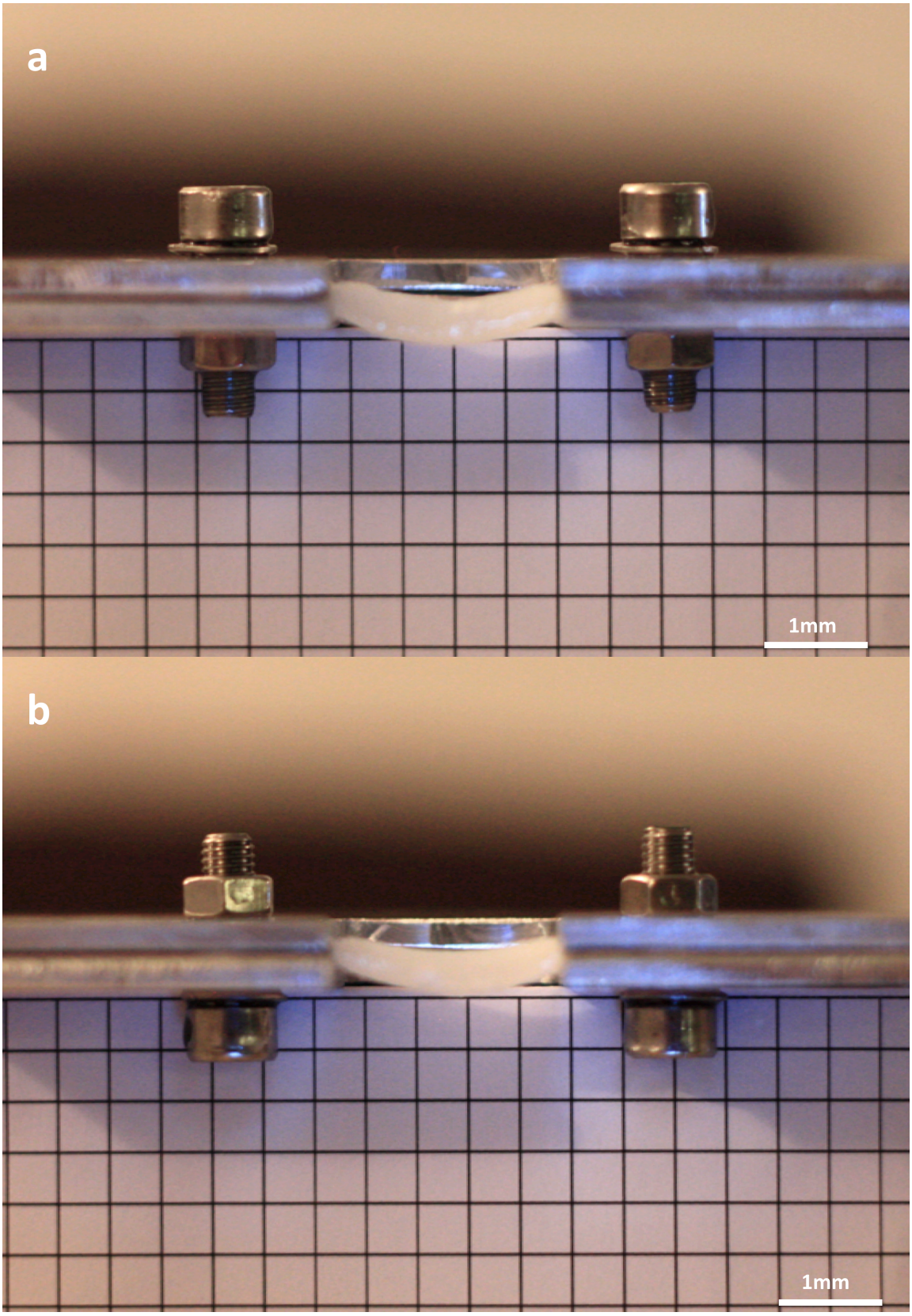


Fig 5.4 Images of self-deflection tests on hydrated tri-layer scaffold in (a) WC and (b) AC directions.

5.3.3 Finite Element Modelling

The experimental stress-strain curve was fitted to determine the material constants for the ODGEN HYPERFOAM model for the hydrated 100%collagen scaffolds, as shown in Fig 5.5. Due to the lack of the experimental data for the 50%collagen-50%elastin scaffolds and the 90%collagen-10%C4S scaffolds, the stress-strain curves for these two types of scaffolds were estimated based on the stress-strain curve of the 100%collagen scaffold and the $E_{bend.wet}$ values. The stress data of the 100%collagen scaffold were multiplied by $\frac{E_{bend.wet}(50\%collagen-50\%elastin)}{E_{bend.wet}(100\%collagen)}$ and $\frac{E_{bend.wet}(90\%collagen-10\%C4S)}{E_{bend.wet}(100\%collagen)}$, and were plotted against the correspondent strain data to produce the estimated stress-strain curves for 50%collagen-50%elastin scaffolds and 90%collagen-10%C4S scaffolds, respectively. These estimated stress-strain curves were then fitted to determine the material constants for the models of the respective scaffolds. The resultant constants for the models of all three types of scaffolds are listed in Table 5.5, and using these models, the simulated self-deflection tests with load values same to experimental situations give load-deflection curves shown in Fig 5.6. For the model of the 100%collagen scaffolds, which was derived from experimental data, the simulated self-deflection test produces a final deflection that is 0.25mm different from the real situation. For the models of the 50%collagen-50%elastin scaffolds and the 90%collagen-10%C4S scaffolds, which were generated with estimation, the differences between the deflections in simulated and real tests are 0.27mm and 0.10mm respectively, comparable to that of the 100%collagen scaffolds. This indicates that the estimation for the models of 50%collagen-50%elastin scaffolds and 90%collagen-10%C4S scaffolds has been reasonable, and that these models could be applied together to the simulation of the self-deflection test of the tri-layer scaffolds.

Table 5.5 Summary of material constants of the ODGEN HYPERFOAM models for the hydrated scaffolds.

	100%collagen	50%collagen-50%elastin	90%collagen-10%C4S
μ	19.85	9.98	17.89
α	43.16	41.26	41.58
β	0.034187	0.034276	0.034627

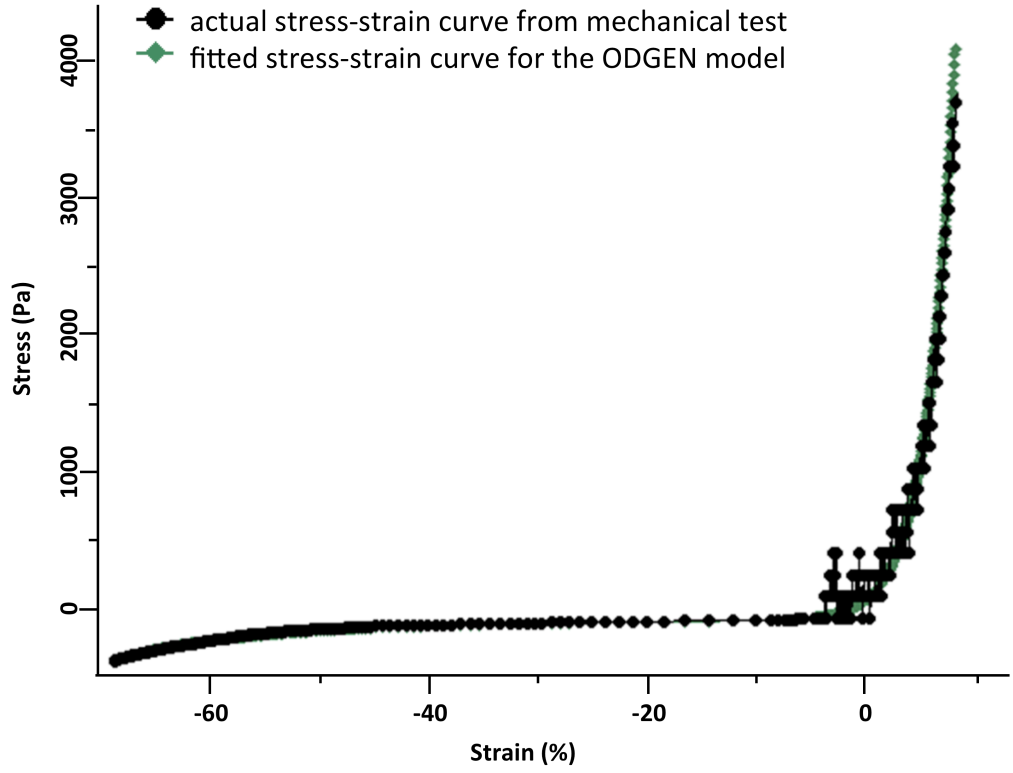


Fig 5.5 Fitted stress-strain curve of the ODGEN HYPERFOAM model for hydrated 1%wt/v 100%collagen scaffold.

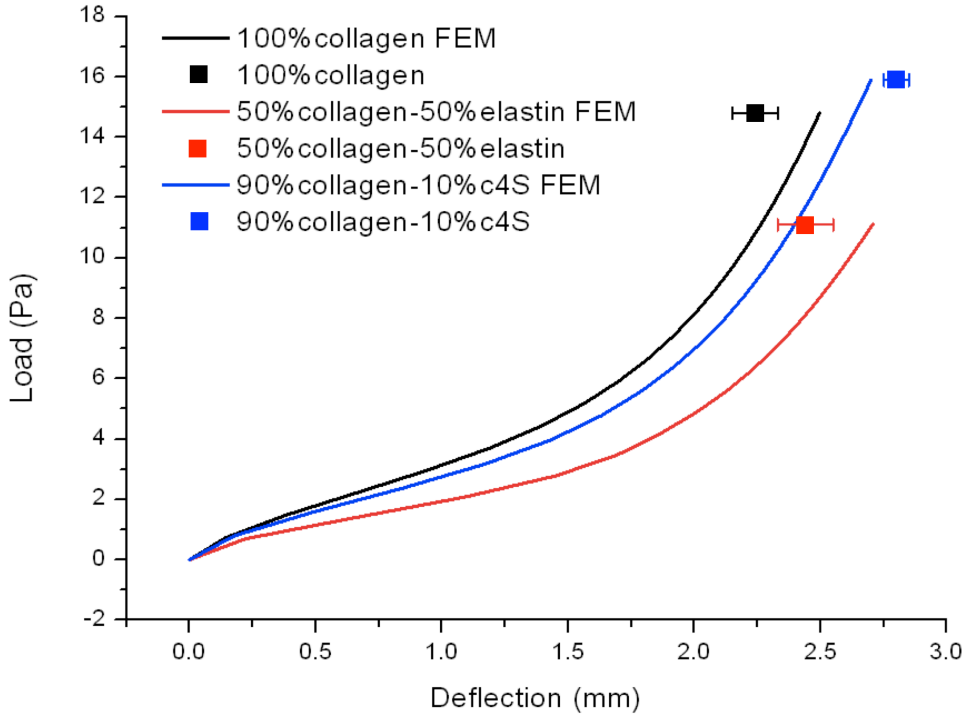


Fig 5.6 Load-deflection curves of simulated self-deflection tests on hydrated uniform-composition scaffolds. The end points of actual self-deflection tests on the scaffolds are also labeled.

The tri-layer scaffold model saw a deflection of 3.09mm in WC direction vs 2.75mm in AC direction in the simulated self-deflection tests (see Fig 5.7). Stress analysis found that, for the longitudinal (X-direction) component, again a larger volume was needed to accommodate the tensile stress when the scaffold was bent in the WC direction (see Fig 5.7), in agreement with the results in Fig 4.12. For the transverse (Y-direction) component, it could be seen that in the WC and AC direction, the scaffolds had relative similar distribution of the compressive stress in most of the volume, within the range of 0~25 Pa (see Fig 5.8).

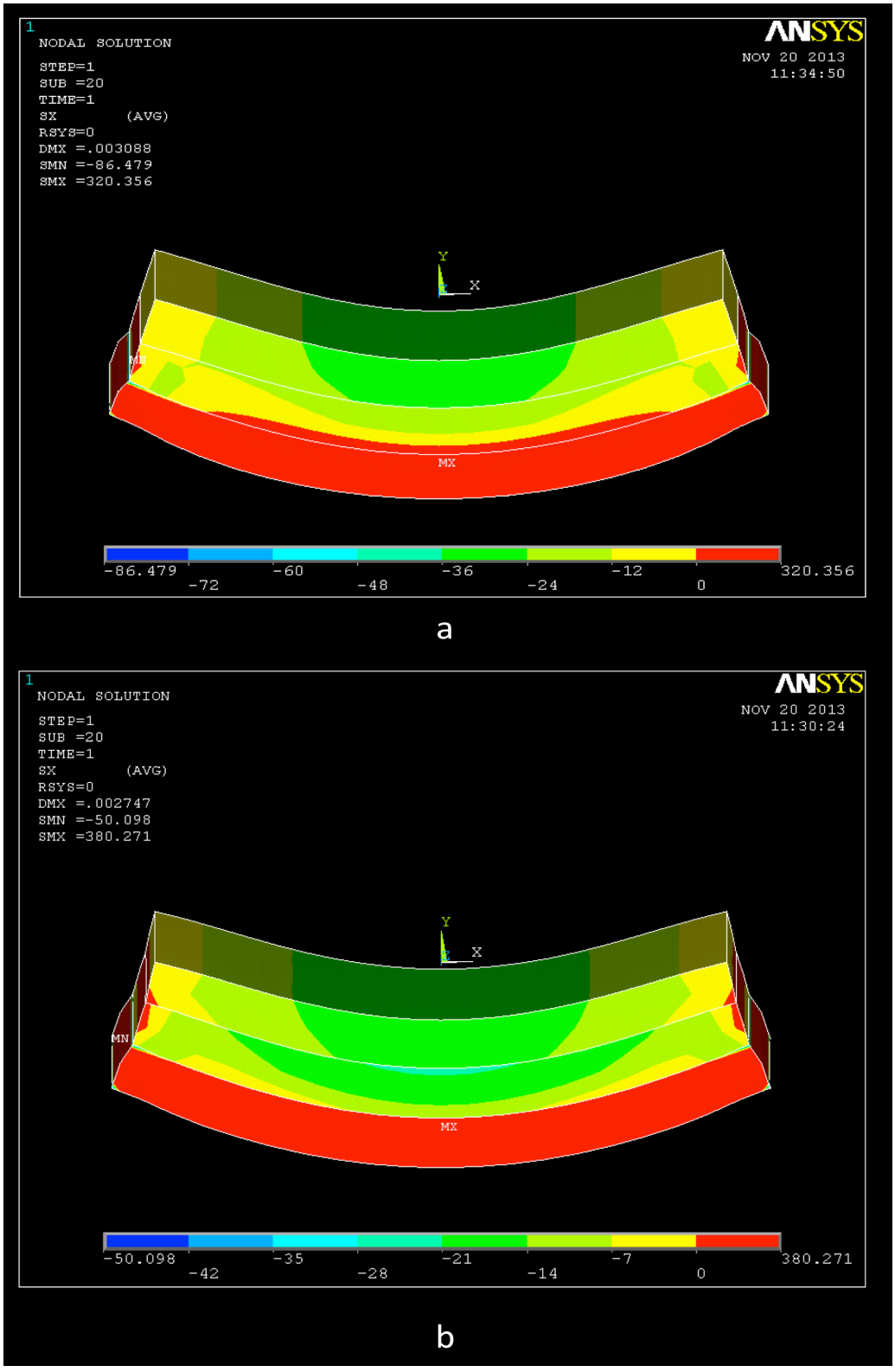


Fig 5.7 Contour plots of the longitudinal (X-direction) component of stress in the model of hydrated 100%collagen/90%collagen-10%C4S/50%collagen-50%elastin scaffold self-deflected in (a) WC direction, and (b) AC direction.

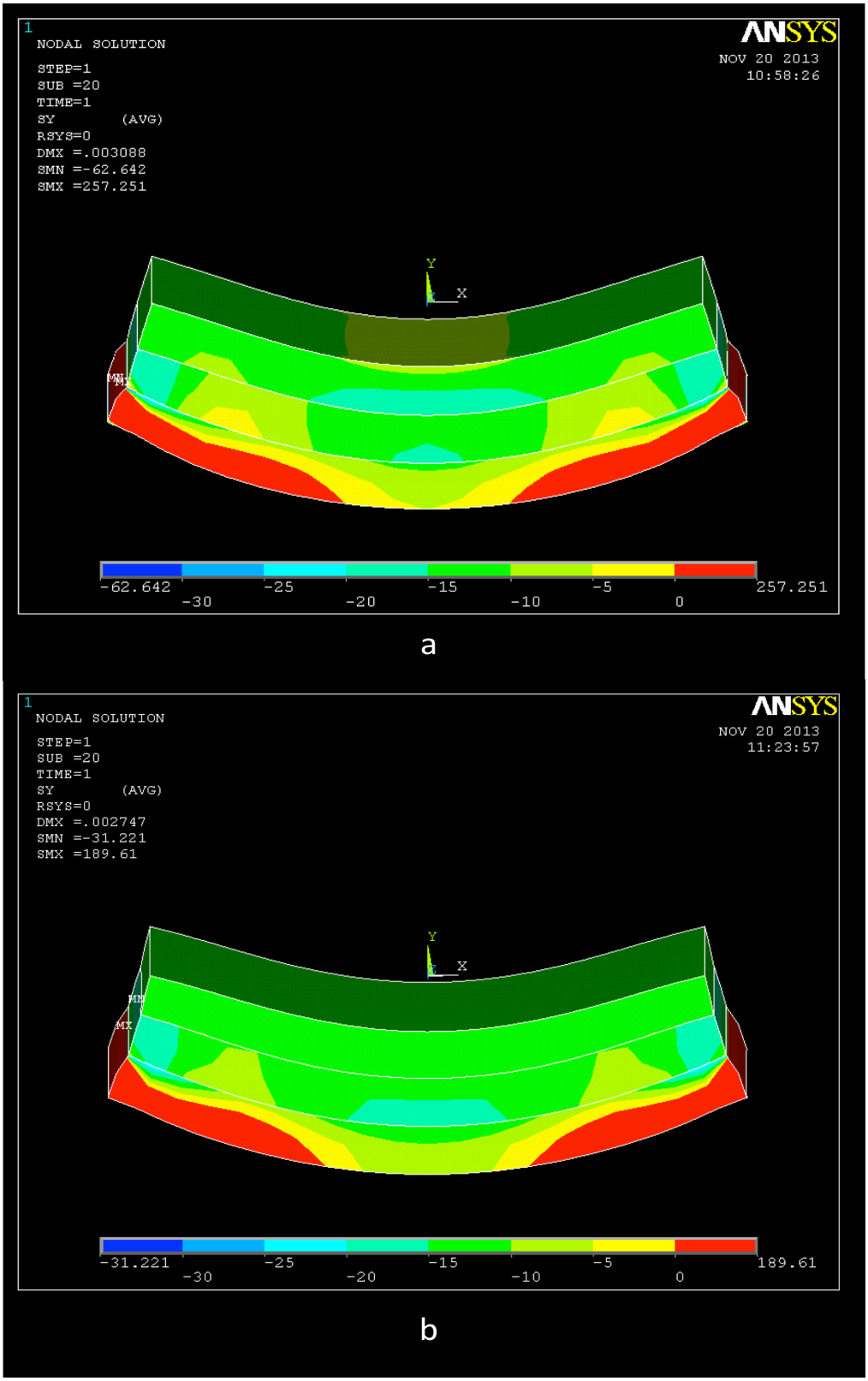


Fig 5.8 Contour plots of the transverse (Y-direction) component of stress in the model of hydrated 100%collagen/90%collagen-10%C4S/50%collagen-50%elastin scaffold self-deflected in (a) WC direction, and (b) AC direction.

5.4 Discussion

The collagen-elastin scaffolds have lower water uptake ratios than the collagen scaffolds probably because of elastin having a larger hydrophobicity than collagen [269]. As is the case in collagen, elastin has glycine accounting for one third of the amino acid residues, and contains a large amount of proline, both of which are hydrophobic amino acid residues. However, elastin has more other hydrophobic amino acid residues such as alanine and valine, which, together with glycine and proline, account for 75% of the residues in elastin [59]. In comparison, apart from glycine and proline, many hydrophilic residues are present in collagen, such as hydroxyproline, glutamic acid, and arginine. Moreover, the few hydrophilic amino acid residues in elastin, for example lysine, are likely to have participated in the forming of crosslinks and therefore are reduced in the water-binding abilities [61, 270].

C4S, on the contrary, is known to increase the water retention in tissues [68], and has demonstrated this ability in the 90%collagen-10%C4S scaffold. The water uptake ratio for the 50%collagen-50%C4S scaffolds, however, is lower than that of 100%collagen scaffolds. This could possibly be explained by the elution of the C4S from the scaffolds to the water. Yannas suggested that in collagen-glycosaminoglycan scaffolds, only around 10% glycosaminoglycan (on the basis of the dry mass of the scaffold) could be grafted onto the collagen [196]. Therefore, here in the 50%collagen-50%C4S scaffolds, a large portion of C4S was suspected to have dissolved in the PBS, leaving the effective masses of the scaffolds much smaller. The water uptake ratio in Table 5.1 calculated using the original dry mass of the scaffold hence has underestimated the ability of hydration of the 50%collagen-50%C4S scaffolds. Preliminary test was conducted, and was able to provide supportive evidence for this explanation: the hydrated 50%collagen-50%C4S scaffolds were aired dry again and their new mass values were

found considerably smaller than their original dry mass values (data not shown). However, other mechanisms might also have been the causes of the mass loss in the scaffolds, such as degradation of collagen in PBS (although very unlikely in such short time). Therefore, for future investigation, quantification of the C4S that dissolves in the PBS is suggested, with more conclusive measurements such as the dimethylmethylene blue (DMB) assay, in which the dimethylmethylene blue can bind to sulphated GAGs (such as C4S) and change its absorption intensity at 525nm, hence providing an accurate way of quantifying GAGs [271, 272].

When bound to the scaffold materials, the water molecules are likely to act as a lubricant between the protein fibres and therefore facilitate them to slide over each other, resulting in the reduced stiffness in the hydrated scaffolds [273, 274]. Despite that, the scaffolds are able to maintain their porous structures when hydrated and still exhibit the characteristic deformation stages of elastomers [151] (see Fig 5.2).

The hydrated scaffolds, when out of the aqueous solution, show a certain amount of shrinkage (see Table 5.3) probably due to the surface tension of the water. The higher hydrophobicity of elastin hence leads to less shrinkage (i.e. larger thickness) on the 50%collagen-50%elastin scaffolds. In the dry status, the 50%collagen-50%elastin scaffolds have similar effective bending modulus to the 90%collagen-10%C4S scaffolds (see Table 4.2 and Table 4.3), while in hydrated status the $E_{bend.wet}$ of the 50%collagen-50%elastin scaffolds is lower (see Table 5.3). This could also be attributed to the larger thickness of the 50%collagen-50%elastin scaffolds.

The self-deflection tests and the finite element modelling on the hydrated tri-layer scaffolds further demonstrate the feasibility of achieving the desirable bending anisotropy by introducing a layered structure to the scaffold. However, neither the

effective bending modulus (around 2kPa) nor the circumferential stress (around 350Pa) is matching those of native heart valves (approx. 500kPa and approx. 200kPa respectively [31, 255]). This issue may partially be addressed when seeding cells onto the scaffolds (which improves the stiffness by several times [157]). It is likely that other means such as crosslinking and structure hierarchy will need to be applied to the scaffolds to achieve more sufficient mechanical properties [142, 157].

It is interesting to find that the tri-layer scaffold also exhibits a different thickness in different bending directions (see Table 5.4). Fig 5.8 reveals that, a large part of the space in the scaffold has the same level of transverse compressive stress for both WC and AC bending directions. Since the collagen layer has a higher compressive modulus than the collagen-elastin layer, it is compressed less when in WC direction than the collagen-elastin layer is in AC direction, hence giving a larger thickness of the scaffold in WC direction. Moreover, from Fig 5.7 and 5.8 we can also find that, while the collagen layer and the collagen-elastin layer (corresponding to the fibrosa and ventricularis in the native valve) are contributing to the bending anisotropy mainly with their different behaviour in tension, the majority of the collagen-C4S layer is in compression in both bending directions and along both X and Y axes. This well correlates with one of the major functions of the spongiosa in the native heart valve: to resist compression and act as a shock absorber [275, 276].

The self-reflection test designed in this chapter was limited in accuracy due to the home-made clamping and imaging system. More importantly, the nature of the ‘one-step’ loading (only the load and deflection data of the end point were available) made it difficult to compare the bending behaviour of the hydrated scaffolds to the dry scaffolds or the finite element models. However, the self-deflection tests were able to give the general trend in the mechanical properties of the hydrated uniform-composition

scaffolds, and to justify using the finite element models (especially the ones generated with estimation) for the layers in the tri-layer scaffolds. Most importantly, it successfully demonstrated the bending anisotropy in the hydrated tri-layer scaffolds.

5.5 Conclusions

The hydrated collagen scaffolds were able to retain water of over 30 times of the scaffolds' dry mass. The elastin incorporated in the scaffolds reduced the water uptake ratio because of its higher hydrophobicity, which also resulted in less surface-tension-caused volume shrinkage of the scaffolds. The hydrophilic C4S was able to improve the water uptake ratio of the scaffolds, on the basis that the increase of the C4S volume fraction in the scaffolds did not jeopardize their effective masses.

The hydrated scaffolds still exhibited elastomeric behaviour, but with much lower tensile and compressive moduli due to the lubricating effects from water. The layered scaffolds also preserved the bending anisotropy in the hydrated status, which validated the findings in the dry scaffolds. The FEM results further proved that each layer in the scaffold had the mechanical function that was in line with the correspondent layer in the native heart valve. The low effective bending modulus, however, called upon future investigation on providing the TEHVs with matching stiffness values to the native ones.

Chapter 6. Cell Behaviour on Scaffolds

6.1 Introduction

A successful tissue engineered heart valve (TEHV) needs to maintain viability both in vitro and in vivo, which is essentially provided and regulated by the cells. Ideally, the cells for TEHVs should be easily obtainable, highly expandable, non-immunogenic, and should have good regenerative capacity [277, 278].

As mentioned in 2.3.2, the two categories of candidate cell sources for TEHVs are the cardiovascular-derived cells and the stem cells, due to either high cardiac tissue commitment, or easy availability and potential of differentiation [165]. A relatively newly discovered cardiac stem cell, cardosphere-drived cells (CDCs) [279], may potentially enjoy the combined advantages of both categories of cells.

Researchers have found that, in adult mammalian heart which was considered to be a postmitotic organ without regenerative capacity, there actually resides cardiac stem cells (mostly in myocardium but can migrate to other regions if needed) [279-282]. These stem cells can be directly grown from adult heart tissues in primary culture, as cardiospheres or their progeny (i.e. CDCs). Percutaneous endomyocardial biopsies are the usual convenient and minimally invasive tissue source for autologous CDCs [283, 284].

The CDCs have been shown to be able to differentiate into all three major cardiac lineages (myocytes, smooth muscle cells, and endothelial cells) [285], with even higher differentiation capability than mesenchymal stem cells [286]. In addition, they have neither the ethical concerns of embryonic stem cells nor the complication of viral gene transfection in induced pluripotent stem cells [287]. Therapeutic efficacy of CDCs in

improving cardiac function has been established in animal models [288, 289], and a clinical trial is currently on-going [283], which all have demonstrated the tissue regenerative capabilities of the CDCs.

This chapter, therefore, chooses CDCs to be the cell source for this thesis, investigates the behaviour (attachment, proliferation, and migration) of the CDCs on the scaffolds, and assesses the biocompatibility of the scaffolds, as well as the effects from the scaffold compositions and the crosslinking conditions.

6.2 Materials and Methods

6.2.1 CDCs Harvest and Isolation

CDCs were isolated from adult Sprague Dawley rats (Harlan Laboratories, UK) and expanded, in accordance with published protocols [289-291]. Firstly, the rat was killed by lethal injection of Euthatal® solution (Merial Animal Health Ltd, UK), and the heart was explanted, washed with Dulbecco's phosphate buffered saline (DPBS; Sigma-Aldrich Ltd, UK), and minced into small explants pieces in 0.05% trypsin-EDTA (Life Technologies Ltd, UK). Explants were then plated onto fibronectin (Sigma-Aldrich Ltd, UK)-coated 60mm petri dishes (Fisher Scientific Ltd, UK) with 1.5 ml of complete explant medium (CEM), comprising Iscove's modified Dulbecco's medium (IMDM; Life Technologies Ltd, UK) supplemented with 20% fetal bovine serum (FBS; Life Technologies Ltd, UK), 1 U/ml penicillin (Life Technologies Ltd, UK), 1 ug/ml streptomycin (Life Technologies Ltd, UK) and 0.2 mM L-glutamine (Life Technologies Ltd, UK), and incubated in a standard tissue culture incubator (BINDER GmbH, Germany) at 37˚C with 5% CO_2. After approximately a week, small, round, phase

bright cells grew out from the explants. Upon reaching 80–90% confluency, these explant-derived cells (EDCs) were isolated using trypsin (Life Technologies Ltd, UK) and re-plated in poly-d-lysine (Sigma-Aldrich Ltd, UK)-coated 24-well plates (Corning Inc, USA) in cardiosphere growth medium (CGM) comprising 65% Dulbecco's modified eagle medium F12 (DMEM-F12; Life Technologies Ltd, UK), 28% IMDM, and 7% FBS, to which the following growth factors were added: 2% B-27® (Life Technologies Ltd, UK), 25 ng/ml cardiotrophin (Peprotech EC Ltd, UK), 10 ng/ml epidermal growth factor (EGF; Peprotech EC, UK), 20 ng/ml basic fibroblast growth factor (FGF; Promega, UK) and 5 units thrombin (Sigma-Aldrich Ltd, UK). Cardiospheres formed after 2–3 days, at which time they were harvested by mechanical trituration and were plated in CEM in fibronectin-coated flasks to culture for cardiosphere-derived cells (CDCs). EDCs could be harvested from the explants for multiple times, in the experiments of this thesis second and third harvest cells were used at passages three to five.

6.2.2 Culture of CDCs on scaffolds

For the culture of CDCs on scaffolds with uniform compositions, disc-shaped scaffolds (1.5 mm in thickness and 12.5mm in diameter) were used (see Fig 3.4 right).

For layered scaffolds, the original 40×12×5 mm^3 scaffolds (see Fig 3.4 left) were sectioned into 1.5×12×5 mm^3 pieces (see Fig 6.1) for the cell culture. This way of seeding enables the cells to attach on all the layers at the same time, rather than having to migrate from one layer to another, and therefore eliminates the effects of the depth limitation of cell migration, and assesses more independently the responses of cells to different compositions on the layered scaffolds. Also, this seeding method eases the demand of a large number of cells to seed the scaffolds with the original layer sizes.

Before cell seeding, the scaffolds (n=6) were sterilized by washing them three times, for 30 minutes each, with 100% ethanol and three times with DPBS. Then, they were placed in CEM. CDCs were harvested using trypsin, counted on a hemocytometer (Laboroptik GmbH, Germany) and diluted to 250,000 cells/ml. The scaffolds were placed in fibronectin-coated 24-well plates and cells were seeded by pipetting 200µL of the diluted cell suspension on top of the scaffold (50,000 cells per scaffold). The cells were cultured for 7 days at 37˚C with 5% CO_2. After the initial four hours of incubation each well was supplemented with 800µL more of CEM medium (to reach 1ml of medium per well), and a total medium change was carried out every 48 hours.

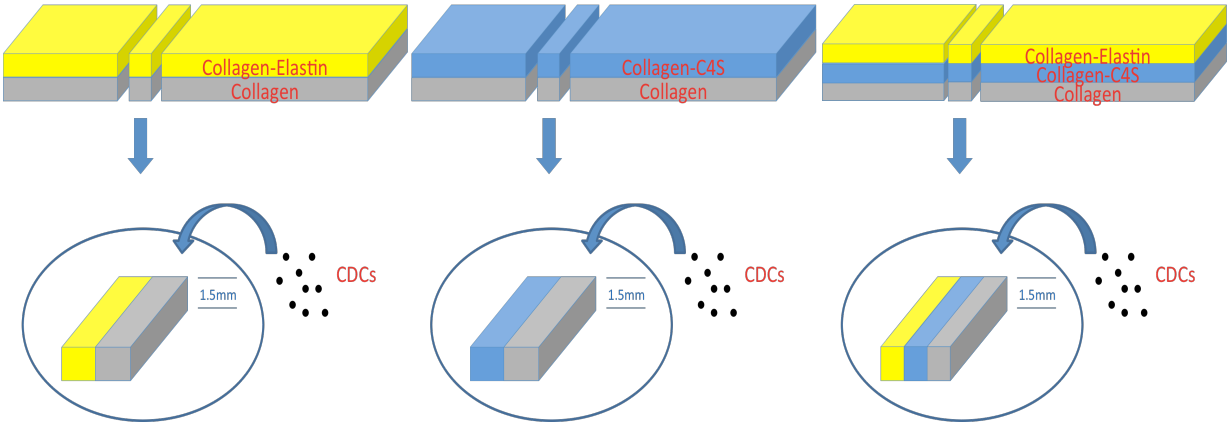


Fig 6.1 Schematic graph of seeding CDCs onto the layered scaffolds. The bi-layer and tri-layer scaffolds are sectioned and seeded in the same approach.

6.2.3 Assessment of CDCs Attachment and Proliferation

The attachment and proliferation of the CDCs was assessed with the alamarBlue® assay (AbD Serotec, UK). AlamarBlue® is an indicator dye that fluoresces in response to the oxidation-reduction (REDOX) reactions in the growth medium. The amount of fluorescence corresponds to the metabolic activity of the cells and is proportional to the cell number [292].

Cell attachment was quantified on day 1 (20 hours after seeding), and cell proliferation was measured on days 1, 4 and 7. On day 1, the scaffolds were first transferred into new 24-well plates and washed with DPBS (for 2×5 minutes). The culture medium in the old 24-well plates was removed, and the plates were also washed with DPBS (for 2×5 minutes). Fresh CEM supplemented with 10% alamarBlue® was then added to both the old and new 24-well plates (1ml per well) and was incubated for three hours, in order to measure the number of cells attached on the scaffolds and left in the old plates respectively. On day 4 and 7, only the new plates containing scaffolds were incubated with the CEM-alamarBlue® solution. After the incubation the supernatant was transferred into μClear black plates with a clear bottom (Greiner bio-one Ltd, UK). Fluorescence was measured using a FLUOstar Optima plate reader (BMG Labtech Ltd, UK) at 544/590 nm excitation/emission wavelengths.

The percentage of alamarBlue® reduction, which represented the amount of the cells in the particular well, was calculated as the following:

$$\%alamarBlue\ Reduction = \frac{FI(Measured\ Well) - FI(Control)}{FI(Max) - FI(Control)} \times 100\% \qquad \text{Eq 6.1}$$

where *FI* means the fluorescence intensity measured, *FI (Control)* was measured from the CEM-alamarBlue® solution that was incubated in empty wells, and *FI (Max)* was measured from the CEM-alamarBlue® solution that was autoclaved for 15 minutes (400/400V, Boxer Laboratory Equipment Ltd, UK), which was considered to have reached 100% reduction [292].

The cell attachment ratio was calculated as the ratio of the number of cells on the scaffolds to the total number of cells on day 1 [147]:

$$\%Attachment = \frac{\%\ alamarBlue\ reduction\ (scaffold)}{\%\ alamarBlue\ reduction\ (scaffold) + \%\ alamarBlue\ reduction\ (well)} \times 100\% \qquad \text{Eq 6.2}$$

All data were reported as means, with the standard deviations as the errors. One-way analysis of variance (ANOVA) followed by Tukey's test was used to compare groups of data, with a probability value of 95% ($p < 0.05$) to determine statistical significance.

6.2.4 Scanning Electronic Microscopy (SEM)

Cell morphologies were characterized using scanning electron microscopy (SEM) JSM840F (JEOL Ltd, Japan) at an accelerating voltage of 4kV. Scaffolds seeded with cells were fixed at day 7 in 4% paraformaldehyde (PFA; Sigma-Aldrich Ltd, UK) overnight at 4˚C. Samples were then dehydrated through exposure to a gradient of alcohol (30%, 50%, 70%, 90% and 100%) followed by hexamethydisilazane (HMDS; Sigma–Aldrich Ltd, UK), and were air-dried [147]. All specimens were coated with 3nm thick platinum by a 208HR sputter coater (Cressington Scientific Instruments Ltd, UK) before observation.

6.2.5 Multi-photon Microscopy (MPM)

Multi-photon microscopy (MPM) is a non-invasive method of fluorescence imaging, most suitable for biological samples [293]. It employs the concept of multi-photon excitation, in which multiple low-energy photons can arrive ‘simultaneously’ at a fluorophore and excite a single high-energy photon [294]. This excitation event limits the fluorescence to the sub-micron-sized beam focus. Therefore, no background noise from the out-of-focus area will be produced, and the signals, even when scattered in the sample, can be all collected and utilized because they are from the same origin [294]. This provides MPM a higher resolution and a larger penetration depth than the conventional confocal microscopy. Moreover, as biological samples may contain many types of endogenous fluorophores such as flavin, lipofuscin, porphyrins, collagen, and elastin [295], they could be imaged simultaneously by MPM without staining. This

thesis used MPM to characterize the distribution of cells on the scaffolds, as well as the distribution of the scaffold materials.

The collagen and elastin are both auto-fluorescent, by second-harmonic generation (SHG) and two-photon excitation (TPE), respectively [296]. The cells were stained with rhodamine phalloidin (Life Technologies Ltd, UK) to be fluorescent. Briefly, scaffolds seeded with cells were fixed on day 7 in 4% PFA for 1 hour, and were permeablised in 0.1% Triton X-100 (Rohm & Haas, USA) in DPBS for 30 minutes. Then the scaffolds were incubated in the blocking buffer (1ml per scaffold) comprising 2% bovine serum albumin (BSA; Sigma–Aldrich Ltd, UK) and 2% fetal bovine serum (FBS) in DPBS for 1 hour. Finally the scaffolds were incubated in the blocking buffer (0.5mL per scaffold) containing 2.5% rhodamine phalloidin for 40 minutes for staining. The scaffolds were washed twice with DPBS and kept at 4˚C until MPM imaging.

The MPM images were generated using a modified BioRad Radiance 2100 MP Multiphoton Microscope (Zeiss, Germany). Near infrared (NIR) laser excitation beams (wavelength = 800 nm) were obtained from a tunable 76 MHz femtosecond pulsed Ti:sapphire laser (Mira 900-F, Coherent Ltd, UK) pumped by a 10 W multiline argon ion laser (Verdi, Coherent Ltd, UK) [297]. The signals from collagen, elastin and cells were collected with 390nm, 525nm, and 595nm band-pass filters respectively, and were shown blue, green and red respectively on the images [297].

For each image, a Z stack was taken, from the surface of the scaffold to the deepest level where signals from cells could be detected, with a step size of 2.55μm for each slide. The frame size of the slides was $316\times252\mu m^2$ for the images of the scaffolds with uniform compositions, and was $379\times303\mu m^2$ for the images of the layered scaffolds. The slide images of the Z stacks were then reconstructed by ImageJ (National Institutes

of Health, USA) into 2-D projections in the Z direction (see Fig 6.2a). For layered scaffolds, several 2-D projections were then connected by Panorama Tools (University of Applied Sciences Furtwangen, Germany) to form a panorama across the sample (see Fig 6.2b). The cell numbers on the images was counted by ImageJ and the cell densities were then calculated with the frame sizes and the depths of the Z stacks.

6.3 Results

6.3.1 CDCs Culture on Scaffolds

Fig 6.3 shows the CDCs attachment ratios on the scaffolds with uniform compositions. We can see that approximately 40% of the CDCs were able to attach to the scaffolds after the initial seeding, and the attachment ratios were similar on the all scaffolds, except for the 50% collagen-50% C4S scaffolds on which the attachment ratio was lower, being around 30%.

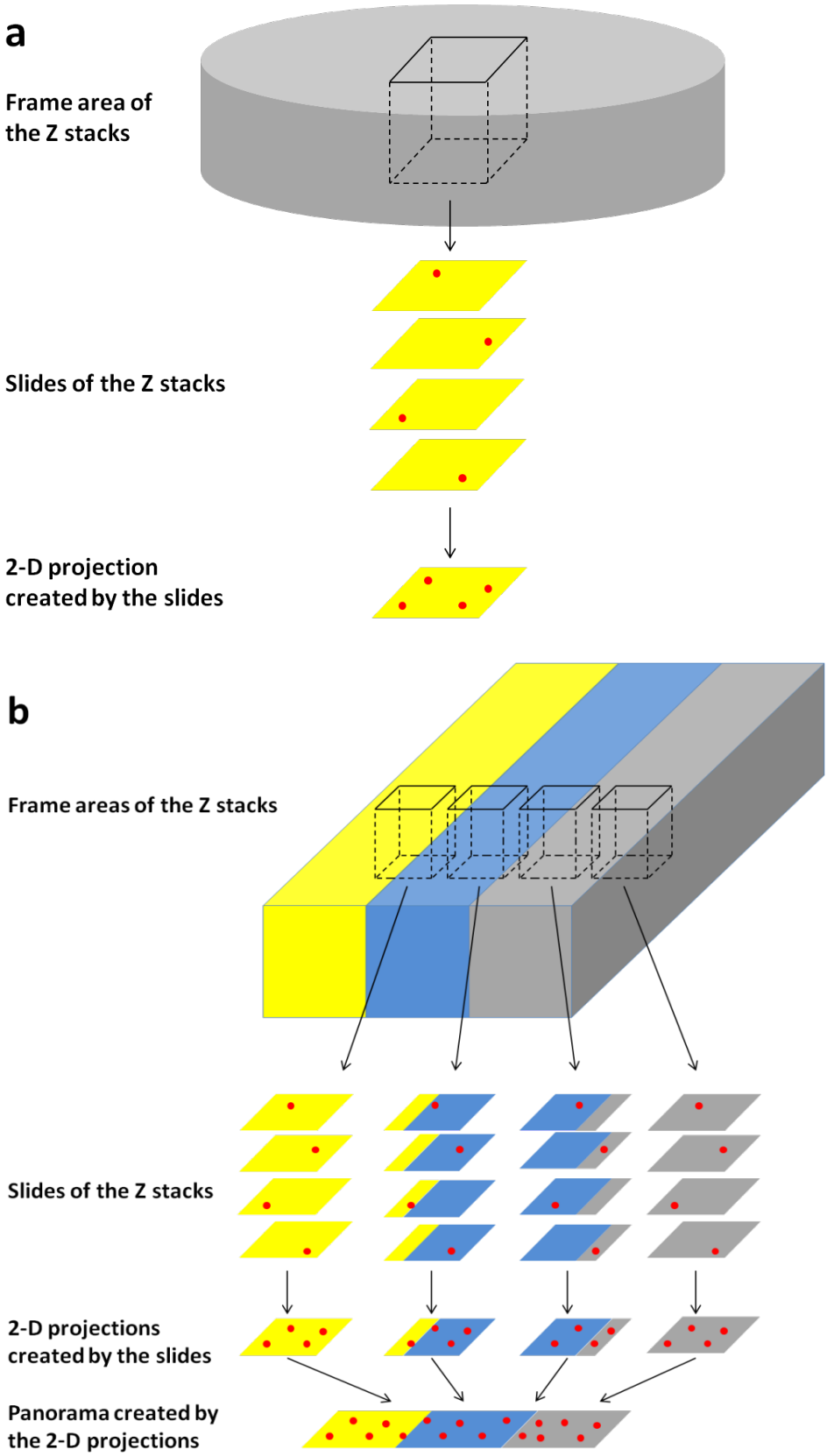


Fig 6.2 Schematic graphs of the procedure of taking MPM images for (a) uniform-composition scaffolds and (b) layered scaffolds.

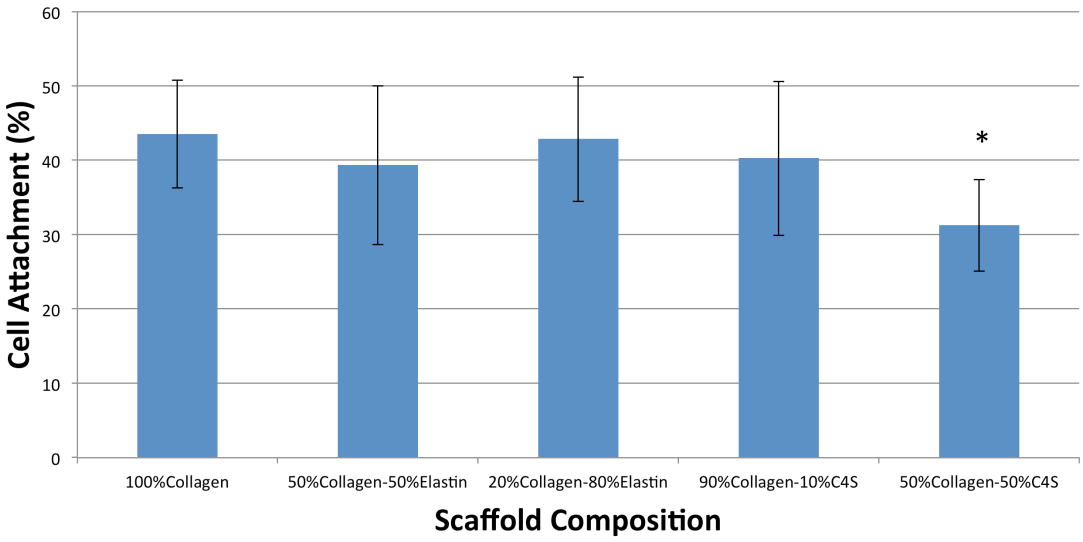
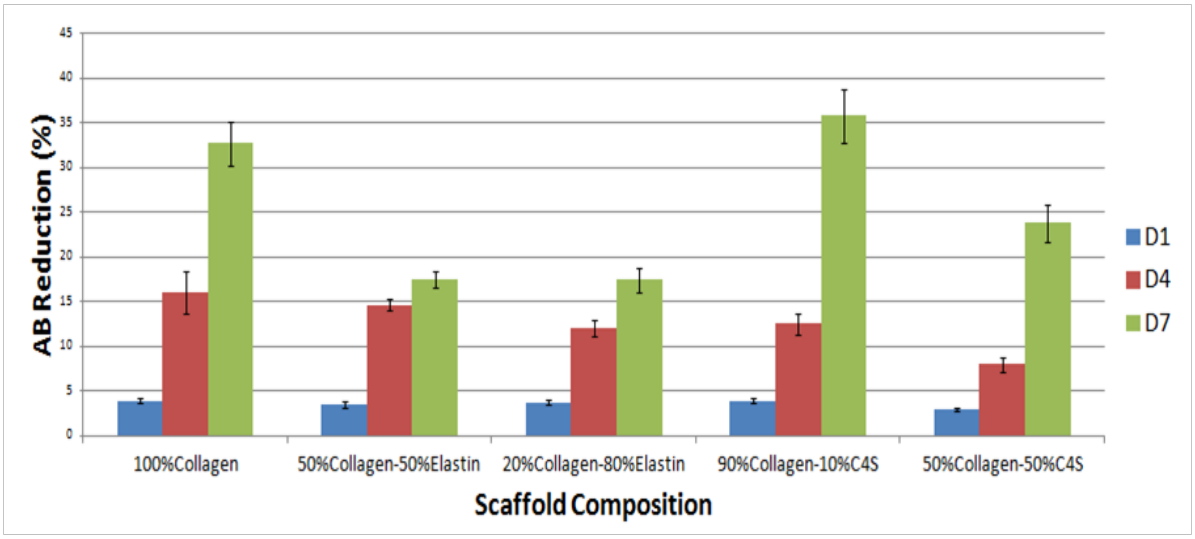


Fig 6.3 CDCs attachment ratios on scaffolds with uniform compositions. * denotes significant difference ($p<0.05$) amongst groups of different compositions.



For every group of scaffolds: D7 > D4 > D1

For D1: 100%Collagen = 50%Collagen-50%Elastin = 20%Collagen-80%Elastin = 90%Collagen-10%C4S > 50%Collagen-50%C4S

For D4: 100%Collagen = 50%Collagen-50%Elastin > 20%Collagen-80%Elastin = 90%Collagen-10%C4S > 50%Collagen-50%C4S

For D7: 90%Collagen-10%C4S > 100%Collagen > 50%Collagen-50%C4S > 50%Collagen-50%Elastin = 20%Collagen-80%Elastin

Fig 6.4 Proliferation of CDCs on scaffolds with uniform compositions from day 1 to day 7. Statistical differences between groups are reported after the figure. > denotes significantly greater value ($p<0.05$), and = denotes no statistically significant difference ($p>0.05$).

Table 6.1 Percentage of alamarBlue® reduction on D4 and D7 normalized to values on D1. Statistical differences between groups are reported after the table. > denotes significantly greater value ($p<0.05$), and = denotes no statistically significant difference ($p>0.05$).

Composition	D4/D1	D7/D1
100%Collagen	4.63±0.32	9.39±0.86
50%Collagen-50%Elastin	4.70±0.39	5.53±0.69
20%Collagen-80%Elastin	3.68±0.30	5.24±0.36
90%Collagen-10%C4S	3.64±0.15	10.29±0.63
50%Collagen-50%C4S	3.10±0.19	9.15±0.95

For D4/D1: 100%Collagen = 50%Collagen-50%Elastin > 20%Collagen-80%Elastin = 90%Collagen-10%C4S > 50%Collagen-50%C4S

For D7/D1: 90%Collagen-10%C4S > 100%Collagen = 50%Collagen-50%C4S > 50%Collagen-50%Elastin = 20%Collagen-80%Elastin

Fig 6.4 shows the results of alamarBlue® assays representing the proliferation of cells on the scaffolds at different culturing time points, and Table 6.1 shows the proliferation of cells in terms of fold changes.

On day 1 the percentage of alamarBlue® reduction was similar for all the scaffolds, as was also indicated by the attachment ratios in Fig 6.3. From the measurements of day 4 and day 7 we can see that CDCs proliferated significantly on all the scaffolds (> 3 folds on day 4 and >5 folds on day 7). However, it was found that the cell proliferation on the collagen-elastin scaffolds was less than that on the collagen scaffolds, especially between day 4 and day 7. In contrast, the cell proliferation was accelerated on the collagen-C4S scaffolds during the time course compared with collagen scaffolds.

After 7 days' culture, certain degree of volume shrinkage was also seen on the scaffolds, see Fig 6.5 and Table 6.2. It was found that the shrinkage was much more obvious on the collagen-elastin scaffolds than on the other scaffolds. Therefore this factor should

also be taken into account when interpreting the the results of alamarBlue® assays for the cell proliferation.

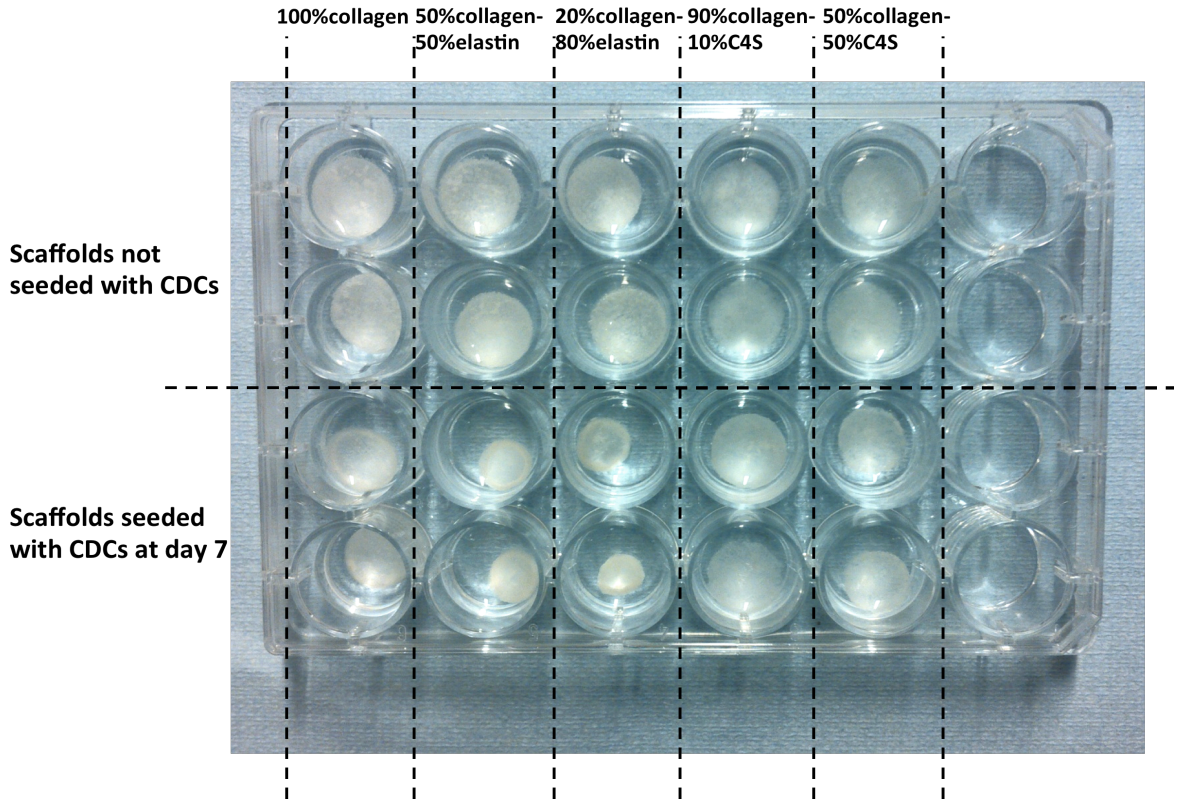


Fig 6.5 Picture of scaffolds before and after cell culture. The 50%collagen-50%elastin and 20%collagen-80%elastin scaffolds exhibited more shrinkage than the other scaffolds.

Table 6.2 Shrinkage of different scaffolds after cell culture (day 7), expressed as percentage of area reduction. Statistical differences between groups are reported after the table. > denotes significantly greater value ($p<0.05$), and = denotes no statistically significant difference ($p>0.05$).

Composition	Shrinkage (%)
100%Collagen	24.4±8.5
50%Collagen-50%Elastin	44.6±2.0
20%Collagen-80%Elastin	52.6±7.1
90%Collagen-10%C4S	5.9±2.9
50%Collagen-50%C4S	20.2±5.7

20%Collagen-80%Elastin = 50%Collagen-50%Elastin > 100%Collagen = 50%Collagen-50%C4S > 90%Collagen-10%C4S

6.3.2 SEM Imaging

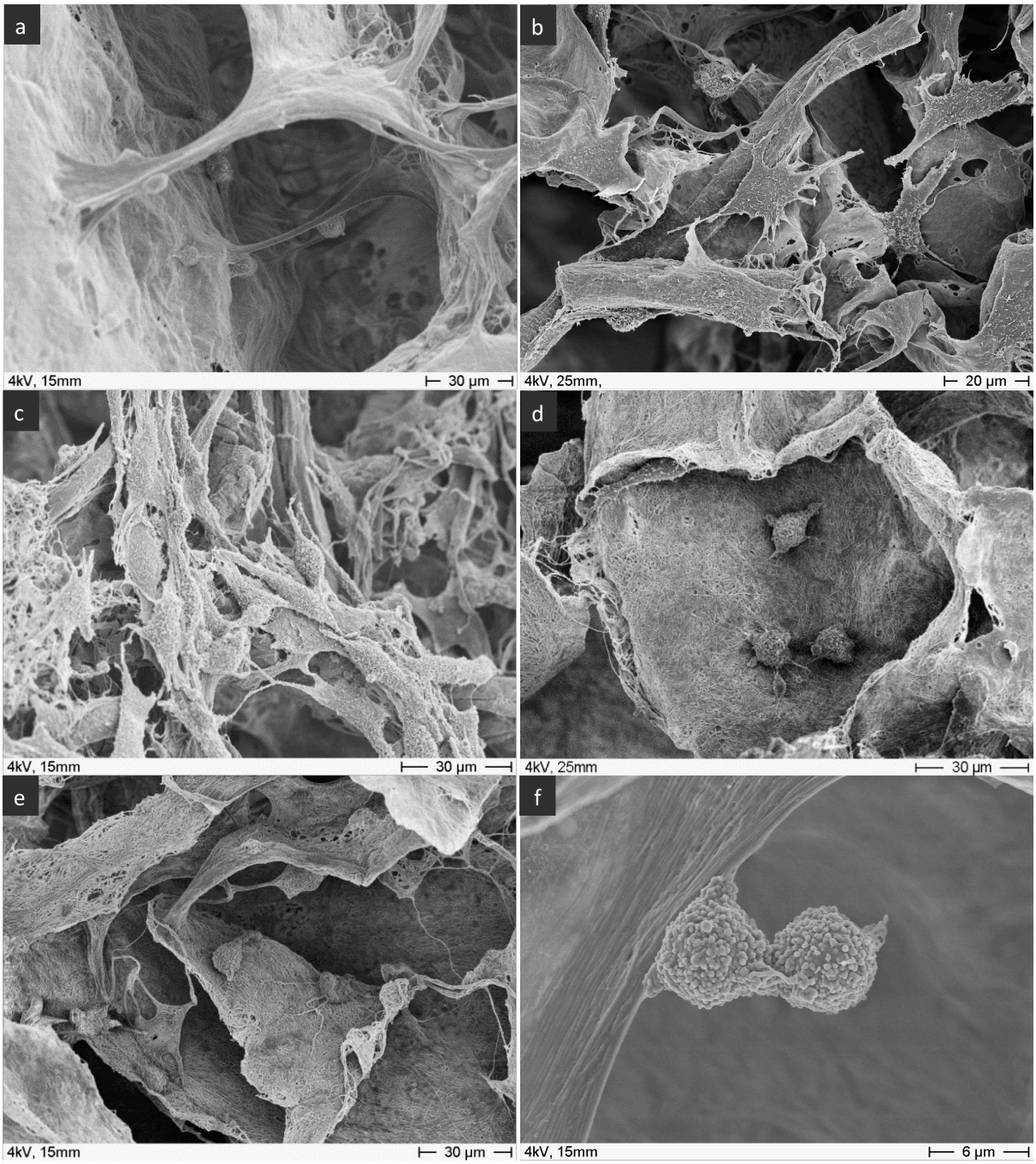


Fig 6.6 SEM micrographs of CDCs at day 7 on (a) 100%Collagen scaffold, (b) 50%Collagen-50%Elastin scaffold, (c) 20%Collagen-80%Elastin scaffold, (d) 90%Collagen-10%C4S scaffold, (e) 50%Collagen-50%C4S scaffold, and (f) 100%Collagen scaffold, at division stage.

Fig 6.6 presents representative SEM images of CDCs seeded on scaffolds of different compositions. CDCs can be seen to be proliferating on all the scaffolds (Fig 6.6 a-e), and direct evidence of cell division can be observed in Fig 6.6 f. The cells assume more rounded shapes on collagen and collagen-C4S scaffolds (Fig 6.6 a, d, e), and assume flatter or more elongated shapes on collagen-elastin scaffolds (Fig 6.6 b, c). Also, Fig 6.6 a, d, e suggest that CDCs are migrating down the interconnected pores that seem to act like miniature channels within the scaffolds for the collagen and collagen-C4S scaffolds. This is less evident for the collagen-elastin scaffolds (see Fig 6.6 b, c), where the cells seemed to remain nearer the surface. The SEM images support the findings from the alamarBlue® assays that cell proliferation occurs in all cases, and that increasing parts of the scaffold are colonized as time increases.

6.3.3 MPM Imaging

MPM imaging was conducted on 100%collagen, 20%collagen-80%elastin, and 90%collagen-10%C4S scaffolds. Fig 6.7 shows the representative images, and Table 6.3 shows the depths and volumes of the Z stacks for the images, and the cell numbers and cell densities in the given stacks. We can see that the stack depth is smaller on the 20%collagen-80%elastin scaffolds and is larger on the 90%collagen-10%C4S scaffolds, indicating lower and higher cell migration respectively. Also, while the cell density is similar on 100%collagen scaffolds and 90%collagen-10%C4S scaffolds, it is much greater on 20%collagen-80%elastin scaffolds.

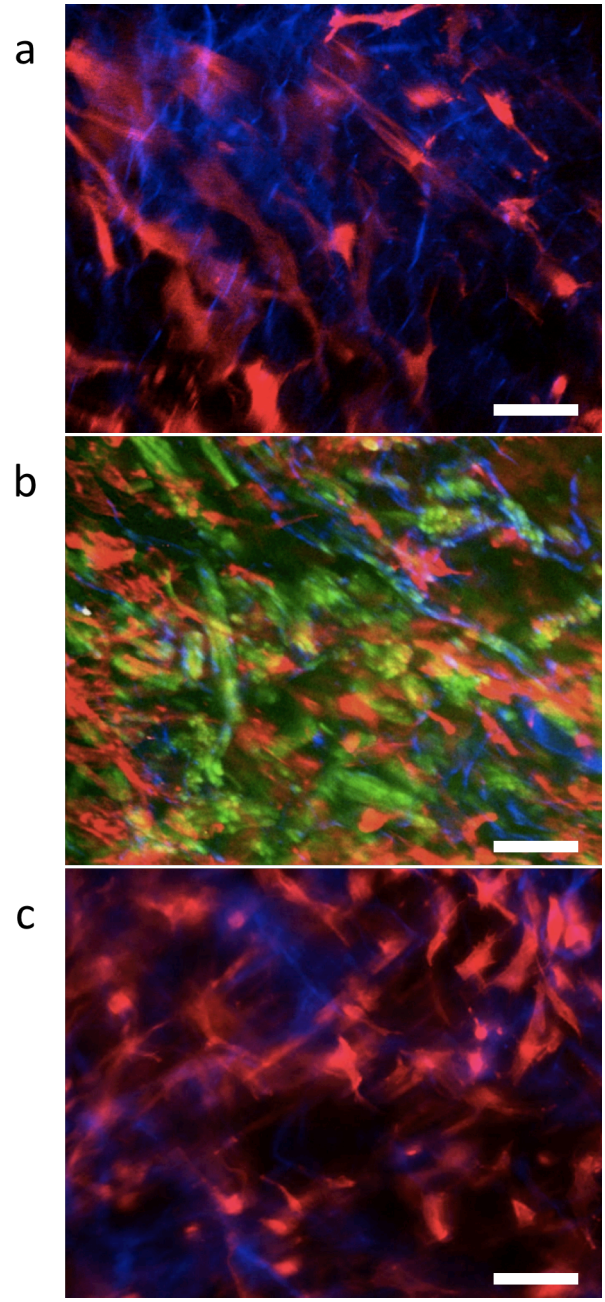


Fig 6.7 MPM micrographs of CDCs on (a) 100%Collagen scaffold, (b) 20%Collagen-80%Elastin scaffold, and (c) 90%Collagen-10%C4S scaffold. Collagen, elastin, and CDCs are shown in blue, green and red respectively. Scale bar is 50µm.

Table 6.3 Summary of information from the MPM micrographs of selected scaffolds with uniform compositions.

	100%Collagen	20%Collagen-80%Elastin	90%Collagen-10%C4S
Stack depth (mm)	0.445	0.169	0.620
Stack volume (mm^3)	0.0313	0.0135	0.0495
Cell number	45	114	69
Cell density (mm^{-3})	1438	8444	1393

For layered scaffolds, 100%collagen/20%collagen-80%elastin, 100%collagen/90%collagen-10%C4S, and 100%collagen/50%collagen-50%C4S/20%collagen-80%elastin scaffolds were selected for MPM imaging. Fig 6.8 and Table 6.4 demonstrate the cell distribution on the bi-layer scaffolds. It can be seen that, on both bi-layer scaffolds, similar values of the stack depth and the cell density are observed for the two layers. Comparing with the results from the scaffolds with uniform compositions, the 100%collagen/90%collagen-10%C4S scaffold shows a similar trend, i.e. cells having a slightly deeper migration and a slightly lower density on the 90%collagen-10%C4S layer. However, the 100%collagen/20%collagen-80%elastin scaffold shows a different cell distribution to that observed on the scaffolds with a uniform composition. The cells, when on the 20%collagen-80%elastin layer of the bi-layer scaffold, seem to have a better migration and a lower density than on the 20%collagen-80%elastin scaffolds. Moreover, the proportions of the layers in the panoramas indicate that the 20%collagen-80%elastin layer and the 90%collagen-10%C4S layer have had larger volume shrinkage than the collagen layers.

Fig 6.9 and Table 6.5 show the cell distribution on the tri-layer scaffold. The results are consistent with those on the bi-layer scaffolds: the cells distribute approximately evenly on different layers, with the collagen-C4S layer having a lightly larger stack depth and a slightly lower cell density. The proportion of each layer remained approximately equal on the panorama, indicating similar degrees of volume shrinkage after the cell culture.

Table 6.4 Summary of information from the MPM micrographs of bi-layer scaffolds.

	100%collagen/20%collagen-80%elastin		100%collagen/90%collagen-10%C4S	
	Collagen layer	Collagen-elastin layer	Collagen layer	Collagen-C4S layer
Stack depth (mm)	0.314	0.314	0.419	0.450
Stack volume (mm^3)	0.0362	0.0362	0.0481	0.0517
Cell number	121	131	160	144
Cell density (mm^{-3})	3342	3621	3327	2785

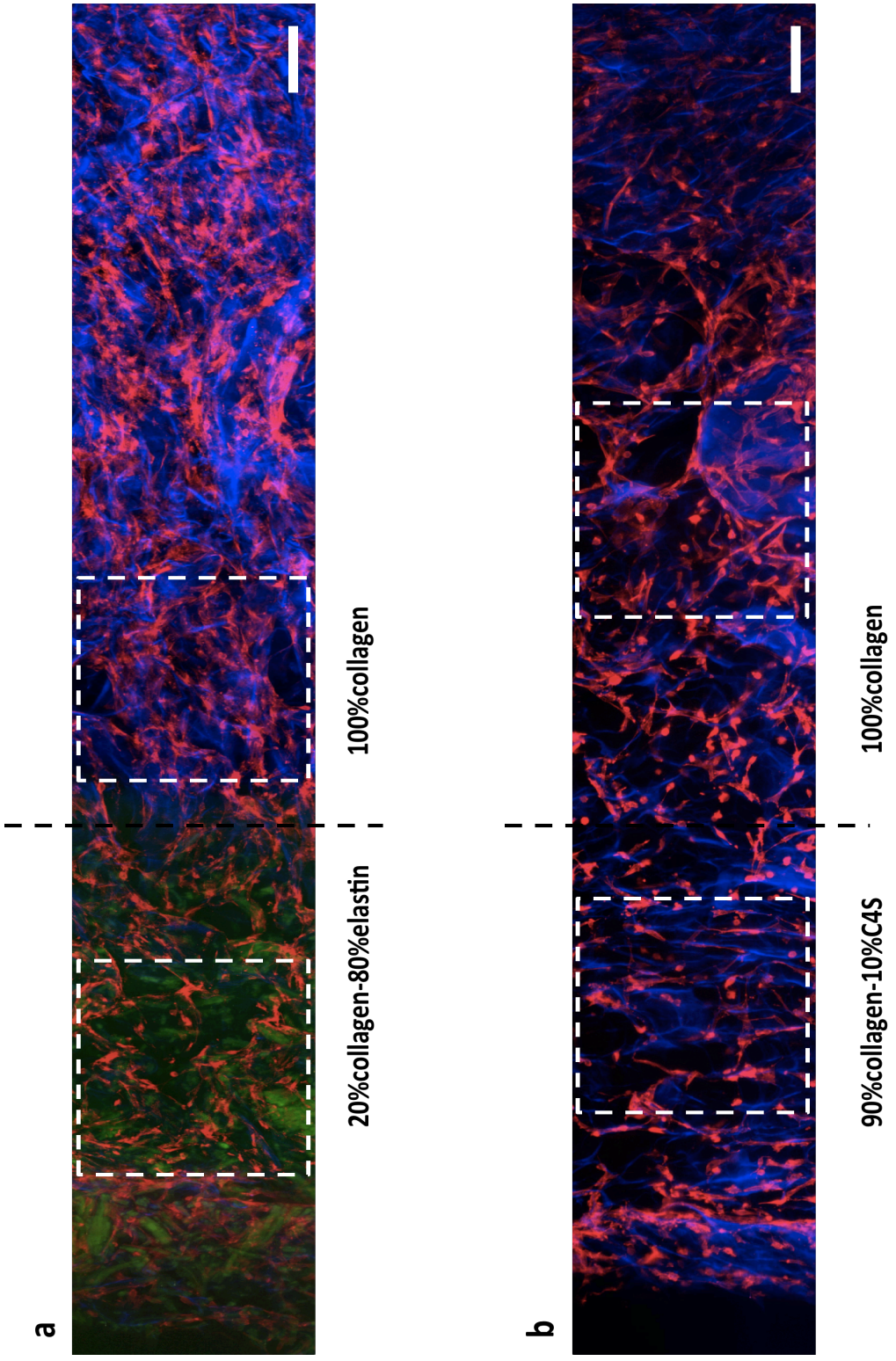


Fig 6.8 MPM micrograph panoramas of CDCs on (a) 100%collagen/20%collagen-80%elastin bi-layer scaffold, and (b) 100%collagen/90%collagen-10%C4S bi-layer scaffold. Scale bar is 100µm. The cell density on each layer was measured in the stack indicated by the dashed lines.

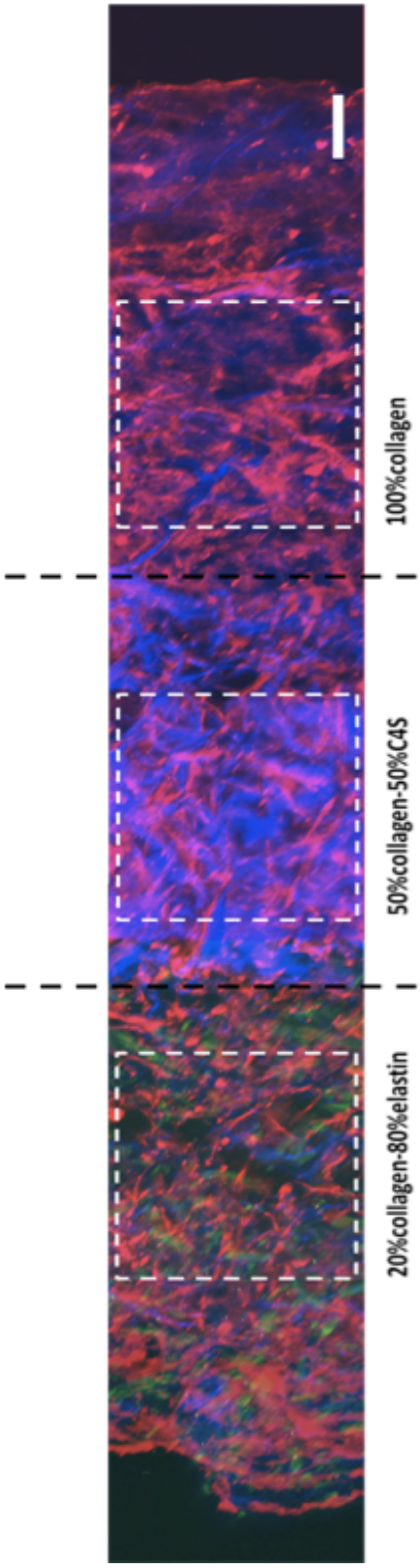


Fig 6.9 MPM micrograph panorama of CDCs on 100%collagen/50%collagen-50%C4S/20%collagen-80%elastin tri-layer scaffold. Scale bar is 100µm. The cell density on each layer was measured in the stack indicated by the dashed lines.

Table 6.5 Summary of information from the MPM micrograph of tri-layer scaffold.

	Collagen layer	Collagen-C4S layer	Collagen-elastin layer
Stack depth (mm)	0.337	0.405	0.315
Stack volume (mm^3)	0.0388	0.0465	0.0362
Cell number	150	152	134
Cell density (mm^{-3})	3869	3268	3704

6.3.4 Effects of Crosslinking

Table 6.6 Proliferation of CDCs on non-crosslinked and crosslinked scaffolds from day 1 to day 7, expressed as the percentage of alamarBlue® (AB) reduction. Significant cell proliferation ($p<0.05$) was found on every group of scaffolds at day 4 and day 7. * indicates statistically significant difference ($p<0.05$) amongst groups of different crosslinking methods at the same time point.

		Non-crosslinked			DHT			UV		
		D1	D4	D7	D1	D4	D7	D1	D4	D7
AB Reduc-tion (%)	100%Collagen	4.16± 0.47*	14.33± 1.76*	24.59± 1.58*	3.21± 0.77*	10.16± 2.83*	17.76± 4.54*	1.40± 0.29*	3.54± 0.98*	5.73± 1.27*
	50%Collagen-50%Elastin	3.67± 0.50*	8.02± 0.92	12.65± 1.95	3.11± 0.29*	7.61± 0.46	13.95± 1.23	1.31± 0.26*	2.35± 0.43*	3.51± 0.76*
	90%Collagen-10%C4S	4.24± 0.36	15.67± 0.94*	24.23± 1.38	3.19± 0.38*	11.08± 1.56*	17.59± 2.60*	3.95± 0.29	13.16± 1.18*	21.97± 2.59

Table 6.6 shows the proliferation of CDCs on non-crosslinked and crosslinked scaffolds in forms of alamarBlue® reduction. We can see that on collagen scaffolds, the DHT

treatment resulted in a CDCs proliferation which is approximately 70% of that on the non-crosslinked samples, while UV irradiation massively reduced the CDCs proliferation.

On collagen-elastin scaffolds, the similar effects of crosslinking were observed. The DHT-treated samples yielded slightly lower or similar CDCs proliferation compared with the non-crosslinked ones, and the UV treated scaffolds also had far less cell proliferation.

On collagen-C4S scaffolds, however, while the DHT-treated samples still exhibited around 70% CDCs proliferation of the non-crosslinked ones, the UV irradiated enjoyed a proliferation of CDCs that was only slightly lower than that on the non-crosslinked samples and higher than that on the DHT-treated samples.

One thing worth noticing in the experiment is that, although little shrinkage occurred during the crosslinking process on the dry scaffolds (see 3.3.3), the crosslinked scaffolds did undergo considerable extent of shrinkage in some occasions when they were in contact with the DPBS during the sterilization process before the cell culture. This also needs to be taken into consideration as an important factor in the effects of crosslinking on the eventual cell proliferation on the scaffolds.

Pictures of crosslinked scaffolds before and after DPBS washes are shown in Fig 6.10, and Table 6.7 lists the percentage of shrinkage of the crosslinked scaffolds in DPBS compared with the non-crosslinked ones. We can see that the UV-irradiated collagen-elastin scaffolds had drastic shrinkage when washed with DPBS.

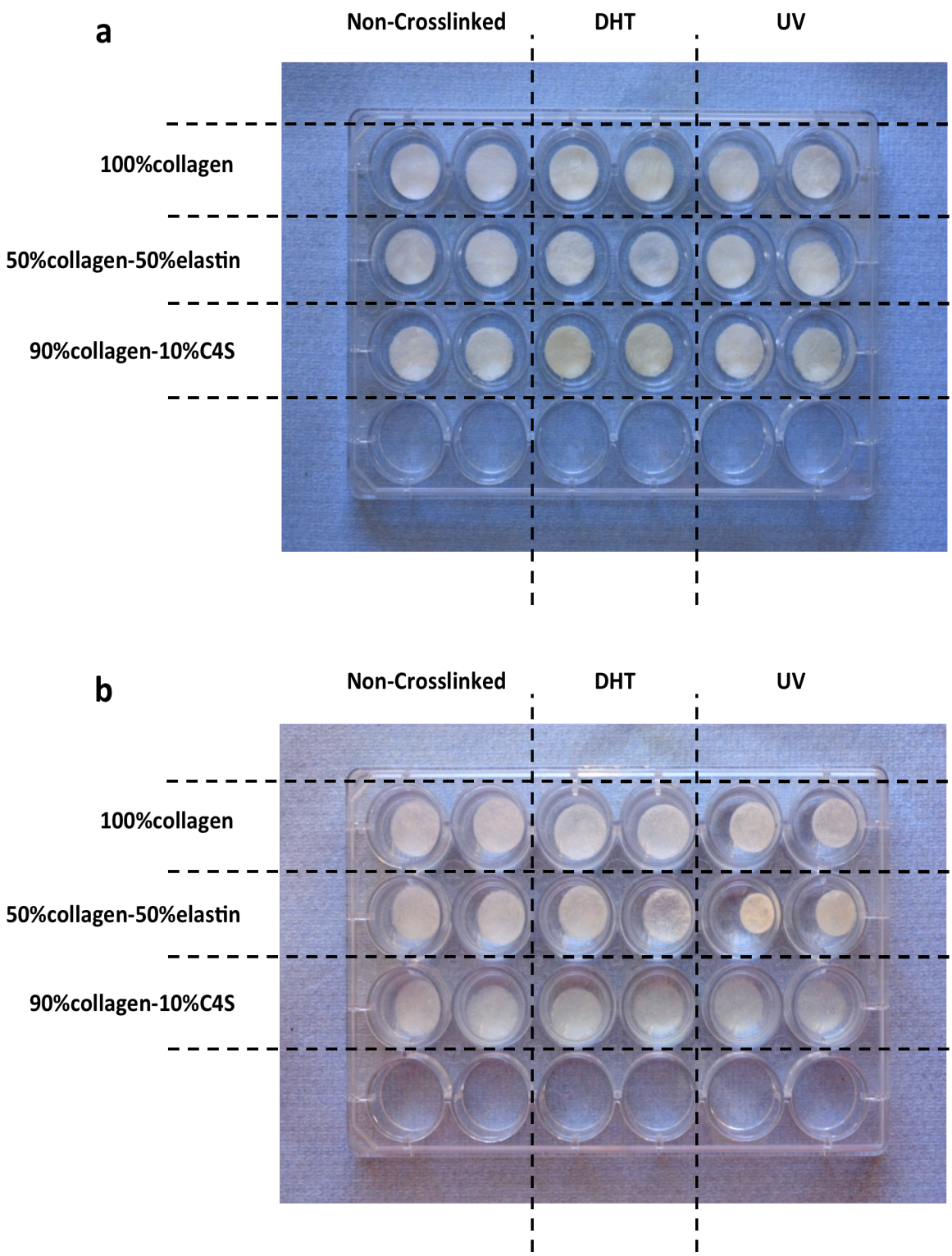


Fig 6.10 Pictures of non-crosslinked and crosslinked scaffolds (a) in dry status, and (b) after DPBS washes.

Table 6.7 Volume shrinkage of crosslinked scaffolds after DPBS washes (expressed as percentage of area reduction). * indicates statistically significant differences ($p<0.05$) amongst groups of different compositions.

Composition	DHT-treated (%)	UV-irradiated (%)
100%Collagen	4.4±4.1	20.2±2.3*
50%Collagen-50%Elastin	7.4±3.6	42.1±7.7*
90%Collagen-10%C4S	8.6±2.4	10.1±4.4*

6.4 Discussion

6.4.1 CDCs Behaviours on Scaffolds

Cells naturally bind to collagen via integrin receptors [195], and therefore show desirable activities on collagen scaffolds (migration and division, see Fig 6.6). GAGs are also believed to have advantageous interactions with cells through their abilities to bind to growth factors or directly to cell surface receptors [298, 299], and have been found to improve tissue growth and regeneration when incorporated into collagen scaffolds [300, 301]. In particular, the GAG used in this study, C4S, is able to enhance the metabolic activities of cells [302], which may explain the increased proliferation (Table 6.1) and the deeper migration (Table 6.3) seen on the collagen-C4S scaffolds. It is worth noting that the 50%collagen-50%C4S scaffolds had a lower attachment of cells initially, although there was a steady cell growth afterwards. As mentioned in 5.4, there is an upper limit of C4S binding to collagen (when the binding sites on the collagen are saturated by C4S) [196], and thus a proportion of the C4S in the scaffolds may have

been dissolved into the culture medium during the seeding process, attracting more cells to attach to the wells and leaving fewer cells to bind to the scaffolds.

Elastin however, based on the alamarBlue® assays, is found to be less favourable to cell proliferation than collagen and C4S. It has been reported that vascular smooth muscle cells are able to alternate between two phenotypic states: a quiescent, contractile state and a proliferative non-contractile state [303-305]. Elastin has been found to induce the contractile phenotype and inhibit the proliferation [306]. Here, the CDCs are speculated to have the similar regime, and therefore proliferate less on the scaffolds with elastin. More importantly, the contractile state cast greater cell contraction and hence greater volume shrinkage on the scaffolds with elastin (see Fig 6.5), resulting in space limitation for cell proliferation, as well as closure or narrowing of the pathways for cell migration, which may have lead to the lower total cell numbers on the scaffolds. This hypothesis then well explains the fact that the cells on the collagen-elastin scaffolds had the same initial attachment ratio with the other scaffolds but much lower proliferation at day 7 (see Fig 6.4). Supports for this hypothesis can be drawn from the SEM images. The flat or elongated cell morphologies exhibited on the collagen-elastin scaffolds (Fig 6.6 b, c) give further credibility of the contractile phenotype of the cells, in which more contact between the cell and the scaffold is needed to provide more resistance to the contractile force generated by the cytoskeleton [307]. The more rounded shape of the cells on the collagen and collagen-C4S scaffolds (Fig 6.6 a, d, e) indicates the non-contractile phenotype, and is also a sign of more cells being in the premitotic stage [308], representing higher proliferation activities. The fact that the cells are more spread at the surface of the collagen-elastin scaffolds is also in line with the suspected space limitation happening in those scaffolds. The MPM image of the 20%collagen-80%elastin scaffold also demonstrates the effects of the volume shrinkage.

There are more cells in a given area on the 20%collagen-80%elastin scaffold (Table 6.3) due to the shrinkage in the radial direction. Meanwhile, the shrinkage also limits the cell migration into the scaffolds, which further results in an even higher cell density (Table 6.3). This cell density, during day 4 to day 7, is likely to be reaching the level of saturation, and therefore explains the reduced proliferation rate on the collagen-elastin scaffolds (Table 6.1).

Nonetheless, the overall proliferation of the cells was significant on all the scaffolds, indicating that the CDCs showed positive responses and viabilities on the collagen-based scaffolds.

The alamarBlue® assay was used here to quantify the attachment and proliferation of cells on the uniform-composition scaffolds, as it measured the metabolic activity of the cells on the scaffold, which was proportional to the number of cells. However, if we would like to make a comparison of the cell numbers across the different scaffold groups and different culturing time points using the results of alamarBlue® assays, one condition needs to be met, that the average metabolic activity of a single cell is same on all different scaffolds and at all different culturing time points. This seemed to be a very bold assumption to be made, especially when the cells were likely to have been in different phenotypic states as mentioned above. Therefore, a CyQUANT® assay, which measures the amount of nucleic acids in the cells and hence the cell numbers [309], was conducted at the end of one batch of cell culturing to verify this assumption. The results (data not shown) revealed that, while the amount of nucleic acids showed the same trend (i.e. higher in collagen and collagen-C4S scaffolds and lower in collagen-elastin scaffolds), the differences in the values measured were not as great as those seen in the alamarBlue® results (for example, the alamarBlue® reduction of the 20%collagen-80%elastin group at day 7 was 50% less than that of the 100%collagen group, while the

nucleic acids content of the 20%collagen-80%elastin group was only 20% less than that of the 100%collagen group) [310]. Therefore, the results of the alamarBlue® assays in Fig 6.4 and Table 6.1 were not believed to be accurate indications of the exact cell numbers. However, interpreted as a reflection of the general proliferation activities, the alamarBlue® assay results were still considered valid. Although the CyQUANT® assay offered a more accurate way to measure the cell numbers on the scaffolds, it is destructive to the cells and hence could not continuously monitor the proliferation of the cells. Therefore, like in many other studies [311-316], the alamarBlue® assay was still used as the preferred method to quantify cell proliferation in this thesis.

On the bi-layer scaffolds, the cells exhibited proliferation and migration at relatively similar levels on different layers. For the 100%collagen/20%collagen-80%elastin scaffold, this was not as expected from the differences observed in the uniform-composition scaffolds. As mentioned above, the signalling pathway between collagen and cells is the binding between collagen and the integrin receptors. Also, the integrin receptor engagement can activate inter-cellular signal transduction pathways [317]. Whereas the cells interact with elastin via a non-intergrin signalling pathway that stimulates actin polymerization, which is likely to have been the cause of the contractile phenotype [306]. Therefore, on the 100%collagen/20%collagen-80%elastin scaffold, more integrin-mediated cellular responses can be transferred from the collagen layer to the collagen-elastin layer by either cell-cell communication or cell movement, which then evens out the different cell behaviours that may have occurred.

Cell contraction was also observed on the bi-layer scaffolds and so was the volume shrinkage. However, it no longer seemed to be a major limiting factor of the cell proliferation. The larger shrinkage on the 20%collagen-80%elastin layer and the 90%collagen-10%C4S layer was possibly due to their lower mechanical properties

compared with the collagen layers, which made them more susceptible to the cell contraction.

The cells exhibited similar behaviours on the tri-layer scaffold (0.3~0.4mm migration depth and 3000~4000 mm^{-3} density) to those in the bi-layer scaffolds, which confirms that the cells are able to consistently form a relatively even distribution on the layered scaffolds, even when dealing with a more complex environment (more layer interfaces and a different C4S content). This suggests the possibilities to fine-tune the design and the mechanical properties of the scaffolds before seeding them with cells, which would allow us to achieve a scaffold better resembling to its natural counterparts.

6.4.2 Effects of Crosslinking

Generally, lower CDCs proliferation is observed on the DHT-treated scaffolds compared with the non-crosslinked ones. Since volume shrinkage is not significant either in dry status or in hydrated status (see Fig 6.10) on all the DHT-treated scaffolds, it is not likely to have been a contributing factor to the lower proliferation of CDCs. Therefore, the explanation of the lower proliferation should be sought from the ultra-structure changes caused by the crosslinking process.

After the DHT treatment, the surface chemistry of the collagen fibres were affected, i.e. they became more hydrophobic [318, 319] (possibly due to the hydrophilic moieties forming crosslinks). This could be responsible for the reduction on the CDCs proliferation, as the cells tend to more readily deposit endogenous fibronectin, which is closely associated with cell attachment, proliferation, and migration [320], on to hydrophilic surfaces [321]. Meanwhile, the un-winding of the collagen triple helix caused by the denaturation effects from the DHT treatment is another possible reason for the lower cell proliferation. It is reported that integrin binding sites on collagen

(α1β1 and α2β1) are dependent on the maintenance of the triple helical conformation of collagen molecule [322, 323].

It is interesting to notice that on the DHT-treated collagen-elastin scaffolds, the proliferation of CDCs has reached the same level of that on the non-crosslinked ones at the later stage of the time course of culturing (day 4 and day 7). This might be attributed to the fact that the effects on cell proliferation from the volume shrinkage caused by cell contraction as mentioned in 6.4.1 have dominated over the crosslinking-related factors, i.e. the surface hydrophobicity and the collagen denaturation, whose effects therefore become negligible.

The UV irradiated scaffolds, although not showing large volume shrinkage when still dry, exhibited considerable shrinkage rather unexpectedly when washed with DPBS (especially the collagen-elastin scaffolds) (see Fig 6.10). This is likely to be because that the free radicals created on non-adjacent collagen chains during the UV irradiation could not fully react with each other in dry status due to movement restrictions, but in the aqueous solution where they can move more freely, further inter-molecular crosslinking occurred, reducing the space between the collagen chains and hence leading to the volume shrinkage of the scaffolds. The resultant smaller surface area for cell attachment, less space available for cell growth, and decreased pore sizes for cell migration are therefore responsible for the much lower amount of cells on these scaffolds. In fact, researchers have found that the UV irradiation could actually improve the hydrophilicity of the collagen surface [324], and it was also found in 3.3.4 that UV irradiation causes less denaturation to the collagen than the DHT treatment. However, these effects which could have helped the CDCs proliferation seem to have been overwhelmed by the volume shrinkage.

The collagen and collagen-elastin scaffolds were freeze-dried from the swollen state in the suspension. Therefore the collagen molecules on these scaffolds were not assembled and were easy to bend in DPBS in order to coordinate the free radicals generated by the UV irradiation. In contrast, the collagen molecules in the collagen-C4S scaffolds were more tightly bundled due to the collagen-C4S co-precipitation effect described in 3.4.1, and were therefore less flexible to deform for the crosslinking in DPBS [325]. This is likely to be the reason why much less shrinkage was seen on the UV irradiated collagen-C4S scaffolds in DPBS. With less space limitation, the proliferation of CDCs again was mostly influenced by the hydrophobicity and the denaturation on the collagen. The lower degree of denaturation caused by UV irradiation than DHT treatment (see 3.3.4) can then explain the higher cell proliferation, compared with the DHT-treated collagen-C4S scaffolds.

6.5 Conclusions

Scaffolds are responsible for mediating the signalling, growth, and metabolism of the cells. This study illustrated that cardiosphere-derived cells were able to attach to and populate the scaffolds, both the uniform-composition ones and the layered ones.

On the uniform-composition scaffolds, cells had similar initial attachment on all the scaffolds (except on the 50%collagen-50%C4S scaffolds due to the elution of C4S), but had different proliferation rates throughout the time course of culturing. While C4S was found to enhance the activities of the collagen-based scaffolds for the cells, elastin showed less favourable effects on improving the cell proliferation due to the elastin-induced cell contraction and scaffold volume shrinkage.

Crosslinking process on the scaffolds affected the cell attachment and proliferation through changing the surface chemistry and ultra-structures of the scaffold materials. It could also cause volume shrinkage of the scaffolds which would have adverse effects on cells colonizing the scaffolds. The effects from the scaffold composition and the crosslinking process worked concomitantly on influencing the cell population on the scaffolds, and could be summarized as in Table 6.8. Generally the proliferation on the crosslinked scaffolds is found less than that on the non-crosslinked ones, and therefore a balance point needs to be sought between better mechanical properties and better biological properties of the scaffolds.

On the layered scaffolds, cells exhibited a more even distribution than on the uniform-composition scaffolds, possibly due to cells communicating between different layers and adopting common signalling pathways. This suggested that the cells recognized the layered scaffold as a well-interconnected environment, and would potentially form an integrated piece of tissue without compromising the desirable mechanical properties that were achieved by the anisotropic layered structures.

The biological characterization supplements the findings in the previous chapters, and enables us to further probe the principles of designing qualified scaffolds for heart valve tissue engineering.

Table 6.8 Summary of contributing factors on the cell proliferation on different scaffolds. O **denotes no change or negligible effects, – denotes negative effects, and + denotes positive effects. The dominant factor is highlighted. The proliferation on non-crosslinked collagen scaffolds is set as the reference.**

Scaffold	Effects from scaffold composition	Effects from crosslinking-caused ultra-strucutre change	Effects from crosslinking-caused volume shrinkage in DPBS
Non-crosslinked collagen	O	O	O
DHT-treated collagen	O	-	O
UV-irradiated collagen	O	-	-
Non-crosslinked collagen-elastin	-	O	O
DHT-treated collagen-elastin	-	-	O
UV-irradiated collagen-elastin	-	-	-
Non-crosslinked collagen-C4S	+	O	O
DHT-treated collagen-C4S	+	-	O
UV-irradiated collagen-C4S	+	-	O

Chapter 7. Conclusions

The aim of this thesis was to characterize the materials properties of the collagen-based scaffolds, and to propose a mechanically and biologically desirable design of scaffolds for heart valve tissue engineering.

The collagen-based scaffolds fabricated by the freeze-drying technique demonstrated high porosities (98%-99.7%) and pore sizes ranging from 33.2μm to 201.5μm depending on the freezing temperature, the relative density and the composition of the suspension. A lower freezing temperature was able to produce smaller pores. A lower proportion of collagen and a lower relative density produced larger pores in the collagen scaffolds and the collagen-elastin scaffolds, but not in the collagen-C4S scaffolds, because the ice crystals were constrained in the collagen or collagen-elastin networks, but not so by the collagen-C4S co-precipitates. The ultra-structures of the scaffold materials saw little change in the freeze-drying process, but underwent esterification and amide formation, as well as protein denaturation, during the DHT treatment or the UV irradiation.

A freezing temperature of -20˚C and a suspension concentration of 1%wt/v were considered to be able to produce the pore sizes in the scaffolds most suitable for the cell growth and therefore were carried onwards for manufacturing the layered scaffolds for heart valve tissue engineering. At the same time, the framework of pore size set out in this study could also provide informative guidance, should these collagen-based scaffolds are to be used in other tissue engineering applications, e.g. skins (optimal pore size 20~125 μm [326]), cartilages (optimal pore size 70~120 μm [327]), and bones (optimal pore size 300~400 μm [236]).

The tri-layer scaffold produced in this study, to the author's knowledge, was the first artificially designed scaffold with the layered structures and compositions that were relatively similar to a native heart valve, stepping forward from the existent single-layer scaffolds [72, 161], and also excelling the decellularized layered scaffolds [328-330] in the controllability of the scaffold structures.

The scaffold manufacturing process could have been more successful if the following aspects were improved. In the freezing step, the suspensions underwent free freezing at given temperatures, and the resultant pore sizes in the scaffolds had relatively wide ranges. O'Brien reported that freezing the suspension with a constant cooling rate followed by an annealing step produced pores with better uniformity [139, 197]. Companies like Millrock and Praxair have also developed devices that can perform controlled ice nucleation to the suspension, by cooling it to a temperature below the equilibrium freezing point but above the temperature of spontaneous nucleation, followed by a depressurization process [331, 332]. These techniques are recommended for the future study in order to better control the pore sizes of the scaffolds. The elastin and C4S, although incorporated into the collagen matrix, did not have an ideal interaction with the collagen. The elastin was attached to the collagen only in a physical manner, and the C4S could only bind to collagen at a relatively small amount. This was hindering some of the characteristic properties of elastin and C4S from being further utilized. It is therefore sensible to introduce to them a better interaction with collagen in the future. For elastin, it might be desirable to prepare the collagen-elastin suspension in other solvents (such as hydrochloric acid or hexafluoroisopropanol), in which collagen and elastin can interact at a lower scale level [333, 334]. C4S, as well as other types of GAGs, could be polymerized (usually by methacrylation) and form an inter-penetrating

network with collagen [335-337], through which the limitation of GAGs binding to collagen can be overcome and the GAGs content in the scaffold can then be increased.

The mechanical properties of the scaffolds (39.8kPa to 1082kPa for E_{ten}, 2.4kPa to 213.9kPa for E_{comp}, and 11.0kPa to 415.8kPa for E_{bend1}) were also influenced by the freezing temperature, the composition and most importantly the relative density, and could be further increased by the crosslinking processes. Pore size alone did not seem to affect the mechanical properties of the scaffolds. However, other factors that resulted from a lower freezing temperature (i.e. more porous walls or mechanically ineffective collagen fibres) had caused lower values of E_{ten} and E_{comp}. The collagen-elastin and collagen-C4S scaffolds exhibited lower mechanical properties than the collagen scaffolds due to the lower volume fraction of the load-bearing collagen. The values of the moduli of the scaffolds had exponential dependence on the relative density, and the dependence factor was larger for the E_{comp} than the E_{ten}. The crosslinking processes were able to increase the mechanical properties of the scaffolds by up to 1.5 times. UV irradiation was more effective on the collagen and collagen-elastin scaffolds and DHT treatment was more effective on the collagen-C4S scaffolds.

The microscopic deformation mechanism of the pores in the scaffolds gave rise to their elastomeric behaviours, which were non-linear and were different in tension and compression: two deformation stages in tension (linear elastic and stiffening), and three deformation stages in compression (linear elastic, stress plateau, and densification). The difference between E_{ten} and E_{comp} was utilised, together with the layered structures that mimicked the structure of a native heart valve, to achieve the characteristic bending anisotropy exhibited by the native heart valve: a higher effective bending modulus in the AC direction than in the WC direction.

Scaffolds showed much lower (1/42~1/20 of dry values) mechanical properties in the hydrated status due to the lubricating effect of water, consistent with other research's finding [151]. The composition of the scaffolds played an important role in the hydration ability. The bending anisotropy was successfully preserved in the hydrated layered scaffolds despite the low effective bending modulus.

Finite element modelling showed that the ODGEN HYPERFOAM models for the scaffolds could serve well in validating the experimental data and in providing a feasible way to predict the mechanical behaviours of the scaffolds when experimental tests were difficult.

Although the effective bending stiffness of the tri-layer scaffold produced in this thesis (24.8±4.4kPa WC, 41.5±8.2kPa AC when dry; 1.62±0.23kPa WC, 2.46±0.18kPa AC when hydrated) was not comparable to that of the native heart valve (500kPa WC, 700kPa AC), the bending anisotropy of the scaffold was derived with the same mechanism, with each layer of the scaffold functioning according to its correspondent layer in the native valve. With this featured property, the tri-layer scaffolds can be applied in the future in bioreactors using bending as a mechanical stimulus [194], where cells in different layers in the scaffolds can experience different strain ranges and in reaction exhibit different mechanical, metabolic, and phenotypic behaviour that could lead to more desirable anisotropies in the TEHVs [338-341]. With the low mechanical properties of the scaffolds in mind, future studies could investigate the possibility of incorporating a stiffer material (such as PLGA) into the collagen matrix [342, 343], providing a higher stiffness while not sacrificing much of the bioactivity of the scaffold. Also, the low effective bending stiffness of the hydrated scaffolds is partly due to the fact that the scaffolds, unlike the incompressible native heart valves, are compressible [105]. Therefore, attaching a less permeable layer around the scaffold (leaving one side

uncovered for cell seeding) could be another attempt to improve the mechanical properties [344, 345].

The cardiosphere-derived cells exhibited good affinity to the collagen-based scaffolds. Difference in the scaffold compositions had effects on the proliferation tendency of the cells: more on the collagen-C4S scaffolds and less on the collagen-elastin scaffolds. Scaffold volume shrinkage was a major factor limiting the long-term proliferation and migration of the cells, and the causing reasons included the cells' phenotypic responses to the scaffolds and the crosslinking conditions. Nonetheless, with inter-layer communication and migration, the cells were observed to form a relatively uniform distribution (over 3000 cells/mm^3 in every layer) on the tri-layer scaffold, which suggested promising viability of the intended tissue engineered heart valve. To date, the regenerative ability of CDCs has been predominantly applied in the cell injection therapies to treat myocardial infarcts [279, 283, 346]. There were several studies where the interactions between CDCs and scaffolds were investigated, however, also for the purpose of cell delivery and retention for the cell therapies [347-349]. Therefore, the study in this thesis, having demonstrated that CDCs are potentially suitable cell source for TEHVs, may well open up a new application for the CDCs: cardiovascular tissue engineering.

Chapter 8. Future Work

A number of important aspects of this study (some already mentioned in previous chapters) were not developed or investigated due to limitation on laboratory facilities and time course, and are therefore recommended for future research.

When examining the effects of freeze-drying and crosslinking on the ultra-structures of the scaffolds, no staining was used in order to avoid any additional effects. As a result, only the collagen ultra-structure was able to be observed under TEM. Having now independently investigated the effects from freeze-drying and crosslinking, it will be worth applying staining to the scaffolds to look at the interactions of the scaffold materials at a microscopic level [233, 243]. As proposed in Chapter 7, attempts will be made to achieve molecular-level binding of collagen and elastin, and an interpenetrating network of collagen and GAGs. If successful, these interactions can then be visualized under TEM with the help of staining processes (sodium tungstate for collagen [233, 350, 351], osmium tetroxide for elastin [352, 353], and cupromeronic blue for GAGs [233, 354]).

The layered scaffolds studied in this thesis have mainly mimicked the native heart valve in the circumferential direction, as shown in Fig 4.14. The behaviour, especially mechanical, of the native heart valves in the radial direction, which is featured by the crests in the fibrosa, is not yet mimicked. Studies have shown that, if the fibrosa is in a flattened state, it has an extensibility of 20% in both radial and circumferential directions [32]. However, in real situations, it needs to extend much more than 20%, in order to keep up with the ventricularis which is extending up to 60% in diastole [27]. It is the crests in the fibrosa that makes this extra radial extension possible, while not

affecting the desirable high stiffness in the circumferential direction. Therefore, periodic crests in the radial direction are recommended to be introduced to the scaffolds, which are proposed to be achieved by aligning a row of thin metal wires at the top of the collagen layer during the casting process. In addition, to better design a mould to produce scaffolds of the semi-lunar shapes same to the native heart valves is also a future task, so that the above-mentioned mechanical properties of the scaffolds in the radial and circumferential directions could be combined and more thoroughly characterised [89].

The mechanical tests conducted on the scaffolds were all quasi-static, and therefore the strain rate (5×10^{-4} s^{-1}) was different from the real situation in native heart valves (~5 s^{-1}). Although a test with dynamic loading could have been more representative of the real load conditions in native heart valves, it could not show the detailed stress- strain curves of the scaffolds, from which their deformation mechanism could be studied and finite element models could be generated. Also, Shergold suggested that, the shear moduli of pig skin and silicone rubber were dependent on the strain rate in a high strain rate range (>40s^{-1}), while the strain rate dependency in low strain rate range (<40s^{-1}) was much less prominent [355]. The strain rates of the quasi-static tests and the native heart valves seemed to fall in the latter range and therefore it was hypothesized that the quasi-static mechanical properties of the scaffolds were sufficiently close to the dynamic properties. For the above reasons, the quasi-static tests were selected for the mechanical characterisation in this thesis. However, upon the completion of the quasti-static tests, the necessity of dynamic tests now needs to be raised again, not only to validate the results and analysis of the quasi-static tests, but also to investigate another important property of a TEHV scaffold, i.e. fatigue resistance, which could not possibly be studied in the quasi-static tests. Gloeckner suggested that porcine bioprosthetic heart

valves suffered a decrease in the bending stiffness by up to 80% after 200 million times of cyclic loading [257]. Therefore it is of great significance that the fatigue resistance of the TEHV scaffolds is carefully studied and reaches an acceptable level for in vivo applications. It is proposed that an accelerated fatigue test to be conducted on the scaffolds [257]. Samples will be subjected to cyclic bending load with a higher frequency than that of the cardiac cycles. It has been established that the higher loading frequency, within a certain range (<20Hz), did not change the deformation mechanism from that under the cardiac frequency [356]. Therefore, this test would yield valuable information concerning the fatigue resistance of the scaffold, especially the damping and interlayer-shearing accommodating roles that the GAGs layer might play [101], and therefore give us guidance for designing more durables scaffold for the aimed purposes.

Furthermore, mechanical tests on scaffolds seeded with cells will also be beneficial, giving a more informative comparison between the mechanical properties of the scaffold-cell constructs and the native heart valves. The samples for these tests would be relatively small in dimensions due to the difficulties of cells populating large samples, and would be in hydrated status as well. Therefore, it is essential to improve the sensitivity of the equipment, as stated in 5.3.2. A load cell with a capacity of <2N is recommended. The self-deflection test, despite the limitations discussed in 5.4, could still be informative if the accuracy is enhanced (for example by incorporating a macro-focus CCD camera).

It seems that the cells seeded on the scaffolds in this work have been suffering from the common problem of cell penetration: the formation of a dense layer of cells on the outer surface putting a limit on the exchange of nutrient and oxygen, and hence constraining the cell penetration to a critical depth of less than 500 μm [111, 357]. To address this issue in future cell culturing, hierarchical structures, such as arrays of channels or

funnels at a scale level higher than the pore sizes [111, 357, 358], can be introduced to the scaffold design to facilitate the cells to populate throughout the whole thickness of the scaffold.

Cell differentiation was not investigated in this thesis due to time limits. Also, external signals, which are one of the three major elements in the tissue engineering technique, were not applied in the cell culture experiments either. These two aspects, however, carry important information regarding the bioactivity of the scaffold and the suitability of the cell source for heart valve tissue engineering, and therefore need to be examined in the future, possibly in a combined scheme. Researchers have demonstrated that biochemical signals, such as vascular endothelial growth factor (VEGF) and fibroblast growth factor-inducible 14 (Fn14), were able to induce the differentiation of stem cells (e.g. mesenchymal stem cells and adipose –derived stem cells) into respective targeted valvular cells: the valvular endothelial cells (VECs) and the valvular interstitial cells (VICs) [188, 359, 360]. Mechanical stimuli were also shown to promote targeted differentiation of mesenchymal stem cells: fluid shear stress for endothelial cells [361, 362] and cyclic strain for smooth muscle cells [362-364]. Since the cardiosphere-derived cells have already been proved to have the capacity to spontaneously differentiate into endothelial cells and smooth muscle cells [289], it is then worth investigating their potential of phenotype-specific differentiation. The chemical and mechanical signals could be applied onto the CDCs-seeded TEHV scaffolds to induce targeted differentiation of CDCs towards different desired phenotypes in different regions, therefore more closely mimicking the native heart valves.

Appendix A

For staggered cubic pores shown in Fig 4.13 with the edge length l, the geometric constants are as following: the constant relating pore volume to l^3, $C = 1$; the number of walls on a single pore, $f = 6$; the number of walls that meet at an edge, $Z_f = 4$; the number of edges per wall, $n = 4$.

Assuming the thickness of the pore edge and the pore walls is t_e and t_w respectively, we can link $\frac{t_e}{l}$ and $\frac{t_w}{l}$ to $\frac{\rho}{\rho_s}$ by Eq.a1 and Eq.a2 [152],

$$\frac{t_w}{l} = \frac{2C}{f}(1-\emptyset)\frac{\rho}{\rho_s} = \frac{1}{3}(1-\emptyset)\frac{\rho}{\rho_s} \qquad \text{Eq.a1}$$

$$\frac{t_e}{l} = (\frac{2Z_f}{n}\frac{C}{f}\emptyset\frac{\rho}{\rho_s})^{\frac{1}{2}} = (\frac{1}{3}\emptyset\frac{\rho}{\rho_s})^{\frac{1}{2}} \qquad \text{Eq.a2}$$

where $\emptyset$ is the fraction of the solid material contained in the pore edges.

For a single cubic pore under tension, the force acting on the pore is causing pore wall bending, pore edge bending, and pore wall stretching as shown in Fig 4.13, and therefore can be expressed by Eq.a3.

$$F_{tension} = F_{wall\ bend} + F_{edge\ bend} + F_{wall\ stretch} \qquad \text{Eq.a3}$$

If the axial elongation of the pore under $F_{tension}$ is δ, we will then have

$$F_{wall\ bend} = \frac{\frac{\delta}{2}48E_s\frac{l{t_w}^3}{12}}{l^3} = \frac{2\delta E_s {t_w}^3}{l^2}$$

$$F_{edge\ bend} = 2\frac{\frac{\delta}{2}48E_s\frac{{t_e}^4}{12}}{l^3} = \frac{4\delta E_s {t_e}^4}{l^3}$$

$$F_{wall\ stretch} = E_s\frac{\delta}{l}lt_w = E_s\delta t_w \ .$$

Therefore the effective tensile modulus of the pore E_{ten} can be written as

$$E_{ten} = \frac{F_{tension}}{l^2\frac{\delta}{l}} = \frac{2E_s{t_w}^3}{l^3} + \frac{4E_s{t_e}^4}{l^4} + \frac{E_s t_w}{l} \qquad \text{Eq.a4}$$

Substituting Eq.a1 and Eq.a2 to Eq.a4, we then have

$$\frac{E_{ten}}{E_s} = 2\left(\frac{1-\emptyset}{3}\frac{\rho}{\rho_s}\right)^3 + 4\left(\frac{\emptyset}{3}\frac{\rho}{\rho_s}\right)^2 + \frac{(1-\emptyset)}{3}\frac{\rho}{\rho_s} \qquad \text{Eq.a5}$$

The contribution of wall bending $2\left(\frac{1-\emptyset}{3}\frac{\rho}{\rho_s}\right)^3$ is negligible compared to the contribution of wall stretching $\frac{(1-\emptyset)}{3}\frac{\rho}{\rho_s}$ due to a small $\frac{\rho}{\rho_s}$ in this study (<0.02).

Therefore Eq.a5 can be reduced to

$$\frac{E_{ten}}{E_s} = 4\left(\frac{\emptyset}{3}\frac{\rho}{\rho_s}\right)^2 + \frac{(1-\emptyset)}{3}\frac{\rho}{\rho_s},$$

with the same form as Gibson-Ashby's equation for closed-cell foams [152]:

$$\frac{E}{E_s} = C_1\emptyset^2\left(\frac{\rho}{\rho_s}\right)^2 + C_2(1-\emptyset)\frac{\rho}{\rho_s}.$$

With typical values of $\emptyset = 0.6\sim0.8$ [152], contribution of edge bending $4\left(\frac{\emptyset}{3}\frac{\rho}{\rho_s}\right)^2$ is at most 8.5% of that of wall stretching $\frac{(1-\emptyset)}{3}\frac{\rho}{\rho_s}$, due to a small $\frac{\rho}{\rho_s}$. Therefore the tensile modulus will appear to be determined by wall stretching and will have an approximately linear dependence on $\frac{\rho}{\rho_s}$, consistent with the experimental data.

Similarly, when the pore is under compression the compressive force will also be comprised of three terms of pore wall bending, pore edge bending and pore wall compressing, and so is the effective compressive modulus:

$$F_{compression} = F_{wall\ bend} + F_{edge\ bend} + F_{wall\ compress} \qquad \text{Eq.a6}$$

$$\frac{E_{comp}}{E_s} = 2\left(\frac{1-\emptyset}{3}\frac{\rho}{\rho_s}\right)^3 + 4\left(\frac{\emptyset}{3}\frac{\rho}{\rho_s}\right)^2 + \frac{(1-\emptyset)}{3}\frac{\rho}{\rho_s}. \quad \text{Eq.a7}$$

However, the compressed walls will start buckling at a critical point when

$$F_{wall\ compress} = \frac{\pi^2 E_s {t_w}^3}{3(1-\mu^2)l}\ [365], \quad \text{Eq.a8}$$

where μ is the Poisson's ratio.

After this critical point, further increase of the axial strain of the compressed walls no longer requests an increase in $F_{wall\ compress}$ due to the buckling effect, i.e. the compressive modulus no longer has the contribution from the wall compressing, and hence can be reduced to:

$$\frac{E_{comp}}{E_s} = 2\left(\frac{1-\emptyset}{3}\frac{\rho}{\rho_s}\right)^3 + 4\left(\frac{\emptyset}{3}\frac{\rho}{\rho_s}\right)^2. \quad \text{Eq.a9}$$

Since the critical strain that corresponds to the critical point

$$\varepsilon_{cr} = \frac{\pi^2 {t_w}^2}{3(1-\mu^2)l^2} = \frac{\pi^2}{3(1-\mu^2)}\left(\frac{1-\emptyset}{3}\right)^2\left(\frac{\rho}{\rho_s}\right)^2 < 0.00025$$

is negligibly small, the compressive modulus can then be considered to follow Eq.a9 rather than Eq.a7 for the linear elastic deformation stage.

Comparing the two terms in Eq.a9, the contribution of wall bending $2\left(\frac{1-\emptyset}{3}\frac{\rho}{\rho_s}\right)^3$ is also much smaller than the contribution of edge bending $4\left(\frac{\emptyset}{3}\frac{\rho}{\rho_s}\right)^2$. Therefore, the compressive modulus is predominated by the edge bending and has squared dependence on $\frac{\rho}{\rho_s}$, also in agreement with the experimental data.

Appendix B

Assuming a scaffold is bent to a curvature of κ, the effective bending modulus can then be expressed with the moment-curvature equation

$$M = \kappa E_{bend} I \qquad \text{Eq.b1}$$

where I is the second moment of area.

On a cross-section of a uniform-composition scaffold, the bending moment results in compressive stress in the upper region and tensile stress in the lower region as shown in Fig b1. Since the scaffold has different tensile and compressive moduli, the neutral axis is not located in the centre of the scaffold.

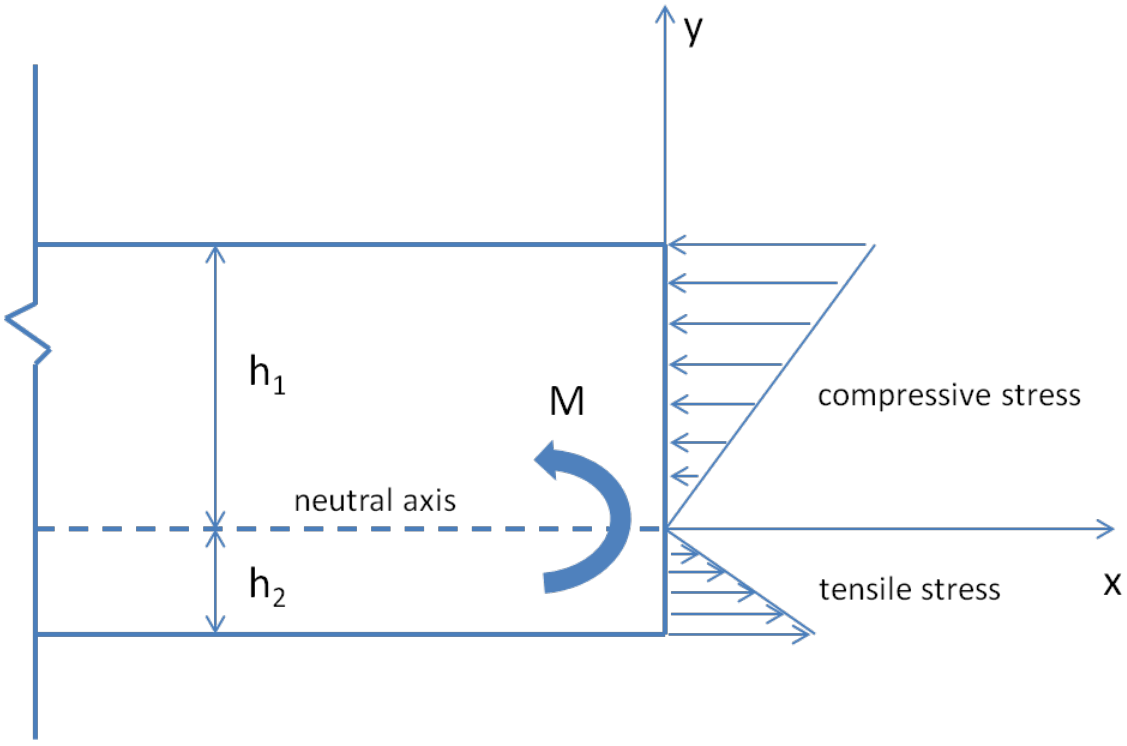


Fig b1. Schematic stress distribution on a cross section of a uniform scaffold in bending [366].

Assuming the neutral axis has a distance of h_1 from the upper surface and h_2 from the lower surface, the tensile and compressive force acting on the cross section are shown by Eq.a11 and Eq.a12 respectively.

$$F_{ten} = \int_0^{h_2} \sigma_{ten} b dy = \int_0^{h_2} E_{ten}(\kappa y) b dy = \kappa E_{ten} \frac{b{h_2}^2}{2} \qquad \text{Eq.b2}$$

$$F_{comp} = \int_0^{h_1} \sigma_{comp} b dy = \int_0^{h_1} E_{comp}(\kappa y) b dy = \kappa E_{comp} \frac{b{h_1}^2}{2} \qquad \text{Eq.b3}$$

Since there is no total resultant force on the cross section, F_{ten} and F_{comp} should be equal. Therefore we have

$$F_{ten} = F_{comp}$$

$$\kappa E_{ten} \frac{b{h_2}^2}{2} = \kappa E_{comp} \frac{b{h_1}^2}{2}$$

$$\frac{h_1}{h_2} = \frac{\sqrt{E_{ten}}}{\sqrt{E_{comp}}} \qquad \text{Eq.b4}$$

and can then locate the position of the neutral axis.

After the position of the neutral axis is determined, the bending moment can also be expressed by the sum of the moment caused by the tensile and compressive stress on the cross-section

$$M = M_{ten} + M_{comp}$$

$$= \int_0^{h_2} E_{ten}(\kappa y) b y dy + \int_0^{h_1} E_{comp}(\kappa y) b y dy$$

$$= \kappa E_{ten} \frac{b{h_2}^3}{3} + \kappa E_{comp} \frac{b{h_1}^3}{3} \qquad \text{Eq.b5}$$

Substituting Eq.b1 into Eq.b5 gives

$$\kappa E_{bend}\frac{b(h_1+h_2)^3}{12} = \kappa E_{ten}\frac{bh_2{}^3}{3} + \kappa E_{comp}\frac{bh_1{}^3}{3} \ ,$$

and together with Eq.b4 we then have the effective bending modulus of a uniform-composition scaffold as

$$E_{bend} = \frac{4}{(\frac{1}{\sqrt{E_{ten}}}+\frac{1}{\sqrt{E_{comp}}})^2} \qquad \text{Eq.b6}$$

References

[1] Iaizzo PA, Bianco RW, Hill AJ, St. Louis JD. Heart Valves: From Design to Clinical Implantation. New York: Springer 2013.
[2] Schoen FJ. Cardiac valves and valvular pathology: Update on function, disease, repair, and replacement. Cardiovascular Pathology 2005;14:189.
[3] Miller GW. King of hearts: The true story of the maverick who pioneered open-heart surgery. New York: Times Books, 2000.
[4] Bolman RM, Black SM. Open Cardiac Repair Under Direct Vision. Journal of Cardiac Surgery 2003;18:328.
[5] Westaby S, Bosher C. Landmarks in Cardiac Surgery. Oxford: Isis Medical Media, 1997.
[6] Donovan TJ, Hufnagel CA, Eastcott HH. Techniques of endocardial anastomosis for circumventing the pulmonic valve. The Journal of thoracic surgery 1952;23:348.
[7] Hufnagel CA, Villegas PD, Nahas H. Experiences with New Types of Aortic Valvular Prostheses. Annals of Surgery 1958;147:636.
[8] Zilla P, Brink J, Human P, Bezuidenhout D. Prosthetic heart valves: Catering for the few. Biomaterials 2008;29:385.
[9] Abbara S, Kalva SP. Problem Solving in Radiology: Cardiovascular Imaging: Elsevier Health Sciences, 2012.
[10] Hoffmann G, Lutter G, Cremer J. Durability of bioprosthetic cardiac valves. Deutsches Ärzteblatt International 2008;105:143.
[11] Schoen FJ, Levy RJ. Calcification of Tissue Heart Valve Substitutes: Progress Toward Understanding and Prevention. The Annals of Thoracic Surgery 2005;79:1072.
[12] Turrentine MW, Ruzmetov M, Vijay P, Bills RG, Brown JW. Biological versus mechanical aortic valve replacement in children. The Annals of Thoracic Surgery 2001;71:S356.
[13] Simon P, Kasimir MT, Seebacher G, Weigel G, Ullrich R, Salzer-Muhar U, Rieder E, Wolner E. Early failure of the tissue engineered porcine heart valve SYNERGRAFT in pediatric patients. European Journal of Cardio-Thoracic Surgery 2003;23:1002.
[14] Yacoub MH, Takkenberg JJM. Will heart valve tissue engineering change the world? Nature Clinical Practice Cardiovascular Medicine 2005;2:2.
[15] Cebotari S, Lichtenberg A, Tudorache I, Hilfiker A, Mertsching H, Leyh R, Breymann T, Kallenbach K, Maniuc L, Batrinac A, Repin O, Maliga O, Ciubotaru A, Haverich A. Clinical Application of Tissue Engineered Human Heart Valves Using Autologous Progenitor Cells. Circulation 2006;114:I.
[16] Mol A, Rutten MCM, Driessen NJB, Bouten CVC, Zünd G, Baaijens FPT, Hoerstrup SP. Autologous Human Tissue-Engineered Heart Valves: Prospects for Systemic Application. Circulation 2006;114:I.
[17] Hoerstrup SP, Sodian R, Daebritz S, Wang J, Bacha EA, Martin DP, Moran AM, Guleserian KJ, Sperling JS, Kaushal S, Vacanti JP, Schoen FJ, Mayer Jr JE. Functional living trileaflet heart valves grown in vitro. Circulation 2000;102:III44.
[18] Thom T, Haase N, Rosamond W, Howard VJ, Rumsfeld J, Manolio T, Zheng ZJ, Flegal K, O'Donnell C, Kittner S, Lloyd-Jones D, Goff Jr DC, Hong Y. Heart disease and stroke statistics - 2006 Update: A report from the American Heart Association Statistics Committee and Stroke Statistics Subcommittee. Circulation 2006;113:e85.

[19] Flanagan TC, Pandit A. Living artificial heart valve alternatives: A review. European Cells and Materials 2003;6:28.
[20] Vongpatanasin W, Hillis LD, Lange RA. Prosthetic heart valves. New England Journal of Medicine 1996;335:407.
[21] Hoffman-Kim D. Tissue Engineering Heart Valves. Science & Medicine 2002:3.
[22] Vesely I. Heart valve tissue engineering. Circulation Research 2005;97:743.
[23] Mol A, Smits AIPM, Bouten CVC, Baaijens FPT. Tissue engineering of heart valves: advances and current challenges. Expert Review of Medical Devices 2009;6:259.
[24] Sacks MS, David Merryman W, Schmidt DE. On the biomechanics of heart valve function. Journal of Biomechanics 2009;42:1804.
[25] Hoffman ACCCW. Pediatric Cardiac Intensive Care. Philadelphia 1998.
[26] Mader SS. Inquiry into life Dubuque ; Oxford : W.C. Brown 1994.
[27] Vesely I. The role of elastin in aortic valve mechanics. Journal of Biomechanics 1997;31:115.
[28] Khan Z, Boughner DR, Lacefield JC. Reconsidering the layer thickness distribution in aortic valve cusps using high-frequency ultrasound. Biomedical Imaging: From Nano to Macro, 2007. ISBI 2007. 4th IEEE International Symposium on, 2007. p.868.
[29] Stella JA, Sacks MS. On the biaxial mechanical properties of the layers of the aortic valve leaflet. Journal of Biomechanical Engineering 2007;129:757.
[30] Sauren AAHJ, Kuijpers W, van Steenhoven AA, Veldpaus FE. Aortic valve histology and its relation with mechanics--Preliminary report. Journal of Biomechanics 1980;13:97.
[31] Christie GW. Anatomy of aortic heart valve leaflets: the influence of glutaraldehyde fixation on function. European Journal of Cardio-Thoracic Surgery 1992;6:S25.
[32] Vesely I, Noseworthy R. Micromechanics of the fibrosa and the ventricularis in aortic valve leaflets. Journal of Biomechanics 1992;25:101.
[33] Fenoglio Jr J, Duc Pham T. Ruptured chordae tendineae. An electron microscopic study. Human Pathology 1972;3:415.
[34] Silverman ME, Hurst JW. The mitral complex: Interaction of the anatomy, physiology, and pathology of the mitral annulus, mitral valve leaflets, chordae tendineae, and papillary muscles. American Heart Journal 1968;76:399.
[35] Kunzelman KS, Cochran RP, Murphree SS, Ring WS, Verrier ED, Eberhart RC. Differential collagen distribution in the mitral valve and its influence on biomechanical behaviour. The Journal of heart valve disease 1993;2:236.
[36] Walmsley R. Anatomy of human mitral valve in adult cadaver and comparative anatomy of the valve. British Heart Journal 1978;40:351.
[37] Culav EM, Clark CH, Merrilees MJ. Connective tissues: Matrix composition and its relevance to physical therapy. Physical Therapy 1999;79:308.
[38] Mol A, Bouten CV, Baaijens FP, Zünd G, Turina MI, Hoerstrup SP. Review article: Tissue engineering of semilunar heart valves: current status and future developments. The Journal of heart valve disease 2004;13:272.
[39] Murata K. Acidic glycosaminoglycans in human heart valves. Journal of Molecular and Cellular Cardiology 1981;13:281.
[40] Kidane AG, Burriesci G, Cornejo P, Dooley A, Sarkar S, Bonhoeffer P, Edirisinghe M, Seifalian AM. Current developments and future prospects for heart valve replacement therapy. Journal of Biomedical Materials Research - Part B Applied Biomaterials 2009;88:290.

[41] Mulholland DL, Gotlieb AI. Cardiac valve interstitial cells:regulator of valve structure and function. Cardiovascular Pathology 1997;6:167.
[42] El-Hamamsy I, Chester AH, Yacoub MH. Cellular regulation of the structure and function of aortic valves. Journal of Advanced Research 2010;1:5.
[43] Rabkin E, Hoerstrup SP, Aikawa M, Mayer JE, Schoen FJ. Evolution of cell phenotype and extracellular matrix in tissue-engineered heart valves during in-vitro maturation and in-vivo remodeling. Journal of Heart Valve Disease 2002;11:8.
[44] Rajamannan NM, Evans FJ, Aikawa E, Grande-Allen KJ, Demer LL, Heistad DD, Simmons CA, Masters KS, Mathieu P, O'Brien KD, Schoen FJ, Towler DA, Yoganathan AP, Otto CM. Calcific Aortic Valve Disease: Not Simply a Degenerative Process: A Review and Agenda for Research From the National Heart and Lung and Blood Institute Aortic Stenosis Working GroupExecutive Summary: Calcific Aortic Valve Disease - 2011 Update. Circulation 2011;124:1783.
[45] Guarda E, Myers PR, Brilla CG, Tyagi SC, Weber KT. Endothelial cell induced modulation of cardiac fibroblast collagen metabolism. Cardiovascular Research 1993;27:1004.
[46] Campbell JH, Campbell GR. Endothelial Cell Influences on Vascular Smooth Muscle Phenotype. Annual Review of Physiology 1986;48:295.
[47] Bashey RI, Torii S, Angrist A. Age-related collagen and elastin content of human heart valves. Journals of Gerontology 1967;22:203.
[48] Ricard-Blum S, Ruggiero F. The collagen superfamily: from the extracellular matrix to the cell membrane. Pathologie Biologie 2005;53:430.
[49] Wasserman RM. Institution Research Healthcare & Biotechnology Initiation Report. Cardium Therapeutics (ASE/CXM), 2010.
[50] Cole WG, Chan D, Hickey AJ, Wilcken DEL. Collagen composition of normal and myxomatous human mitral heart valves. Biochemical Journal 1984;219:451.
[51] Brinckmann, Brinckmann J, Notbohm H, Müller PK. Collagen : primer in structure, processing and assembly. Berlin: Springer, 2005.
[52] Baer E, Cassidy James J, Hiltner A. Hierarchical Structure of Collagen Composite Systems. Viscoelasticity of Biomaterials, vol. 489. American Chemical Society, 1992. p.2.
[53] Cribb AM, Scott JE. Tendon response to tensile-stress - an ultrastructural investigation of collagen-proteoglycan interactions in stresses tendon. Journal of Anatomy 1995;187:423.
[54] Gosline J, Lillie M, Carrington E, Guerette P, Ortlepp C, Savage K. Elastic Proteins: Biological Roles and Mechanical Properties. Philosophical Transactions: Biological Sciences 2002;357:121.
[55] Wuyts FL, et al. Elastic properties of human aortas in relation to age and atherosclerosis: a structural model. Physics in Medicine and Biology 1995;40:1577.
[56] Chapman JA, Tzaphlidou M, Meek KM, Kadler KE. The collagen fibril-A model system for studying the staining and fixation of a protein. Electron Microscopy Reviews 1990;3:143.
[57] Kvist AJ, Johnson AE, Mörgelin M, Gustafsson E, Bengtsson E, Lindblom K, Aszódi A, Fässler R, Sasaki T, Timpl R, Aspberg A. Chondroitin Sulfate Perlecan Enhances Collagen Fibril Formation. Journal of Biological Chemistry 2006;281:33127.
[58] Gunning P. Collagen Fibrils. FEI Image Gallery: Smith & Nephew, 2009.
[59] Daamen WF, Veerkamp JH, van Hest JCM, van Kuppevelt TH. Elastin as a biomaterial for tissue engineering. Biomaterials 2007;28:4378.
[60] Banga I. Structure and function of elastin and collagen Budapest : Akadémiai Kiadó 1966.

[61] Bailey AJ. Collagen and elastin fibres. Journal of clinical pathology. Supplement (Royal College of Pathologists) 1978;12:49.
[62] Powell JT, Vine N, Crossman M. On the accumulation of D-aspartate in elastin and other proteins of the ageing aorta. Atherosclerosis 1992;97:201.
[63] Gray WR, Sandberg LB, Foster JA. Molecular model for elastin structure and function. Nature 1973;246:461.
[64] Debelle L, Alix AJP, Wei SM, Jacob MP, Huvenne JP, Berjot M, Legrand P. The secondary structure and architecture of human elastin. European Journal of Biochemistry 1998;258:533.
[65] Cleary EG, Gibson MA. Elastin-associated microfibrils and microfibrillar proteins. International Review of Connective Tissue Research 1983;VOL.10:97.
[66] Wuyts FL, Vanhuyse VJ, Langewouters GJ, Decraemer WF, Raman ER, Buyle S. Elastic properties of human aortas in relation to age and atherosclerosis: A structural model. Physics in Medicine and Biology 1995;40:1577.
[67] Moore J, Thibeault S. Insights Into the Role of Elastin in Vocal Fold Health and Disease. Journal of Voice 2012;26:269.
[68] Chakrabarti B, Park JW. Glycosaminoglycans: structure and interaction. CRC critical reviews in biochemistry 1980;8:225.
[69] Karamanos NK, Hjerpe A, Tsegenidis T, Engfeldt B, Antonopoulos CA. Determination of iduronic acid and glucuronic acid in glycosaminoglycans after stoichiometric reduction and depolymerization using high-performance liquid chromatography and ultraviolet detection. Analytical Biochemistry 1988;172:410.
[70] Prithason. Chondroitin Sulfate Structure. National Toxicology Program, National Institutes of Health, 2006.
[71] Maroudas A, Evans H, Almeida L. Cartilage of the hip joint. Topographical variation of glycosaminoglycan content in normal and fibrillated tissue. Annals of the Rheumatic Diseases 1973;32:1.
[72] Flanagan TC, Wilkins B, Black A, Jockenhoevel S, Smith TJ, Pandit AS. A collagen-glycosaminoglycan co-culture model for heart valve tissue engineering applications. Biomaterials 2006;27:2233.
[73] Corsi A, Xu T, Chen XD, Boyde A, Liang J, Mankani M, Sommer B, Iozzo RV, Eichstetter I, Robey PG, Bianco P, Young MF. Phenotypic effects of biglycan deficiency are linked to collagen fibril abnormalities, are synergized by decorin deficiency, and mimic Ehlers-Danlos-like changes in bone and other connective tissues. Journal of Bone and Mineral Research 2002;17:1180.
[74] Jackson RL, Busch SJ, Cardin AD. Glycosaminoglycans: Molecular properties, protein interactions, and role in physiological processes. Physiological Reviews 1991;71:481.
[75] Boström H, Moretti A, Whitehouse M. Studies on the biochemistry of heart valves I. On the biosynthesis of mucopolysaccharides in bovine heart valves. Biochimica et Biophysica Acta 1963;74:213.
[76] Stephens EH, Chu C-K, Grande-Allen KJ. Valve proteoglycan content and glycosaminoglycan fine structure are unique to microstructure, mechanical load and age: Relevance to an age-specific tissue-engineered heart valve. Acta Biomaterialia 2008;4:1148.
[77] Grande-Allen KJ, Calabro A, Gupta V, Wight TN, Hascall VC, Vesely I. Glycosaminoglycans and proteoglycans in normal mitral valve leaflets and chordae: association with regions of tensile and compressive loading. Glycobiology 2004;14:621.

[78] Torii S, Bashey RI, Nakao K. Acid mucopolysaccharide composition of human-heart valve. Biochimica et Biophysica Acta (BBA)-Mucoproteins and Mucopolysaccharides 1965;101:285.
[79] Moretti A, Whitehouse MW. Changes in mucopolysaccharide composition of bovine heart valves with age. Biochemical Journal 1963;87:396.
[80] Cheitlin MD. Cardiovascular Physiology - Changes With Aging. The American Journal of Geriatric Cardiology 2003;12:9.
[81] Grande-Allen KJ, Osman N, Ballinger ML, Dadlani H, Marasco S, Little PJ. Glycosaminoglycan synthesis and structure as targets for the prevention of calcific aortic valve disease. Cardiovascular research 2007;76:19.
[82] Stephens EH, Grande-Allen KJ. Age-related changes in collagen synthesis and turnover in porcine heart valves. The Journal of heart valve disease 2007;16:672.
[83] Rossvoll O, Samstad S, Torp HG, Linker DT, Skjaerpe T, Angelsen BA, Hatle L. The velocity distribution in the aortic anulus in normal subjects: a quantitative analysis of two-dimensional Doppler flow maps. Journal of the American Society of Echocardiography : official publication of the American Society of Echocardiography 1991;4:367.
[84] Yoganathan AP, He Z, Jones SC. Fluid mechanics of heart valves. Annual Review of Biomedical Engineering, vol. 6, 2004. p.331.
[85] Reul H TN. Heart valve mechanics. In: NHC Hwang DG, DJ Patel, editor. Quantitative Cardiovascular Studies Clinical and Research Applications of Engineering Principles. Baltimore: Univ. Park Press, 1979. p.527.
[86] Trowbridge A, Crofts C. Comparison of the in vivo and in vitro mechanical properties of aortic valve leaflets. Journal of Thoracic and Cardiovascular Surgery 1987;93:794.
[87] Mendelson K, Schoen FJ. Heart valve tissue engineering: Concepts, approaches, progress, and challenges. Annals of Biomedical Engineering 2006;34:1799.
[88] Sacks MS, Smith DB, Hiester ED. The aortic valve microstructure: Effects of transvalvular pressure. Journal of Biomedical Materials Research 1998;41:131.
[89] Thubrikar M, Piepgrass WC, Deck JD, Nolan SP. Stresses of Natural versus Prosthetic Aortic Valve Leaflets in Vivo. The Annals of Thoracic Surgery 1980;30:230.
[90] Ranga A, Mongrain R, Galaz RM, Biadillah Y, Cartier R. Large-displacement 3D structural analysis of an aortic valve model with nonlinear material properties. Journal of Medical Engineering & Technology 2004;28:95.
[91] Missirlis YF, Chong M. Aortic valve mechanics--Part I: material properties of natural porcine aortic valves. Journal of bioengineering 1978;2:287.
[92] Rousseau EPM, Sauren A, Van Hout MC, Van Steenhoven AA. Elastic and viscoelastic material behaviour of fresh and glutaraldehyde-treated porcine aortic valve tissue. Journal of biomechanics 1983;16:339.
[93] Broom ND, Thomson FJ. Influence of fixation conditions on the performance of glutaraldehyde-treated porcine aortic valves: towards a more scientific basis. Thorax 1979;34:166.
[94] Sauren A, Van Hout MC, Van Steenhoven AA, Veldpaus FE, Janssen JD. The mechanical properties of porcine aortic valve tissues. Journal of biomechanics 1983;16:327.
[95] Mavrilas D, Missirlis Y. An approach to the optimization of preparation of bioprosthetic heart valves. Journal of biomechanics 1991;24:331.
[96] Merryman WD, Engelmayr Jr GC, Liao J, Sacks MS. Defining biomechanical endpoints for tissue engineered heart valve leaflets from native leaflet properties. Progress in Pediatric Cardiology 2006;21:153.

[97] Schmidt DE. Multi-scale Biomechanical Modeling of Heart Valve Tissue: Proquest, UMI Dissertation Publishing, 2011.
[98] Sacks MS, Yoganathan AP. Heart valve function: A biomechanical perspective. Philosophical Transactions of the Royal Society B: Biological Sciences 2007;362:1369.
[99] David Merryman W, Shadow Huang H-Y, Schoen FJ, Sacks MS. The effects of cellular contraction on aortic valve leaflet flexural stiffness. Journal of Biomechanics 2006;39:88.
[100] Jiang H, Campbell G, Boughner D, Wan W-K, Quantz M. Design and manufacture of a polyvinyl alcohol (PVA) cryogel tri-leaflet heart valve prosthesis. Medical Engineering & Physics 2004;26:269.
[101] Schoen FJ, Levy RJ. Tissue heart valves: current challenges and future research perspectives. Journal of biomedical materials research 1999;47:439.
[102] Simionescu DT, Lovekamp JJ, Vyavahare NR. Glycosaminoglycan-degrading enzymes in porcine aortic heart valves: implications for bioprosthetic heart valve degeneration. Journal of Heart Valve Disease 2003;12:217.
[103] Talman EA, Boughner DR. Internal shear properties of fresh porcine aortic valve cusps: implications for normal valve function. The Journal of heart valve disease 1996;5:152.
[104] Vesely I, Boughner D. Analysis of the bending behaviour of porcine xenograft leaflets and of natural aortic valve material: bending stiffness, neutral axis and shear measurements. Journal of biomechanics 1989;22:655.
[105] Anssari-Benam A, Bader DL, Screen HRC. A combined experimental and modelling approach to aortic valve viscoelasticity in tensile deformation. Journal of Materials Science: Materials in Medicine 2011;22:253.
[106] Song T, Vesely I, Boughner D. Effects of dynamic fixation on shear behaviour of porcine xenograft valves. Biomaterials 1990;11:191.
[107] Eckert CE, Fan R, Mikulis B, Barron M, Carruthers CA, Friebe VM, Vyavahare NR, Sacks MS. On the biomechanical role of glycosaminoglycans in the aortic heart valve leaflet. Acta biomaterialia 2013;9:4653.
[108] Buchanan RM, Sacks MS. Interlayer micromechanics of the aortic heart valve leaflet. Biomechanics and modeling in mechanobiology 2013:1.
[109] Sacks MS, Schoen FJ, Mayer Jr JE. Bioengineering challenges for heart valve tissue engineering. Annual Review of Biomedical Engineering, vol. 11, 2009. p.289.
[110] Hetzer HCR. Tissue Engineering in Cardiovascular Surgery. 2000.
[111] Sachlos E, Czernuszka JT. Making tissue engineering scaffolds work. Review: the application of solid freeform fabrication technology to the production of tissue engineering scaffolds. European cells & materials 2003;5:29.
[112] Taylor PM, Cass AEG, Yacoub MH. Extracellular matrix scaffolds for tissue engineering heart valves. Progress in Pediatric Cardiology 2006;21:219.
[113] Buttafoco L, Engbers-Buijtenhuijs P, Root AA, Dijkstra PJ, Daamen WF, Van Kuppeveit TH, Vermes I, Feijen J. First steps towards tissue engineering of small-diameter blood vessels: preparation of flat scaffolds of collagen and elastin by means of freeze drying. Journal of Biomedical Materials Research - Part B Applied Biomaterials 2006;77:357.
[114] Williams SF, Martin DP, Horowitz DM, Peoples OP. PHA applications: Addressing the price performance issue I. Tissue engineering. International Journal of Biological Macromolecules 1999;25:111.
[115] Stock UA, Nagashima M, Khalil PN, Nollert GD, Herden T, Sperling JS, Moran A, Lien J, Martin DP, Schoen FJ, Vacanti JP, Mayer Jr JE. Tissue-engineered valved

conduits in the pulmonary circulation. Journal of Thoracic and Cardiovascular Surgery 2000;119:732.
[116] Brody S, Pandit A. Approaches to heart valve tissue engineering scaffold design. Journal of Biomedical Materials Research Part B: Applied Biomaterials 2007;83:16.
[117] Leyh RG, Wilhelmi M, Walles T, Kallenbach K, Rebe P, Oberbeck A, Herden T, Haverich A, Mertsching H. Acellularized porcine heart valve scaffolds for heart valve tissue engineering and the risk of cross-species transmission of porcine endogenous retrovirus. The Journal of thoracic and cardiovascular surgery 2003;126:1000.
[118] Dohmen PM, Konertz W. Tissue-engineered heart valve scaffolds. Annals of Thoracic and Cardiovascular Surgery 2009;15:362.
[119] Steinhoff G, Stock U, Karim N, Mertsching H, Timke A, Meliss RR, Pethig K, Haverich A, Bader A. Tissue engineering of pulmonary heart valves on allogenic acellular matrix conduits: In vivo restoration of valve tissue. Circulation 2000;102:III50.
[120] Kim S-S, Lim S-H, Hong Y-S, Cho S-W, Ryu JH, Chang B-C, Choi CY, Kim B-S. Tissue Engineering of Heart Valves In Vivo Using Bone Marrow-derived Cells. Artificial Organs 2006;30:554.
[121] Simon P, Kasimir MT, Seebacher G, Weigel G, Ullrich R, Salzer-Muhar U, Rieder E, Wolner E. Early failure of the tissue engineered porcine heart valve SYNERGRAFT® in pediatric patients. European journal of cardio-thoracic surgery 2003;23:1002.
[122] Dohmen PM, Lembcke A, Hotz H, Kivelitz D, Konertz WF. Ross operation with a tissue-engineered heart valve. The Annals of Thoracic Surgery 2002;74:1438.
[123] Breuer CK, Mettler BA, Anthony T, Sales VL, Schoen FJ, Mayer JE. Application of tissue-engineering principles toward the development of a semilunar heart valve substitute. Tissue Engineering 2004;10:1725.
[124] Shinoka T, Shum-Tim D, Ma PX, Tanel RE, Langer R, Vacanti JP, Mayer Jr JE. Tissue-engineered heart valve leaflets: does cell origin affect outcome? Circulation 1997;96:II.
[125] Shinoka T, Ma PX, Shum-Tim D, Breuer CK, Cusick RA, Zund G, Langer R, Vacanti JP, Mayer Jr JE. Tissue-engineered heart valves. Autologous valve leaflet replacement study in a lamb model. Circulation 1996;94:II164.
[126] Shinoka T, Breuer CK, Tanel RE, Zund G, Miura T, Ma PX, Langer R, Vacanti JP, Mayer Jr JE. Tissue engineering heart valves: Valve leaflet replacement study in a lamb model. The Annals of Thoracic Surgery 1995;60, Supplement 3:S513.
[127] Sodian R, Sperling JS, Martin DP, Stock U, Mayer Jr JE, Vacanti JP. Tissue engineering of a trileaflet heart valve-early in vitro experiences with a combined polymer. Tissue engineering 1999;5:489.
[128] Sodian R, Hoerstrup SP, Sperling JS, Martin DP, Daebritz S, Mayer Jr JE, Vacanti JP. Evaluation of biodegradable, three-dimensional matrices for tissue engineering of heart valves. Asaio Journal 2000;46:107.
[129] Hoerstrup SP, Kadner A, Melnitchouk S, Trojan A, Eid K, Tracy J, Sodian R, Visjager JF, Kolb SA, Grunenfelder J, Zund G, Turina MI. Tissue engineering of functional trileaflet heart valves from human marrow stromal cells. Circulation 2002;106:I143.
[130] Sodian R, Hoerstrup SP, Sperling JS, Daebritz S, Martin DP, Moran AM, Kim BS, Schoen FJ, Vacanti JP, Mayer JE. Early in vivo experience with tissue-engineered trileaflet heart valves. Circulation 2000;102:Iii.
[131] Bronzino JD. The biomedical engineering handbook: Boca Raton : CRC/Taylor & Francis, 2006

[132] Chevallay B, Herbage D. Collagen-based biomaterials as 3D scaffold for cell cultures: Applications for tissue engineering and gene therapy. Medical and Biological Engineering and Computing 2000;38:211.
[133] Garg S, Arora, Murthy. Scaffold: a novel carrier for cell and drug delivery. Critical reviews in therapeutic drug carrier systems 2012;29:63.
[134] Matthews JA, Wnek GE, Simpson DG, Bowlin GL. Electrospinning of collagen nanofibers. Biomacromolecules 2002;3:232.
[135] Beachley V, Wen X. Polymer nanofibrous structures: Fabrication, biofunctionalization, and cell interactions. Progress in Polymer Science 2010;35:868.
[136] Beachley V, Wen X. Fabrication of nanofiber reinforced protein structures for tissue engineering. Materials Science and Engineering: C 2009;29:2448.
[137] Sell SA, McClure MJ, Garg K, Wolfe PS, Bowlin GL. Electrospinning of collagen/biopolymers for regenerative medicine and cardiovascular tissue engineering. Advanced drug delivery reviews 2009;61:1007.
[138] Vasita R, Katti DS. Nanofibers and their applications in tissue engineering. International journal of nanomedicine 2006;1:15.
[139] Murphy CM, Haugh MG, O'Brien FJ. The effect of mean pore size on cell attachment, proliferation and migration in collagen-glycosaminoglycan scaffolds for bone tissue engineering. Biomaterials 2010;31:461.
[140] O'Brien FJ, Harley BA, Yannas IV, Gibson L. Influence of freezing rate on pore structure in freeze-dried collagen-GAG scaffolds. Biomaterials 2004;25:1077.
[141] Ouellette J. Phase diagram of water. 2006.
[142] Chen Q, Bruyneel A, Clarke K, Carr C, Czernuszka JT. Collagen-Based Scaffolds for Potential Application of Heart Valve Tissue Engineering. Jounal of Tissue Science and Engineering 2012;3.
[143] Wood A. CO_2 Phase Diagram. 2006.
[144] Tseng Y-T, Wahl DA, Chang NA, Czernuszka JT. Characterisation of CPD and freeze dried collagen scaffold for tissue engineering. . 8th World Biomaterials Congress. Amsterdam Netherlands 2008.
[145] Khor E. Methods for the treatment of collagenous tissues for bioprostheses. Biomaterials 1997;18:95.
[146] Weadock K, Olson RM, Silver FH. Evaluation of collagen crosslinking techniques. Biomaterials Medical Devices and Artificial Organs 1983;11:293.
[147] Yahyouche A, Zhidao X, Czernuszka JT, Clover AJP. Macrophage-mediated degradation of crosslinked collagen scaffolds. Acta Biomaterialia 2011;7:278.
[148] Haugh MG, Jaasma MJ, O'Brien FJ. The effect of dehydrothermal treatment on the mechanical and structural properties of collagen-GAG scaffolds. Journal of Biomedical Materials Research Part A 2009;89A:363.
[149] Weadock KS, Miller EJ, Bellincampi LD, Zawadsky JP, Dunn MG. Physical cross-linking of collagen-fibers - comparison of unltraviolet-irradiation and dehydrothermal treatment. Journal of Biomedical Materials Research 1995;29:1373.
[150] Lo CM, Wang HB, Dembo M, Wang YL. Cell movement is guided by the rigidity of the substrate. Biophysical Journal 2000;79:144.
[151] Harley BA, Leung JH, Silva ECCM, Gibson LJ. Mechanical characterization of collagen-glycosaminoglycan scaffolds. Acta Biomaterialia 2007;3:463.
[152] Gibson LJ, Ashby MF. Cellular solids : structure and properties. Cambridge: Cambridge University Press, 1997
[153] Gibson LJ. Biomechanics of cellular solids. Journal of Biomechanics 2005;38:377.

[154] Kanungo BP, Gibson LJ. Density-property relationships in collagen-glycosaminoglycan scaffolds. Acta Biomaterialia 2010;6:344.
[155] Neal RA, Jean A, Park H, Wu PB, Hsiao J, Engelmayr GC, Jr., Langer R, Freed LE. Three-Dimensional Elastomeric Scaffolds Designed with Cardiac-Mimetic Structural and Mechanical Features. Tissue Engineering Part A 2012;19:793.
[156] Gentleman E, Lay AN, Dickerson DA, Nauman EA, Livesay GA, Dee KC. Mechanical characterization of collagen fibers and scaffolds for tissue engineering. Biomaterials 2003;24:3805.
[157] Tilley JMR, Chaudhury S, Hakimi O, Carr AJ, Czernuszka JT. Tenocyte proliferation on collagen scaffolds protects against degradation and improves scaffold properties. Journal of Materials Science-Materials in Medicine 2012;23:823.
[158] Taylor PM, Allen SP, Dreger SA, Yacoub MH. Human cardiac valve interstitial cells in collagen sponge: a biological three-dimensional matrix for tissue engineering. The Journal of heart valve disease 2002;11:298.
[159] Taylor PM, Sachlos E, Dreger SA, Chester AH, Czernuszka JT, Yacoub MH. Interaction of human valve interstitial cells with collagen matrices manufactured using rapid prototyping. Biomaterials 2006;27:2733.
[160] Dreger SA, Thomas P, Sachlos E, Chester AH, Czernuszka JT, Taylor PM, Yacoub MH. Potential for Synthesis and Degradation of Extracellular Matrix Proteins by Valve Interstitial Cells Seeded onto Collagen Scaffolds. Tissue Engineering 2006;12:2533.
[161] Colazzo F, Sarathchandra P, Smolenski RT, Chester AH, Tseng Y-T, Czernuszka JT, Yacoub MH, Taylor PM. Extracellular matrix production by adipose-derived stem cells: Implications for heart valve tissue engineering. Biomaterials 2010;32:119.
[162] Stock UA, Vacanti JP. Tissue engineering: Current state and prospects. Annual Review of Medicine, vol. 52, 2001. p.443.
[163] Hoerstrup SP, Zünd G, Schoeberlein A, Ye Q, Vogt PR, Turina MI. Fluorescence activated cell sorting: A reliable method in tissue engineering of a bioprosthetic heart valve. The Annals of Thoracic Surgery 1998;66:1653.
[164] Zünd G, Hoerstrup SP, Schoeberlein A, Lachat M, Uhlschmid G, Vogt PR, Turina M. Tissue engineering: A new approach in cardiovascular surgery; Seeding of human fibroblasts followed by human endothelial cells on resorbable mesh. European Journal of Cardio-Thoracic Surgery 1998;13:160.
[165] Schmidt D, Hoerstrup SP. Tissue engineered heart valves based on human cells. Swiss Medical Weekly 2006;136:618.
[166] Webera B, Emmerta MY, Hoerstrupa SP. Stem cells for heart valve regeneration. Swiss Med Wkly 2012;142:w13622.
[167] Schmidt D, Achermann J, Odermatt B, Breymann C, Mol A, Genoni M, Zund G, Hoerstrup SP. Prenatally Fabricated Autologous Human Living Heart Valves Based on Amniotic Fluid-Derived Progenitor Cells as Single Cell Source. Circulation 2007;116:I.
[168] Schmidt D, Achermann J, Odermatt B, Genoni M, Zund G, Hoerstrup SP. Cryopreserved amniotic fluid-derived cells: a lifelong autologous fetal stem cell source for heart valve tissue engineering. The Journal of heart valve disease 2008;17:446.
[169] Schmidt D, Mol A, Breymann C, Achermann J, Odermatt B, Gössi M, Neuenschwander S, Prêtre R, Genoni M, Zund G. Living autologous heart valves engineered from human prenatally harvested progenitors. Circulation 2006;114:I.
[170] Schmidt D, Mol A, Odermatt B, Neuenschwander S, Breymann C, Gössi M, Genoni M, Zund G, Hoerstrup SP. Engineering of biologically active living heart valve

leaflets using human umbilical cord-derived progenitor cells. Tissue engineering 2006;12:3223.
[171] Caspi O, Lesman A, Basevitch Y, Gepstein A, Arbel G, Huber I, Habib M, Gepstein L, Levenberg S. Tissue engineering of vascularized cardiac muscle from human embryonic stem cells. Circulation Research 2007;100:263.
[172] Liau B, Christoforou N, Bursac N. Electromechanically Functional Cardiac Tissue Constructs Engineered From Embryonic Stem Cells. Circulation 2009;120:S810.
[173] Parrag IC, Zandstra PW, Woodhouse KA. Fiber alignment and coculture with fibroblasts improves the differentiated phenotype of murine embryonic stem cell-derived cardiomyocytes for cardiac tissue engineering. Biotechnology and Bioengineering 2011;109:813.
[174] Forsberg M, Hovatta O. Challenges for the therapeutic use of pluripotent stem derived cells. Frontiers in physiology 2012;3.
[175] Takahashi K, Yamanaka S. Induction of pluripotent stem cells from mouse embryonic and adult fibroblast cultures by defined factors. cell 2006;126:663.
[176] Takahashi K, Tanabe K, Ohnuki M, Narita M, Ichisaka T, Tomoda K, Yamanaka S. Induction of pluripotent stem cells from adult human fibroblasts by defined factors. cell 2007;131:861.
[177] Schenke-Layland K, Rhodes KE, Angelis E, Butylkova Y, Heydarkhan-Hagvall S, Gekas C, Zhang R, Goldhaber JI, Mikkola HK, Plath K, MacLellan WR. Reprogrammed Mouse Fibroblasts Differentiate into Cells of the Cardiovascular and Hematopoietic Lineages. STEM CELLS 2008;26:1537.
[178] Narazaki G, Uosaki H, Teranishi M, Okita K, Kim B, Matsuoka S, Yamanaka S, Yamashita JK. Directed and Systematic Differentiation of Cardiovascular Cells From Mouse Induced Pluripotent Stem Cells. Circulation 2008;118:498.
[179] Vismara R, Soncini M, Talò G, Dainese L, Guarino A, Redaelli A, Fiore GB. A bioreactor with compliance monitoring for heart valve grafts. Annals of biomedical engineering 2010;38:100.
[180] Gandaglia A, Bagno A, Naso F, Spina M, Gerosa G. Cells, scaffolds and bioreactors for tissue-engineered heart valves: a journey from basic concepts to contemporary developmental innovations. European Journal of Cardio-Thoracic Surgery 2011;39:523.
[181] Jockenhoevel S, Zund G, Hoerstrup SP, Schnell A, Turina M. Cardiovascular tissue engineering: a new laminar flow chamber for in vitro improvement of mechanical tissue properties. ASAIO journal 2002;48:8.
[182] Barron V, Lyons E, Stenson-Cox C, McHugh PE, Pandit A. Bioreactors for Cardiovascular Cell and Tissue Growth: A Review. Annals of Biomedical Engineering 2003;31:1017.
[183] Topper JN, Gimbrone Jr MA. Blood flow and vascular gene expression: Fluid shear stress as a modulator of endothelial phenotype. Molecular Medicine Today 1999;5:40.
[184] O'Callaghan CJ, Williams B. Mechanical strain-induced extracellular matrix production by human vascular smooth muscle cells: Role of TGF-β1. Hypertension 2000;36:319.
[185] Hubbell JA. Biomaterials in Tissue Engineering. Nat Biotech 1995;13:565.
[186] Dvorin EL, Wylie-Sears J, Kaushal S, Martin DP, Bischoff J. Quantitative evaluation of endothelial progenitors and cardiac valve endothelial cells: Proliferation and differentiation on poly-glycolic acid/poly-4-hydroxybutyrate scaffold in response to vascular endothelial growth factor and transforming growth factor beta(1). Tissue Engineering 2003;9:487.

[187] Ota T, Sawa Y, Iwai S, Kitajima T, Ueda Y, Coppin C, Matsuda H, Okita Y. Fibronectin-Hepatocyte Growth Factor Enhances Reendothelialization in Tissue-Engineered Heart Valve. The Annals of Thoracic Surgery 2005;80:1794.
[188] Bin F, Yinglong L, Nin X, Kai F, Laifeng S, Xiaodong Z. Construction of Tissue-Engineered Homograft Bioprosthetic Heart Valves In Vitro. ASAIO Journal 2006;52:303.
[189] Sales VL, Engelmayr GC, Mettler BA, Johnson JA, Sacks MS, Mayer JE. Transforming Growth Factor-β Modulates Extracellular Matrix Production, Proliferation, and Apoptosis of Endothelial Progenitor Cells in Tissue-Engineering Scaffolds. Circulation 2006;114:193.
[190] Lanza RP, Langer RS, Vacanti J. Principles of tissue engineering Amsterdam ; London : Elsevier/Academic Press, 2007
[191] Ratcliffe A, Niklason LE. Bioreactors and bioprocessing for tissue engineering. Annals of the New York Academy of Sciences, vol. 961, 2002. p.210.
[192] Anthony Atala RPL. Methods of tissue engineering. San Diego, Calif: London : Academic Press 2002.
[193] Brown MA, Iyer RK, Radisic M. Pulsatile perfusion bioreactor for cardiac tissue engineering. Biotechnology Progress 2008;24:907.
[194] Engelmayr Jr GC, Rabkin E, Sutherland FWH, Schoen FJ, Mayer Jr JE, Sacks MS. The independent role of cyclic flexure in the early in vitro development of an engineered heart valve tissue. Biomaterials 2005;26:175.
[195] Tuckwell D, Humphries M. Integrin-collagen binding. Seminars in Cell & Developmental Biology 1996;7:649.
[196] Yannas IV. Tissue regeneration by use of collagen-glycosaminoglycan copolymers. Clinical Materials 1992;9:179.
[197] Haugh MG, Murphy CM, O'Brien FJ. Novel Freeze-Drying Methods to Produce a Range of Collagen-Glycosaminoglycan Scaffolds with Tailored Mean Pore Sizes. Tissue Engineering Part C-Methods 2009;16:887.
[198] Friess W. Collagen - biomaterial for drug delivery. European Journal of Pharmaceutics and Biopharmaceutics 1998;45:113.
[199] Gustavson KH. The chemistry and reactivity of collagen New York: New York : Academic Press, 1956.
[200] Tseng Y-T. Heart Valve Tissue Engineering. Department of Materials. Oxford: University of Oxford, 2010.
[201] Sachlos E, Reis N, Ainsley C, Derby B, Czernuszka JT. Novel collagen scaffolds with predefined internal morphology made by solid freeform fabrication. Biomaterials 2003;24:1487.
[202] Lew D-H, Liu PH-T, Orgill DP. Optimization of UV cross-linking density for durable and nontoxic collagen GAG dermal substitute. Journal of Biomedical Materials Research Part B-Applied Biomaterials 2007;82B:51.
[203] Achilli M, Lagueux J, Mantovani D. On the Effects of UV-C and pH on the Mechanical Behavior, Molecular Conformation and Cell Viability of Collagen-Based Scaffold for Vascular Tissue Engineering. Macromolecular Bioscience 2010;10:307.
[204] Kamińska A, Sionkowska A. Effect of UV radiation on the infrared spectra of collagen. Polymer Degradation and Stability 1996;51:19.
[205] Kirsch KM, Zelickson BD, Zachary CB, Tope WD. ULtrastructure of collagen thermally denatured by microsecond domain pulsed carbon dioxide laser. Archives of Dermatology 1998;134:1255.

[206] Rubin S, Bonnier E, Sandt C, Venteo L, Pluot M, Baehrel B, Manfait M, Sockalingum GD. Analysis of structural changes in normal and aneurismal human aortic tissues using FTIR microscopy. Biopolymers 2008;89:160.
[207] BOCSciences. Product Infomation. 2012.
[208] Bonnier F, Rubin S, Venteo L, Krishna CM, Pluot M, Baehrel B, Manfait M, Sockalingum GD. In-vitro analysis of normal and aneurismal human ascending aortic tissues using FT-IR micro spectroscopy. Biochimica Et Biophysica Acta-Biomembranes 2006;1758:968.
[209] Smith BC. Infrared spectral interpretation : a systematic approach. Boca Raton :: CRC Press, 1999.
[210] Everaerts FJL. A novel approach in cross-linking of bioprosthetic heart valves. Enschede: University of Twente, 2007.
[211] Belbachir K, Noreen R, Gouspillou G, Petibois C. Collagen types analysis and differentiation by FTIR spectroscopy. Analytical and Bioanalytical Chemistry 2009;395:829.
[212] Garnjanagoonchorn W, Wongekalak L, Engkagul A. Determination of chondroitin sulfate from different sources of cartilage. Chemical Engineering and Processing 2007;46:465.
[213] Amrutkar JR, Gattani SG. Chitosan-chondroitin sulfate based matrix tablets for colon specific delivery of indomethacin. AAPS PharmSciTech 2009;10:670.
[214] Wang D-A, Varghese S, Sharma B, Strehin I, Fermanian S, Gorham J, Fairbrother DH, Cascio B, Elisseeff JH. Multifunctional chondroitin sulphate for cartilage tissue-biomaterial integration. Nat Mater 2007;6:385.
[215] Lachezar Radev NYM, Irena Michailova, Isabel M. M. Salvado, Maria H. V. Fernandes. In Vitro Bioactivity of Collagen/Calcium Phosphate SilicateComposites, Cross-Linked with Chondroitin Sulfate. International Journal of Materials and Chemistry 2012;2:1.
[216] Doyle BB, Blout ER, Bendit EG. Infrared spectroscopy of collagen and collagen like polypeptides. Biopolymers 1975;14:937.
[217] Severcan F, Toyran N, Kaptan N, Turan B. Fourier transform infrared study of the effect of diabetes on rat liver and heart tissues in the C-H region. Talanta 2000;53:55.
[218] Tian H, Chen Y, Ding C, Li G. Interaction study in homogeneous collagen/chondroitin sulfate blends by two-dimensional infrared spectroscopy. Carbohydrate Polymers 2012;89:542.
[219] Wang XH, Li DP, Wang WJ, Feng QL, Cui FZ, Xu YX, Song XH, van der Werf M. Crosslinked collagen/chitosan matrix for artificial livers. Biomaterials 2003;24:3213.
[220] Sung N. Structure and properties of collagen and gelatine in the hydrated and anhydrous state. vol. Ph.D. Cambridge, MA: MIT, 1972.
[221] Muyonga JH, Cole CGB, Duodu KG. Fourier transform infrared (FTIR) spectroscopic study of acid soluble collagen and gelatin from skins and bones of young and adult Nile perch (Lates niloticus). Food Chemistry 2004;86:325.
[222] Edelmann L. Freeze-dried and resin-embedded biological material is well suited for ultrastructure research. Journal of Microscopy 2002;207:5.
[223] Grunbaum BW, Wellings SR. Freeze-drying apparatus for preservation of ultrastructure. Journal of Ultrastructure Research 1960;4:117.
[224] Davis RB. Ultrastructural characteristics of freeze-dried human blood platelets. The American journal of pathology 1972;68:303.

[225] Highberger JH. The Isoelectric Point of Collagen. Journal of the American Chemical Society 1939;61:2302.
[226] Crabb RAB, Chau EP, Evans MC, Barocas VH, Hubel A. Biomechanical and Microstructural Characteristics of a Collagen Film-Based Corneal Stroma Equivalent. Tissue Engineering 2006;12:1565.
[227] Gutsmann T, Fantner GE, Kindt JH, Venturoni M, Danielsen S, Hansma PK. Force Spectroscopy of Collagen Fibers to Investigate Their Mechanical Properties and Structural Organization. Biophysical Journal 2004;86:3186.
[228] Gu L, Kim YK, Liu Y, Ryou H, Wimmer CE, Dai L, Arola DD, Looney SW, Pashley DH, Tay FR. Biomimetic Analogs for Collagen Biomineralization. Journal of Dental Research 2011;90:82.
[229] Raspanti M, Ottani V, Ruggeri A. Different architectures of the collagen fibril: morphological aspects and functional implications. International Journal of Biological Macromolecules 1989;11:367.
[230] Lillie JH, MacCallum DK, Scaletta LJ, Occhino JC. Collagen structure: Evidence for a helical organization of the collagen fibril. Journal of Ultrastructure Research 1977;58:134.
[231] Debelle L, Tamburro AM. Elastin: molecular description and function. The International Journal of Biochemistry & Cell Biology 1999;31:261.
[232] Wright NT, Humphrey JD. Denaturation of collagen via heating: An irreversible rate process. Annual Review of Biomedical Engineering 2002;4:109.
[233] Pieper JS, Hafmans T, Veerkamp JH, van Kuppevelt TH. Development of tailor-made collagen-glycosaminoglycan matrices: EDC/NHS crosslinking, and ultrastructural aspects. Biomaterials 2000;21:581.
[234] O'Brien FJ, Harley BA, Yannas IV, Gibson LJ. The effect of pore size on cell adhesion in collagen-GAG scaffolds. Biomaterials 2005;26:433.
[235] Franks F. Freeze-Drying of Pharmaceuticals and Biopharmaceuticals: Principles and Practice: Royal Society of Chemistry, 2007.
[236] Oh SH, Park IK, Kim JM, Lee JH. In vitro and in vivo characteristics of PCL scaffolds with pore size gradient fabricated by a centrifugation method. Biomaterials 2007;28:1664.
[237] Zeltinger J, Sherwood JK, Graham DA, Müeller R, Griffith LG. Effect of pore size and void fraction on cellular adhesion, proliferation, and matrix deposition. Tissue Engineering 2001;7:557.
[238] Wahl D, Sachlos E, Liu C, Czernuszka J. Controlling the processing of collagen-hydroxyapatite scaffolds for bone tissue engineering. Journal of Materials Science: Materials in Medicine 2007;18:201.
[239] Atkins E. Conformation in polysacchrides and complex carbohydrates. Journal of Biosciences 1985;8:375.
[240] The water-sucrose system. Cambridge: Dissemination of IT for the promotion of Materials Science, 2004.
[241] Donald L. Wise DJT, David E. Altobelli, Joseph D. Gresser, Michael J. Yaszemski. Encyclopedic Handbook of Biomaterials and Bioengineering: CRC Press, 1995.
[242] Brice JC. The growth of crystals from the melt. Amsterdam;: North-Holland Publishing Company, 1965.
[243] Daamen WF, van Moerkerk HTB, Hafmans T, Buttafoco L, Poot AA, Veerkamp JH, van Kuppevelt TH. Preparation and evaluation of molecularly-defined collagen-elastin-glycosaminoglycan scaffolds for tissue engineering. Biomaterials 2003;24:4001.

[244] Kane RJ, Roeder RK. Effects of hydroxyapatite reinforcement on the architecture and mechanical properties of freeze-dried collagen scaffolds. Journal of the Mechanical Behavior of Biomedical Materials 2012;7:41.
[245] Engelmayr GC, Jr., Cheng M, Bettinger CJ, Borenstein JT, Langer R, Freed LE. Accordion-like honeycombs for tissue engineering of cardiac anisotropy. Nature Materials 2008;7:1003.
[246] Stella JA, D'Amore A, Wagner WR, Sacks MS. On the biomechanical function of scaffolds for engineering load-bearing soft tissues. Acta Biomaterialia 2010;6:2365.
[247] ANSYS. ANSYS Structural analysis guide: ANSYS release 11.0: ANSYS Inc., 2007.
[248] Redaelli A, Vesentini S, Soncini M, Vena P, Mantero S, Montevecchi FM. Possible role of decorin glycosaminoglycans in fibril to fibril force transfer in relative mature tendons-a computational study from molecular to microstructural level. Journal of Biomechanics 2003;36:1555.
[249] Shah SR, Vyavahare NR. The effect of glycosaminoglycan stabilization on tissue buckling in bioprosthetic heart valves. Biomaterials 2008;29:1645.
[250] Tu DD, Chung YG, Gil ES, Seth A, Franck D, Cristofaro V, Sullivan MP, Di Vizio D, Gomez Iii P, Adam RM, Kaplan DL, Estrada Jr CR, Mauney JR. Bladder tissue regeneration using acellular bi-layer silk scaffolds in a large animal model of augmentation cystoplasty. Biomaterials 2013;34:8681.
[251] Zhang S, Chen L, Jiang Y, Cai Y, Xu G, Tong T, Zhang W, Wang L, Ji J, Shi P, Ouyang HW. Bi-layer collagen/microporous electrospun nanofiber scaffold improves the osteochondral regeneration. Acta Biomaterialia 2013;9:7236.
[252] Zhang W, Chen J, Tao J, Hu C, Chen L, Zhao H, Xu G, Heng BC, Ouyang HW. The promotion of osteochondral repair by combined intra-articular injection of parathyroid hormone-related protein and implantation of a bi-layer collagen-silk scaffold. Biomaterials 2013;34:6046.
[253] Ju YM, Choi JS, Atala A, Yoo JJ, Lee SJ. Bilayered scaffold for engineering cellularized blood vessels. Biomaterials 2010;31:4313.
[254] Vaz CM, van Tuijl S, Bouten CVC, Baaijens FPT. Design of scaffolds for blood vessel tissue engineering using a multi-layering electrospinning technique. Acta Biomaterialia 2005;1:575.
[255] Merryman W, Huang H-Y, Schoen FJ, Sacks MS. The effects of cellular contraction on aortic valve leaflet flexural stiffness. Journal of Biomechanics 2006;39:88.
[256] Billiar KL, Sacks MS. Biaxial mechanical properties of the natural and glutaraldehyde treated aortic valve cusp - part I: experimental results. Journal of biomechanical engineering 2000;122:23.
[257] Gloeckner DG, Bihir KL, Sacks MS. Effects of Mechanical Fatigue on the Bending Properties of the Porcine Bioprosthetic Heart Valve. ASAIO Journal 1999;45:59.
[258] Westaby S, Karp RB, Blackstone EH, Bishop SP. Adult human valve dimensions and their surgical significance. The American Journal of Cardiology 1984;53:552.
[259] Engelmayr Jr GC, Papworth GD, Watkins SC, Mayer Jr JE, Sacks MS. Guidance of engineered tissue collagen orientation by large-scale scaffold microstructures. Journal of Biomechanics 2006;39:1819.
[260] Masoumi N, Johnson KL, Howell MC, Engelmayr Jr GC. Valvular interstitial cell seeded poly(glycerol sebacate) scaffolds: Toward a biomimetic in vitro model for heart valve tissue engineering. Acta Biomaterialia 2013;9:5974.

[261] Madaghiele M, Sannino A, Yannas IV, Spector M. Collagen-based matrices with axially oriented pores. Journal of Biomedical Materials Research Part A 2008;85A:757.
[262] Wu X, Liu Y, Li X, Wen P, Zhang Y, Long Y, Wang X, Guo Y, Xing F, Gao J. Preparation of aligned porous gelatin scaffolds by unidirectional freeze-drying method. Acta Biomaterialia 2010;6:1167.
[263] Stokols S, Tuszynski MH. The fabrication and characterization of linearly oriented nerve guidance scaffolds for spinal cord injury. Biomaterials 2004;25:5839.
[264] Bigi A, Panzavolta S, Rubini K. Relationship between triple-helix content and mechanical properties of gelatin films. Biomaterials 2004;25:5675.
[265] Ma L, Gao C, Mao Z, Zhou J, Shen J, Hu X, Han C. Collagen/chitosan porous scaffolds with improved biostability for skin tissue engineering. Biomaterials 2003;24:4833.
[266] Whitson BA, Cheng BC, Kokini K, Badylak SF, Patel U, Morff R, O'Keefe CR. Multilaminate resorbable biomedical device under biaxial loading. Journal of Biomedical Materials Research 1998;43:277.
[267] Ma J, Wang H, He B, Chen J. A preliminary in vitro study on the fabrication and tissue engineering applications of a novel chitosan bilayer material as a scaffold of human neofetal dermal fibroblasts. Biomaterials 2001;22:331.
[268] Adekogbe I, Ghanem A. Fabrication and characterization of DTBP-crosslinked chitosan scaffolds for skin tissue engineering. Biomaterials 2005;26:7241.
[269] Chalmers GW, Gosline JM, Lillie MA. The hydrophobicity of vertebrate elastins. Journal of experimental biology 1999;202:301.
[270] Sandberg LB, Soskel NT, Leslie JG. Elastin Structure, Biosynthesis, and Relation to Disease States. New England Journal of Medicine 1981;304:566.
[271] Farndale RW, Buttle DJ, Barrett AJ. Improved quantitation and discrimination of sulphated glycosaminoglycans by use of dimethylmethylene blue. Biochimica et Biophysica Acta (BBA) - General Subjects 1986;883:173.
[272] Chandrasekhar S, Esterman MA, Hoffman HA. Microdetermination of proteoglycans and glycosaminoglycans in the presence of guanidine hydrochloride. Analytical Biochemistry 1987;161:103.
[273] Donatelli R, Owens-Burkhart H. Effects of Immobilization on the Extensibility of Periarticular Connective Tissue. Journal of Orthopaedic & Sports Physical Therapy 1981;3:67.
[274] Woo SLY, Matthews JV, Akeson WH, Amiel D, Richard Convery F. Connective tissue response to immobility. Arthritis & Rheumatism 1975;18:257.
[275] Tseng H, Grande-Allen KJ. Elastic fibers in the aortic valve spongiosa: A fresh perspective on its structure and role in overall tissue function. Acta Biomaterialia;7:2101.
[276] Eldred JR, Rogers K, Boughner D. Tissue Engineering the Aortic Valve Spongiosa Using Matrigel-Cell-Scaffold-Composites (MCSCs). The FASEB Journal 2008;22:903.6.
[277] Marbán E, Cingolani E. Heart to heart: Cardiospheres for myocardial regeneration. Heart Rhythm 2012;9:1727.
[278] Leor J, Amsalem Y, Cohen S. Cells, scaffolds, and molecules for myocardial tissue engineering. Pharmacology & Therapeutics 2005;105:151.
[279] Smith RR, Barile L, Cho HC, Leppo MK, Hare JM, Messina E, Giacomello A, Abraham MR, Marban E. Regenerative potential of cardiosphere-derived cells expanded from percutaneous endomyocardial biopsy specimens. Circulation 2007;115:896.

[280] Quaini F, Urbanek K, Beltrami AP, Finato N, Beltrami CA, Nadal-Ginard B, Kajstura J, Leri A, Anversa P. Chimerism of the Transplanted Heart. New England Journal of Medicine 2002;346:5.
[281] Urbanek K, Quaini F, Tasca G, Torella D, Castaldo C, Nadal-Ginard B, Leri A, Kajstura J, Quaini E, Anversa P. Intense myocyte formation from cardiac stem cells in human cardiac hypertrophy. Proceedings of the National Academy of Sciences 2003;100:10440.
[282] Beltrami AP, Barlucchi L, Torella D, Baker M, Limana F, Chimenti S, Kasahara H, Rota M, Musso E, Urbanek K, Leri A, Kajstura J, Nadal-Ginard B, Anversa P. Adult Cardiac Stem Cells Are Multipotent and Support Myocardial Regeneration. Cell 2003;114:763.
[283] Makkar RR, Smith RR, Cheng K, Malliaras K, Thomson LEJ, Berman D, Czer LSC, Marbán L, Mendizabal A, Johnston PV, Russell SD, Schuleri KH, Lardo AC, Gerstenblith G, Marbán E. Intracoronary cardiosphere-derived cells for heart regeneration after myocardial infarction (CADUCEUS): a prospective, randomised phase 1 trial. The Lancet 2012;379:895.
[284] McCarthy RE, Boehmer JP, Hruban RH, Hutchins GM, Kasper EK, Hare JM, Baughman KL. Long-term outcome of fulminant myocarditis as compared with acute (nonfulminant) myocarditis. New England Journal of Medicine 2000;342:690.
[285] Davis DR, Zhang Y, Smith RR, Cheng K, Terrovitis J, Malliaras K, Li T-S, White A, Makkar R, Marbán E. Validation of the Cardiosphere Method to Culture Cardiac Progenitor Cells from Myocardial Tissue. PLoS ONE 2009;4:e7195.
[286] Johnston PV, Sasano T, Mills K, Evers R, Lee S-T, Smith RR, Lardo AC, Lai S, Steenbergen C, Gerstenblith G. Engraftment, differentiation, and functional benefits of autologous cardiosphere-derived cells in porcine ischemic cardiomyopathy. Circulation 2009;120:1075.
[287] Li Z, Guo X, Matsushita S, Guan J. Differentiation of cardiosphere-derived cells into a mature cardiac lineage using biodegradable poly (N-isopropylacrylamide) hydrogels. Biomaterials 2011;32:3220.
[288] Lee S-T, White AJ, Matsushita S, Malliaras K, Steenbergen C, Zhang Y, Li T-S, Terrovitis J, Yee K, Simsir S, Makkar R, Marbán E. Intramyocardial Injection of Autologous Cardiospheres or Cardiosphere-Derived Cells Preserves Function and Minimizes Adverse Ventricular Remodeling in Pigs With Heart Failure Post-Myocardial Infarction. Journal of the American College of Cardiology 2011;57:455.
[289] Carr CA, Stuckey DJ, Tan JJ, Tan SC, Gomes RSM, Camelliti P, Messina E, Giacomello A, Ellison GM, Clarke K. Cardiosphere-Derived Cells Improve Function in the Infarcted Rat Heart for at Least 16 Weeks - an MRI Study. PLoS ONE 2011;6:e25669.
[290] Messina E, De Angelis L, Frati G, Morrone S, Chimenti S, Fiordaliso F, Salio M, Battaglia M, Latronico MVG, Coletta M, Vivarelli E, Frati L, Cossu G, Giacomello A. Isolation and Expansion of Adult Cardiac Stem Cells From Human and Murine Heart. Circulation Research 2004;95:911.
[291] Tan J-J, Carr CA, Stuckey DJ, Ellison GM, Messina E, Giacomello A, Clarke K. Isolation and Expansion of Cardiosphere-Derived Stem Cells. Current Protocols in Stem Cell Biology. John Wiley & Sons, Inc., 2007.
[292] Serotec A. alamarBlue® Technical Datasheet. 2008.
[293] Zipfel WR, Williams RM, Webb WW. Nonlinear magic: multiphoton microscopy in the biosciences. Nature biotechnology 2003;21:1368.
[294] Williams RM, Zipfel WR, Webb WW. Multiphoton microscopy in biological research. Current Opinion in Chemical Biology 2001;5:603.

[295] König K. Multiphoton microscopy in life sciences. Journal of Microscopy 2000;200:83.
[296] Zipfel WR, Williams RM, Christie R, Nikitin AY, Hyman BT, Webb WW. Live tissue intrinsic emission microscopy using multiphoton-excited native fluorescence and second harmonic generation. Proceedings of the National Academy of Sciences 2003;100:7075.
[297] Cui ZF, Xu X, Trainor N, Triffitt JT, Urban JPG, Tirlapur UK. Application of multiple parallel perfused microbioreactors and three-dimensional stem cell culture for toxicity testing. Toxicology in Vitro 2007;21:1318.
[298] Wissink MJB, Beernink R, Pieper JS, Poot AA, Engbers GHM, Beugeling T, van Aken WG, Feijen J. Binding and release of basic fibroblast growth factor from heparinized collagen matrices. Biomaterials 2001;22:2291.
[299] Sugahara K, Mikami T, Uyama T, Mizuguchi S, Nomura K, Kitagawa H. Recent advances in the structural biology of chondroitin sulfate and dermatan sulfate. Current Opinion in Structural Biology 2003;13:612.
[300] Hubbell JA. Materials as morphogenetic guides in tissue engineering. Current Opinion in Biotechnology 2003;14:551.
[301] Ferdous ZZ, Grande-Allen KJKJ. Utility and control of proteoglycans in tissue engineering. Tissue engineering 2007;13:1893.
[302] Uygun BE, Stojsih SE, Matthew HW. Effects of immobilized glycosaminoglycans on the proliferation and differentiation of mesenchymal stem cells. Tissue engineering. Part A 2009;15:3499.
[303] Raines EW, Ross R. Smooth-muscle cells and the pathogenesis of the leision of atherosclerosis. British Heart Journal 1993;69:S30.
[304] Owens GK. Molecular control of vascular smooth muscle cell differentiation. Acta physiologica Scandinavica 1998;164:623.
[305] Thyberg J. Phenotypic modulation of smooth muscle cells during formation of neointimal thickenings following vascular injury. Histology and histopathology 1998;13:871.
[306] Karnik SK, Brooke BS, Bayes-Genis A, Sorensen L, Wythe JD, Schwartz RS, Keating MT, Li DY. A critical role for elastin signaling in vascular morphogenesis and disease. Development 2003;130:411.
[307] Vernon RB, Lane TF, Angello JC, Sage H. Adhesion, shape, proliferation, and gene-expression of mouse Leydig-cells are influenced by extracellular-matrix in vitro. Biology of Reproduction 1991;44:157.
[308] Evanko SP, Angello JC, Wight TN. Formation of hyaluronan- and versican-rich pericellular matrix is required for proliferation and migration of vascular smooth muscle cells. Arteriosclerosis Thrombosis and Vascular Biology 1999;19:1004.
[309] Jones LJ, Gray M, Yue ST, Haugland RP, Singer VL. Sensitive determination of cell number using the CyQUANTÂ® cell proliferation assay. Journal of Immunological Methods 2001;254:85.
[310] Bruyneel A. Unpublished Results: Comparison of CyQUANT® assay and alamarBlue® assay for cell number quantification. 2013.
[311] Li Z, Ramay HR, Hauch KD, Xiao D, Zhang M. Chitosan-alginate hybrid scaffolds for bone tissue engineering. Biomaterials 2005;26:3919.
[312] Wang Y, Kim U-J, Blasioli DJ, Kim H-J, Kaplan DL. In vitro cartilage tissue engineering with 3D porous aqueous-derived silk scaffolds and mesenchymal stem cells. Biomaterials 2005;26:7082.
[313] Li M, Mondrinos MJ, Gandhi MR, Ko FK, Weiss AS, Lelkes PI. Electrospun protein fibers as matrices for tissue engineering. Biomaterials 2005;26:5999.

[314] Mandal BB, Kundu SC. Cell proliferation and migration in silk fibroin 3D scaffolds. Biomaterials 2009;30:2956.
[315] Linnes MP, Ratner BD, Giachelli CM. A fibrinogen-based precision microporous scaffold for tissue engineering. Biomaterials 2007;28:5298.
[316] Wilson CE, Dhert WJA, Van Blitterswijk CA, Verbout AJ, De Bruijn JD. Evaluating 3D bone tissue engineered constructs with different seeding densities using the alamarBlue® assay and the effect on in vivo bone formation. Journal of Materials Science: Materials in Medicine 2002;13:1265.
[317] Gille J, Swerlick RA. Integrins: Role in Cell Adhesion and Communication. Annals of the New York Academy of Sciences 1996;797:93.
[318] Cornwell KG, Lei P, Andreadis ST, Pins GD. Crosslinking of discrete self-assembled collagen threads: Effects on mechanical strength and cell-matrix interactions. Journal of Biomedical Materials Research Part A 2007;80A:362.
[319] Ber S, Kose GT, Hasirci V. Bone tissue engineering on patterned collagen films: an in vitro study. Biomaterials 2005;26:1977.
[320] Grinnell F, Feld MK. Adsorption characteristics of plasma fibronectin in relationship to biological-ativity. Journal of Biomedical Materials Research 1981;15:363.
[321] Grinnell F, Feld MK. Fibronectin adsorption on hydrophilic and hydrophobic surfaces detected by antibody binding and analyzed during cell adhesion in serum-containing medium. Journal of Biological Chemistry 1982;257:4888.
[322] Grab B, Miles AJ, Furcht LT, Fields GB. Promotion of fibroblast adhesion by triple-helical peptide models of type I collagen-derived sequences. Journal of Biological Chemistry 1996;271:12234.
[323] Kuhn K, Eble J. The structural bases of integrin-ligand interactions. Trends in cell biology 1994;4:256.
[324] Skopinska-Wisniewska J, Sionkowska A, Kaminska A, Kaznica A, Jachimiak R, Drewa T. Surface characterization of collagen/elastin based biomaterials for tissue regeneration. Applied Surface Science 2009;255:8286.
[325] Inoue N, Bessho M, Furuta M, Kojima T, Okuda S, Hara M. A novel collagen hydrogel cross-linked by gamma-ray irradiation in acidic pH conditions. Journal of Biomaterials Science, Polymer Edition 2006;17:837.
[326] Yannas IV, Lee E, Orgill DP, Skrabut EM, Murphy GF. Synthesis and characterization of a model extracellular matrix that induces partial regeneration of adult mammalian skin. Proceedings of the National Academy of Sciences 1989;86:933.
[327] Griffon DJ, Sedighi MR, Schaeffer DV, Eurell JA, Johnson AL. Chitosan scaffolds: interconnective pore size and cartilage engineering. Acta biomaterialia 2006;2:313.
[328] Tedder ME, Simionescu A, Chen J, Liao J, Simionescu DT. Assembly and Testing of Stem Cell-Seeded Layered Collagen Constructs for Heart Valve Tissue Engineering. Tissue Engineering Part A 2010;17:25.
[329] De Cock LJ, De Koker S, De Vos F, Vervaet C, Remon J-P, De Geest BG. Layer-by-Layer Incorporation of Growth Factors in Decellularized Aortic Heart Valve Leaflets. Biomacromolecules 2010;11:1002.
[330] Elkins RC, Dawson PE, Goldstein S, Walsh SP, Black KS. Decellularized human valve allografts. Annals of Thoracic Surgery 2001;71:S428.
[331] Siew A. Controlling Ice Nucleation During the Freezing Step of Lyophilization. Pharmaceutical Technology 2013;37:36.

[332] Geidobler R, Winter G. Controlled ice nucleation in the field of freeze-drying: Fundamentals and technology review. European Journal of Pharmaceutics and Biopharmaceutics;85:214.
[333] Buttafoco L, Kolkman NG, Engbers-Buijtenhuijs P, Poot AA, Dijkstra PJ, Vermes I, Feijen J. Electrospinning of collagen and elastin for tissue engineering applications. Biomaterials 2006;27:724.
[334] Boland ED, Matthews JA, Pawlowski KJ, Simpson DG, Wnek GE, Bowlin GL. Electrospinning collagen and elastin: Preliminary vascular tissue engineering. Frontiers in Bioscience 2004;9:1422.
[335] Jain N, Sharma PK, Banik A, Gupta A, Bhardwaj V. Pharmaceutical and Biomedical Applications of Interpenetrating Polymer Network. Current Drug Therapy 2011;6:8.
[336] Brigham MD, Bick A, Lo E, Bendali A, Burdick JA, Khademhosseini A. Mechanically Robust and Bioadhesive Collagen and Photocrosslinkable Hyaluronic Acid Semi-Interpenetrating Networks. Tissue Engineering Part A 2009;15:1645.
[337] Guo Y, Yuan T, Xiao Z, Tang P, Xiao Y, Fan Y, Zhang X. Hydrogels of collagen/chondroitin sulfate/hyaluronan interpenetrating polymer network for cartilage tissue engineering. Journal of Materials Science: Materials in Medicine 2012;23:2267.
[338] Merryman WD, Youn I, Lukoff HD, Krueger PM, Guilak F, Hopkins RA, Sacks MS. Correlation between heart valve interstitial cell stiffness and transvalvular pressure: implications for collagen biosynthesis, 2006.
[339] Merryman WD, Liao J, Parekh A, Candiello JE, Lin H, Sacks MS. Differences in tissue-remodeling potential of aortic and pulmonary heart valve interstitial cells. Tissue engineering 2007;13:2281.
[340] Chester AH, Taylor PM. Molecular and functional characteristics of heart-valve interstitial cells. Philosophical Transactions of the Royal Society B: Biological Sciences 2007;362:1437.
[341] Anssari-Benam A, Gupta HS, Screen HRC. Strain transfer through the aortic valve. Journal of biomechanical engineering 2012;134:061003.
[342] Chen G, Sato T, Ushida T, Ochiai N, Tateishi T. Tissue engineering of cartilage using a hybrid scaffold of synthetic polymer and collagen. Tissue Engineering 2004;10:323.
[343] Chen G, Sato T, Ohgushi H, Ushida T, Tateishi T, Tanaka J. Culturing of skin fibroblasts in a thin PLGA-collagen hybrid mesh. Biomaterials 2005;26:2559.
[344] Chen G, Akahane D, Kawazoe N, Yamamoto K, Tateishi T. Chondrogenic differentiation of mesenchymal stem cells in a leakproof collagen sponge. Materials Science and Engineering: C 2008;28:195.
[345] Roelofs LAJ, Eggink AJ, Hulsbergen-van de Kaa CA, van den Berg PP, van Kuppevelt TH, van Moerkerk HTB, Crevels AJ, Lotgering FK, Feitz WFJ, Wijnen RMH. Fetal abdominal wall repair with a collagen biomatrix in an experimental sheep model for gastroschisis. Tissue Engineering Part A 2008;14:2033.
[346] Kreke M, Smith RR, Marban L, Marban E. Cardiospheres and cardiosphere-derived cells as therapeutic agents following myocardial infarction. Expert review of cardiovascular therapy 2012;10:1185.
[347] Chan A, Higuichi T, Sun D, Strehin I, Lin X, Lu Q, Armstrong P, O'Rourke B, Elisseeff J, Abraham MR. Autologous Tissue Engineering Scaffolds for Cellular Cardiomyoplasty. Circulation 2011;124.
[348] Chang CY, Chan AT, Armstrong PA, Luo H-C, Higuchi T, Strehin IA, Vakrou S, Lin X, Brown SN, O'Rourke B, Abraham TP, Wahl RL, Steenbergen CJ, Elisseeff

JH, Abraham MR. Hyaluronic acid-human blood hydrogels for stem cell transplantation. Biomaterials 2012;33:8026.
[349] Chimenti I, Rizzitelli G, Gaetani R, Angelini F, Ionta V, Forte E, Frati G, Schussler O, Barbetta A, Messina E, Dentini M, Giacomello A. Human cardiosphere-seeded gelatin and collagen scaffolds as cardiogenic engineered bioconstructs. Biomaterials 2011;32:9271.
[350] Scott JE. Collagen--proteoglycan interactions. Localization of proteoglycans in tendon by electron microscopy. Biochem. J 1980;187:887.
[351] Scott JE, Orford CR. Dermatan sulphate-rich proteoglycan associates with rat tail-tendon collagen at the d band in the gap region. Biochem. j 1981;197:213.
[352] Duplan-Perrat F, Damour O, Montrocher C, Peyrol S, Grenier G, Jacob M-P, Braye F. Keratinocytes Influence the Maturation and Organization of the Elastin Network in a Skin Equivalent1. Journal of investigative dermatology 2000;114:365.
[353] Tsuji T, Hamada T. Age-related changes in human dermal elastic fibres. British Journal of Dermatology 1981;105:57.
[354] Scott JE, Haigh M. Proteoglycan-type I collagen fibril interactions in bone and non-calcifying connective tissues. Bioscience reports 1985;5:71.
[355] Shergold OA, Fleck NA, Radford D. The uniaxial stress versus strain response of pig skin and silicone rubber at low and high strain rates. International Journal of Impact Engineering 2006;32:1384.
[356] Broom ND. The stress/strain and fatigue behaviour of glutaraldehyde preserved heart-valve tissue. Journal of Biomechanics 1977;10:707.
[357] Lu H, Ko Y-G, Kawazoe N, Chen G. Cartilage tissue engineering using funnel-like collagen sponges prepared with embossing ice particulate templates. Biomaterials 2010;31:5825.
[358] Silva MMCG, Cyster LA, Barry JJA, Yang XB, Oreffo ROC, Grant DM, Scotchford CA, Howdle SM, Shakesheff KM, Rose FRAJ. The effect of anisotropic architecture on cell and tissue infiltration into tissue engineering scaffolds. Biomaterials 2006;27:5909.
[359] Colazzo F, Chester AH, Taylor PM, Yacoub MH. Induction of Mesenchymal to Endothelial Transformation of Adipose-Derived Stem Cells. Journal of Heart Valve Disease, vol. 19, 2010. p.736.
[360] Huang W, Xiao D-Z, Wang Y, Shan Z-X, Liu X-Y, Lin Q-X, Yang M, Zhuang J, Li Y, Yu X-Y. Fn14 Promotes Differentiation of Human Mesenchymal Stem Cells into Heart Valvular Interstitial Cells by Phenotypic Characterization. Journal of Cellular Physiology 2014;229:580.
[361] Dong J-d, Gu Y-q, Li C-m, Wang C-r, Feng Z-g, Qiu R-x, Chen B, Li J-x, Zhang S-w, Wang Z-g, Zhang J. Response of mesenchymal stem cells to shear stress in tissue-engineered vascular grafts. Acta Pharmacologica Sinica 2009;30:530.
[362] Engelmayr GC, Jr., Sales VL, Mayer JE, Jr., Sacks MS. Cyclic flexure and laminar flow synergistically accelerate mesenchymal stem cell-mediated engineered tissue formation: Implications for engineered heart valve tissues. Biomaterials 2006;27:6083.
[363] Park JS, Chu JSF, Cheng C, Chen F, Chen D, Li S. Differential effects of equiaxial and uniaxial strain on mesenchymal stem cells. Biotechnology and bioengineering 2004;88:359.
[364] Riha GM, Wang X, Wang H, Chai H, Mu H, Lin PH, Lumsden AB, Yao Q, Chen C. Cyclic strain induces vascular smooth muscle cell differentiation from murine embryonic mesenchymal progenitor cells. Surgery 2007;141:394.

[365] Jawad MH. Design of plate and shell structures: New York, NY: ASME Press; Professional Engineering Publishing, 2004.
[366] Gere JM, Timoshenko SP. Mechanics of Materials. Cheltenham: Stanley Thornes Ltd, 1999